Title

Characterization of Effective Built-in Curling and Concrete Pavement Cracking on the Palmdale Test Sections

Authors

Rao, Shreenath
Roesler, Jeffery R.

Publication Date

2005-05-01

Peer reviewed

DRAFT

Characterization of Effective Built-in Curling and Concrete Pavement Cracking on the Palmdale Test Sections

By:

Shreenath Rao and Jeffery Roesler, Ph.D., P.E.

University of Illinois at Urbana-Champaign
Urbana, Illinois

University of California Berkeley
Institute of Transportation Studies
Pavement Research Center

May 2005

TABLE OF CONTENTS

LIST OF FIGURES

LIST OF TABLES

LIST OF ACRONYMS AND ABBREVIATIONS

AASHTO	American Association of State Highway and Transportation Officials
AC	Asphalt Concrete
APT	Accelerated Pavement Testing
ASTM	American Society for Testing and Materials
Caltrans	California Department of Transportation
CB	Corner Break
COV	Coefficient of Variation
CSIR	Council for Scientific and Industrial Research
DMD	Deflection Measurement Devices
EBITD	Effective Built-In Temperature Difference
EICM	Enhanced Integrated Climatic Model
ESAL	Equivalent Single Axle Load
FHWA	Federal Highway Administration
FSHCC	Fast-Setting Hydraulic Cement Concrete
FD	Fatigue Damage
FWD	Falling Weight Deflectometer
HRWR	High-Range Water Reducer (Superplasticizer)
HVS	Heavy Vehicle Simulator
HWD	Heavy Weight Deflectometer
LC	Longitudinal Crack
LEFM	Linear Elastic Fracture Mechanics
LLPRS	Long Life Pavement Rehabilitation Strategies
LTE	Load Transfer Efficiency
LVDT	Linear Variable Displacement Transducer
MDD	Multi Depth Deflectometer
MR	Modulus of Rupture
PCA	Portland Cement Association
PCC	Portland Cement Concrete
RH	Relative Humidity
RMS	Root Mean Square

SD	Standard Deviation
SEL	Size Effect Law
SR	Stress Ratio
TC	Transverse Crack
TELTD	Total Effective Linear Temperature Difference
UCB	University of California, Berkeley

ABSTRACT

Differential expansion and contraction between the top and bottom of a concrete slab results in curling. Curling affects stresses and deflections and is an important component of any mechanistic-empirical design procedure. A significant portion of curling can be attributed to the combined effects of nonlinear "built-in" temperature gradients, irreversible shrinkage, moisture gradients, and creep, which can be represented by an effective built-in temperature difference (EBITD).

Several instrumented test sections utilizing several design features were constructed and evaluated using the Heavy Vehicle Simulator (HVS) in Palmdale, California. These instrumented slabs were loaded with a half-axle edge load without wander in order to study the effects of curling and fail the slab sections under accelerated pavement testing. A procedure for estimating EBITD using loaded slab deflections was developed using the HVS results. The advantages of using loaded slab deflections are that they can be used for measuring EBITD of slabs with high negative built-in curl and can also be adapted for a Falling Weight Deflectometer, making the procedure efficient and cost-effective for the back-calculation of EBITD of in-service pavements. Differences in restraints and variability in concrete material properties resulted in EBITDs ranging from –5ºC to greater than –30ºC.

The HVS field tests were also used to examine Miner's hypothesis along with various fatigue damage models. Results indicate test slabs cracked at cumulative damage levels significantly different from unity. New models that incorporate stress range and loading rate along with peak stresses were developed. The coefficients for these models were developed to incorporate transverse cracking, longitudinal cracking, and corner breaks. The models can also be used for slabs that exhibit high negative EBITD. For slabs susceptible to high shrinkage gradients, microcracking resulting from restraint stresses during early ages can significantly

reduce the slab's nominal strength. Early-age restraint can vary considerably from one slab to another, depending on restraint. A procedure to model slab strength reduction and slab size was developed using nonlinear fracture mechanics principles. A parameter called the "effective initial crack depth" is introduced to characterize the early-age surface microcracking.

ACKNOWLEDGEMENT

The research included in this paper was conducted under a grant from the University of California at Berkeley Pavement Research Center and the support of the California Department of Transportation (Caltrans). Their support of the research effort is greatly appreciated.

1.0 INTRODUCTION

Like many porous materials, concrete expands and contracts with changes in temperature and moisture content. The influence of temperature and moisture gradients through the concrete slab depth on slab responses has long been recognized by researchers. Hatt (1925) was one of the first researchers to report that curling of the slab could occur due to temperature and moisture differences within the concrete slab. Carlson (1934) conducted experiments on slabs drying from the top and observed that greater moisture loss and shrinkage occurred near the exposed concrete surface. Temperature and moisture gradients through the vertical profile of a slab result in differential expansion and contraction between the top and the bottom of the slab. The expansion of the top of the slab relative to the bottom results in a convex curvature (downward curl) and is equivalent to a void beneath the middle of the slab. Contraction of the top of the slab relative to the bottom results in a concave curvature (upward curl) and is equivalent to voids beneath the corners and edges of the slab.

Hveem (1949) defined curling as "the tendency of a concrete pavement to bend or warp, usually developing high joints" and was one of the first researchers to study the cracking and failure of curled concrete pavement slabs in detail, as seen in his diagrammatic sketches showing the progress of a truck and trailer unit across a series of 6.1-m slabs (Figure 1-1). He stated that "…both moisture and temperature are prone to vary throughout the depth of the slab and it is inevitable that the expansion or shrinkage of a concrete pavement will rarely be confined to simple horizontal movement alone…It is almost certain that the expansion or contraction will be greater either on the surface or on the underside of the slab with the result that any overall expansion is invariably accompanied by warping or curling of the slabs." He observed that the length of the slab that departs from the plane of the pavement (curled unsupported portion of the slab) ranges from 1 to 2 m in length for California pavements. In referring to Figure 1-1, Hveem

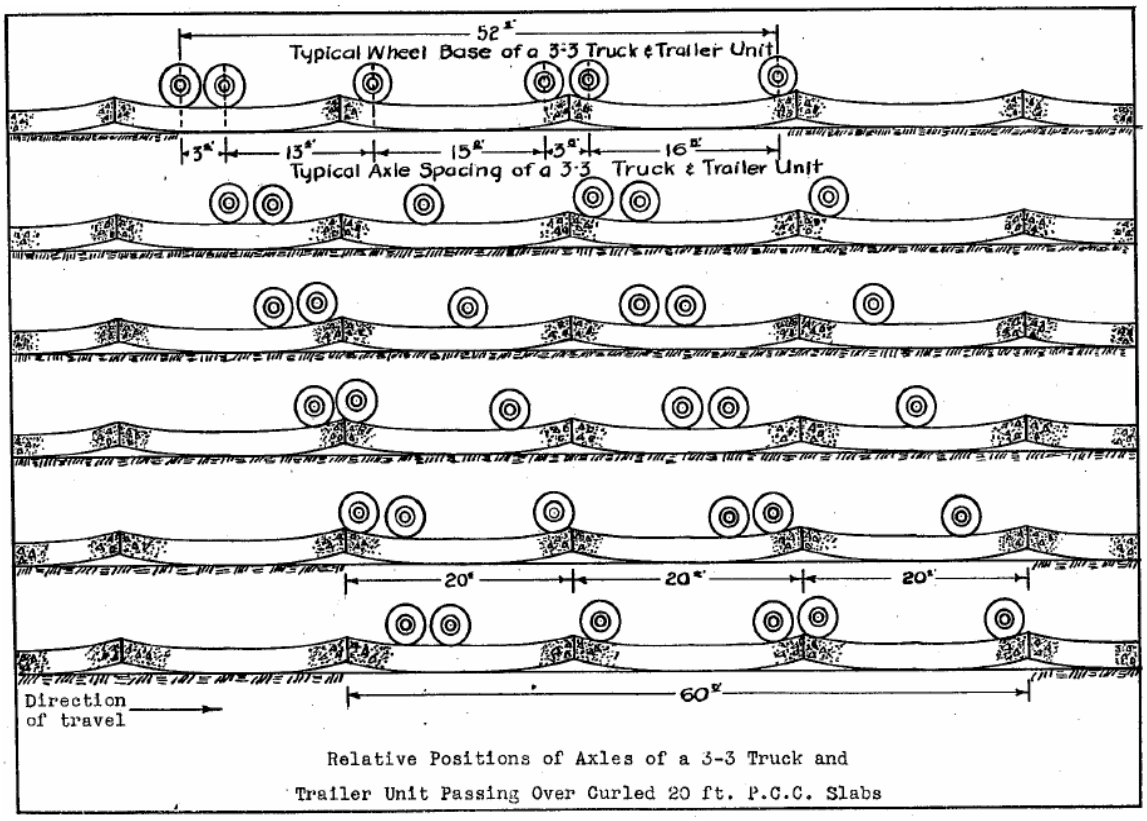

1 ft = 0.305 m

Figure 1-1. Progress of truck and trailer unit across curled concrete slabs (from Hveem, 1949).

added that "The rapid progress of such a truck and trailer unit across each slab from left to right produces many very complicated stresses and reaction in the slab."

Curling of a concrete slab in the field is restrained by the slab's self-weight, shoulder and adjacent slabs through aggregate interlock, load transfer devices, and tie bars, and through nonuniform friction between the base layer and concrete slab (Poblete et al., 1987; Rao and Roesler, 2005A). This restraint may vary from one location of the slab to another, resulting in asymmetric curling of the slab as shown in Figure 1-2, and from one slab to another, resulting in variability in performance of the slabs. The resulting loss of contact between the slab and the

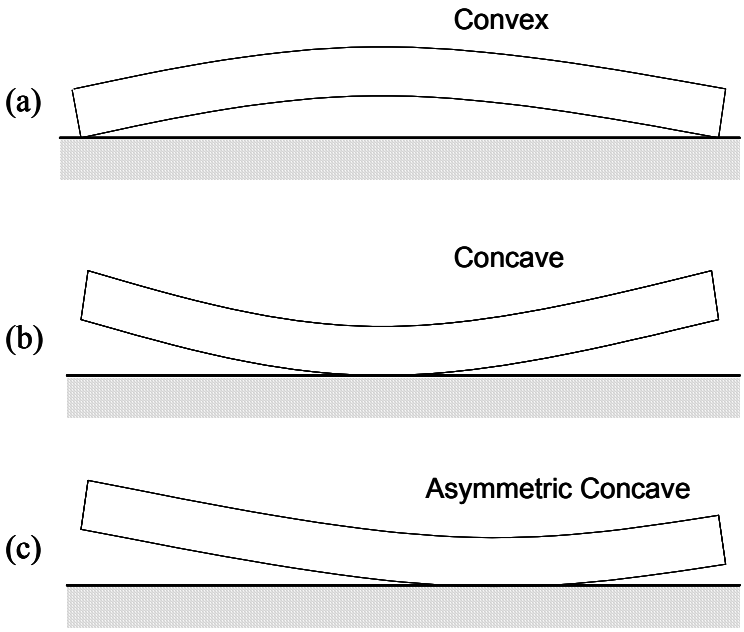

Figure 1-2. Slab shapes deformed by curling (side view).

base due to curling causes increased stresses and deflections, and consequently, increased slab cracking, which is one of the primary modes of failure in jointed plain concrete pavements.

1.1 Problem Statement

It is widely accepted that curling is a significant factor that affects the cracking performance of concrete pavements. One of the first procedures to include curling in concrete pavement design was presented in the Zero-Maintenance study (Darter and Barenberg, 1977) and was also a key aspect in the 2002 Design Guide (Yu et al., 2004). Curling is a crucial consideration in the design of concrete pavements using mechanistic-empirical design procedures (Zollinger and Barenberg, 1989; Darter et al., 2001; Hiller and Roesler, 2002). As such, a thorough characterization of curling and its influence on the long-term cracking performance of a slab is imperative to understanding concrete pavement behavior for use in design and construction of long-lasting concrete pavements.

1.1.1 Problem Statement One: Back-calculation of Effective Built-In Curling

As described in Chapter 3, curling is the result of a combination of five nonlinear components. One of these components is the nonlinear temperature gradients in the slab, which change over the course of a typical day, and can be measured using embedded thermocouples or other temperature measuring instruments. They can also be modeled with reasonable accuracy using programs such as the Enhanced Integrated Climatic Model (EICM) (Larson and Dempsey, 1997). The other four components—built-in temperature gradient, differential drying shrinkage, moisture gradients, and creep—change to a smaller extent through the life of the pavement and have traditionally been grouped together into an effective "built-in" curl. These components primarily develop during the early ages of the concrete.

Currently, no comprehensive procedure exists to model or estimate potential effective built-in curl based on material properties, ambient conditions during concrete set, curing conditions, and restraint mechanisms during set. Traditional methods of back-calculating built-in curling of in-service pavements using unloaded slab deflections have been cumbersome and involve instrumentation and measurement of movement of individual slabs over a 24-hour period. As a result, very little information exists on the magnitude of effective built-in curl and how various design features affect it. The available information on built-in temperature curling is limited to a handful of research projects.

Due to this limitation, in the development of the 2002 Design Guide, while moisture gradients were modeled using monthly/seasonal fluctuations in ambient relative humidity, the other three components of the effective built-in curl were grouped together as the "permanent" curl and obtained through calibration as –5.6ºC (Yu et al., 2004). While this value may be used as an average value representative of a large number of test sections across the country, it would

likely have less validity for use in the analysis of individual sections, and more specifically, individual slabs for which the magnitude of built-in curl can deviate significantly from the mean.

Another drawback of the traditional methods of back-calculating built-in curl is that they cannot be used for slabs with high negative built-in curl because the slab corners never come in contact with the base.

To overcome these drawbacks, a procedure to back-calculate built-in curl based on loaded slab deflections was developed. The load can be either traffic loading, such as using a Heavy Vehicle Simulator (HVS), or simulated loading, such as using a Heavy Weight Deflectometer (HWD) or a Falling Weight Deflectometer (FWD).

1.1.2 Problem Statement Two: Modeling Fatigue Damage in Concrete Pavements

Cracking in concrete pavements due to fatigue damage from repeated application of thermo-mechanical loading is a complex problem, the mechanisms of which are not clearly understood. It is generally accepted that high peak stresses contribute to early fatigue cracking. Existing procedures to model fatigue cracking use a "cumulative damage" approach, as detailed in Chapter 4. For new construction, the slab is assumed to start with zero initial damage and the damage due to each subsequent load application is added to the existing damage. The damage due to each load application is calculated as a function of the ratio of peak stress to flexural strength. The coefficients for this function are obtained through empirical calibration. In the development of existing procedures to model fatigue cracking, the contribution of other aspects of repeated loading, such as stress range, stress reversal, stress history, loading rate, variable load amplitude, etc., have not been included. The result is a loss of generality of the models. Also, as shown in Chapter 4, using peak stresses to calculate cumulative damage may result in discrepancies between predicted locations of maximum damage and observed cracking locations.

Another concern regarding the use of existing fatigue models is that while some were developed for failure of laboratory beam specimens, others do not incorporate curling stresses. Only two models—the calibrated mechanistic design model (Salsilli et al., 1993; Thompson and Barenberg, 1992) and the 2002 Design Guide model (Darter et al., 2001; Yu et al., 2004)—incorporate both load and curling stresses. None of the existing design procedures were calibrated for longitudinal cracking and corner breaks, or for slabs with high negative built-in curl.

While developing a process that accounts for all of the above-mentioned shortcomings of existing procedures is beyond the scope of this research, a model that incorporates stress range and loading rate along with peak stresses was developed. The procedure was calibrated for transverse cracking, longitudinal cracking, and corner breaks, and because of the inclusion of stress range, can also be used for slabs that exhibit high negative built-in curl.

1.1.3 Problem Statement Three: Modeling Fatigue Damage in Concrete Pavements

In existing procedures for modeling fatigue cracking, for a given project, all slabs are assumed to have equal strength. Variability within a project is incorporated through transfer functions that relate fatigue damage to percent slabs cracked. The coefficients for the transfer functions are obtained through calibration and typically correspond to 50 percent slab cracking for cumulative damage of 1.0. However, this approach is not suitable for analysis of individual slabs. For concrete slabs that are susceptible to high shrinkage gradients, restraint stresses during early ages can significantly reduce the nominal strength of the slab, as elaborated in Chapter 5. Early-age restraint can vary considerably from one slab to another, depending on slab self-weight, slab-base friction, and load transfer with adjacent slabs and shoulders. Therefore, large differences can exist in the performance of individual slabs. A secondary consideration is that

slabs of all thicknesses are assumed to have equal strength. However, fracture mechanics principles suggest that the nominal strength of concrete decreases with increase in size.

A procedure to model slab strength reduction due to surface microcracking from early-age restraint stresses and slab size was developed using nonlinear fracture mechanics principles. A new parameter called the "effective initial crack depth" is introduced to characterize the early-age microcracking at the slab surface.

1.2 Research Objective

The principal objective of the research study was to characterize curling, particularly the "built-in" component of curling, and to develop a nondestructive procedure to back-calculate effective built-in curling of in-service pavements. The second objective of the research was to develop a fatigue cracking failure model that can be more generally applicable than current fatigue models, and that is inclusive of slabs that exhibit significant curling and reduction in strength due to microcracking caused by early-age restraint stresses that developed as a result of differential shrinkage between the top and bottom of the slab. Field-test data of full-scale instrumented test sections loaded past fatigue failure using a Heavy Vehicle Simulator (HVS) were used to accomplish the research objectives. The following three hypotheses are proposed, developed, and validated through this research:

- Hypothesis 1: Back-calculation of built-in curl based on loaded slab deflections is an enhancement over methods based on unloaded slab deflections.
- Hypothesis 2: A fatigue model that incorporates both peak stresses and stress ranges is more generally applicable and is an improvement over existing fatigue models that only use peak stresses.

- Hypothesis 3: A fracture mechanics-based approach can be used to account for the large variability in performance of individual slabs due to disparities in nominal strengths between slabs resulting from differences in early-age restrained microcracking.

The product of this research is an improved procedure for back-calculation of effective built-in curl and an enhanced understanding of cracking behavior in concrete pavement slabs due to built-in curling and combined thermo-mechanical loading.

1.3 Field Test Background

As part of the Caltrans Long Life Pavement Rehabilitation Strategies (LLPRS), a high early strength hydraulic cement concrete pavement section was field tested using an HVS, illustrated in Figure 1-3 and shown in Figure 1-4. Two full-scale test pavement sections, each approximately 210 m in length, were constructed on State Route 14 about 8 km south of Palmdale, California, using an 80/20 blend of Ultimax® to Type II portland cement. The test sections were located adjacent to the in-service pavement, one on the north side of the highway ("North Tangent") and one on the south side of the highway ("South Tangent"). The sections were constructed using three different design thicknesses and design features (dowels, tie bars, and widened truck lanes). This fast-setting hydraulic cement concrete (FSHCC) was designed to gain enough strength to allow it to be opened to traffic within 4 hours of placement. The objective of the HVS tests was to evaluate the performance of these full-scale pavement test sections under the influence of controlled loading and both controlled and ambient temperature conditions.

Overall weight		59,646 kg
Load weight of the test wheel tire		20-100 kN with truck tire 20-200 kN with aircraft tire
Dimensions of tested area of pavement		1.5 m × 8 m maximum
Velocity of the test wheel		10 km/hr maximum
Maximum trafficking rate		1000 repetitions/hr
Average trafficking rate		750 repetitions/hr
Average daily repetitions		16,000
Dimensions:	Length	22.56 m
	Width, overall	3.73 m
	Height	3.7 m
	Wheel base	16.7m
Number of axles		3 (1 in rear, 2 in front)

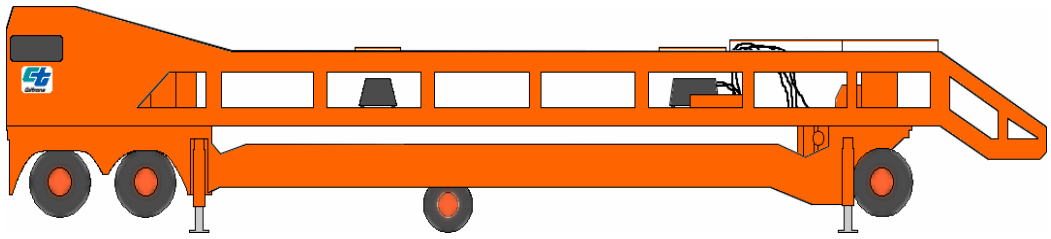

Figure 1-3. Diagram and specifications of the Heavy Vehicle Simulator (adapted from Roesler et al., 2000).

Figure 1-4. Heavy Vehicle Simulator with temperature control chamber (from du Plessis, 2002B).

1.4 Calculation Engine—Finite Element Program ISLAB2000

The finite element program ISLAB2000 (Khazanovich et al., 2000), was used during several stages of the research. ISLAB2000 is the latest version of ILLI-SLAB, a two-dimensional finite element program developed at the University of Illinois (Tabatabaie, 1977; Tabatabaie and Barenberg, 1980). The program was developed for the analysis of one- and two-layer jointed concrete pavement systems, with or without mechanical load transfer system at the joints. ILLI-SLAB is based on medium-thick plate theory over a dense liquid or Winkler foundation (Timoshenko et al., 1959), and can be used to evaluate the structural response of a pavement system with any slab size, joint locations, and load location, size, and configuration. Through the years, ILLI-SLAB has undergone a number of improvements and additions, including the incorporation of different subgrade support models and nonlinear temperature gradients, resulting in a significant enhancement of its modeling capabilities (Ioannides et al., 1985; Khazanovich, 1994). ILLI-SLAB has been widely tested over the past 20 years. The results of the finite element analysis using ILLI-SLAB were found to be comparable to available theoretical solutions and experimental studies (Tabatabaie et al., 1979; Ioannides et al., 1985).

The following assumptions are inherent in the use of plate theory, ILLI-SLAB, and ISLAB2000 for the structural analysis of concrete pavements:

1. Slab and base layers are elastic, homogeneous, medium-thick plates.
2. All forces on the surfaces of the slab are normal to the surfaces—no shear forces are present on surfaces.
3. The slab is of uniform stiffness—constant elastic modulus and thickness.
4. There are no in-plane forces.
5. Deformations within the elements normal to the slab surfaces are small and can be ignored—slab will not change in thickness when load is applied.

6. Shear deformations are small compared with bending deformations and can be ignored.
7. Full strain compatibility exists at a bonded interface, while shear stresses at unbonded interfaces are zero.
8. Dowel bars are linear elastic and located at the neutral axis of the slab.
9. When the load transfer between adjacent slabs is through aggregate interlock, only shear load is transferred from one slab to another. Both moment and shear are transferred across joints when dowel bars are used.

The ILLI-SLAB Fortran code was rewritten for ISLAB2000 in C++ to take advantage of the greater efficiency and power in the execution of mathematical functions, to increase analysis capacity, and to fix some known bugs in ILLI-SLAB thus improving program reliability. A graphical user interface was also included to process input data factorially, automate finite element grid generation, and display output results. Recently, ISLAB2000 was extensively used as the principal calculation engine for rigid pavement analysis in the 2002 Design Guide (Darter et al., 2001).

1.5 Research Methodology and Chapter Organization

The field data and laboratory data used in this research were collected by the Pavement Research Center at the University of California at Berkeley (UCB) and its subcontractors, Dynatest, Inc., and the Roads and Transport Technology Division of the Council for Scientific and Industrial Research (CSIR) of South Africa as part of the Accelerated Pavement Testing (APT) program undertaken by Caltrans. Details of the field project, instrumentation, data collection, results of relevant laboratory testing, and a performance summary of test sections, are included in Chapter 2.

The objective of characterizing curling and the modeling of fatigue cracking in curled concrete pavements were achieved in three stages. The first stage, covered in Chapter 3, entailed development of a non-destructive procedure to estimate effective built-in curling of existing slabs and identification of factors that affect curling in field concrete slabs. Field-measured loaded and unloaded slab deflections, vertical slab temperature profiles, and joint load transfers, along with slab geometries, subgrade support conditions, and layer material properties, were used as inputs to ISLAB2000. The results of the finite element analysis were used to develop a detailed procedure to back-calculate built-in curling at several slab locations. The procedure was also adapted for slab corner loading using the deflections from a falling weight deflectometer (FWD). The 20 to 80 kN incremental loading data from the test sections along with the FWD results were used to validate the built-in curling back-calculation procedure. The back-calculated curling results from the test slabs were used to quantify the influence of various design features such as slab thickness, joint spacing, use of load transfer devices, tied concrete shoulders, etc., on effective built-in curl, and to identify factors that affect it.

Chapter 4 presents the second part of the research study: the development of a new procedure for modeling fatigue cracking. Several existing fatigue cracking models were first evaluated using the repeated loading results of the field test sections. Peak stresses at critical locations for each load application on a particular test slab were computed using ISLAB2000 for all test slabs. The peak stresses were used in the fatigue models to calculate damage at the critical location due to that single load application. For each field test section, the cumulative damage was calculated for all load applications until the first observed crack. For the development of the new procedure, a static rolling wheel analysis was used to compute peak stresses and stress ranges, which were then used to obtain coefficients for an improved fatigue model that

incorporates nonlinearity of temperature and moisture gradients, stress range due to moving load, and loading frequency.

Chapter 5 presents the third segment of the research. In this segment, fracture mechanics principles were used in the new fatigue cracking model to account for size effect due to slab thickness and the reduction in strength resulting from early-age surface microcracking due to restrained differential shrinkage. A finite element program that models cracked slabs, ILSL962, was used to develop the geometric factor, which in turn, was used to model the effect of size and crack depth on the slab nominal strength. A parameter called the "effective initial crack depth" was introduced to represent the early-age microcracking at the slab surface. The effective initial crack depth for the field test slabs were used to modify the fatigue model to incorporate the effect of differences in restraints among slabs.

Chapter 6 presents the conclusions from all three stages of the research project and recommendations for further research.

2.0 FIELD PROJECT AND DATA COLLECTION

Two full-scale test pavement sections incorporating multiple slab thicknesses and design features were constructed near Palmdale, California. These sections are located on the north and south sides adjacent to State Route 14, and are referred to as the North Tangent and the South Tangent. The sections were constructed to evaluate the performance of full-scale instrumented concrete pavement test slabs under the influence of controlled loading using the HVS, and both controlled and ambient temperature conditions. The experiment design, along with construction, instrumentation, collection and documentation of all laboratory and field data, were performed by the Pavement Research Center at UCB and its subcontractors. A summary of the experimental layout, loading history, instrumentation and field data collection relevant to this research, is included in this chapter. Also included are summaries of relevant material properties obtained from laboratory tests and the field-observed cracking performance of all test sections.

2.1 Layouts and Details of Test Sections

Various test sections, consisting of combinations of concrete slab thicknesses, base types, tied concrete shoulders, doweled transverse joints, and widened lanes, were constructed and evaluated using the HVS over a 2-year period. The slab widths on the test sections were 3.7 m except for the widened lane sections, which were 4.2 m. The slabs had perpendicular transverse joints with joint spacing varying from 3.7 m to 5.8 m. The South Tangent was constructed with 100-, 150-, and 200-mm nominal thickness concrete slabs on 150-mm thick Class 2 aggregate base over a compacted granular subgrade. None of the pavement structures on the South Tangent had dowel bars, tie bars, or widened lanes.

The North Tangent sections were 200-mm nominal thickness concrete over 100-mm nominal thickness cement treated base with three design features: no dowels + asphalt concrete

shoulders, dowels + PCC shoulders, and dowels + widened lanes. Figure 2-1 and Figure 2-2 show the pavement structure diagrams for the South Tangent and North Tangent sections, respectively. A brief summary of the design features of all test sections is shown in Table 2-1.

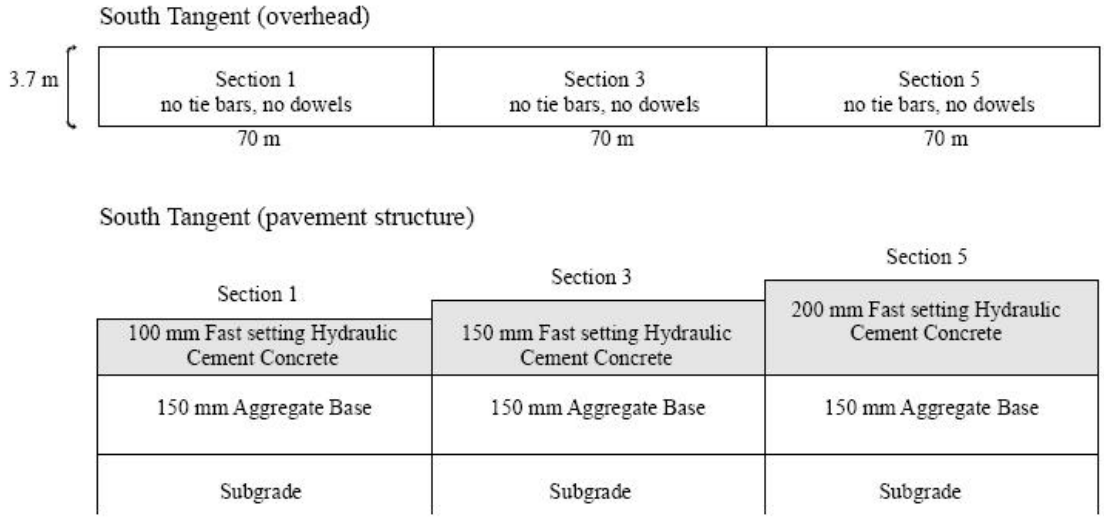

Figure 2-1. South Tangent layout and pavement structure diagram (from Roesler et al., 2000).

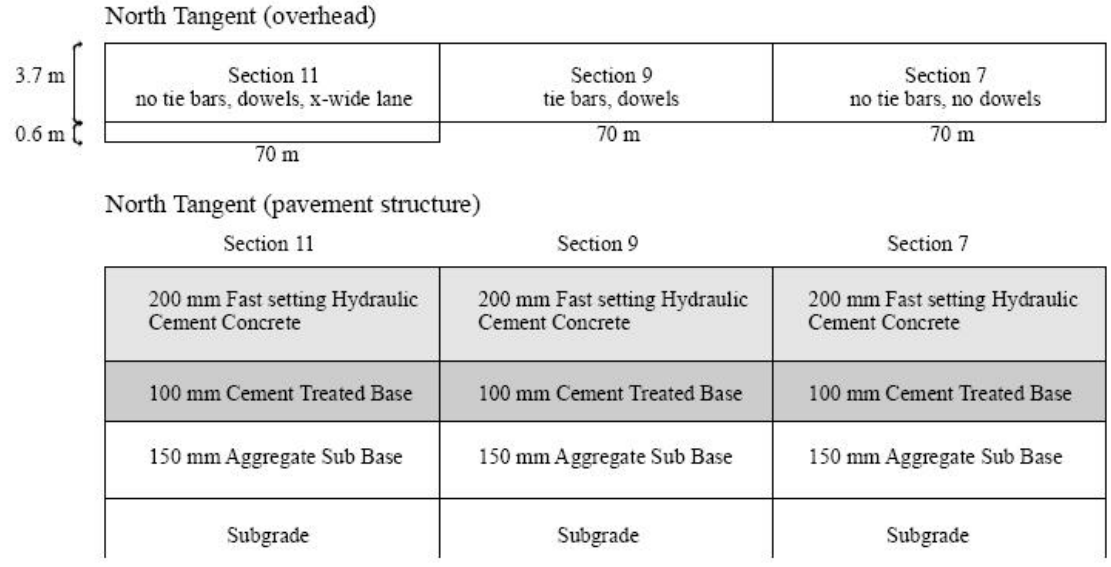

Figure 2-2. North Tangent layout and pavement structure diagram (from Roesler et al., 2000).

Table 2-1 Summary of Design Features and Properties

Section Location and Base Type	Section ID	Load Transfer Devices	Shoulder Type	Nominal Design Thickness, mm	Actual Slab Thickness, mm	Concrete Density, kg/m^3	Joint Spacing: Left Slab-Test Slab-Right Slab, m
South Tangent 150mm aggregate base	519FD	None	AC	100	94	2,480	5.42 5.81 3.97
	520FD				109	2,450	5.45 5.78 4.03
	521FD				129	2,440	5.51 5.77 3.78
	522FD*				114	2,390	3.98 3.69 5.51
	523FD	None	AC	150	171	2,370	3.63 5.49 5.83
	524FD				165	2,420	5.60 5.72 3.98
	525FD				175	2,400	5.78 3.89 3.61
	526FD				185	2,390	5.80 4.01 3.56
	527FD				170	2,400	3.89 3.61 5.60
	528FD	None	AC	200	195	2,420	5.73 4.03 3.60
	529FD				188	2,400	5.84 3.95 3.65
	530FD				220	2,440	5.78 3.96 3.67
	531FD				204	2,420	3.93 3.70 5.39
North Tangent 100mm cement-treated base over 150mm aggregate base	532FD	None	AC	200	225	2,350	5.82 3.95 3.64
	533FD				220	2,240	5.79 4.03 3.65
	534FD				228	2,310	5.91 3.86 3.90
	535FD				220	2,470	4.11 3.71 5.35
	536FD	Dowel bars	Tied concrete	200	220	2,350	5.81 3.96 3.62
	537FD				213	2,290	5.78 3.94 3.66
	538FD				221	2,390	5.86 3.92 3.75
	539FD	Dowel bars	600 mm widened lane with AC	200	203	2,420	5.86 3.85 3.71
	540FD				223	2,420	5.86 3.80 3.80
	541FD				244	2,390	5.91 3.89 3.67

*Static load test – not used in analysis

2.2 Loading History

All dynamic data was collected with the HVS wheel running at creep speed (2 km per hour) for the South Tangent sections and two North Tangent sections (532FD and 533FD), and 10 km per hour for the rest of the North Tangent sections. The loads were applied through a dual truck wheel (tire pressure = 690 kPa) or single aircraft wheel configuration (tire pressure = 1,100 kPa), typically bi-directionally (with the exception of two North Tangent sections run uni-directionally), and without any wheel wander. HVS tests were run past fatigue failure to observe the performance of the slabs after the initial crack. Temperature control was used on some of the tests while others were performed under ambient conditions. Prior to fatigue loading, some of the

North Tangent slabs were monitored over a 24-hour cycle without any applied load, and over a 24-hour cycle under a slow-moving 40-kN rolling load using the HVS. The construction date, fatigue testing dates, testing conditions, and loading history for all test sections are shown in Table 2-2.

2.3 Data Collection and Instrumentation

Data collected at two-hour intervals included visual distress surveys, vertical temperature profile measured using thermocouples, mid-slab edge and corner surface deflections measured using Deflection Measuring Devices (DMDs), and vertical deflections (interior slab location) at multiple depths of the pavement structure measured using Multi-Depth Deflectometers (MDDs). Thermocouples were taped and spaced on wooden dowels in order to measure the temperature at the top, mid-depth, and bottom of the concrete slab. For North Tangent sections, thermocouple stacks were placed at four locations on each test section: in the sun, in the shade of the HVS, inside the temperature control area, and near the traffic barrier (k-rail). A typical instrumentation layout for a North Tangent test section (Section 535FD) is shown in Figure 2-3. Other environmental data such as rainfall, wind direction, and wind speed were continuously recorded using a Davis automatic weather station. Detailed descriptions of all devices, including their placement and installation at the Palmdale test site, are covered in Roesler et al. (2000). Instrumentation layout details specific to individual test sections are included in du Plessis (2002A and 2002B).

Table 2-2 Construction Date, Fatigue Testing Dates, and Loading History

Section ID	Construction Date	Testing Start Date	Testing End Date	Temperature Control Box Used During Testing?	Load, kN	Load Repetitions	Cumulative Load Repetitions
519FD	06/11/98	07/15/98 (34)	07/19/98 (38)	Yes	25 50 100	55,448 984 3,731	55,448 56,432 60,163
520FD	06/11/98	07/23/98 (42)	07/30/98 (49)	Yes	35 100	51,240 23,080	51,240 74,320
521FD	06/11/98	08/10/98 (60)	08/28/98 (78)	Yes	20 80	157,719 10,600	157,719 168,319
522FD*	06/11/98	09/02/98 (83)	09/02/98 (83)	Ambient	n/a	n/a	n/a
523FD	06/11/98	09/14/98 (95)	09/29/98 (110)	Yes	45	151,151	151,151
524FD	06/11/98	10/02/98 (113)	10/13/98 (124)	Yes	45	119,784	119,784
525FD	06/11/98	10/15/98 (126)	10/18/98 (129)	Ambient	45	5,000	5,000
526FD	06/11/98	10/19/98 (130)	10/22/98 (133)	Yes	85	23,625	23,625
527FD	06/11/98	10/26/98 (137)	01/21/99 (224)	Ambient	35	1,233,969	1,233,969
528FD	06/11/98	01/27/99 (230)	02/02/99 (236)	Yes	40	83,045	83,045
529FD	06/11/98	02/07/99 (241)	03/04/99 (266)	Ambient	40 60	88,110 264,214	88,110 352,324
530FD	06/10/98	03/10/99 (273)	05/14/99 (338)	Yes	40 60 90	64,227 752,447 30,170	64,227 816,674 846,844
531FD	06/10/98	05/19/99 (343)	05/21/99 (345)	Yes	40 60	31,318 33,997	31,318 65,315
532FD	06/18/98	06/07/99 (354)	07/26/99 (403)	Yes	40 70	24,337 177,965	24,337 202,302
533FD	06/18/98	08/06/99 (414)	11/01/99 (501)	Yes	40 70 90	44,164 210,003 116,983	44,164 254,167 371,150
534FD	06/17/98	12/15/99 (546)	03/14/00 (636)	Yes	40 70 90	126,580 858,022 299,758	126,580 984,602 1,284,360
535FD	06/17/98	03/29/00 (651)	04/04/00 (657)	Yes	90	80,002	80,002
536FD	06/17/98	04/17/00 (670)	07/12/00 (756)	Yes	90 70A 90A 110A 130A 150A	750,000 500 500 500 500 88,450	750,000 750,500 751,000 751,500 752,000 840,450
				Ambient	150A	152,332	992,782
537FD	06/17/98	07/20/00 (764)	08/21/00 (796)	Ambient	40 70 90 150A	13,230 500 310,004 65,002	13,230 13,730 323,734 388,736
538FD	06/17/98	01/03/01 (931)	01/18/01 (946)	Ambient	70 90	500 188,882	500 189,382
539FD	06/16/98	09/01/00 (808)	09/29/00 (836)	Ambient	40 70 90	13,342 500 305,004	13,342 13,842 318,846
540FD	06/16/98	10/07/00 (844)	11/28/00 (896)	Yes	40 90 150A	13,003 392,062 142,398	13,003 405,065 547,463
541FD	06/16/98	12/02/00 (900)	12/27/00 (925)	Ambient	70 90 150A	500 167,777 110,011	500 168,277 278,288

*Static load test – not used in analysis
Number in parenthesis following start and end dates are days since construction
A = Aircraft load

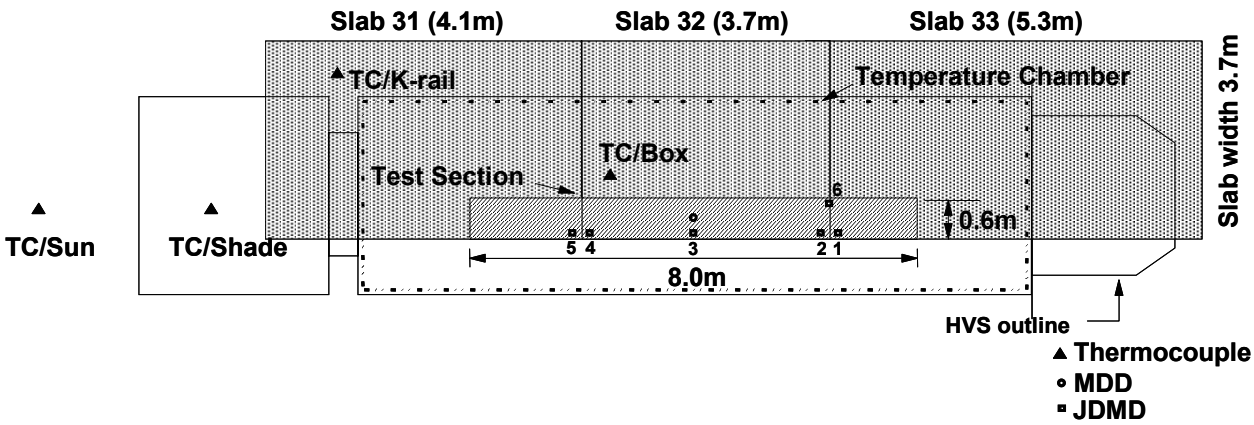

Figure 2-3. Instrumentation layout of North Tangent test Section 535FD (adapted from du Plessis, 2002B).

2.4 Data Collection and Instrumentation

Data collected at two-hour intervals included visual distress surveys, vertical temperature profile measured using thermocouples, mid-slab edge and corner surface deflections measured using Deflection Measuring Devices (DMDs), and vertical deflections (interior slab location) at multiple depths of the pavement structure measured using Multi-Depth Deflectometers (MDDs). Thermocouples were taped and spaced on wooden dowels in order to measure the temperature at the top, mid-depth, and bottom of the concrete slab. For North Tangent sections, thermocouple stacks were placed at four locations on each test section: in the sun, in the shade of the HVS, inside the temperature control area, and near the traffic barrier (k-rail). A typical instrumentation layout for a North Tangent test section (Section 535FD) is shown in Figure 2-3. Other environmental data such as rainfall, wind direction, and wind speed were continuously recorded using a Davis automatic weather station. Detailed descriptions of all devices, including their placement and installation at the Palmdale test site, are covered in Roesler et al. (2000). Instrumentation layout details specific to individual test sections are included in du Plessis (2002A and 2002B).

2.4.1 Deflection Measurement Devices

DMDs were used to measure vertical and horizontal joint displacement under dynamic loads and temperature changes. The DMDs consisted of Linear Variable Displacement Transducers (LVDTs), and were used to measure vertical displacements under combined rolling wheel and temperature loading. To measure vertical deflections, an anchor rod was driven into the ground adjacent to the slab for absolute deflection measurement at the slab edges and corners. An illustration of the placement of DMDs with respect to the test section is shown in Figure 2-4. DMDs were installed at the lane-shoulder edge and at only one of the two slab corners for the South Tangent Sections 519FD through 531FD, and the two North Tangent Sections 532FD and 533FD. For North Tangent Sections 534FD through 541FD, all DMDs shown in Figure 2-4 were installed.

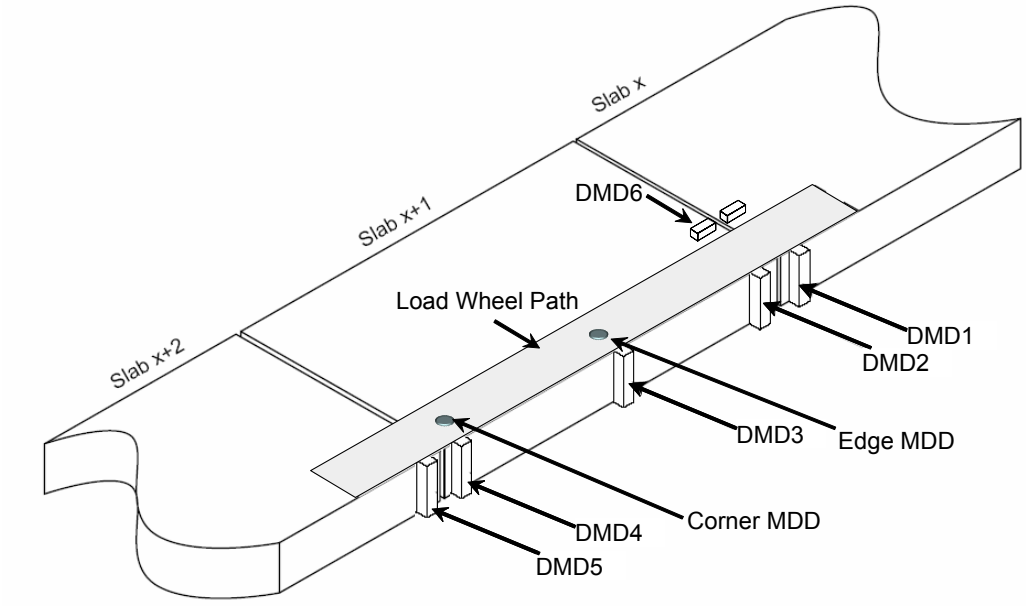

Sections 519FD – 533FD: DMD1 through DMD3.
Section 534FD: DMD1 through DMD5.
Sections 535FD – 541FD: DMD1 through DMD6.

Figure 2-4. Placement of deflection measurement device (DMD) sensors and multi-depth deflectometers (MDDs) relative to test section (adapted from du Plessis, 2002B).

2.4.2 Multi-Depth Deflectometers

For some of the test sections, MDDs were installed after pavement construction by drilling a 3.3-m deep hole from the surface of the pavement into the subgrade. An anchor was fixed with concrete at the bottom of the hole in the subgrade. A center rod consisting of ferrous material "slugs" that served as targets for the MDD modules was connected to the anchor. Each MDD module contained an LVDT that read displacement relative to the slugs. Each module was affixed to the sides of the hole at specified depths, to measure total pavement deflection above that location. A schematic of the MDD setup is shown in Figure 2-5. Figure 2-4 shows the typical location of MDDs on a test section relative to the DMD sensors and HVS wheel path.

2.4.3 Thermocouples

Type K thermocouples were placed in the test sections to read temperature at multiple depths. The thermocouples were continuously monitored by the data acquisition system.

2.4.4 Data Acquisition System

Deflection and temperature data under HVS loading was primarily collected using a National Instrument SCXI data acquisition system. The dynamic data system was triggered on and off by laser sensors at a fixed repetition interval. The dynamic system included a rotary encoder input from the HVS wheel in order to determine the position of the wheel relative to the deflection sensors on the pavement. The static data was collected using the CR10X system manufactured by Campbell Scientific. Four CR10X units were installed at the Palmdale test site: one on the South Tangent and three on the North Tangent. The units were placed approximately 4 m from the edge of the pavement. Each unit was placed in the ground and surrounded by a concrete containment box with a steel cover to prevent damage to the unit during construction.

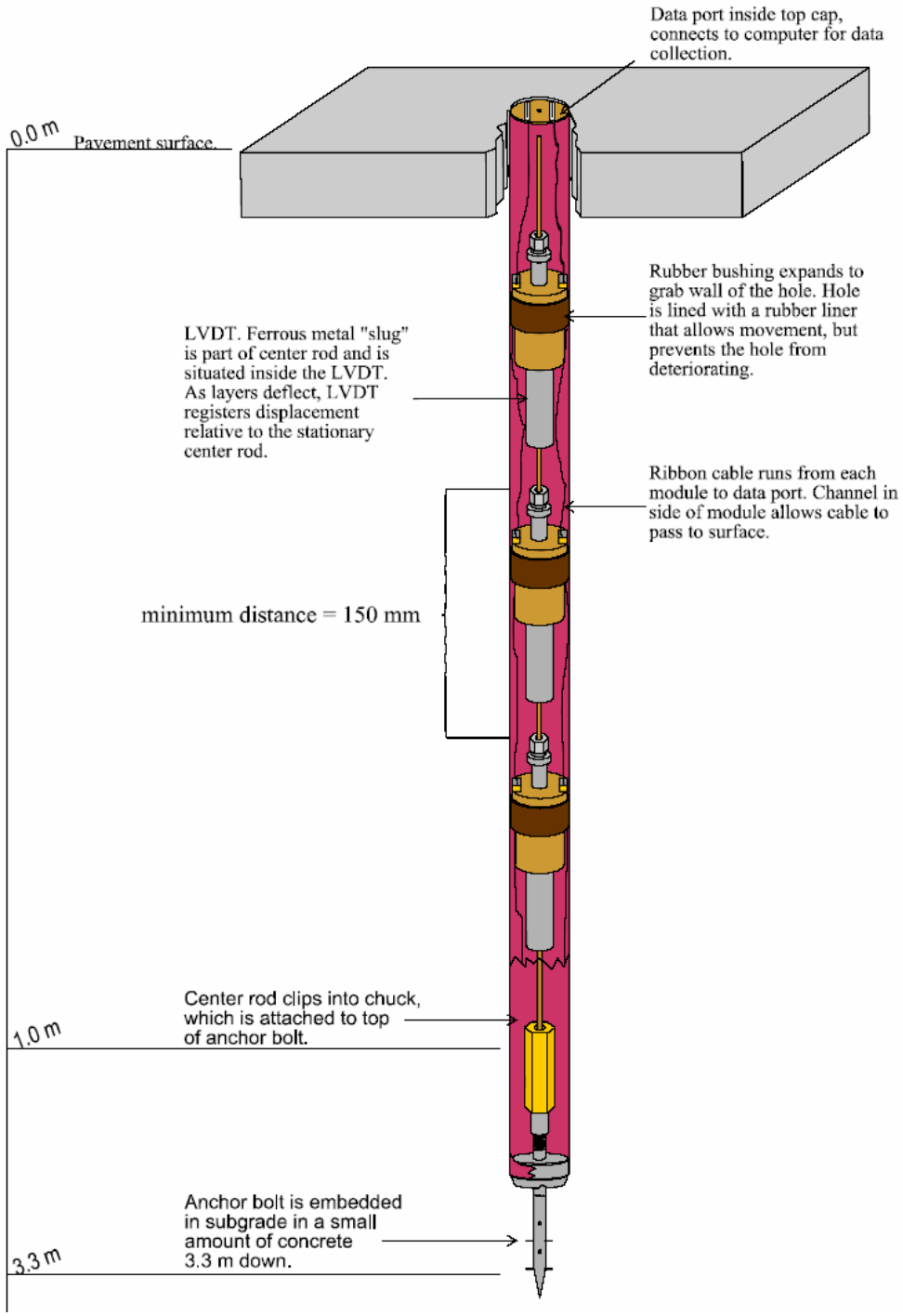

Figure 2-5. Schematic of multi-depth deflectometer array (from Roesler et al., 2000).

The system was used to continuously monitor and record data from thermocouples, LVDTs, MDDs, etc., due to the environment only. The stored data was then downloaded to a PC. Details of the data acquisition system and instrumentation of each section are included in Roesler et al. (2000) and du Plessis (2002A).

2.5 Material Properties

The concrete placed at the Palmdale test sections contained an 80/20 blend of Ultimax® to Type II portland cement, and included one coarse aggregate, one fine aggregate, water, air entraining agent, and a retarder. The main chemical constituent of Ultimax cement is calcium sulfoaluminate. The proportion of each mix constituent (stock weights) for one cubic meter of mix is shown in Table 2-3. The coarse and fine aggregate had moisture contents of 1 and 4 percent greater than their saturated surface dry condition, respectively. The water-to-cement ratio was 0.39, which includes the mix water and excess water from the coarse and fine aggregate.

Table 2-3 Target FSHCC Mix Design (Stock Weights)

Mix Constituent	**Batch Weight, kg/m^3**
Coarse aggregate (25 mm maximum size)	1,080
Fine aggregate	848
Ultimax® cement	332
Type II portland cement	83
Water	117
Delvo® retarder (oz)	95.5
Micro-Air® air entraining agent (oz)	1.36

Inputs for finite element analysis and fatigue damage analysis of concrete slabs include material properties such as layer moduli, modulus of subgrade reaction, concrete coefficient of thermal expansion, and concrete modulus of rupture (flexural strength). These and other relevant properties such as concrete compressive strength and shrinkage characteristics for the Palmdale

concrete slabs were tested and reported by personnel at UCB and are summarized in the following sections.

2.5.1 Concrete Flexural Strength

The FSHCC used for the Palmdale test site construction was a blend of Ultimax® and Type II cement. The consistency of the concrete mix varied considerably from one truck to another. Many of the mixes arriving at the site were fairly inconsistent and often required the addition of water. Each of the six groups of sections (South Tangent groups 1, 3, and 5, and North Tangent groups 7, 9, and 11) required approximately 10 truckloads of concrete. For each group, two of these trucks were selected at random to cast beams for 8-hour, 7-day, and 90-day flexural strength tests. Two beams were tested at each of these ages for each truckload.

For the South Tangent sections, the average flexural strength increased over 90 percent from the 8-hour to the 7-day test. The 7- to 90-day average flexural strength gain was 30 percent. The variability in the 90-day flexural strength ranged from 11 to 22 percent. Much of the variation was due to the variation in strengths between beams taken from two separate trucks. Since several different truckloads were used for each test section, and only two trucks were tested for flexural strength, it was not possible to ascertain the flexural strength characteristics for each section on an individual basis. Because the variation in strength between trucks was higher than (or of the order of) the variation in strength between section groups, the average flexural strength values representative of all South Tangent test sections was used in the analysis. The average flexural strength of the beam specimens tested is summarized in Table 2-4. The strength gain curve based on the average for all South Tangent sections is shown in Figure 2-6. A strength gain model developed using the average laboratory flexural strength data is shown in Equation 2-1.

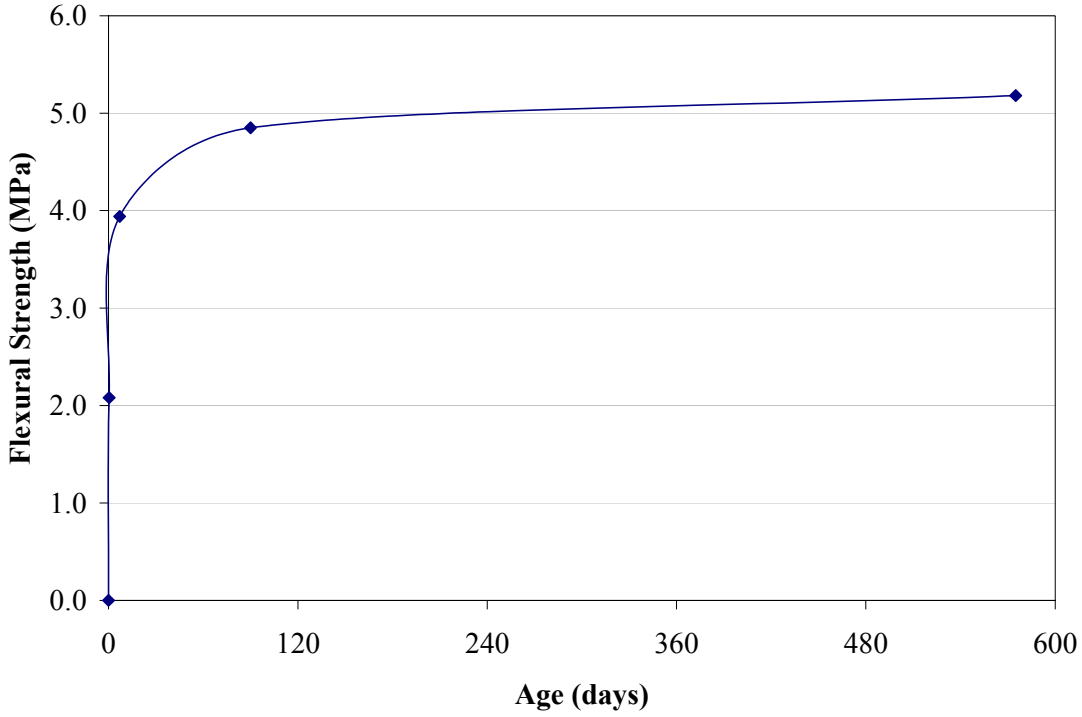

Figure 2-6. Average flexural strength gain curve for South Tangent test sections.

$$\textbf{FSHCC Flexural Strength (MPa)} = 0.0075A^3 - 0.2562A^2 + 1.491A + 2.858 \qquad \textbf{(2-1)}$$

where,
A = Log (Age since construction, days).

This strength gain curve was used to estimate the expected average strength for the South Tangent sections at the time of HVS testing based on age during testing as shown in Table 2-5. For simplicity of analysis and because of the high variability in FSHCC strength between different truckloads relative to the effect of average strength gain over time, the FSHCC strengths are combined into the three groups based on the nominal thicknesses. For the 100-mm nominal thickness sections, the average age during testing ranged from 36 days to 83 days, during which the average flexural strength is estimated as 4.71 MPa. For the 150-mm nominal

Table 2-4 Average Flexural Strengths for South Tangent Sections

Nominal Thickness (mm)	8 Hours			7 Days			90 Days			575 Days (North Tangent)		
	Mean (MPa)	SD (MPa)	COV (%)	Mean (MPa)	SD (MPa)	COV (%)	Mean (MPa)	SD (MPa)	COV (%)	Mean (MPa)	SD (MPa)	COV (%)
100	1.87	0.14	7	3.48	0.37	10	4.34	0.50	11			
150	1.92	0.60	31	3.86	0.71	18	4.92	1.10	22			
200	2.45	0.16	7	4.48	0.49	11	5.31	0.97	18			
All Sections	*2.08*	*0.39*	*19*	*3.94*	*0.65*	*17*	*4.85*	*0.90*	*19*	*5.18*	*0.25*	*5*

Table 2-5 Estimated Expected Average Flexural Strength for South Tangent Test Sections

Section ID	Average Age During HVS Testing (days)	Flexural Strength, MPa	Average Flexural Strength (MPa)
519FD	36	4.59	4.71
520FD	46	4.66	
521FD	69	4.78	
522FD	83	4.83	
523FD	103	4.88	4.93
524FD	119	4.92	
525FD	128	4.93	
526FD	132	4.94	
527FD	181	5.00	
528FD	233	5.05	5.08
529FD	254	5.07	
530FD	306	5.10	
531FD	344	5.11	

thickness sections, the average age during testing ranged from 103 days to 181 days, with the average flexural strength estimated as 4.93 MPa. The average flexural strength for the 200-mm nominal thickness South Tangent test sections is estimated as 5.08 MPa. These slabs were tested at ages ranging from 233 to 344 days. The average age during HVS testing for the North Tangent sections ranged from 379 days to 913 days since construction. Therefore, the average long-term strength of 5.20MPa was used in analysis as the flexural strength for all North Tangent sections.

2.5.2 Concrete Compressive Strength

For each of the six groups of sections (South Tangent section groups 1, 3, and 5, and North Tangent section groups 7, 9, and 11) twelve cylinders were sampled from two random trucks per section. Of the six cylinders sampled per truck, two cylinders were tested for compressive strength (ASTM C 39) at 8 hours, two at 7 days, and two at 90 days. The results of the compressive strength testing are shown in Table 2-6. The average long-term compressive strength based on cores taken from test sections after completion of HVS testing was 61.7 MPa.

The gain in compressive strength shown in Figure 2-7 can be modeled using the following equation:

$$\textbf{FSHCC Compressive Strength (MPa)} = -0.0023A^3 + 1.555A^2 + 10.826A + 18.42 \qquad \textbf{(2-2)}$$

where,
A = Log (Age since construction, days).

Table 2-6 Average Compressive Strengths, Cylinder Specimens

	8 hours			7 days			90 days		
Location	**Mean (MPa)**	**SD (MPa)**	**COV (%)**	**Mean (MPa)**	**SD (MPa)**	**COV (%)**	**Mean (MPa)**	**SD (MPa)**	**COV (%)**
South Tangent	12.95	3.43	26	26.22	5.37	20	45.99	8.24	15
North Tangent	14.19	1.47	10	31.15	3.65	12	45.02	7.54	17
All Sections	13.57	2.65	20	28.68	5.15	18	45.50	7.74	17

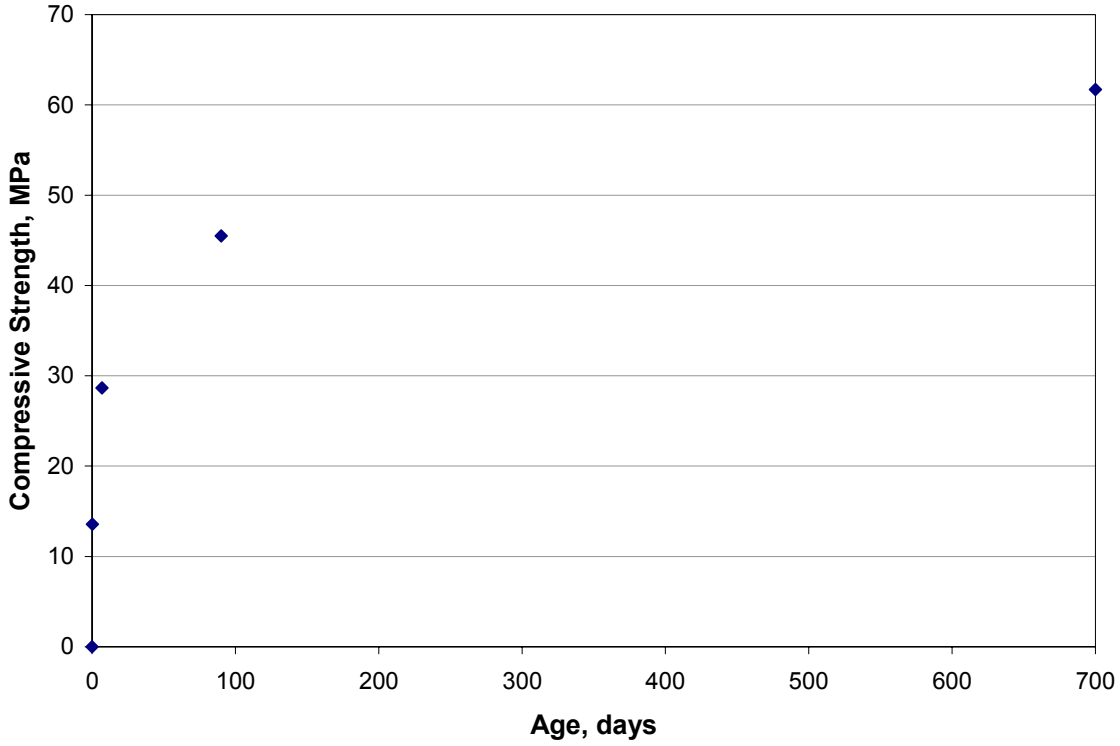

Figure 2-7. Average compressive strength gain for all test sections.

Using Equation 2-2, the average 28-day compressive strength was estimated as 37.34 MPa.

2.5.3 Coefficient of Thermal Expansion

The concrete coefficient of thermal expansion was determined using two different test methods: American Society for Testing and Materials, ASTM C531-85 and United States Army Corp of Engineers, USACE test method CRD-C39-81. The coefficient of thermal expansion was measured after curing at 20ºC either under water or in a temperature-controlled room with a relative humidity of approximately 40 percent. Tests were performed after 28 days of curing and after 90 days of curing with three replicates for each test. The average value for the coefficient of thermal expansion of the FSHCC was 8.14×10^{-6} mm/mm/ºC. Details of the tests are described in Heath and Roesler (1999).

2.5.4 Back-calculated Layer Elastic Modulus and Modulus of Subgrade Reaction

Elastic modulus for concrete slabs was back-calculated using FWD (Falling Weight Deflectometer) deflections at the Palmdale test site on both the South Tangent and the North Tangent sections at several concrete ages (1 day, 7 day, 50 day, and 90 day) by Roesler et al. (2000) using the Dynatest ELCON program (Ullidtz, 1987). The elastic modulus back-calculated for the 200-mm nominal thickness sections on the South Tangent averaged 37,600 MPa. Back-calculation for the 100-mm and 150-mm nominal thickness sections on the South Tangent produced unreliable results due to the thin slabs. The average elastic modulus of the concrete slabs on the North Tangent was approximately 42,500 MPa. Because of the uniform FSHCC thickness on the North Tangent sections, the FWD data for the North Tangent was more consistent than that of the South Tangent. The elastic modulus of the cement-treated base on the

North Tangent sections back-calculated from FWD data measured directly on the base layer was 1,400 MPa.

The average dynamic modulus of subgrade reaction for the North Tangent test sections using the 50-day and 90-day FWD data was back-calculated as 100 MPa/m by Roesler et al. (2000). For the South Tangent sections, the average dynamic modulus of subgrade reaction was back-calculated as 120 MPa/m. As part of this research, the values for elastic modulus and modulus of subgrade reaction calculated by Roesler et al. were compared with those obtained using AREA7, a procedure for back-calculation of concrete pavement properties developed by Hall et al. (1997). The results were consistent with those obtained by Roesler et al., with less than 10 percent difference between the two procedures. The static modulus of subgrade reaction, which is about 50 percent of the dynamic modulus of subgrade reaction, was used in the analysis conducted in this research.

2.5.5 Poisson's Ratio of the Concrete

Laboratory tests were not conducted to measure the Poisson's ratio of the FSHCC. The FSHCC for the Palmdale test sections consisted of Gabbro coarse aggregate (Heath and Roesler, 1999). Gabbro is formed by magma that cools very slowly into hard rock below or within the Earth's crust. It is an igneous rock with properties similar to basalt and granite. Kliszczewicz and Ajdukiewicz (2002) performed laboratory tests to measure Poisson's ratio of high-performance concrete made with various kinds of aggregates. The results of their study, shown in Figure 2-8, indicate average Poisson's ratio of 0.173 for high-performance concrete with granite coarse aggregate and 0.205 for high-performance concrete with basalt coarse aggregate. For analysis purposes in the present study, a Poisson's ratio of 0.18 was used for the FSHCC at Palmdale.

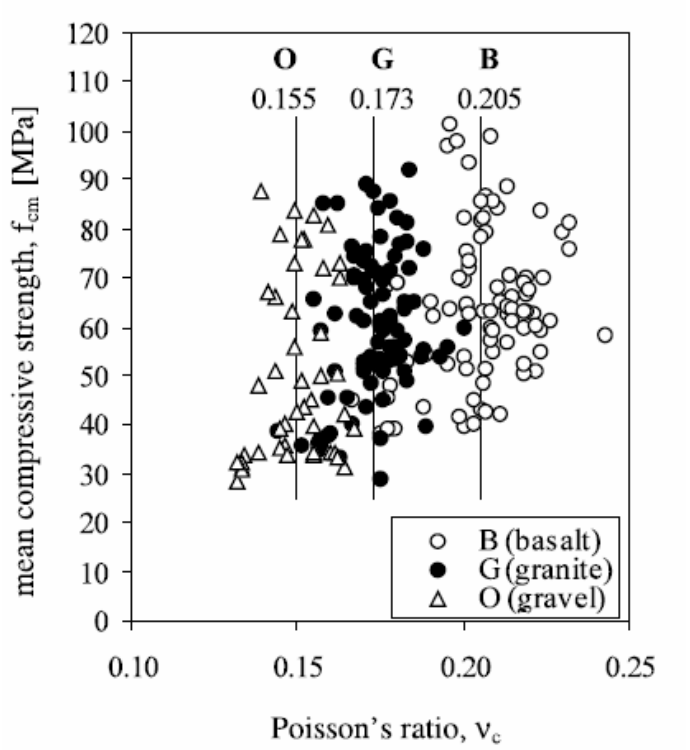

Figure 2-8. Poisson's ratio test results with mean values for high-performance concrete with basalt, granite, and gravel (from Kliszczewicz and Ajdukiewicz, 2002).

2.5.6 Concrete Shrinkage Properties

The shrinkage properties of the cement used at the Palmdale test sections were also tested by personnel at UCB. Three different methods of assessing drying shrinkage were used to compare shrinkage characteristics of the cement used in Palmdale against a commercially available Type II cement. The first and second methods measured the shrinkage of cement mortar according to ASTM C596-96 and California Test CT527, respectively. The third method measured the shrinkage of small concrete beams according to ASTM C157-93. All three test methods involve measuring the length change of replicate unrestrained samples after curing for 7, 14, 21, 28 and 90 days under different curing conditions. Details of the shrinkage tests are described in Heath and Roesler (1999). The results of the ASTM C596-96 shrinkage tests are shown in Figure 2-9.

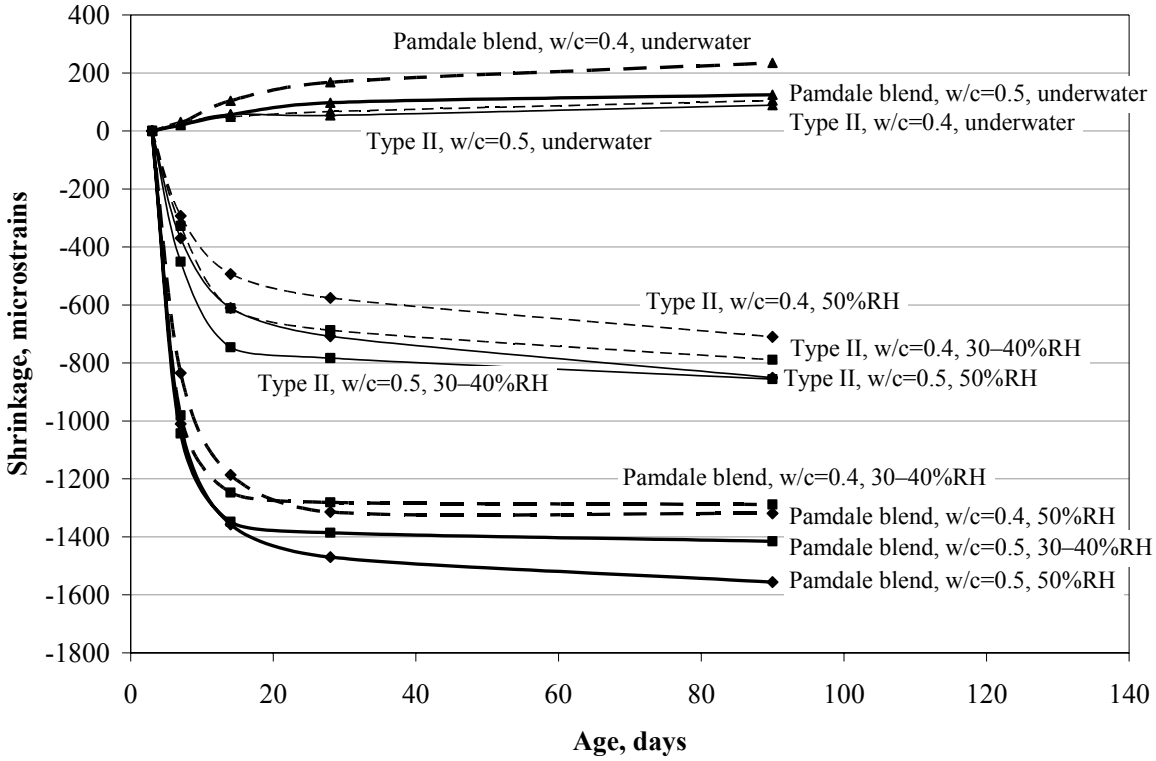

Figure 2-9. Average shrinkage of mortar bars using ASTM C596-96.

The Palmdale blend cement bars had between 130 to 200 percent more shrinkage than the Type II cement bars after 7 days (early age), and between 63 to 80 percent more shrinkage after 90 days (longer term). The differential shrinkage (difference between 30-50 percent relative humidity and underwater tests) for the Palmdale blend was almost twice that of the Type II cement and as high as 1,680 microstrains after 90 days. The results of California Test CT527 were similar. The results of shrinkage tests on concrete beams from ASTM C157-93 also showed significantly higher shrinkage (particularly differential shrinkage) for the concrete with the Palmdale blend cement as compared to the concrete with Type II cement. All of the laboratory shrinkage tests confirm that the Palmdale slabs were highly vulnerable to shrinkage and to differential shrinkage (between top of the slab and bottom of the slab).

2.6 Performance Summary of Test Sections

A summary of slab cracking for the Palmdale test sections until the appearance of the first crack along with the associated load and number of repetitions is shown in Table 2-7. Since no dynamic loading was applied to Section 522FD, the corresponding visual observations are not included. For the sake of comparison with historic traffic information, the equivalent 80-kN single axle loads (ESALs) are also shown. The ESALs were estimated in order to determine the approximate magnitude of traffic-induced damage. Caution must be used in interpreting ESALs since temperature and moisture curling are not considered in the calculation of ESALs. The same load on different sections could produce failure at different ESAL levels due to the changes in temperature curling during the testing. This would not necessarily be accounted for if ESALs are used, and therefore, an approach based on load spectra and cumulative damage is preferred in the analysis of the results. For each test section, the ESALs were calculated using the formula:

$$\text{ESALs} = 20\sum_{i=1}^{k} n_i \left(\frac{P_i}{40}\right)^{4.2} \quad \textbf{(2-3)}$$

where:

P_i = Half-axle wheel load, kN
n_i = Number of applications of load P_i
k = Number of unique loads P_i

The ratio of P_i to 40 was used because 40 kN is the half-axle load for an 80-kN single axle load and the test sections at Palmdale were loaded with half axle edge loads. The multiplicative factor of 20 was used to convert the edge loaded HVS trafficking without wander into wheelpath loaded highway trafficking with wander (Zollinger and Barenberg, 1989; Packard and Tayabji, 1983).

All three 100-mm nominal thickness sections had corner breaks or cracks on adjacent slabs prior to HVS loading. In addition, Section 520FD had a corner crack on the leave end of

Table 2-7 Summary of First Crack Occurrence for South Tangent Test Sections

Section ID	Crack Type	Load, kN **	Repetitions	Estimated Equivalent Single Axle Loads, ESALs	Transverse Distance from Corner Measured on Transverse Joint, m	Longitudinal Distance from Corner Measured on Lane-Shoulder Joint, m
519FD	LC	25	2,105	5,800	1.1, 1.3	-
520FD	LC	35	1,000	11,400	1.1, 1.2	-
521FD	LC*	20	500	500	1.3	-
523FD	CB	45	89,963	2.951,000	1.8	2.4
524FD	LC*	45	64,332	2,110,000	1.8	-
525FD	CB	45	1,000	32,800	1.7	1.8
526FD	CB	85	100	47,400	1.4	1.8
527FD	LC	35	129,805	1,482,000	1.5	-
528FD	TC	40	56,912	1,138,000	-	2.1
529FD	LC*	40 60	88,110 234,423	25,740,000	1.7	-
530FD	CB	40 60 90	64,227 752,448 13,789	92,218,000	1.4	1.4
531FD	CB	40 70	31,318 31,495	7,234,000	1.3	1.4
532FD	CB	40 70	24,337 124,990	26,709,000	1.4	1.6
533FD	Did not fail	40 70 90	44,164 210,003 116,983	115,461,000	-	-
534FD	CB	40 70 90	126,580 858,022 288,932	356,716,000	1.8	1.9
535FD	CB	90	67,935	40,953,000	1.6	3.2
536FD	Did not fail	90 70A 90A 110A 130A 150A	750,000 500 500 500 500 240,782	1,695,110,000	-	-
537FD	TC	40 70 90	13,230 500 30,000	18,454,000	-	1.3
538FD	Did not fail	70 90	500 188,882	113,969,000	-	-
539FD	TC	40 70 90	13,342 500 207,522	125,473,000	-	1.6
540FD	CB	40 90 150A	13,003 392,062 65,000	571,477,000	1.7	2.0
541FD	Did not fail	70 90 150A	500 167,777 110,011	668,004,000	-	-

*Progressed after additional loading to CB.
** A = aircraft wheel (for loads above 100 kN)
LC = Longitudinal crack, CB = Corner break, TC = Transverse crack

the test slab prior to loading. However, the first crack to occur on all of the test slabs after HVS loading was a longitudinal crack at a distance of between 1.1 and 1.4 m from the slab corners.

Some of the 150-mm nominal thickness test sections had corner breaks or cracks on adjacent slabs prior to HVS loading. However, the first crack to occur on all test slabs after HVS loading was a longitudinal crack or a corner break at a transverse distance of between 1.5 and 1.7 m from the slab corners.

For the 200 mm nominal thickness sections, none of the test sections or the adjacent slabs had any cracks prior to HVS loading. However, the first crack to occur on three of the 200-mm test slabs after HVS loading was a longitudinal crack (or a corner break) at a transverse distance of between 1.4 and 1.7 m from the slab corners. Section 528FD never developed a corner break or a longitudinal crack through the course of the HVS loading. The only crack on this section was a short transverse crack.

Three of the four undoweled sections on the North Tangent failed via corner breaks at a transverse distance between 1.4 and 1.8 m. The fourth undoweled section, Section 533FD, did not fail at the point testing was terminated. Two of the three doweled sections with tied concrete shoulders did not fail at the point the testing was terminated. Only Section 537FD exhibited transverse cracking after approximately 44,000 repetitions. Of the three doweled sections with widened lanes, Section 541FD did not fail. Section 540FD failed via a corner break and Section 539FD exhibited transverse cracking.

A large amount of variability was observed between the fatigue performance of individual test sections with the same design and identical load levels. For example, while a longitudinal crack was observed on Section 524FD after more than 64,000 repetitions of 45-kN loading, a replicate section, 525FD, had a corner break after only 1,000 repetitions of 45-kN

loading. Similarly, while Section 535FD cracked after less than 68,000 repetitions of 90-kN loading, Section 534FD (a similar section) carried more than a million repetitions of 40-, 70-, and 90-kN loading before the first crack was observed. Similar differences were observed between other replicate sections (i.e., Sections 536FD and 537FD).

3.0 CURLING IN CONCRETE SLABS

Curling in concrete slabs is a combination of 5 nonlinear components (summarized in Table 3-1):

- **Temperature gradient through the slab**—During daytime, the top of the concrete slab is typically warmer than the bottom, resulting in a positive temperature gradient through the slab. During nighttime, the top of the concrete slab is typically cooler than the bottom, resulting in a negative temperature gradient through the slab. Temperature gradients through the depth of the slab cause differences in elongation strains between the top of the slab and the bottom of the slab, resulting in curling. Field studies (Armaghani et al., 1986; Yu et al., 1998) have shown that these temperature gradients are nonlinear, and that the daily fluctuation in temperature is greater on the surface than at the bottom of the slab. Air temperature, solar radiation, cloud cover, and precipitation affect temperature gradients in concrete slabs.
- **Built-in temperature gradient**—Concrete paving is typically performed during the daytime in warmer months of the year. During daytime paving, the top of the slab is typically warmer than the bottom of the slab at the concrete set time. Since the concrete slab sets under this condition, the flat slab condition is not associated with a zero temperature gradient. When the temperature gradient in the slab is zero, the slab curls upward rather than remaining flat. Thus, an effective negative temperature gradient is "built into" the slab, and is referred to as the built-in construction temperature gradient. The magnitude of the built-in temperature gradient is affected by air temperature and weather conditions during set and curing conditions (Eisenmann and Leykauf, 1990; Yu et al., 1998).

- **Moisture gradient through the slab**—The surface of the slab (depth < 50 mm) is typically only partially saturated compared to the bottom, which is usually saturated (Janssen, 1986; Grasley, 2003; Lim et al., 2004). The difference in internal relative humidity in concrete pores between the top of the slab and the bottom of the slab causes differential shrinkage strains, resulting in curling. The curling associated with these reversible shrinkage strains is primarily affected by changes in atmospheric temperature and relative humidity, weather phenomenon such as rainfall, snow, etc., and design factors such as pavement layer materials (permeable base vs. poorly draining base).
- **Differential irreversible shrinkage**—Drying shrinkage is defined as "the reduction in concrete volume resulting from a loss of water from the concrete after hardening" (Mather, 1964). Significant irreversible drying occurs in a concrete pavement only to a shallow depth (approx. 50 mm) (Janssen, 1986; Suprenant, 2002). The drying shrinkage at the surface is affected by early-age curing conditions. The drying shrinkage at the bottom of the slab is significantly lower due to the high relative humidity in the pores at that portion of the slab. Autogenous shrinkage, which is a special case of drying shrinkage, is due to self-desiccation when insufficient hydration moisture is not present in the concrete. Differences in irreversible shrinkage between the top of the slab and the bottom of the slab result in permanent differences in shrinkage strains between the top of the slab and the bottom of the slab, which causes the slab to curl or warp.
- **Creep**—Creep is defined as the increase in strain over time of concrete subjected to constant stress and is inversely proportional to the strength of the concrete at the time

of applied stress (Neville and Meyers, 1964). For a curled slab, stresses caused by restraints from shoulder and adjacent slabs, as well as from slab self-weight, result in creep, particularly during the early ages of concrete strength development. Differential creep strains between the top of the slab and the bottom of the slab effectively result in the recovery of a portion of the fixed curling in the slab (built-in temperature gradient + differential irreversible shrinkage) (Schmidt, 2000; Rao et al., 2001). Tensile creep mechanisms reduce shrinkage strain in restrained concrete by at least 50 percent (Altoubat and Lange, 2001).

Table 3-1 Five Components of Curling in Concrete Pavement Slabs

Cause of Slab Curling	Frequency (Best Description)	Comments
Temperature gradient	Intraday variation + weather (e.g., snow, wind, rainfall, cloud cover)	Result of differential temperature changes through the slab; affected by intraday fluctuations in air temperature, solar radiation, and weather phenomena.
Built-in temperature gradient	Fixed	Result of temperature gradients during concrete set; affected by cement heat of hydration, air temperature and weather phenomena during set.
Moisture gradient	Seasonal variation + weather (e.g. rainfall)	Result of differential changes in slab moisture/internal relative humidity; affected by atmospheric temperature and humidity, weather phenomena, and drainage.
Differential drying shrinkage	Majority develops during early-age	Result of the irreversible differential loss of moisture in concrete; affected by curing conditions, concrete material constituents, and environmental conditions.
Creep	Short + long-term change	Result of stresses arising from restraints and slab self-weight; affected by magnitude of stresses and concrete material constituents.

These components are affected by material properties such as coefficient of thermal expansion, thermal conductivity, permeability, etc., and depend on mix design parameters such as aggregate type, cement content and type, water content, admixtures, etc. (Ytterberg, 1987; Tremper and Spellman, 1963).

The total amount of curling in a slab due to a combination of these five factors can be represented as a temperature difference—the total effective linear temperature difference (*TELTD*), ΔT_{tot}:

$$\mathbf{\Delta T_{tot} = \Delta T_{tg} + \Delta T_{mg} + \Delta T_{bi} + \Delta T_{shr} - \Delta T_{crp}} \quad \textbf{(3-1)}$$

where,

ΔT_{tg} = Temperature difference between top and bottom of a slab equivalent to (producing similar deflection response to) nonlinear vertical temperature gradients in the slab.

ΔT_{mg} = Temperature difference between top and bottom of a slab equivalent to (producing similar deflection response to) nonlinear vertical moisture gradients in the slab. This represents the reversible portion of the differential drying shrinkage between the top and the bottom of the slab.

ΔT_{bi} = Temperature difference between top and bottom of a slab equivalent to (producing similar deflection response to) nonlinear built-in construction temperature gradient.

ΔT_{shr} = Temperature difference between top and bottom of a slab equivalent to (producing similar deflection response to) irreversible differential drying shrinkage between the top and the bottom of the slab.

ΔT_{crp} = Portion of ΔT_{bi} and ΔT_{shr} recovered through creep.

The cumulative effect of built-in temperature gradient, drying shrinkage gradient, moisture gradient, and creep can be defined as an effective built-in temperature difference (*EBITD*), ΔT_{ebi}. The EBITD is the linear temperature difference between the top and bottom of a concrete slab that produces the same deflection response as the cumulative effects of nonlinear built-in temperature gradient, nonlinear moisture gradient, and nonlinear shrinkage gradient, reduced over time by creep (Rao and Roesler, 2005A).

$$\mathbf{\Delta T_{ebi} = \Delta T_{bi} + \Delta T_{shr} + \Delta T_{mg} - \Delta T_{crp}} \quad \textbf{(3-2)}$$

$$\mathbf{\Delta T_{tot} = \Delta T_{tg} + \Delta T_{ebi}} \quad \textbf{(3-3)}$$

$$\boldsymbol{TELTD = \Delta T_{tg} + EBITD} \quad \textbf{(3-4)}$$

The four components of *EBITD* are generally grouped together because they are relatively stable over a longer time period as compared to ΔT_{tg}, which changes intraday to a considerably greater extent. The *EBITD* has traditionally been reported by researchers as "locked-in curvature" (Byrum, 2000), "zero-stress temperature" (Eisenmann and Leykauf, 1990), "equivalent temperature gradient" (Rao et al., 2001; Fang, 2001), and "built-in curl" (Yu et al., 1998; Beckemeyer et al., 2002). *EBITD* is also the sum of the "permanent curl" defined in the 2002 Design Guide (Yu et al. 2004) and ΔT_{mg}.

3.1 Factors Affecting Slab Effective Built-In Temperature Difference

Wide ranges of factors affect the various components of *EBITD*. As discussed in Section 2.4.5, the cement used at Palmdale resulted in the concrete slab being highly vulnerable to shrinkage and to differential shrinkage strains through the depth of the slab. Because of this, as is typically the case, irreversible differential shrinkage was the primary component responsible for *EBITD* for the test slabs. A brief discussion on the factors affecting the various components of *EBITD* follows in this section. A comprehensive literature review describing these factors is included in Appendix B.

3.1.1 Factors Affecting Differential Shrinkage through the Depth of the Slab

Tremper and Spellman (1963) measured curling in the field from profilograms of various highway pavements. Curling was taken as the maximum distance along a perpendicular from the slab profile to a straight line drawn between profile high points at either adjacent slab joints. Prisms were made at the same time the slabs were cast, and were tested in the laboratory for shrinkage. Figure 3-1, developed by Suprenant (2002) using data from Tremper and Spellman, shows that for a given project, curling deflection increases as drying shrinkage increases.

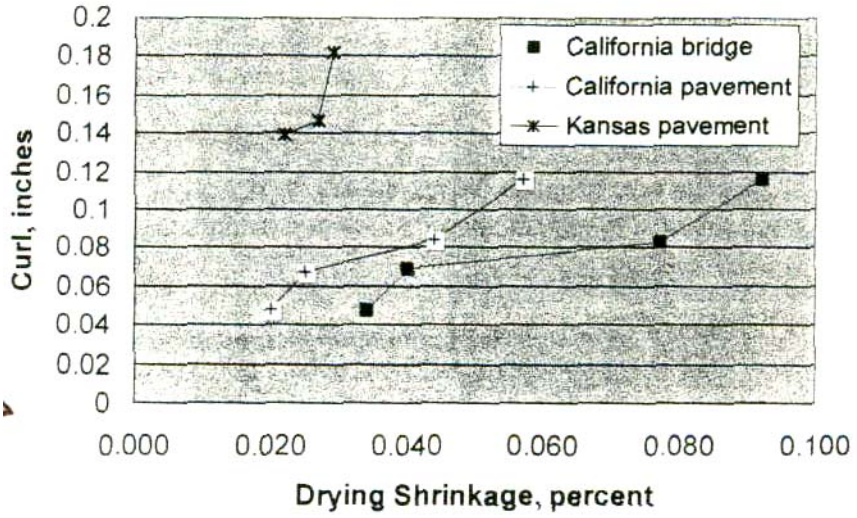

1 in = 25.4 mm

Figure 3-1. Relationship between drying shrinkage of test specimens and the amount of curling deflection of full-size test slabs for three different sections (from Suprenant, 2002; Tremper and Spellman, 1963).

However, due to the influence of other factors such as material properties, concrete mix properties, ambient relative humidity, moisture content of underlying layers, slab geometry, etc., the magnitude of the effect of drying shrinkage on slab curling differs among projects. Because of the significant effect of drying shrinkage on effective built-in curl, these factors that affect drying shrinkage, and in particular, drying shrinkage gradients, are also factors that affect *EBITD*. These issues and how they affect drying shrinkage and drying shrinkage differentials are discussed in detail in Appendix B.

The factors involved in shrinkage potential of a concrete mix can have a cumulative effect as shown in the example in Table 3-2 developed by Mather (1964) using results from Powers (1959). A similar analysis was presented by Tremper and Spellman (1963) as shown in Table 3-3. These tables suggest that up to a 5- to 7-fold increase in slab shrinkage can occur, depending on presence/absence of various factors that affect shrinkage. Although both these

Table 3-2 Individual and Cumulative Effects of Various Factors on Concrete Shrinkage Assuming Constant Water-Cement Ratio (Mather, 1964; Powers, 1959)

Factor		Effect*	
Favorable	**Unfavorable**	**Individual**	**Cumulative**
Cement of optimum SO_3	SO_3 deficiency	1.5	1.5
Cement with 15 percent retained on No. 200	0 percent retained on No. 200	1.25	1.9
Less compressible aggregate (quartz)	More compressible (Elgin gravel)	1.25	2.4
Large aggregate (38 mm [1½ in.] max. size)	Small aggregate (6 mm (¼ in) max. size)	1.3	3.1
More aggregate (stiff mixture)	Less aggregate (wet mixture)	1.2	3.7
No clay in aggregate	Much bad clay in aggregate	2.0	7.4

* Multiplication factor for potential increase in shrinkage

Table 3-3 Cumulative Effect of "Adverse" Factors on Shrinkage (Tremper and Spellman, 1963)

"Poor" Practices That Can Cause Increased Shrinkage in Concrete Slabs	**Equivalent Increase in Shrinkage, Percent**	**Cumulative Effect**
Temperature of concrete at discharge allowed to reach 27 °C (80 °F), whereas with reasonable precautions, a temperature of 16 °C (60 °F) could have been maintained	8	1.00 × 1.08 = 1.08
Use of 150 to 180 mm (6 to 7 in) slump where 75 to 100 mm (3 to 4 in) slump could have been used	10	1.08 × 1.10 = 1.19
Excessive haul in transit mixer, too long a waiting period at job site, or too many revolutions at mixing speed	10	1.19 × 1.10 = 1.31
Use of 19 mm (3/4 in) maximum size aggregate under conditions where 38 mm (1-1/2 in) aggregate could have been used	25	1.31 × 1.25 = 1.64
Use of cement having relatively high shrinkage characteristics	25	1.64 × 1.25 = 2.05
Excessive "dirt" in aggregate due to insufficient washing or contamination during handling	25	2.05 × 1.25 = 2.56
Use of aggregates of poor inherent quality with respect to shrinkage	50	2.56 × 1.50 = 3.84
Use of an admixture that produces high shrinkage	30	3.84 × 1.30 = 5.00
TOTAL INCREASE (percent)	Summation = 183	Cumulative = 400

tables suggest that the effects listed are independent (which is likely an incorrect assumption), they do point to the large effect that adverse factors can have on concrete shrinkage.

3.1.2 Factors Affecting Creep Due to Slab Restraints

Restraint of shrinkage leads to stress development, which in turn causes the material to creep, particularly at early age following concrete placement. The shrinkage of concrete usually occurs simultaneously with creep (Kovler, 1999). Creep strains due to tensile restraint stresses tend to counteract the effect of shrinkage. Tensile creep tests, in parallel with free shrinkage tests and basic creep tests, were carried out by Kovler (1999) on replicate 40 × 40 × 1000 mm specimens. Figure 3-2 shows that total strain of specimen with 1 MPa applied tensile stress was lower in magnitude than the free shrinkage strain. The difference between the free shrinkage strain and the total strain is the total creep contributing to an effective reduction in shrinkage. The total creep during drying was greater than the creep under conditions of no moisture movement, also known as basic creep, as first observed by Pickett (1942), who introduced the idea of "drying creep" to denote the difference between the total creep and the basic creep.

Curling in field slabs is reduced by creep stresses from restraints caused by several factors including: weight of the slab, load transfer between the slab and adjacent slabs and/or shoulder, and friction between the slab and underlying base layer. At early ages, these restraints cause tensile creep at the top of the slabs, which results in an effective reduction in the *EBITD*. Suprenant (2002) states that "Generally, the length of lost subbase contact is about 10 percent of the slab length (measured between joints) at joints that have load transfer (doweled or sawcut joints), and about 20 percent at joints with no load transfer," suggesting more curling in slabs without load transfer as compared to slabs with load transfer. One of the effects of the restraint due to load transfer and slab-base friction is that different corners of the same slab can have

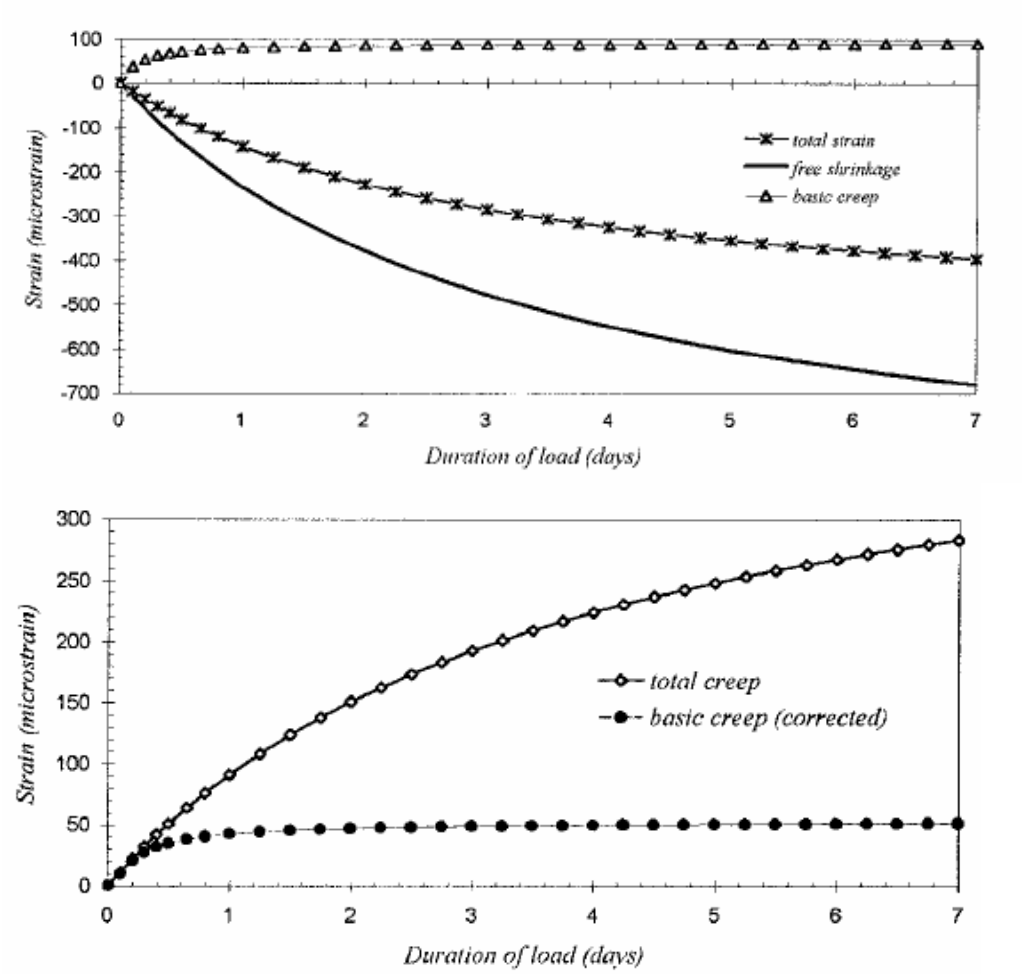

Figure 3-2. Experimental dependency of free shrinkage strain, total strain under simultaneous drying and loading by tensile stress of 1 MPa, and basic creep under same stress of concrete cured 1 day (from Kovler, 1999).

different amounts of curling deflections and *EBITD*, particularly for undoweled pavements (depending on local conditions) which will result in asymmetric slab curvature as shown in Figure 1-2. A discussion on some of the factors that affect creep is included in Appendix B.

3.1.3 Factors Affecting Built-In Curling from Ambient Conditions during Concrete Set

Pavement slabs are typically placed during the daytime, and often in the hot summer months. In this case, a positive temperature gradient exists through the depth of the slab at the

time of concrete set. Because the concrete is fluid prior to set, it hardens flat on the base/subbase layer. The flat slab condition then corresponds to a positive temperature gradient in the slab. After set, the slab will be flat only when the same positive temperature gradient is applied to the slab. When the actual temperature gradient through the slab is zero, the slab will be in a concave condition analogous to a slab with a negative temperature gradient through the depth of the slab. This negative temperature gradient is the built-in curling in the slab, and an equivalent positive temperature gradient through the depth of the slab is required for the slab to come in contact with the base (Yu et al. 1998; Hansen et al., 2002).

The magnitude of built-in curling due to hot weather construction can be as high as -0.055ºC/mm on many highway pavements (Eisenmann and Leykauf, 1990). The built-in curling is affected by air temperature, solar radiation, base/subbase thermal conductivity and temperature, weather conditions during set, and concrete curing procedure. Also, temperatures in the slab during set and the time to set are functions of heat of hydration, and depend on mix and material properties such as cement type, cement fineness, water/cement ratio, admixtures, etc.

3.1.4 Effect of Modulus of Elasticity, Slab Thickness, and Joint Spacing

3.1.4.1 Modulus of Elasticity

The concrete's modulus of elasticity can affect the magnitude of the concrete curling. The higher the modulus, the greater is the amount of curling, and lesser the downward relaxation of the curled edges over time due to creep (Walker and Holland, 1999). For a fixed amount of differential strain between the top and bottom of a slab caused by the various components of curling, the higher elastic modulus results in greater amount of stress responsible for curling the slab. Leonards and Harr (1959) computed a 60 percent increase in curling deflections when the

concrete compressive strength increased from 21 to 52 MPa with a corresponding increase in modulus from 21 GPa to 35 GPa. Al-Nasra and Wang (1994) using finite element modeling, computed a 35 percent increase in curling deflections for the same change in strength and modulus (Figure 3-3).

3.1.4.2 Slab Thickness

A majority of the shrinkage strains (and opposing tensile creep strains) that are responsible for upward curling of the slab occur at the top of the slab. For a given amount of differential strain between the top and bottom of a slab (with a given elastic modulus), the moments responsible for curling the slab are proportional to the slab thickness. However, the weight of the slab also increases with slab thickness (and concrete density), resulting in less

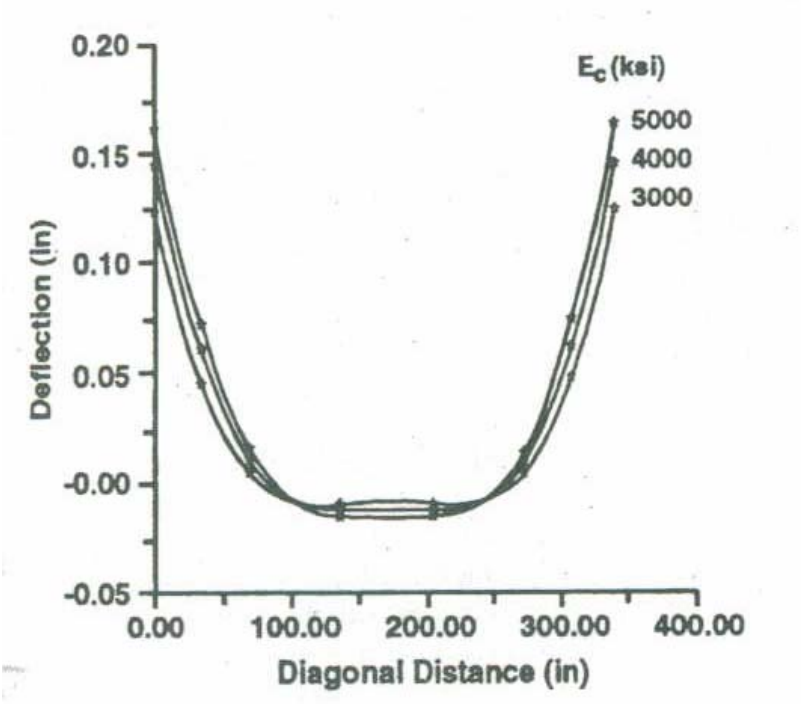

1 in = 25.4 mm, 1 ksi = 6.89 MPa

Figure 3-3. Effect of concrete modulus of elasticity on curling of floor slabs (from Al-Nasra and Wang, 1994).

curling. Childs and Kapernick (1958) observed that corner curling deflections for 150-mm and 200-mm slabs were 2.8 and 1.3 mm, respectively. An analysis performed by Leonards and Harr (1959) also showed that as slab thickness increases, upward corner deflections due to curling decreased. The analysis assumed that a majority of shrinkage occurred at the top of the slab and both slabs had similar *EBITD* of –17ºC. A similar analysis by Eisenmann and Leykauf (1990), who assumed a shrinkage depth of 40 to 60 mm from the top of the slab, showed that thicker slabs had lower upward deflection due to curling as compared to thinner slabs (Figure 3-4).

3.1.4.3 Joint Spacing

The cumulative effect of shrinkage at the top of the slab relative to the bottom is that longer slabs have more net shrinkage difference between the top and the bottom and greater curl than shorter slabs. Ytterberg (1987) showed that reducing joint spacing from 6.1 m to 4.6 m

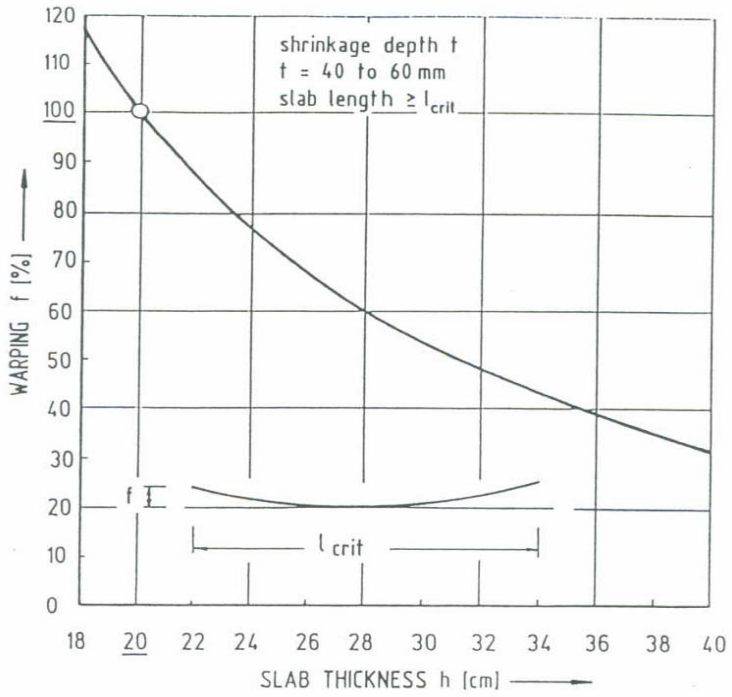

Figure 3-4. Percentage upward deflection f (relative to 20-cm slabs) due to curling as a function of slab thickness (from Eisenmann and Leykauf, 1990).

decreases the amount of upward deflection but does not eliminate it. However, due to the restraining effect of the weight of the slab corners, beyond a joint spacing of 7.6 m to 9.1 m, the increase in curl in minimal. Eisenmann and Leykauf (1990) analytically calculated the upward deflection due to curling (assuming that shrinkage occurred in the top 50 mm of the slab) for various values of shrinkage strains and moduli of elasticity. Their results indicate that the upward deflection increases with slab length up to the critical value, l_{crit}, beyond which, the upward deflection remains constant (Figure 3-5).

3.1.5 Support from Underlying Layers

For structural analysis purposes, the *EBITD* is a measure of the lack of contact or support between the concrete slab and the underlying layer, and not of the curvature of the surface of the slab. Consequently, support from underlying layers is also a factor that affects *EBITD*. According to Ytterberg (1987), "As the free ends of a slab lift off the subgrade, the unit gravity load increases on the remaining supporting subgrade and the center of the slab buries itself into the subgrade and amount which varies inversely with the modulus of subgrade reaction, k…Only a few feet of the slab ends are actually cantilevered above the subgrade."

This phenomenon is illustrated in Figure 3-6, and is the reason why surface profiles cannot be used to accurately determine the *EBITD*, as emphasized by Yu et al. (2004) in the curling and warping analysis for the 2002 Design Guide for Rigid Pavements. As illustrated in Figure 3-7, if the slab is placed on a stiff subgrade or a treated base without significant settlement, the measured *EBITD* can be higher than that of a slab placed on a soft subgrade or subbase.

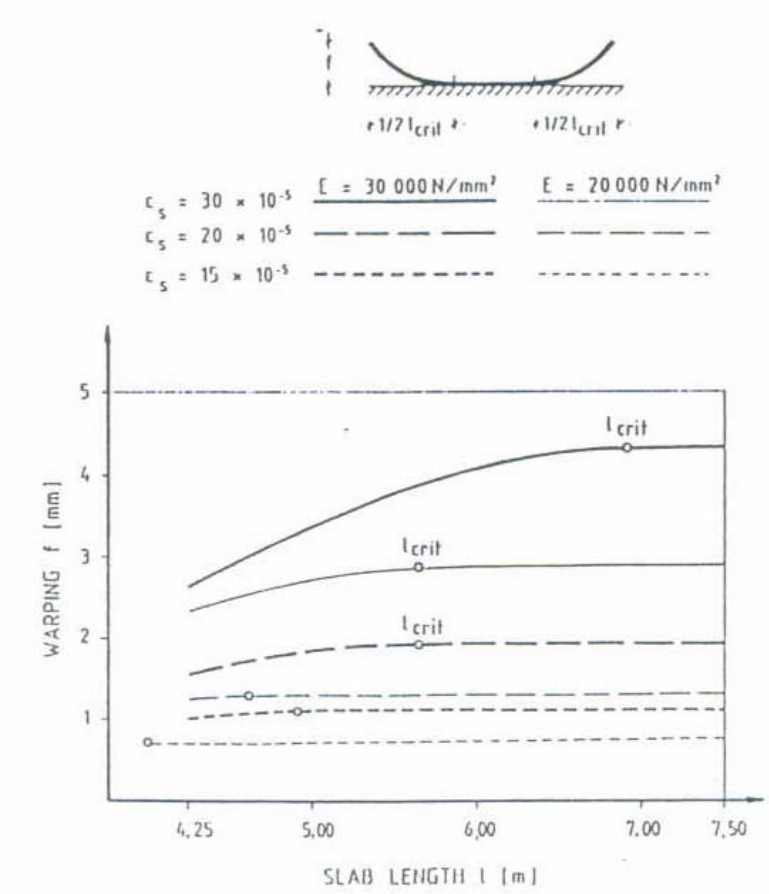

Figure 3-5. Upward deflection f (relative to 20 cm slabs) due to curling as a function of joint spacing for various values of elastic moduli and shrinkage strains (Eisenmann and Leykauf, 1990).

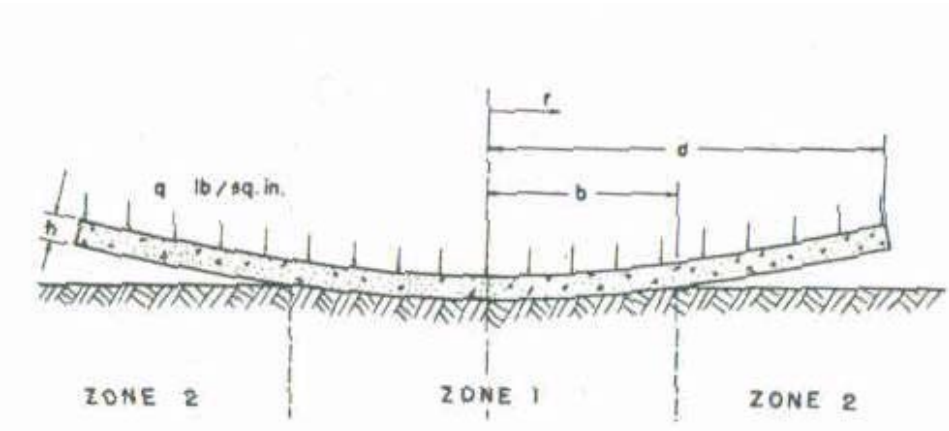

Figure 3-6. Upward slab curling and sinking of slab into the subgrade (from Ytterberg, 1987).

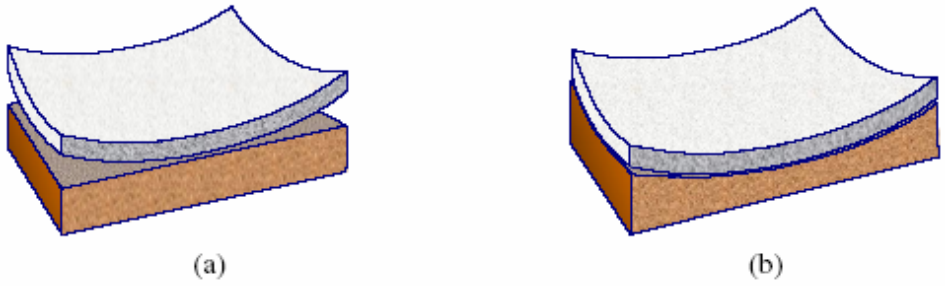

Figure 3-7. Illustration of support condition under pavement slabs (a) assuming flat foundation and (b) including the effects of settlement (from Yu et al., 2004).

3.2 Estimating Slab Effective Built-In Temperature Difference (EBITD)

In recent years, a few researchers have conducted studies to measure *EBITD*, also described variously as locked-in curvature, zero-stress temperature, equivalent temperature gradient, and built-in curl. Some researchers have used thermocouples and MDD or surface profile measurements to identify when the slab comes in contact with the base or reaches a "no curl" condition. The temperature difference measured across the slab under this "zero-stress state" condition is then the *EBITD*.

Vandenbossche (2003) used slab surface "dipstick" measurements to calculate slab "curvature" and develop regression equations for curvature, corner displacements, and curling/warping voids, for doweled and undoweled slabs. In Florida, Armaghani et al. (1986) used surface profile measurements and embedded thermocouples in 225-mm slabs and estimated 5ºC as the temperature at which the slab reaches a no-curl condition, suggesting and *EBITD* value of -5ºC. The drawback of using surface profiles is that the measured surface profile may not represent the level of support received by the slabs from the base and subbase layers, which is a more analytically useful way of characterizing *EBITD* (Yu et al., 2004). Another drawback is the limited resolution of the dipstick, resulting in higher errors from slabs with low *EBITD*.

Using data from instrumented slabs at Denver International Airport, Fang (2001) observed "equivalent temperature gradient" ranging from –4.5 to –12.2ºC for 450-mm nominal thickness slabs. He used MDD data along with embedded thermocouples to estimate the temperature at which the bottom of the slab came in contact with the top of the base. A limitation of this procedure is the difficulty in determining flat slab condition or when the slab corner first comes in contact with the base. Another limitation is that the bottoms of the slab and the top of the base have to be instrumented in order to determine when they come in contact; which makes this procedure inefficient when *EBITD* is to be calculated for a large number of slabs.

Other studies have used measured unloaded slab corner vertical deflections, measured using LVDTs, and temperature profiles over a 24-hour period to determine the *EBITD*. Finite element analysis programs were used to estimate the *EBITD* that best matched the measured deflections with the predicted deflections. In Colorado, Yu et al. (1998) observed "built-in curl" of -11.1ºC for 295-mm thick slabs. For 350-mm doweled slabs in Arizona, Rao et al. (2001) estimated "equivalent temperature gradient" of –20.0ºC to –29.1ºC, forty days after construction. In Pennsylvania, Beckemeyer et al. (2002) found that "built-in curl" for concrete slabs on open-graded granular bases and asphalt-treated permeable bases were –9ºC and –7ºC, respectively, based on a procedure outlined by Yu and Khazanovich (2001). Rufino (2004) reported *EBITD* at Denver International Airport to be between –5 and –8ºC based on rolling aircraft deflection data. The unloaded slab deflection analysis for the Palmdale test sections and the limitations of using unloaded slab deflections to back-calculate *EBITD* for in-service slabs with significant built-in curling are discussed in the following sections.

While the researchers mentioned above have measured *EBITD* using various means, no systematic study has been conducted on full-scale test sections to determine factors affecting the

magnitude of *EBITD* in the field. The Palmdale sections were the first of their kind designed to study the effect of various design features on *EBITD*.

3.2.1 24-Hour Unloaded Slab Deflections for Palmdale Sections

24-hour tests were conducted on several North Tangent sections to evaluate the intraday response of the test slabs to daily temperature fluctuations under different conditions (no HVS + no temperature control box, HVS + no temperature control box, HVS + temperature control box). In these tests, when the HVS was present above the test slab, no load was applied onto the test slab. The temperature control box covered part of the HVS trafficked slab and the adjacent slabs, in order to reduce the influence of temperature curling on the slab responses.

Deflections measured at two corners (DMD2 and DMD4) and one midslab edge (DMD3) along with the temperature difference between the top and bottom thermocouples measured at four slab locations with no HVS and no temperature control box (direct exposure to sunlight) are shown in Figure 3-8. 535FD was a section without dowels at the transverse joints and an asphalt concrete shoulder. The deflections in Figure 3-8 are presented relative to the first data point and not relative to the flat slab condition. This first data point may have significant curvature due to built-in curling and therefore the plotted data is not representative of the magnitude of curling in the slab. Figure 3-8 shows the deflection at the three slab locations moved downward as the temperature difference increased, while the corner and edges moved upward as the temperature difference decreased. Corner deflections (DMD2 and DMD4) had similar deflection magnitude while the edge deflection (DMD3) was smaller for the same change in temperature difference.

The unloaded slab deflections measured with the HVS placed on the test section and with the operation of the temperature control box are shown in Figure 3-9. The thermocouples in the slab under the temperature control box showed very little change over the 24-hour period. The

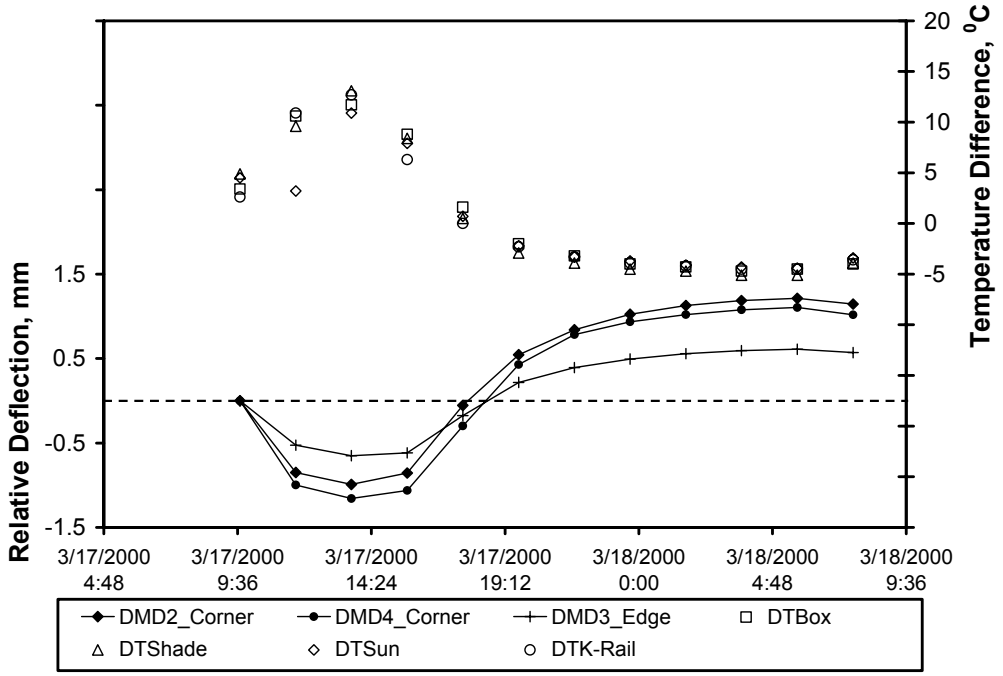

Figure 3-8. 24-hour unloaded slab relative deflections with no HVS and no temperature control box (Section 535FD).

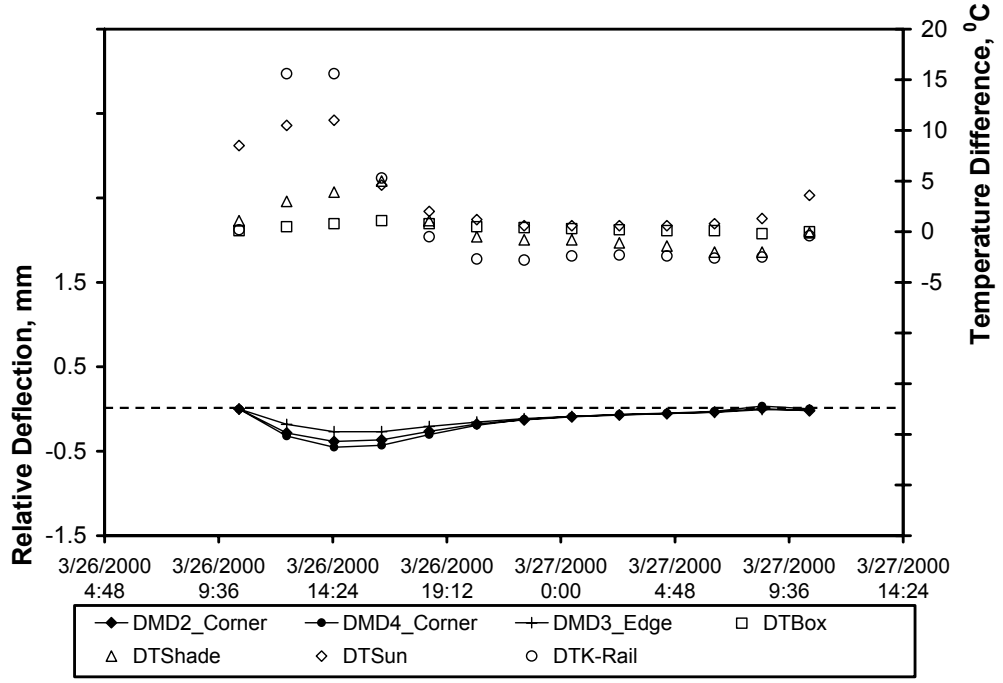

Figure 3-9. 24-hour unloaded slab relative deflections with HVS and temperature control box (Section 535FD).

thermocouples in the shade and directly exposed to the sunlight showed a greater variation over the 24-hour period. Even though the part of the slab corresponding to the DMD locations were completely covered by the temperature control box, the DMDs were affected by the temperature cycling of the exposed portion of the slab. The magnitudes of corner and edge deformations were much smaller with the temperature box and HVS present on the test section.

The 24-hour unloaded slab deflections for the rest of the North Tangent test sections where such data was collected—Sections 537FD through 541FD—are shown in Appendix A, Figures A-1 through A-8.

3.2.2 24-Hour Unloaded Slab Deflection Analysis

In order to determine if any effective built-in curl was present in the concrete slabs, ISLAB2000 was used to model the test section slab configurations. Using ISLAB2000, the total temperature difference responsible for a measured deflection (relative to flat slab condition, when the corner is just in contact with the base) can be calculated for a known set of slab geometry, material/layer properties, etc.

The use of unloaded slab deflections to estimate *EBITD* using finite element analysis requires a reference point for the investigation. The reference point has to be one where the exact position of the slab (and the temperature difference across the slab) is known relative to the flat slab condition. The reference point could also be the deflection sensor reading corresponding to the flat slab condition. When collecting field data, it is not possible to easily identify a flat slab condition. Neither the North Tangent nor the South Tangent Palmdale data includes such a reference point and therefore the raw unloaded slab deflections themselves could not be used to estimate the *EBITD*.

The range of the deflection data over the 24-hour cycle or the deflection relative to the first data point can also be used to estimate the *EBITD*. This is illustrated in Figure 3-10, which shows the predicted relative slab corner deflections using ISLAB2000 for 0ºC *EBITD*, –10ºC *EBITD*, –25ºC *EBITD*, and –35ºC *EBITD*. By matching the ranges of movement at different estimated values of *EBITD* to the measured range of movement, an estimate of the *EBITD* can be obtained. However, this procedure can only be used when the *EBITD* magnitude is less than the range of the measured temperature difference (over the 24-hour cycle, typically around 15 to 20ºC for slabs exposed to ambient air and sunlight). When this is true, the slab comes in contact with the base at least once over the 24-hour cycle. If the *EBITD* is highly negative, then the slab corner never comes in contact with the base over the 24-hour cycle, and the relative unloaded slab deflections cannot be used to estimate *EBITD*. This can be seen in Figure 3-10, where there

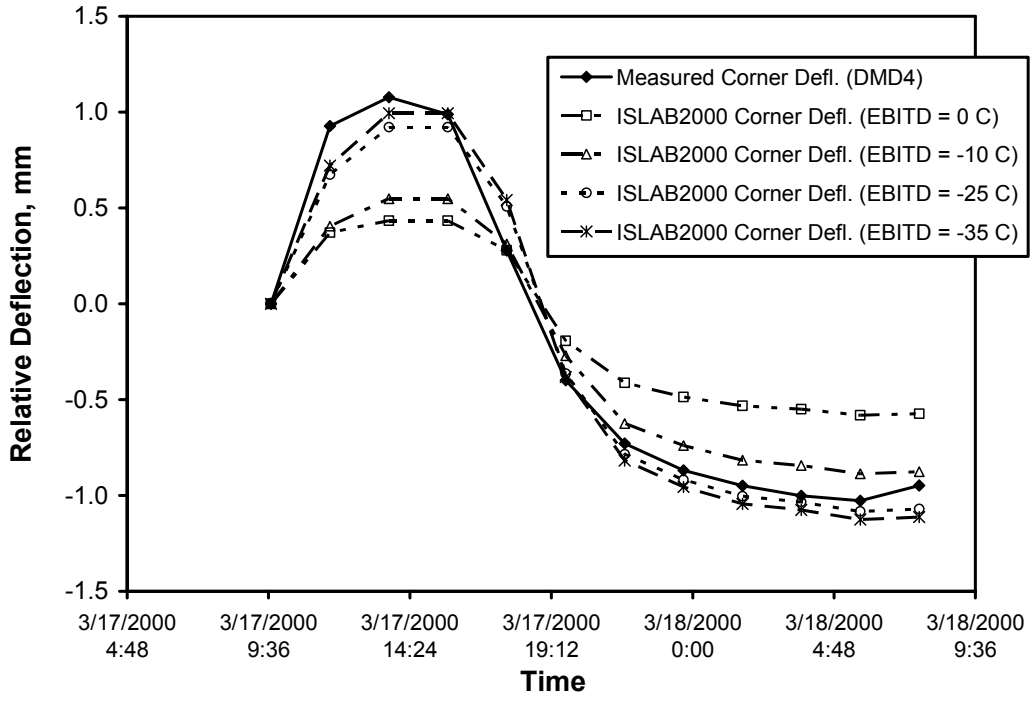

Figure 3-10. Predicted unloaded slab corner relative deflections assuming 0ºC, –10ºC, –25ºC, and –35ºC effective built-in temperature difference and measured deflections (Section 535FD, DMD4) under ambient conditions.

is little difference between using –25ºC *EBITD* and –35ºC *EBITD* (within the field data margin of error), and either one of those values could be the actual *EBITD*.

The drawback of using 24-hour unloaded slab deflection data is that it cannot be used when the *EBITD* is less than about –20ºC (slabs with high negative curl). In these cases, the slab corners do not come into contact with the base during the 24-hour monitoring period, and thus the temperature-based movement is not sensitive to the initial curling of the slab as shown in Figure 3-11. For *EBITD* between –20ºC and 0ºC, the temperature-based deflection range of the slab corner is a function of the *EBITD*. A second drawback of using 24-hour unloaded slab deflections is that an accurate measurement of the surface temperature of the test slab is required during the daytime and nighttime peaks, because of its significant effect on deflection range. However, the temperature profile through the depth of the slab can be highly nonlinear and variable, particularly during the daytime peak, as shown in Figure 3-12 from Yu et al. (2004) making it difficult to estimate the slab surface temperatures using embedded thermocouple sensor data, as discussed below.

For the Palmdale test slabs, since the thermocouple sensors were not located exactly on the surface of the slab, the thermocouple data needed to be extrapolated to account for the difference in temperature between the sensor location and the surface of the slab. This extrapolation was performed using the mid-slab sensor and the sensor near the top of the slab, approximately 10 to 30 mm beneath the surface. However, because of the limited number of temperature sensors, the method of extrapolation used significantly affected the estimated surface temperature. Two such possible extrapolations are shown in Figure 3-13. Because of the high variability in slab temperature profile, as seen in Figure 3-12, the actual temperature

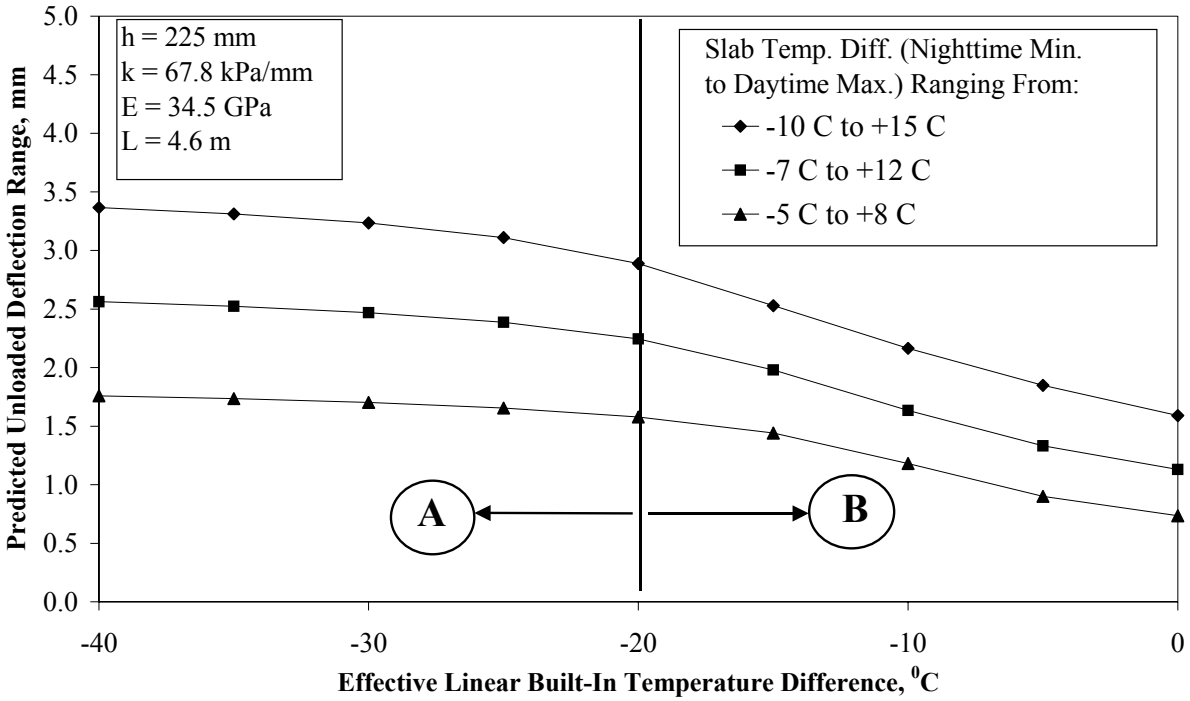

Region A (*EBITD* < -20 ºC):
Slab corner does not come in contact with base over 24-hour cycle;
Corner deflection range not sensitive to *EBITD* and cannot be used to estimate *EBITD*.
Region B (-20 ºC < *EBITD* < 0 ºC):
Slab corner comes in contact with base over 24-hour cycle;
Corner deflection range can be used to estimate *EBITD*.

Figure 3-11. Predicted unloaded slab deflection range versus effective built-in temperature difference for DMD4 (corner) of slab, Section 535FD.

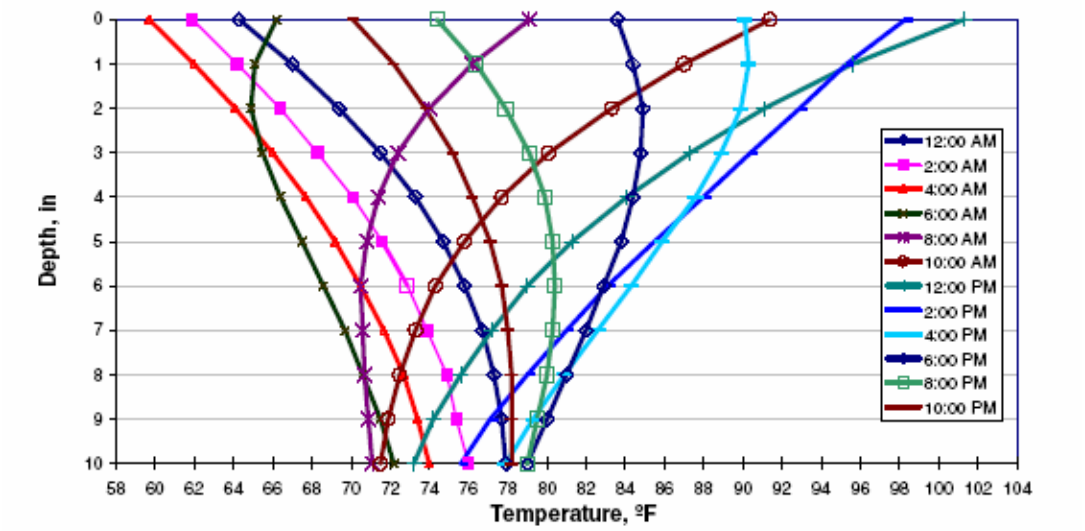

1 in = 2.54 mm, ºF = ºC × 1.8 + 32

Figure 3-12. Example of temperature profile through a 250-mm concrete slab for a typical spring day (from Yu et al., 2004).

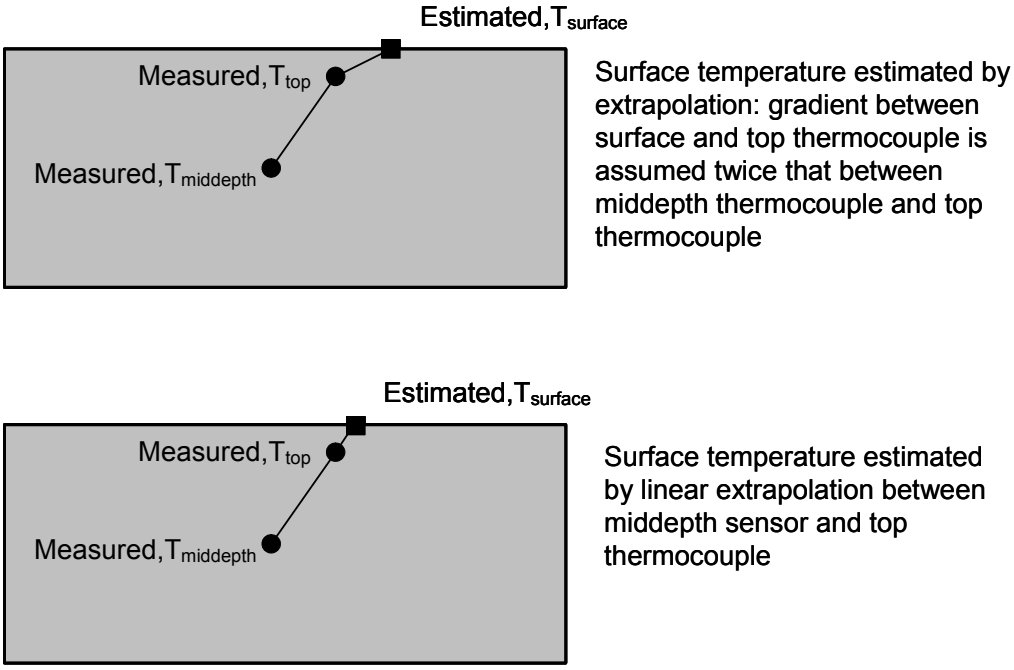

Figure 3-13. Estimation of slab surface temperature by extrapolation of embedded thermocouple readings.

gradient at any given time between the top thermocouple and the slab surface is not known. Therefore, a true measure of the slab surface temperature could not be obtained.

An example of the consequence of not accurately knowing the surface temperature is shown in Figure 3-14, which is the analysis for DMD4 (left corner deflection) for Section 535FD. The measured deflection range (difference between highest DMD4 reading and lowest DMD4 reading) is approximately 2.1 mm. The predicted unloaded deflection range matches the measured unloaded deflection range at *EBITD* value of –33ºC, assuming linear interpolation between the mid-depth and top sensor. However, using a higher gradient between the surface of the slab and the top thermocouple, the predicted unloaded deflection range matches the measured unloaded deflection range at *EBITD* of –17ºC.

Because the actual gradient between the surface of the slab and the top thermocouple is not known, and because the Palmdale test sections have large *EBITD* as evidenced by the

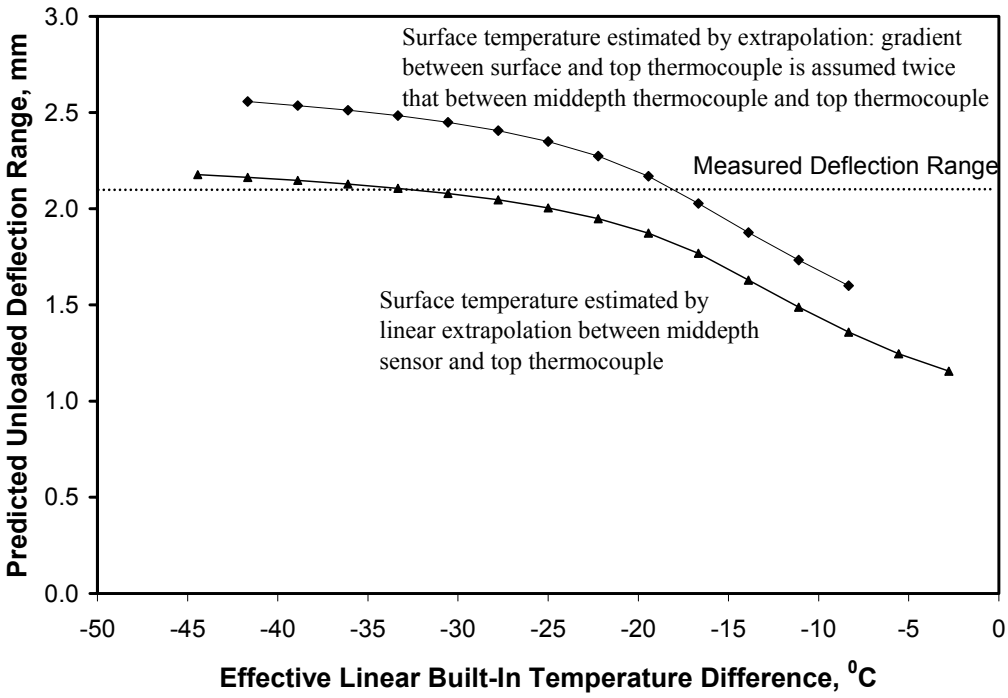

Figure 3-14. Effect of extrapolation on estimated effective built-in temperature difference using unloaded slab deflection range.

analysis in the following section, an accurate estimate of the true *EBITD* could not be obtained using unloaded slab deflection range.

The limitations associated with using unloaded slab deflections make them less suitable, and in cases of slabs with high built-in curl, unsuitable for back-calculating *EBITD* of in-service slabs. A procedure for back-calculating *EBITD* using loaded slab deflections is developed in the following sections.

3.2.3 24-Hour Loaded Slab Deflections for Palmdale Sections

Several North Tangent sections—535FD and 537FD through 541FD—were loaded over a 24-hour cycle with a rolling 40-kN dual-wheel load, with and without the use of temperature control. These 24-hour load tests were conducted to evaluate the intraday response of the test

slabs to daily temperature fluctuations. Deflections were measured relative to the unloaded slab (not relative to the flat slab condition).

Deflections for Section 535FD, measured at two corners (DMD2 and DMD4) and one mid-slab edge (DMD3), along with the temperature difference between the top and bottom thermocouples measured at four slab locations with HVS loading and without the temperature control box are shown in Figure 3-15. The deflections are presented relative to the unloaded slab (not relative to the flat slab condition). Figure 3-15 shows that the slab corners and edge deflected less under positive temperature differences because of the reduction in slab lift-off. As expected, the deflections at the mid-slab edge were lower than those at the two slab corners. At two corners of the same slab, the loaded deflections were significantly different from each other. Some of this was a result of the asymmetry of the slab configuration, but much of it was likely due to differences in *EBITD* arising from difference in restraints between the two slab corners.

This is in contrast with the unloaded slab deflections, shown in Figure 3-8. This figure shows that the two corners had similar deflection ranges. As described earlier, the reason for this apparent discrepancy is that for slabs with large upward curling, the slab corners do not come into contact with the base during the 24-hour unloaded slab monitoring period, and thus the temperature-based movement is not sensitive to the initial curling of the slab. The two corners of the slab can have different values of *EBITD*, resulting in dissimilar loaded deflections, but have comparable unloaded slab deflection range. This further validates the fact that unloaded slab deflections cannot be used to back-calculate *EBITD* for slabs with high built-in curl.

The loaded slab deflections for Section 535FD with the operation of the temperature control box are shown in Figure 3-16. The thermocouples in the slab under the temperature control box showed very little change over the 24-hour period. The thermocouples in the shade

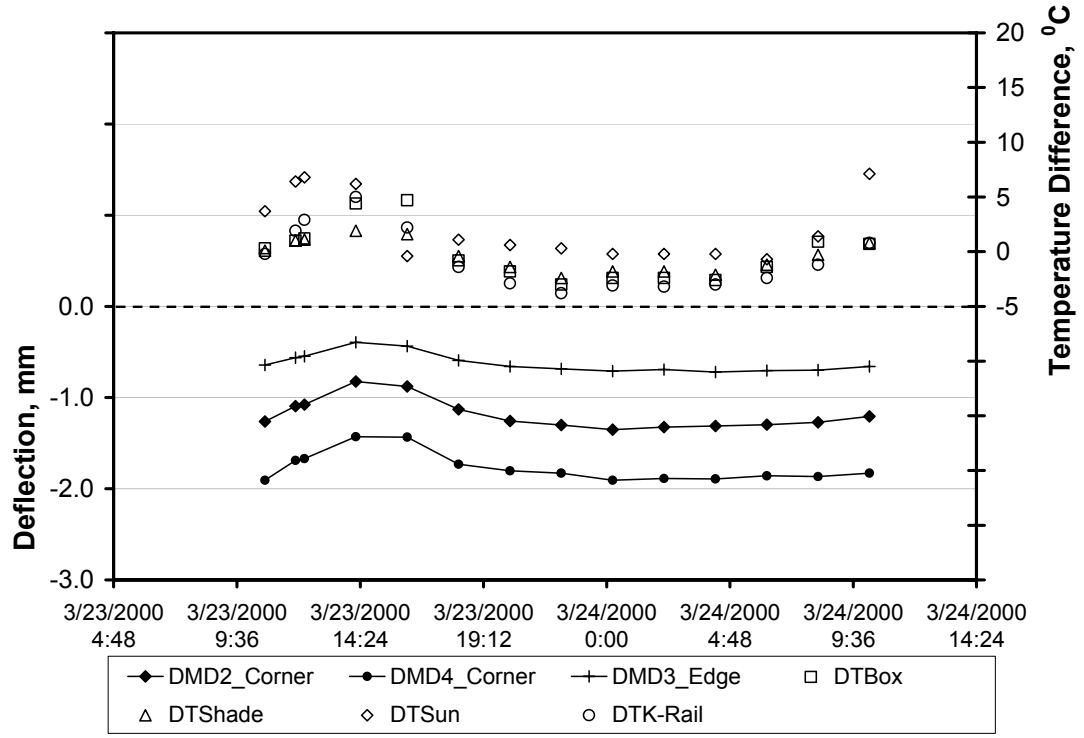

Figure 3-15. 24-hour 40-kN dual-wheel half-axle loaded slab deflections without using the temperature control box, Section 535FD.

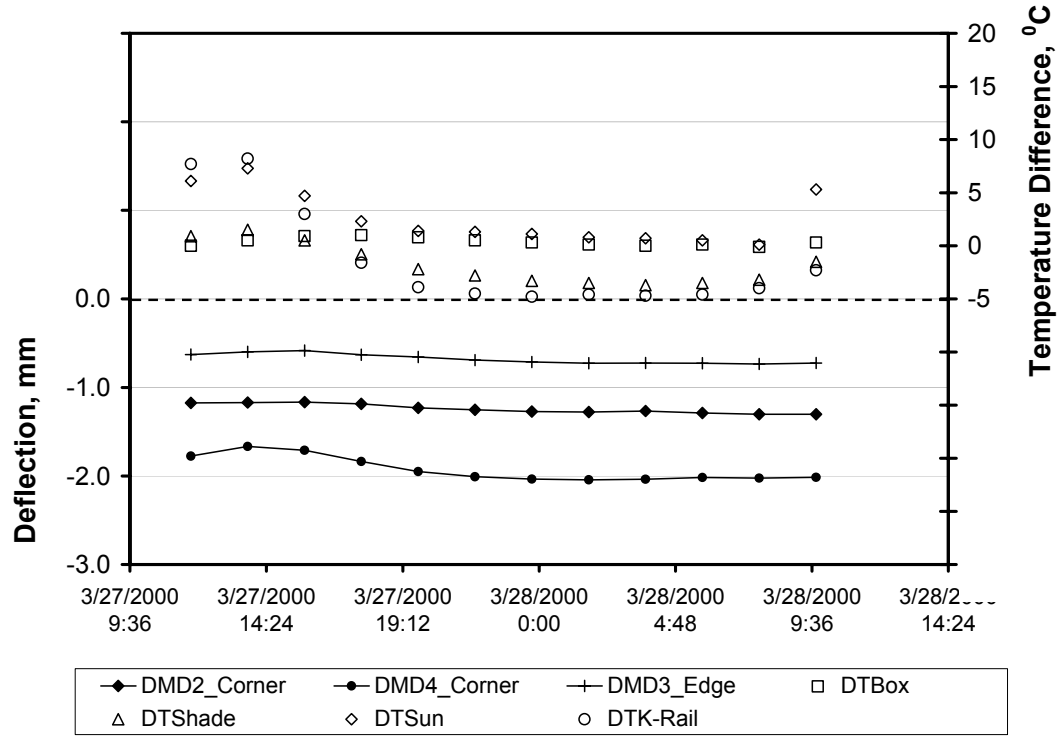

Figure 3-16. 24-hour 40-kN dual wheel half-axle loaded slab deflections with use of the temperature control box, Section 535FD.

and directly exposed to the sunlight showed a greater variation over the 24-hour period. As in the case of the unloaded slab deflections, even though the part of the slab corresponding to the DMD locations were completely covered by the temperature control box, the DMDs were affected by the temperature cycling of the exposed portion of the slab. Again, corner deflections measured at the left corner by DMD4 were much greater than those measured at the right corner by DMD2, implying higher *EBITD* at the left corner as compared to the right corner.

The 24-hour loaded slab deflections for the rest of the North Tangent test sections where such data was collected—Sections 537FD through 541FD—are shown in Appendix A.

3.2.4 24-Hour Loaded Slab Deflection Analysis

For slabs with permanent curling, loaded slab deflections are more suitable for calculating the *EBITD* in the slab as compared to unloaded slab deflections. Loaded deflections are a function of the *TELTD* in the slab (or total curl of the slab). Figure 3-17 shows a plot of the 40-kN loaded slab deflections (calculated using ISLAB2000) versus *TELTD* in the slab for three sections. At low negative or positive *TELTD*, the loaded corner deflection is not sensitive to *TELTD*, and thus cannot be used to estimate *TELTD*, and consequently *EBITD*. In these situations, the corner of the slab (or edge of the slab) comes in contact with the base under the action of the load. When the slab is in full contact with the base, the corner deflections do not depend on the total temperature difference in the slab. However, at higher negative *TELTD*, the predicted corner deflections are proportional to the *TELTD* and *EBITD*.

A second advantage of using loaded slab deflections is that an accurate estimate of the surface temperature is not required. This is because all data points over the 24-hour loading period can be used to estimate *EBITD*, as opposed to the unloaded slab deflection range where only the two data points corresponding to the two extremes of the daily temperature (daytime

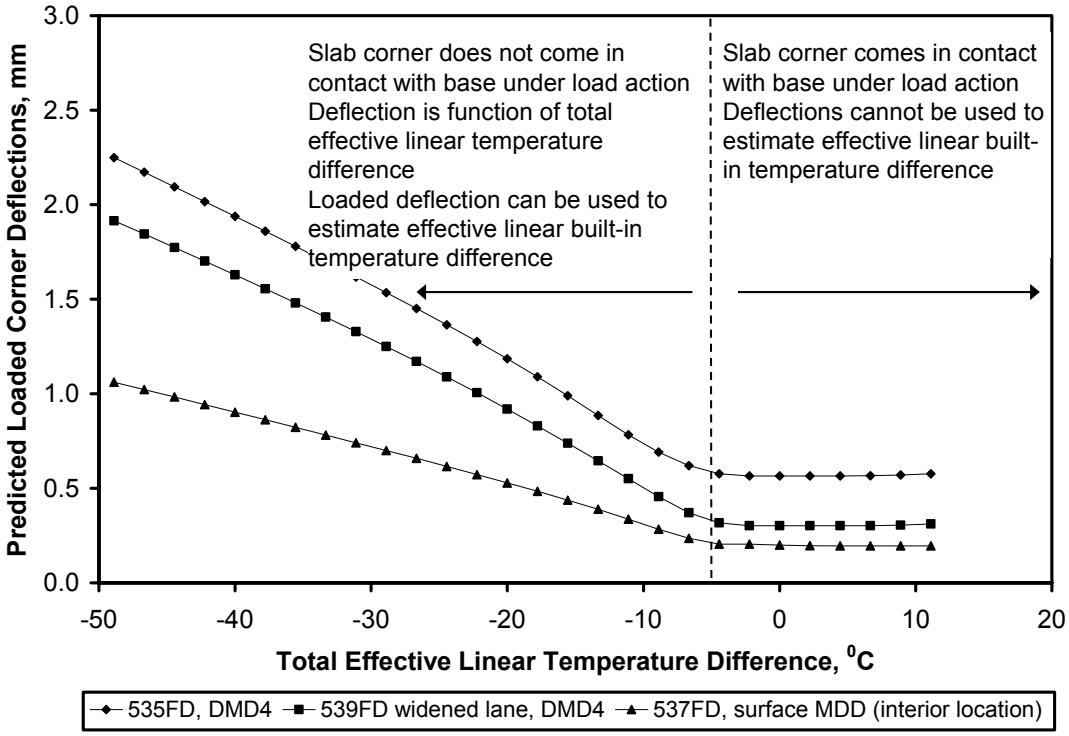

Figure 3-17. Predicted loaded slab deflections under influence of 40-kN dual wheel for Section 535FD (DMD4, slab corner deflection, slab corner loading), Section 537FD (interior MDD location deflection, slab corner loading), and widened lane Section 539FD (DMD4, slab corner deflection, interior loading) as a function of total effective linear temperature difference.

maximum and nighttime minimum) are used. Because the temperature gradient between the top thermocouple and the slab surface fluctuates throughout the day, using several data points over the 24-hour loading period results in lower error than using the two daily extreme temperatures.

To calculate the *EBITD* for the 24-hour 40-kN load slab response testing, ISLAB2000 was used to perform the analysis as follows:

1. An *EBITD* between the top and the bottom of the slab was assumed and added to the measured temperature difference obtained through linear interpolation of the sensor readings as shown in Figure 3-13. The analysis was performed separately for the

thermocouple in the shade and the thermocouple inside the temperature control box, with the average *EBITD* being reported. Although the measured gradients in the slab are typically nonlinear, for computational ease they were assumed linear. This assumption did not significantly affect the results (< 1 to 2ºC) because when the temperature control box was used, the temperature differences and the amount of temperature nonlinearity were small. When the box was not used, the extent of the nonlinearity was small for a majority of the data points because of the shade provided by the HVS.

2. ISLAB2000 was used to calculate the predicted slab deflections due to the 40-kN load and *TELTD* for each of the two-hour time intervals for the specific concrete slab geometry and layer properties.
3. For each two-hour time interval, a residual was calculated based on the difference in measured versus predicted deflection.
4. An iterative procedure was used to calculate the value of the *EBITD* that minimized the sum of square of the residuals over the 24-hour cycle.
5. The analysis was repeated using the measured temperature difference obtained through nonlinear interpolation of the sensor readings. The difference in estimated *EBITD* between the two types of interpolation was negligible (< 1ºC). This is because for most of the two-hour time intervals, the temperature differences between the top and the bottom of the slab were small (particularly with the temperature control box in use), resulting in only a small effect of temperature nonlinearity. As described earlier, all data points are used in calculating *EBITD* using loaded slabs, and not just the daytime and nighttime extremes, which can be highly nonlinear, as in the case of

unloaded slab deflections. In this research, the average of the two interpolations—linear interpolation and nonlinear interpolation—is reported as the back-calculated *EBITD*.

The process described above was performed on both slab corners and the mid-slab edge for all test sections. The inputs used for the ISLAB2000 finite element analysis for each test slab are summarized below:

- Subgrade Properties—back-calculated modulus of subgrade reaction as described in Section 2.4.4.
- Slab Properties—back-calculated modulus of elasticity as described in Section 2.4.4, laboratory-measured coefficient of thermal expansion as described in Section 2.4.3, Poisson's ratio as described in Section 2.4.5, section-specific slab thicknesses and densities obtained from coring data and shown in Table 2-1.
- Base Properties—back-calculated modulus of elasticity as described in Section 2.4.4, nominal base thicknesses as shown in Figure 2-1 and Figure 2-2, density of 2,100 kg/m^3 for cement-treated base and 2,000 kg/m^3 for aggregate base (from nuclear density gage measurements), Poisson's ratio of 0.20 for cement-treated base (assumed) and 0.30 for aggregate base (assumed).
- Slab-Base Interface—unbonded.
- Load-Transfer Efficiency—section-specific average LTE calculated using corner DMD deflections.
- Geometry—three slabs in longitudinal direction (left adjacent slab + test slab + right adjacent slab) by two slabs in transverse direction (shoulder slab + test slab) for slabs with concrete shoulder. Three slabs in longitudinal direction by one slab in transverse

direction, for slabs with bituminous shoulder. The geometry was selected based on sensitivity analysis, of various combinations of slabs (3 × 1, 3 × 2, and 5 × 1 for slabs with bituminous shoulders, and 3 × 2, 3 × 3, and 5 × 2 for slabs with concrete shoulders). The sensitivity analysis showed that for the low load levels used to back-calculate *EBITD*, the deflections calculated using the selected geometry were within 3 percent of the deflections calculated using other geometries, but it considerably reduced the ISLAB2000 computation time.

- Joint Spacing—section-specific joint spacings as shown in Table 2-1 (if adjacent slabs exhibited full-length transverse cracks, the average distances from the joint to the crack were used for the corresponding slab length).
- Temperature—for each test section, loaded and unloaded slab deflections calculated for *TELTD*s ranging from +10 to –50ºC in increments of 2ºC. The difference between the loaded slab deflection and the unloaded slab deflection for a given *TELTD* is the deflection due to the load application, which is then compared to the measured loaded deflection.
- Load—corner and edge loading as described in Section 2.2.
- Mesh—node spacing in the longitudinal direction ranging from 60 to 95 mm, node spacing in the transverse direction ranging from 80 to 100 mm resulting in a minimum of 2,600 elements on the test slabs.

The *EBITD* analysis results for the test sections are summarized in Table 3-4. The average *EBITD* was based two independent calculations of *EBITD*: with and without the temperature control box. As seen in Table 3-4, the *EBITD* values of the slabs were similar, whether they were calculated with or without the temperature control box.

Table 3-4 Summary of Estimated Effective Built-in Temperature Difference (ºC) for the North Tangent Sections at JDMD Locations

Section	Estimated Built-in Temperature Difference, ºC								
	Left Corner			Midslab			Right Corner		
	Temperature Control Box Used?		Average	Temperature Control Box Used?		Average	Temperature Control Box Used?		Average
	No	Yes		No	Yes		No	Yes	
535FD	–31.6	–35.0	–33.3	–19.9	–22.0	–20.9	–21.4	–22.2	–21.8
537FD	> –5.0	> –5.0	> –5.0	> –5.0	> –5.0	> –5.0	–9.2	–12.6	–10.9
538FD	–14.7	–	–14.7	> –5.0	–	> –5.0	–18.5	–	–18.5
539FD	–10.5	–11.2	–10.8	–6.0	–5.5	–5.7	–13.4	–12.7	–13.0
540FD	–14.0	–10.0	–12.0	–11.3	–8.3	–9.8	–17.3	–16.8	–17.1
541FD	–5.5	–	–5.5	> –5.0	–	> –5.0	–8.5	–	–8.5

The *EBITD* varied considerably among sections and from one corner of the slab to the other. The highest *EBITD* occurred on Section 535FD (–33.3ºC), which had the least amount of restraint on the slab (i.e., no dowels or tied concrete shoulders). The widened lane and tied concrete shoulder sections with dowels at the transverse joints (Sections 537FD to 541FD) had smaller *EBITD* values compared to sections with plain joints and an asphalt shoulder. Dowels reduced the *EBITD* by restraining the slab from lifting off the base layer. Furthermore, the doweled sections gave similar *EBITD* values at both joints, suggesting a more uniform restraint against upward curl.

Figure 3-18 through 3-20 show the residuals (difference between measured deflections and predicted deflections) as a function of temperature difference through the depth of the slab, measured deflections, and predicted deflections. The three figures show that the residuals are normally distributed about zero and are typically less than 10 percent of the measured deflections. The residuals also do not show any significant trend with temperature difference, measured deflection, or predicted deflection indicating true randomness and no other systemic cause for the difference between measured and predicted deflections. Any significant trend of the

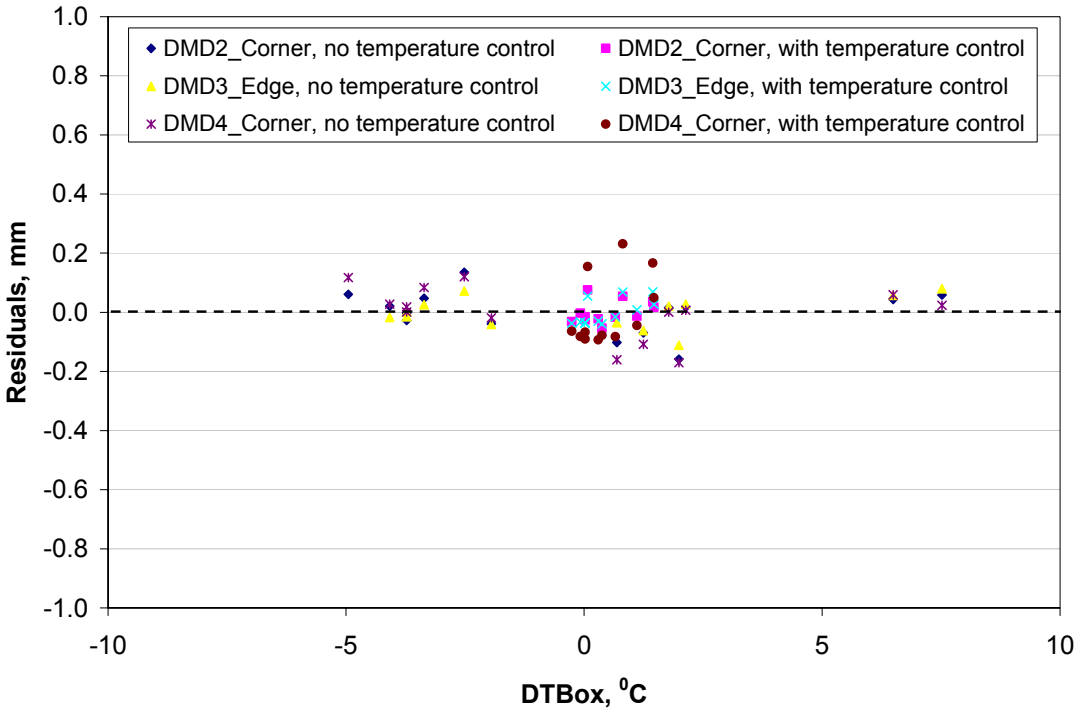

Figure 3-18. Residuals (difference in measured deflections and predicted deflections) as a function of temperature difference for DMD2, DMD3, and DMD4 measured with and without temperature control for Section 535FD.

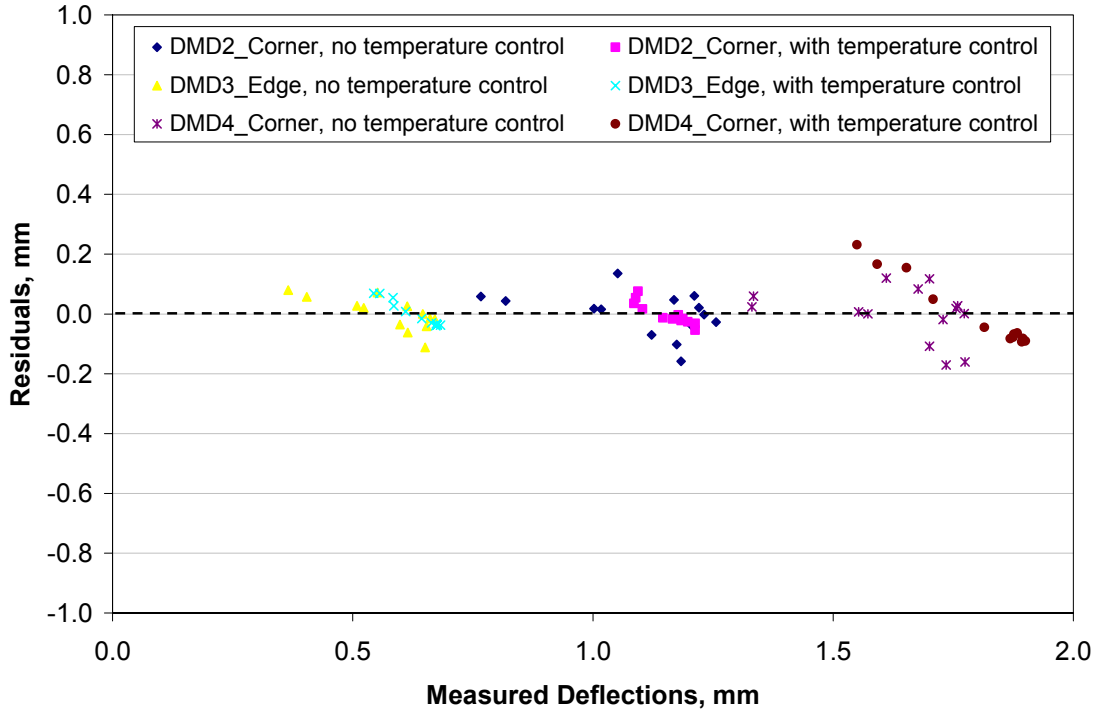

Figure 3-19. Residuals (difference in measured deflections and predicted deflections) as a function of measured deflections for DMD2, DMD3, and DMD4 measured with and without temperature control for Section 535FD.

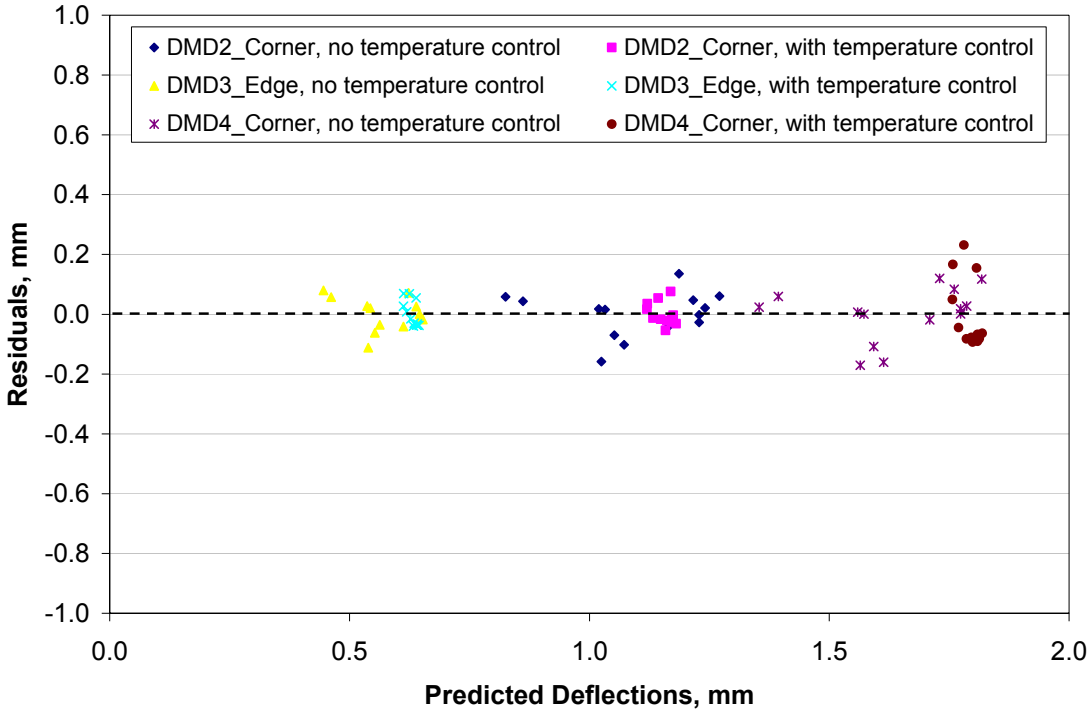

Figure 3-20. Residuals (difference in measured deflections and predicted deflections) as a function of predicted deflections for DMD2, DMD3, and DMD4 measured with and without temperature control for Section 535FD.

residuals versus temperature difference, measured deflections, or predicted deflections, would suggest a systemic source of error such as an inaccurate assumption for an input. The residuals for the rest of the North Tangent test sections, Sections 537FD through 541FD, are shown in Appendix A.

For Section 535FD, the estimated *EBITD*s were –33.3ºC, 20.9ºC, and –21.8ºC, for the left corner, midslab edge, and right corner, respectively. The *EBITD* along the slab longitudinal edge was asymmetric. Although the *EBITD* appeared high in Section 535FD, the concrete slabs satisfied many conditions relevant to high *EBITD*, including: (a) fast-setting high-early-strength concrete with superplasticizer, (b) more than 400 kg/m^3 of high shrinkage cement in the mix, (c) desert conditions with low ambient humidity, (d) daytime construction, (e) high concrete elastic

modulus, and (e) low restraint (no dowels and AC shoulders). The results were consistent with those observed by Byrum (2000) who calculated *TELTD*s of –35ºC to +44ºC for 200-mm slabs. The results are further supported by the fact that all of the long slabs at the test site had cracked prior to any load application (Heath and Roesler, 2000).

In Table 3-4, several sections had calculated *EBITD* > –5.0ºC (more positive). This occurred on 3 out of 6 mid-slab locations. As illustrated in Figure 3-17, when the slab comes into contact with the base during loading, the deflections do not depend on the total temperature difference in the slab. This occurs at low negative or positive *TELTD*. An accurate estimate of *EBITD* was not possible under loading for these locations. However, since the upward curl of the slab is small, in these cases, the *EBITD* does not significantly affect slab stresses.

3.2.5 Multi-Depth Deflectometer Deflections

The analysis presented in Section 3.2.4 using the 24-hour loaded slab deflections was also performed for interior vertical surface deflections measured by the MDDs for sections where MDD data was collected. The MDD locations and the results for the analysis sections are summarized in Table 3-5. Although the *EBITD* values calculated from the MDD measurements were less than the JDMD results, the magnitudes of the *EBITD* values were of the same order, verifying the high built-in curl that existed in the concrete slabs. As shown in Figure 3-17, the slope of the deflection versus *TELTD* is flatter for the MDD location relative to the JDMDs. Subsequently, slight errors in deflection will result in larger errors in *TELTD* as compared with the JDMDs.

The 24-hour loaded MDD deflections for Section 535FD, without and with use of the temperature control box, are shown in Figure 3-21 and Figure 3-22, respectively. The MDD deflections shown correspond to an interior location—mid-slab wheel path (0.3 m from shoulder

Table 3-5 Summary of Estimated Effective Built-in Temperature Difference (ºC) for the North Tangent Sections at MDD Locations

Section	MDD Location	Temperature Control Box Used?		Average
		No	Yes	
535FD	Midslab, 0.3m from shoulder	-18.9	-20.6	-19.7
537FD	Right corner, 0.3m from shoulder, 0.3m from joint	>-5.0	>-5.0	>-5.0
538FD	No MDD	-	-	-
539FD	Right corner, 0.3m from lane edge (0.9m from shoulder), 0.3m from joint	-6.9	-6.8	-6.9
540FD	Right corner, 0.3m from lane edge (0.9m from shoulder), 0.3m from joint	-17.5	-15.5	-16.5
541FD	No MDD	-	-	-

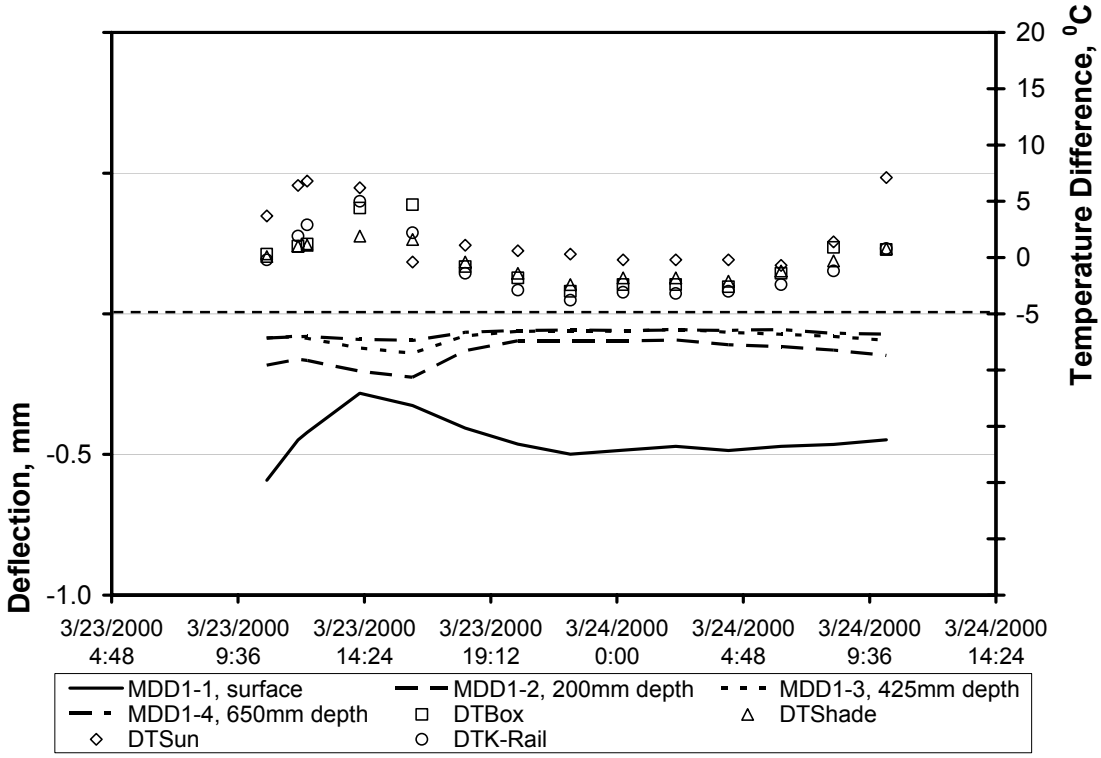

Figure 3-21. MDD deflections for Section 535FD measured over a loaded 24-hour cycle without temperature control.

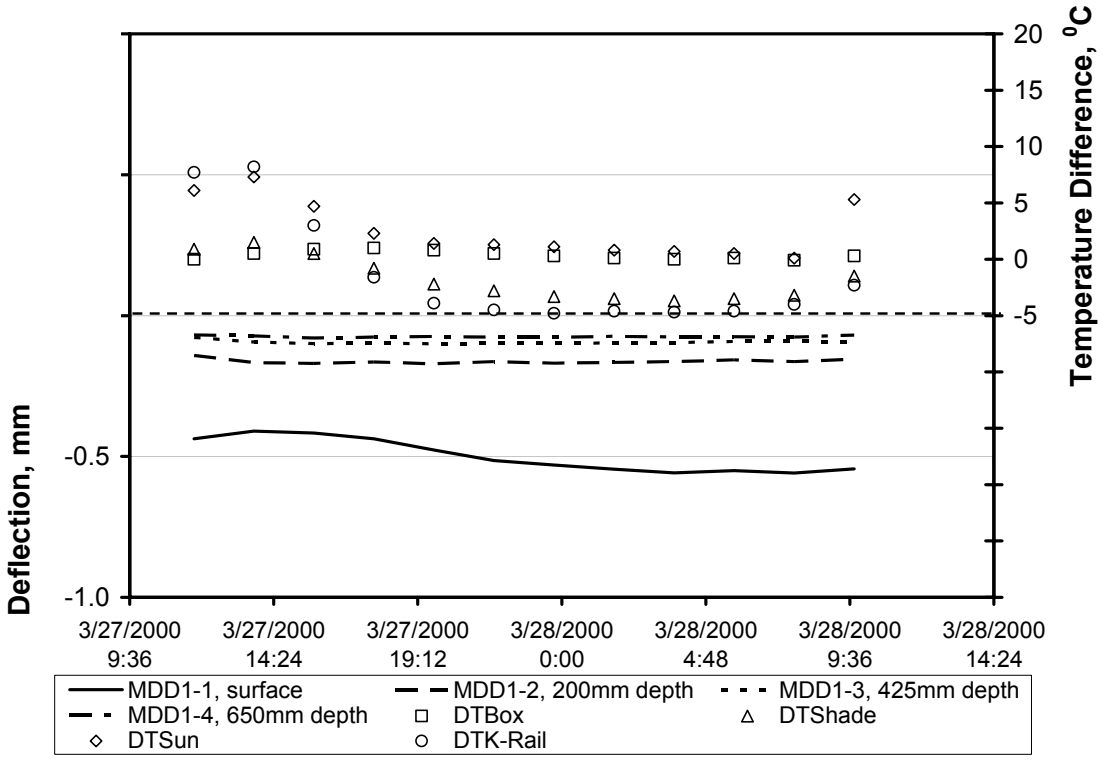

Figure 3-22. MDD deflections for Section 535FD measured over a loaded 24-hour cycle with use of the temperature control box.

joint). MDD1-1 corresponds to the deflection of the concrete slab, while MDD1-2 corresponds to that of the base course. MDD1-3 and MDD1-4 correspond to subbase and subgrade deflections, respectively. As expected, MDD1-1 deflected in tandem with the mid-slab edge deflection (DMD3 from Figure 3-15 and Figure 3-16) and deflected less under positive temperature differences. However, the deflections in the base, subbase, and subgrade were significant only when the temperature difference was positive, resulting in contact of the slab with the base. This is the reason for the opposing deflection trends of MDD1-1 versus MDD1-2 through MDD1-4. When the temperature difference in the slab was negative or small, the slab did not come in contact with the base and MDD1-2 through MDD1-4 only registered a small amount of elastic deformation, not affected by temperature difference in the slab. The MDD deflections for

Section 535FD are consistent with the higher *EBITD* values back-calculated using DMD deflections.

The 24-hour loaded MDD deflections for the remaining North Tangent test sections where such data was collected—Sections 537FD, 539FD and 540FD, with and without use of the temperature control box, are shown in Figure 3-23 through Figure 3-28. The MDD deflections for Section 537FD (Figure 3-23 and Figure 3-24) correspond to the right corner of the slab, 0.3 m from the shoulder joint and 0.3 m from the transverse joint. As expected, MDD1-1 deflected in tandem with the right corner deflection (JDMD2 from Figure A-9 and Figure A-10 in Appendix A), and less under positive temperature differences. However, the slab did not come in contact with the base and MDD1-2 through MDD1-4 only registered a small amount of elastic deformation, not affected by temperature difference in the slab.

The MDD deflections for Section 539FD and 540FD (Figure 3-25 through Figure 3-28) correspond to the right corner of the lane, 0.3 m from the lane edge (0.9 m from the shoulder joint) and 0.3 m from the transverse joint. In both cases, the MDD deflections of the treated base were high and on the order of the slab deflections. This suggests that at this interior location (0.9 m from the lane-shoulder joint), when loaded, the slab came in contact with the base.

3.2.6 Validation with 20-80 kN Incremental Load Deflections

As part of the 24-hour loading analysis of the North Tangent sections, each test slab was subject to rolling dual-wheel loads ranging from 20 to 80 kN in increments of 10 kN. These loads were typically applied within 5 minutes of each other, and the entire set of incremental loading for a given section was completed within an hour. Deflections resulting from the rolling HVS load were collected using DMDs. The vertical temperature profile data in the slab were also

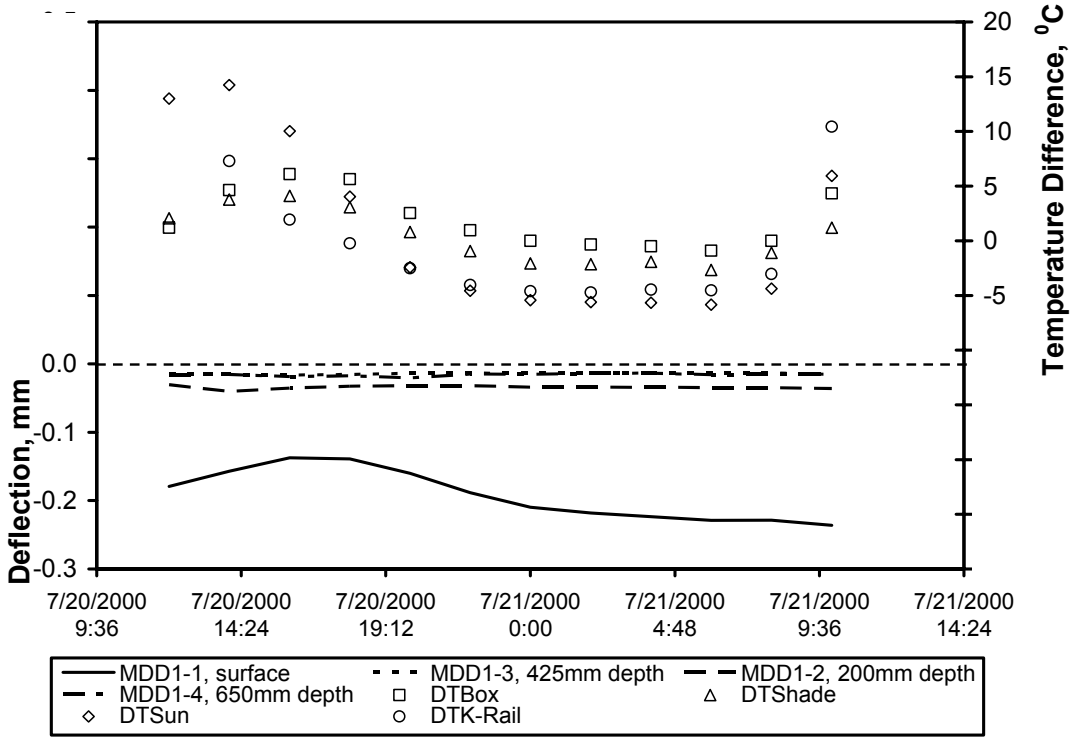

Figure 3-23. MDD deflections for Section 537FD measured over a loaded 24-hour cycle without temperature control.

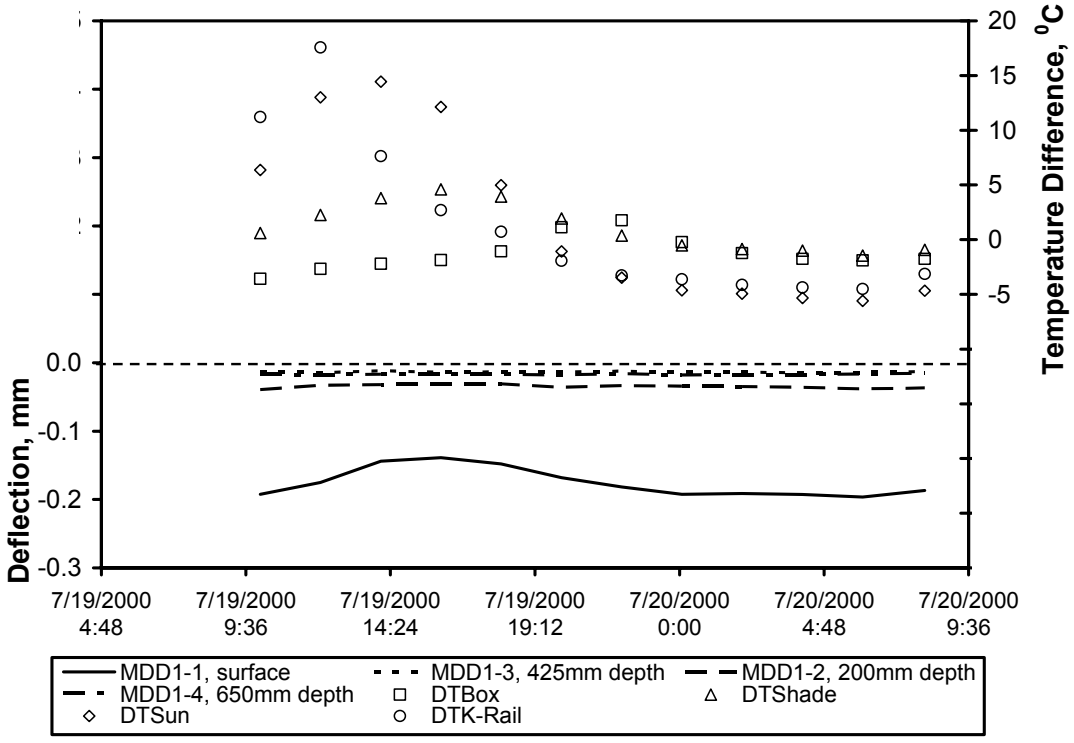

Figure 3-24. MDD deflections for Section 537FD measured over a loaded 24-hour cycle with use of the temperature control box.

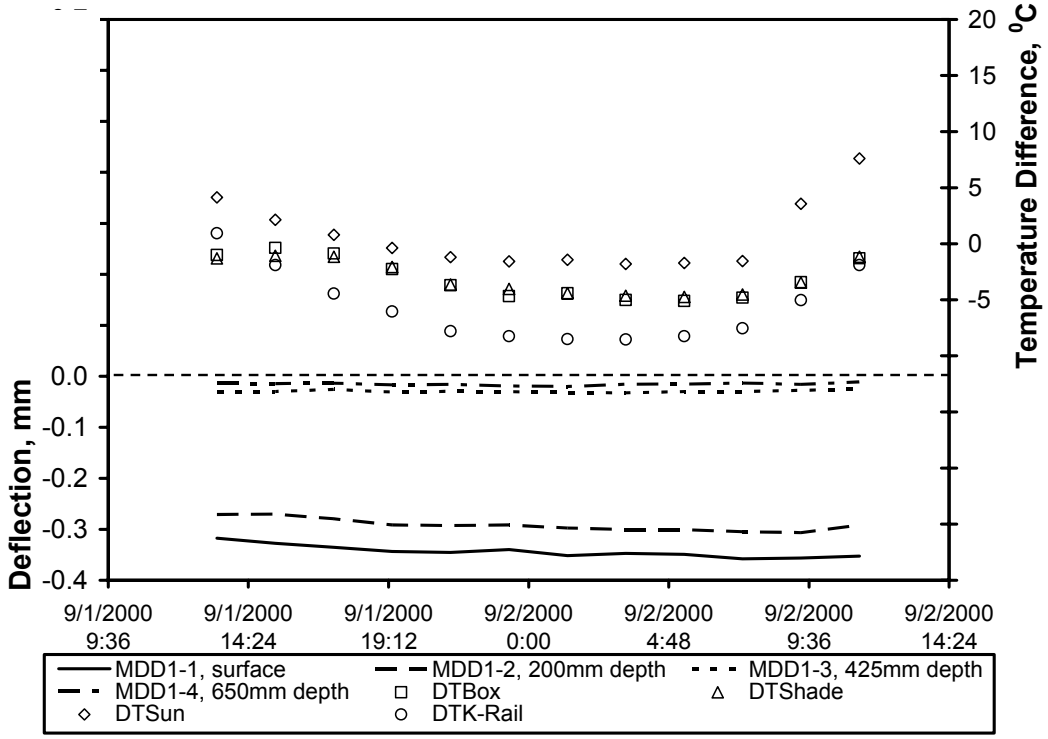

Figure 3-25. MDD deflections for Section 539FD measured over a loaded 24-hour cycle without temperature control.

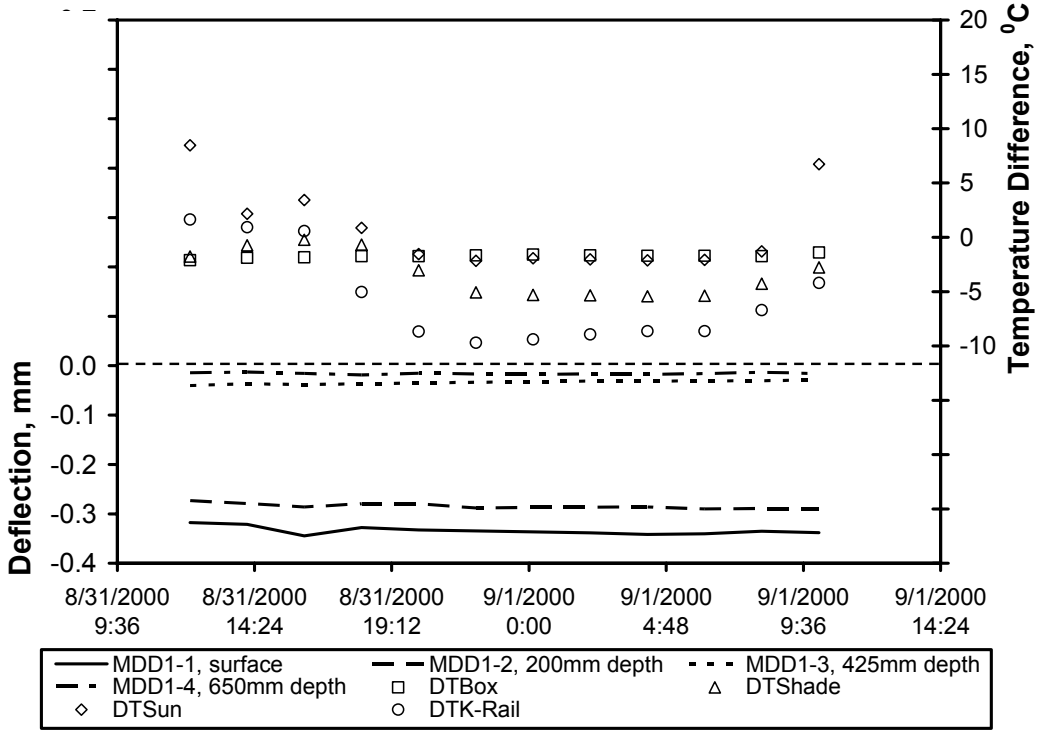

Figure 3-26. MDD deflections for Section 539FD measured over a loaded 24-hour cycle with use of the temperature control box.

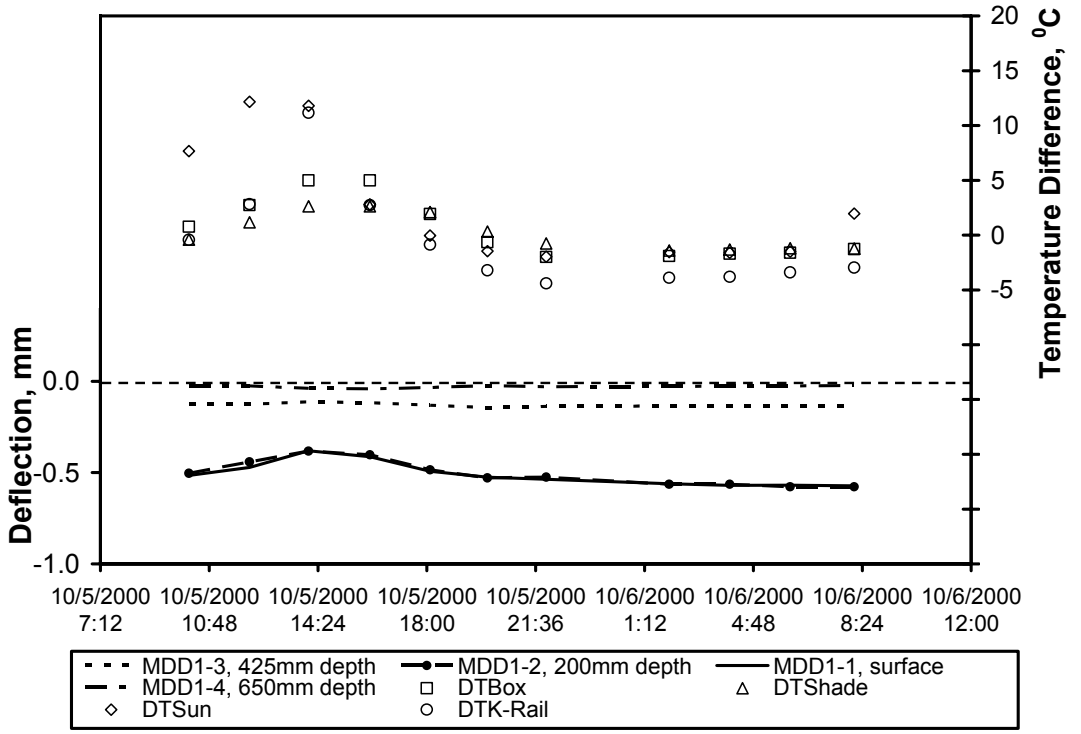

Figure 3-27. MDD deflections for Section 540FD measured over a loaded 24-hour cycle without temperature control.

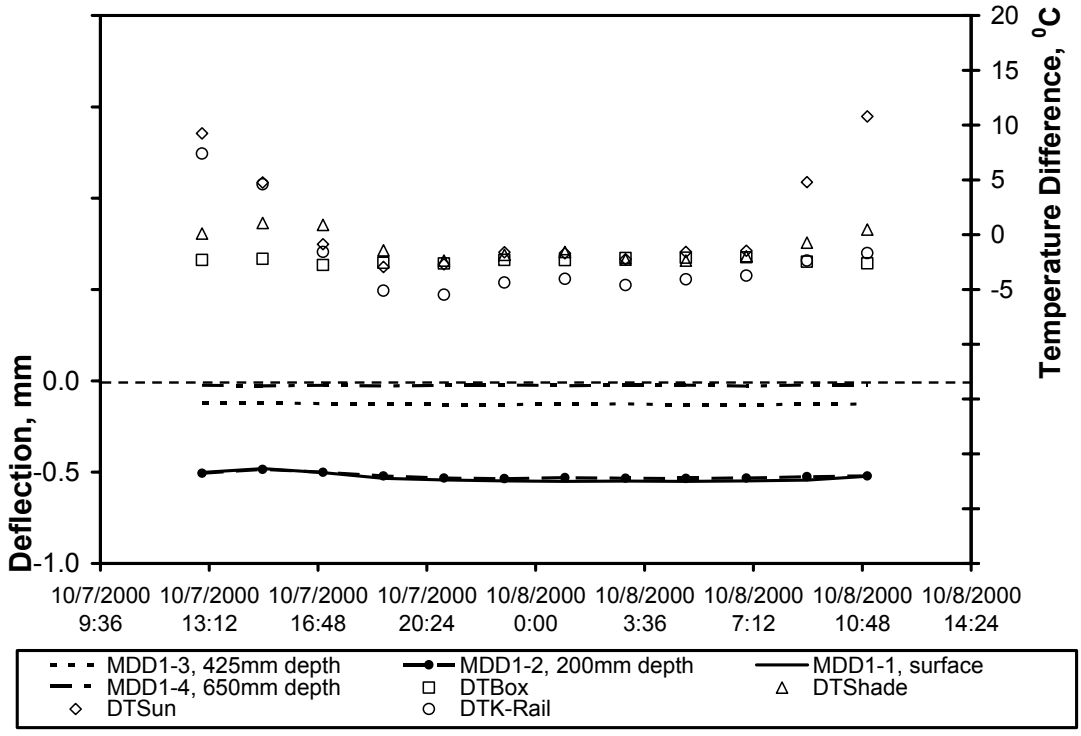

Figure 3-28. MDD deflections for Section 540FD measured over a loaded 24-hour cycle with use of the temperature control box.

collected using the embedded thermocouples. Since the data for each section was collected within an hour, there was no significant difference in thermocouple readings among the load increments.

An analysis was performed on the incremental loaded corner and midslab edge deflection data to verify *EBITD* results from the 40-kN 24-hour loaded tests. The average estimated *EBITD* was added to the temperature difference measured by the embedded thermocouples to obtain the *TELTD* in the slab. Using known layer properties and slab geometry, ISLAB2000 was used to calculate the slab deflections corresponding to each load increment. These calculations were performed for both corners and the mid-slab edge of the test slabs.

The measured corner (DMD2 and DMD4) and edge (DMD3) deflections for Section 535FD and corresponding deflections predicted using the average *EBITD* values obtained from the 40-kN analysis are shown in Figure 3-29. Predicted versus measured deflections are shown in Figure 3-30. The predicted deflections showed good agreement with the measured deflections at the three slab locations further verifying the *EBITD* estimates from the DMD and MDD analysis.

The predicted versus measured deflections due to incremental loading for Sections 537FD through 541FD are shown in Appendix A, Figures A-32 through A-36. The results of the incremental load analysis showed good agreement between the deflections predicted using calculated *EBITD* and ISLAB2000 and the measured deflections at the test locations for Sections 535FD, 537FD, 540FD, and 541FD. For Sections 538FD and 539FD, the measured deflections did not increase with the load at low load levels, which was unexpected. This could have been a result of the HVS load not being set correctly. The HVS load level is set manually and read through a dial gage, which may have been the source of the discrepancy for Sections 538FD and 539FD.

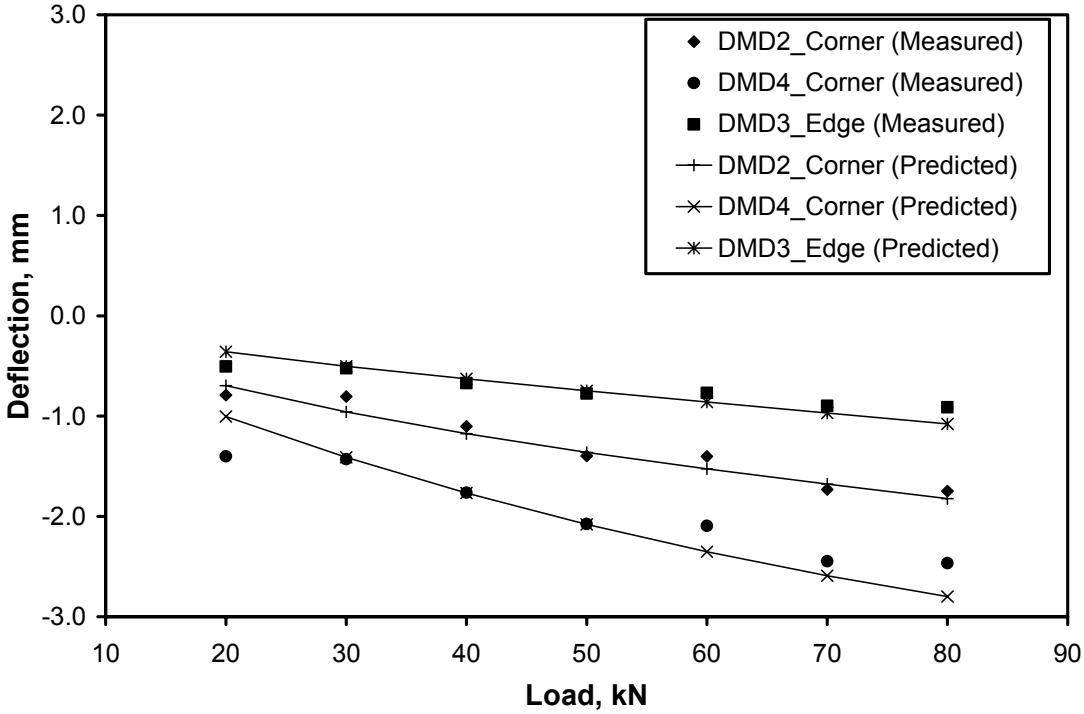

Figure 3-29. Measured and predicted corner (DMD2 and DMD4) and edge (DMD3) deflections for Section 535FD under the influence of 20- to 80-kN loads in 10-kN increments with no significant differences in slab temperature gradients.

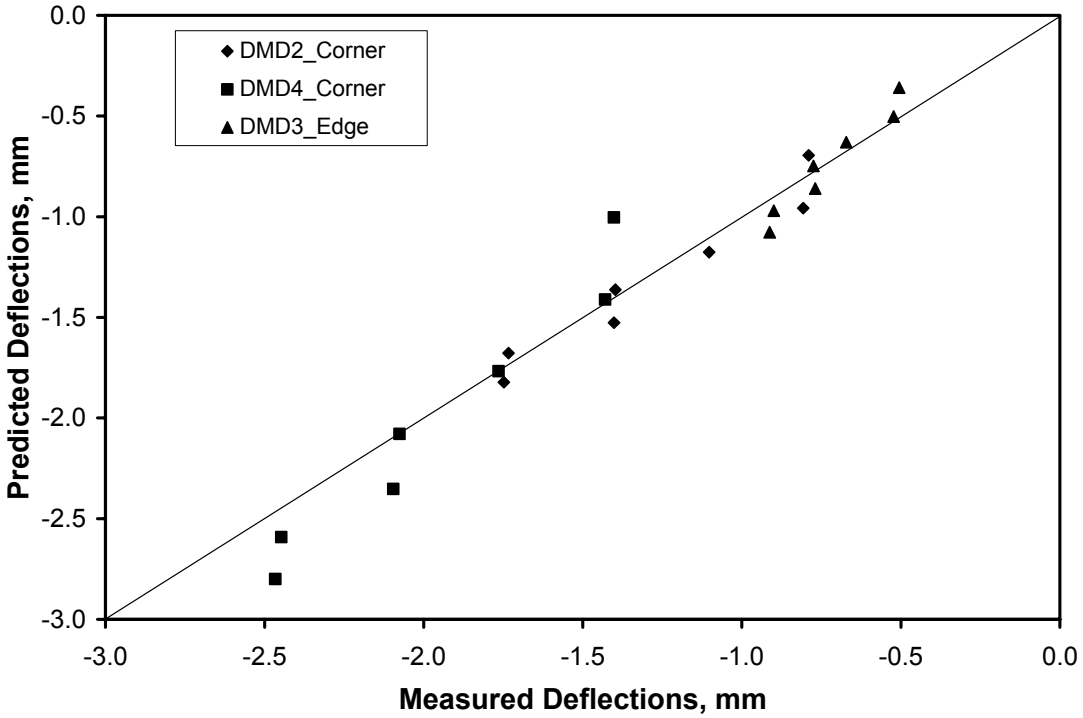

Figure 3-30. Predicted versus measured corner (DMD2 and DMD4) and edge (DMD3) deflections for Section 535FD under the influence of 20- to 80-kN loads in 10-kN increments.

3.2.7 Back-calculation of Effective Built-In Temperature Difference Using Falling Weight Deflectometer

The slab loading used to estimate *EBITD* can either be traffic loading, such as from a Heavy Vehicle Simulator (HVS), or simulated loading, such as from a Heavy Weight Deflectometer (HWD) or a Falling Weight Deflectometer (FWD). The procedure for using an FWD involves dropping a load at the slab corner and measuring deflections beneath the load plate and across the transverse joint. When the corner of a curled slab is loaded, the corner deflections due to the action of the load are a function of the total amount of curl in the slab and the applied load as shown in Figure 3-31. The greater the slab curling due to the combined effect of temperature and built-in gradients, the greater the deflection of the slab corners. A rigid pavement finite element analysis program (ISLAB2000) is used to determine the total effective linear temperature difference, *TELTD*, in the slab that results in the same measured deflection beneath the FWD load plate. The *EBITD* can then be calculated as the difference between the *TELTD* and the field-measured temperature difference. Rao and Roesler (2005B) summarizes the mechanics of the procedure.

A similar procedure has been used to determine the presence of voids resulting from pumping and loss of support beneath concrete slab corners (Crovetti and Darter, 1985; FHWA, 1998). The void procedure uses corner FWD deflection data at several load levels extrapolated to zero load level to determine the existence or absence of voids beneath the slab corners. In contrast, the procedure for estimating *EBITD* uses corner FWD deflection data along with a finite element program to estimate the magnitude of corner curl in the slab.

FWD data was collected on the North Tangent sections at three different load levels (low, medium, and high) at the leave corner of the lane. The low load level was of the order of 40 to 45 kN, medium level of the order of 60 to 70 kN, and the high load level of the order of 85 to

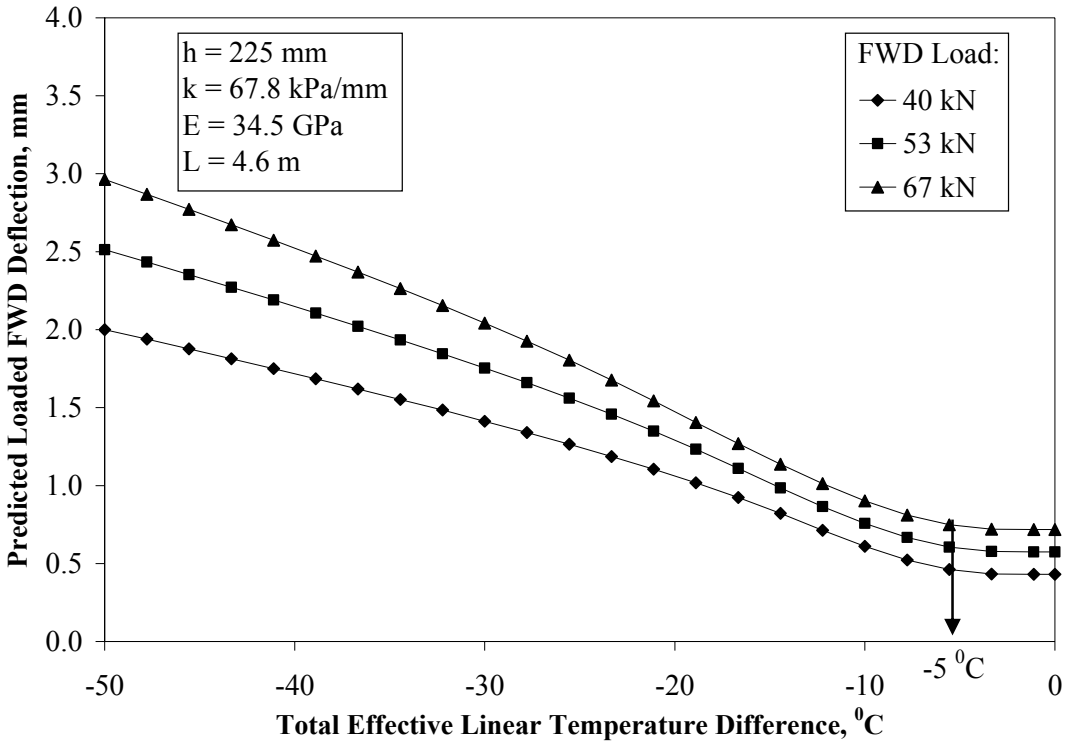

Figure 3-31. Predicted falling weight deflectometer loaded slab corner deflection versus total effective linear temperature difference for a typical slab.

95 kN. ISLAB2000 was used to calculate the estimated deflections (beneath the load plate) due to the FWD loads at the leave corner of the test slab for a range of *EBITD* values. Since no thermocouple data was available during the FWD data collection, the linear temperature difference in the slab was estimated based on air temperature, slab surface temperature, and time of day. The *EBITD* value corresponding to a match between the ISLAB2000 predicted deflection and the measured deflection is the estimated *EBITD* value. The results of this analysis are shown in Table 3-6.

The results show good agreement between *EBITD* estimated using DMD deflections and FWD deflections for Sections 535FD, 537FD, and 538FD. The results of the widened lane Sections 539FD and 540FD show a greater difference between the FWD and the DMD estimate.

Table 3-6 Estimated Effective Built-in Temperature Difference (Right Corner) in ºC from DMD Analysis and from FWD Analysis

Section	DMD (Predicted)	FWD Low Load: 40 to 45 kN	FWD Medium Load: 60 to 70 kN	FWD High Load: 85 to 95 kN	FWD (Average)
535FD	-21.8	-22.7	-22.4	-22.8	-22.6
537FD	-10.9	-9.4	-9.9	-10.3	-9.9*
538FD	-18.5	-17.3	-17.8	-18.3	-17.8
539FD	-13.0	-14.9	-15.9	-16.8	-15.9
540FD	-17.1	-12.4	-13.1	-13.6	-13.0*
541FD	-8.5	-21.1	-21.3	-22.7	-21.7

It should be noted that for the widened lane sections, while the DMD data was collected at the slab corners, the FWD data was collected at the lane corner, more than 0.6 m from the lane shoulder joint. Also, the FWD data was collected several years after the 24-hour 40-kN loaded analysis and after HVS trafficking of the slabs. The only section with significant difference between the *EBITD* estimated using DMD deflections and FWD deflections was 541FD. A possible explanation is that following the repeated fatigue load application, this section had significant damage at critical locations and was approaching failure, resulting in higher than expected FWD deflections. In cases of slabs with significant damage, the loaded slab deflection procedure (and even the unloaded slab deflection procedure) cannot be used to back-calculate *EBITD* because the deflections calculated using ISLAB2000 are for a continuous slab (no cracks) with uniform thickness and modulus of elasticity.

3.3 Summary of Loaded Slab Deflections for Back-calculation of Effective Built-In Temperature Difference

A new procedure for back-calculating *EBITD* of in-service pavements using loaded slab deflections was developed as part of this research. The advantages of using loaded slab deflections are:

1. Loaded slab deflection analysis is the only procedure that can be used for slabs with *EBITD* less than –20ºC (slabs with high negative curl). Unloaded slab deflections and procedures based on flattening of slab surface curvature or slab-base contact cannot be used in these cases because the slab never completely flattens or comes in full contact with the base over a typical 24-hour cycle.
2. *EBITD* back-calculated using loaded slab deflections is a measure of support received by the slabs from the base and subbase layers, and not just the curvature of the surface, which is a more analytically useful way of characterizing *EBITD.*
3. The flat slab condition, or when the slab corner first comes in contact with the base, does not have to be determined. Surface profile measurements are not required and the bottom of the slab and top of the base do not have to be instrumented.
4. *EBITD* can be back-calculated with loaded slab deflections using a single data point and does not require 24-hour monitoring as in procedures based on slab surface curvature or slab-base contact. *EBITD* back-calculated using unloaded slab deflections also require 24-hour monitoring to capture the daytime and nighttime extreme deflections.
5. If loaded slab deflection data is not collected during the daytime or nighttime extremes, the nonlinearity of slab surface temperature is not a major factor affecting back-calculation of *EBITD* using loaded slab deflections. As described in Section 3.3.2 and 3.3.4, nonlinearity of slab surface temperature can affect *EBITD* back-calculation using unloaded slab deflections.
6. Loaded slab deflection procedure for back-calculating *EBITD* can be adapted for the FWD or the HWD. A large number of slabs can be tested over a relatively short

period of time without any embedded instrumentation, making it an efficient and cost-effective procedure to back-calculate *EBITD* of in-service pavements.

The limitations of using loaded slab deflections to back-calculate *EBITD* are as follows:

1. Loaded slab deflections cannot be used for slabs with low negative or positive *TELTD* (> –5ºC). In these cases, only nighttime data can likely be used to estimate *EBITD*.
2. A finite element analysis program is required to calculate predicted deflections for the applied load and a range of temperature differences through the depth of the slab. This is also a limitation of using unloaded slab deflections. Finite element analysis programs are not required for procedures based on slab surface curvature or slab-base contact.
3. A wide range of material inputs such as subgrade properties and layer moduli, densities, thicknesses, Poisson's ratios, and coefficient of thermal expansions, are required for the finite element analysis program. This is also a limitation of using unloaded slab deflections. These material inputs are not required for procedures based on slab surface curvature or slab-base contact.

The assumptions based upon which loaded slab deflections can be used to back-calculate *EBITD* for in-service slabs are as follows:

1. All plate theory assumptions and assumptions pertaining to the use of finite element analysis for concrete pavements as listed in Section 1.5.

2. For a given pavement structure, geometry, layer properties, and thermo-mechanical loading, deflections can be reasonably predicted using the finite element analysis program, ISLAB2000.
3. All layer thicknesses and material properties for a given test section are uniform and do not deviate significantly from the average values used.
4. Linear superposition of *EBITD* and measured temperature difference is valid.
5. All test slabs are intact and without any significant microcracking damage that can result in measured deflections that are higher than predicted.
6. No erosion or absence of erosion-related voids in the subgrade, base, and subbase layers.

3.4 Estimated Effective Built-In Temperature Difference for Palmdale Test Sections

24-hour loaded slab deflection data was not collected for the South Tangent and several North Tangent test sections. In these cases, the *EBITD* was back-calculated using loaded deflection data collected during the early repetitions of fatigue loading. Since fewer data points were used for any individual test section, the margin of error is likely higher than in the case of *EBITD* back-calculated using 24-hour loaded slab deflections. Also, several sections had DMDs at only one corner of the test slab. A summary of the back-calculated *EBITD* values for all test sections using (1) corner deflections measured using DMDs during early fatigue load repetitions, (2) 24-hour 40-kN loaded slab deflections measured using DMDs, and (3) FWD deflections measured at slab corners after all fatigue testing was completed, is shown in Table 3-7.

Table 3-7 Summary of Back-calculated *EBITD* values (ºC) for Palmdale Test Sections

Section Location and Base Type	Section ID	Pavement Type	Data Used				
			Early Fatigue Loading Repetitions		24-Hour 40-kN Loaded Slab Deflections		Falling Weight Deflectometer*
			Left Corner	Right Corner	Left Corner	Right Corner	Right Corner
South Tangent 150 mm aggregate base	519FD	100 mm nominal thickness AC shoulder no dowels	-	-29.3	-	-	-
	520FD		-25.5	-	-	-	-
	521FD		LVDT Malfunction		-	-	-
	523FD	150 mm nominal thickness AC shoulder no dowels	-	-24.1	-	-	-
	524FD		-	-27.6	-	-	-
	525FD		-	-40.0	-	-	-
	526FD		-	-36.5	-	-	-
	527FD		-	-40.3	-	-	-
	528FD	200 mm nominal thickness AC shoulder no dowels	-	-28.0	-	-	-
	529FD		LVDT Malfunction		-	-	-
	530FD		-	-29.7	-	-	-
	531FD		-	-31.8	-	-	-
North Tangent 100 mm cement-treated base over 150mm aggregate base	532FD	200 mm nominal thickness AC shoulder no dowels	-26.6	-	-	-	-
	533FD		-24.8	-23.6	-	-	-
	534FD		-32.1	-27.6	-	-	-
	535FD		-30.8	-22.0	-33.3	-21.8	-22.6
	536FD	200 mm nominal thickness PCC shoulder dowels	Very high variability in deflections not correlated with temperature		-	-	-
	537FD		>-5.0	-10.7	>-5.0	-10.9	-9.9
	538FD		-14.6	-17.3	-14.7	-18.5	-17.8
	539FD	200 mm nominal thickness widened lane with AC shoulder dowels	-12.0	-14.1	-10.8	-13.0	-15.9
	540FD		-9.8	-15.4	-12.0	-17.1	-13.0
	541FD		-6.5	-10.6	-5.5	-8.5	-21.7

* FWD data collected several years after fatigue testing of all sections was completed

3.5 Factors Affecting Effective Built-In Temperature Difference

As stated earlier, the Palmdale test slabs were constructed with fast-setting high-early-strength concrete with superplasticizer and approximately 400 kg/m^3 of high shrinkage cement. The slabs were paved during daytime and in desert conditions with low ambient humidity. These factors resulted in high *EBITD* values (–20ºC to –35ºC) for sections with low restraint (undoweled Sections 519FD through 535FD) and low to moderate *EBITD* values (0ºC to –20ºC) for sections with higher restraint (doweled Sections 537FD through 541FD). The restraints due to load transfer devices such as dowel bars appear to restrict the upward curl of the slabs during early age, likely through tensile creep mechanisms, resulting in lower *EBITD* for doweled slabs.

Slab self-weight also acts as a restraint to the curling of the slab. The 150-mm nominal thickness slabs typically had higher *EBITD* as compared to the 200-mm nominal thickness slabs. However, the 100-mm slabs typically had lower *EBITD* values than several of the 150-mm slabs. This can be explained by the fact that the most significant component of *EBITD* is the differential drying shrinkage between the top 50 mm of the slab and the bottom of the slab. As slabs get closer to 50 mm in thickness, the differential drying shrinkage is reduced, resulting in lower *EBITD* contribution from differential drying shrinkage. A 50-mm slab would have almost zero differential drying shrinkage and almost all of the shrinkage is manifested as an increase in the transverse joint opening, assuming limited slab-base friction.

The presence or absence of the cement-treated base course did not seem to be a factor in the curling of the slabs. On all sections, the corners of the slab had a higher *EBITD* compared with the mid-slab edge. The doweled sections had more uniform restraint at the joints resulting in similar *EBITD* for both sides of the slabs. The slabs with undoweled joints may or may not have an asymmetric curvature because the *EBITD* depends on the aggregate interlock restraint between adjacent slabs, which could vary from one joint to another. The dependence of *EBITD*

on aggregate interlock restraint can result in *EBITD* values that vary from slab to slab. This is consistent with research conducted by Armaghani et al. (1986) who observed a 13 percent difference in unloaded deflections at the corners of two adjacent, undoweled slabs (identical geometry and layer properties).

4.0 CUMULATIVE FATIGUE DAMAGE MODELING

4.1 Fatigue Cracking

Fatigue cracking in concrete pavements is a key failure mechanism, and is the result of repeated application of load at stress levels less than the flexural strength of the concrete slab (Roesler, 1998). Under environmental loading conditions (no traffic loading), the magnitude and sign (tension versus compression) of the slab stresses changes with the horizontal and vertical location in the slab, resulting in a stress field which depends on the following factors:

- Climatic conditions: temperature and moisture gradients in the slab
- Effective built-in curl: effective built-in temperature difference (*EBITD*) resulting from a combination of built-in temperature gradients and irreversible moisture gradients
- Slab dimensions: length, width, and thickness
- Layer properties: coefficient of thermal expansion, elastic modulus, Poisson's ratio, unit weight, bond between layers, etc.
- Subgrade support: modulus of subgrade reaction
- Other factors: adjacent slab properties, shoulder type and properties, load transfer, etc.

With the application of a moving traffic load, the new stress field is a function of the load location(s), magnitude(s), contact pressure(s), and axle type configuration, in addition to all of the above factors. The removal of the traffic load resets the slab stresses back to its latent or residual state. The effect of these stress changes at any particular slab location can result in damage or microcracking. After repeated load applications, damage or more accurately

microcracks accumulate and propagate in the concrete. The crack eventually extends and propagates to the surface (or to the bottom), resulting in transverse cracks, longitudinal cracks, and/or corner breaks.

4.2 Miner's Hypothesis

Mechanistic-empirical design procedures (Barenberg and Thompson, 1992; Darter et al., 2001; Hiller and Roesler, 2002) use cumulative damage at locations of critical stress to assess probability of slab cracking and failure. Since slab stress states change depending on the conditions and factors listed above, a method of combining the damage over time is needed for structural analysis and design. The fatigue damage concept, published by Miner (1945), has been widely used for this purpose in pavement design and evaluation. Miner's fatigue damage accumulation hypothesis, which assumes that damage accumulates linearly, is empirically based and is given as follows:

$$Fatigue\ Damage, FD = \sum \frac{n_i}{N_i} \quad \textbf{(4-1)}$$

where,

n_i = Number of actual load applications under conditions represented by i.

N_i = Number of allowable load applications until failure under conditions represented by i.

Miner's hypothesis allows the summation of fatigue damage from loads of varying magnitudes under changing environmental conditions. According to Miner's hypothesis, materials should fracture when the fatigue damage equals 1.0, although under a calibrated system with reliability, this damage sum does not necessarily have to be unity (Zollinger and Barenberg, 1989).

4.3 Fatigue Models

4.3.1 Stress Ratio

The stress ratio experienced by a concrete pavement has been related to the logarithm of the number of load applications required to produce fatigue-related failure, where the stress ratio, SR, is the ratio of the total tensile bending stress experienced by the slab to the concrete modulus of rupture.

$$SR = \frac{\sigma}{MR} \quad \textbf{(4-2)}$$

where,

σ = Total tensile stress due to traffic and environmental load at critical location.

MR = Modulus of rupture (PCC strength)

The concrete modulus of rupture is typically obtained from the third-point loading configuration of beams, after 28 days of curing. Roesler (1998) observed that the flexural strength of plain concrete varies by as much as 30 percent if tested in a beam configuration versus a slab configuration. More recently, Roesler et al. (2003) and Littleton (2003) found that the ratio of the slab flexural strength to beam flexural strength depends on the slab geometric properties, material properties, support conditions, and boundary conditions, and the slab flexural strength can be more than two times higher than the beam flexural strength.

4.3.2 Fatigue Models

Several fatigue curves for concrete pavement have been developed using field and laboratory data that relate the stress ratio to the number of loads until failure. These include:

- Zero-Maintenance Design Beam Fatigue Model (Darter and Barenberg, 1976; Darter and Barenberg, 1977; Darter, 1977)—Developed using concrete beams with failure defined as complete beam fracture. Load stresses were calculated at the bottom of the beam using the bending beam equation"

$$\log N = 17.61 - 17.61SR \quad \textbf{(4-3)}$$

where
N = Number of stress applications to failure for the given stress ratio SR.

- Calibrated Mechanistic Design Field Fatigue Model (Salsilli et al., 1993; Thompson and Barenberg, 1992) —Developed using Corp of Engineers (COE) field aircraft data and American Association of State Highway Officials (AASHO) Road Test data, with failure defined as 50 percent slab cracking. Load and temperature curling stresses were calculated at the slab edge using the finite element program, ILLI-SLAB

$$\log N = \left[\frac{-SR^{-5.367}\log(1-P)}{0.0032}\right]^{0.2276}, \; SR < 1.25 \quad \textbf{(4-4)}$$

where,
P = Cracking probability.

For P = 50 percent, the above equation is reduced to:

$$\log N = 2.8127SR^{-1.2214} \quad \textbf{(4-5)}$$

For SR > 1.25,

$$\log N = 4.284 - 1.7136SR \quad \textbf{(4-6)}$$

- ERES/COE Field Fatigue Model (Darter, 1988)—Developed using Corp of Engineers (COE) field aircraft data, with failure defined as 50 percent slab cracking. Load

stresses were calculated at the slab edge using the influence chart software, H-51, and reduced by a factor of 0.75 to account for load transfer and support conditions.

$$\log N = 2.13SR^{-1.2} \quad \textbf{(4-7)}$$

- Foxworthy Field Fatigue Model (Foxworthy, 1985)—Developed using Corp of Engineers (COE) field aircraft data, with failure defined as 50 percent slab cracking. Load stresses were calculated at the slab edge using the finite element program, ILLI-SLAB.

$$\log N = 1.323\left(\frac{1}{SR}\right) + .588 \quad \textbf{(4-8)}$$

- PCA Beam Fatigue Model (Packard, 1973; Packard and Tayabji, 1983)—Developed using concrete beams, with failure defined as complete fracture of 5 percent of the beams. Load stresses were calculated at the bottom of the beam using the bending beam equation.

$$\log N = 11.737 - 12.077SR1 \qquad \text{for SR} \geq 0.55 \quad \textbf{(4-9)}$$

$$N = \left[\frac{4.2577}{SR - 0.4325}\right]^{3.268} \qquad \text{for } 0.45 < \text{SR} < 0.55 \quad \textbf{(4-10)}$$

$$N = \text{unlimited} \qquad \text{for SR} \leq 0.45 \quad \textbf{(4-11)}$$

- 2002 Design Guide (Darter et al., 2001; Yu et al., 2004)—Developed using several highway databases (such as LTPP—Long Term Pavement Performance Database) with failure defined as 50 percent slab cracking. Load and temperature stresses were calculated at the lane-shoulder joint slab edge using neural networks developed from ISLAB2000. This model is similar in form to the ERES/COE model.

$$\log N = 2.00 SR^{-1.22} \quad \textbf{(4-11)}$$

Table 4-1, adapted from Smith and Roesler (2003), summarizes the differences used in the approach for the development of these various fatigue models.

Table 4-1 Summary of Concrete Fatigue Models (Adapted from Smith and Roesler, 2003)

Fatigue Model	Data Source(s)	Failure Definition	Aspects of Stress Computation Used in Development of Fatigue Model			Concrete Strength Characterization
			Location	Stress Types	Computation Method*	
Zero-Maintenance (1977)	Concrete Beams	50% beams completely fractured	Bottom of Beam	Load Only	Beam Bending Equation	28-day MR (third point loading)
Calibrated Mechanistic Design (1993)	COE Field Aircraft Data & AASHO Road Test Data	50% of slabs cracked	Edge	Load and Temperature Curling	Finite Element (ILLI-SLAB)	28-day MR (third point loading)
ERES/COE (1988)	COE Field Aircraft Data	50% of slabs cracked	Edge*0.75	Load Only	H-51	28-day MR (third point loading)
Foxworthy (1985)	COE Field Aircraft Data	50% of slabs cracked	Edge	Load Only	Finite Element (ILLI-SLAB)	28 & 90-day MR (third point loading)
Portland Cement Association (1983)	Concrete Beams	5% beams completely fractured	Bottom of Beam	Load Only	Beam Bending Equation	90-day MR (third point loading)
2002 Design Guide (2002)	Several highway databases	50% of slabs cracked	Edge	Load and Temperature Curling	Finite Element (ISLAB2000)	28-day MR (third point loading)

Method of computing the stress used in the stress ratio term during the development of the fatigue model (and not the method used in the design procedure for computing slab stresses).

4.4 Evaluation of Applicability of Fatigue Models to Palmdale Field Data

In practical applications of the above fatigue models (Section 4.3) for pavement analysis and design, typically only a limited amount of data is available, and assumptions have to be made regarding several input variables required to compute stresses and allowable number of

load repetitions to failure used in modeling slab cracking performance. The full-scale test sections at Palmdale, loaded using the HVS, had more accurate and detailed information on mechanical load levels and load position on the slab (channelized trafficking without any wander), environmental loading parameters (measured temperatures through the depth of the slabs), pavement layer geometric and material properties (back-calculated site-specific modulus of subgrade reaction, layer elastic moduli, *EBITD*, laboratory-measured modulus of rupture, coefficient of thermal expansion, and concrete density), and the time of concrete fatigue failure (load repetition history at time of first observed crack) relative to field monitored test sections. Evaluating existing fatigue models using the Palmdale data should provide useful insights into the applicability of these models.

4.4.1 Fatigue Analysis Procedure

For each test section, pavement responses due to the combined effects of traffic and environmental loading were computed using ISLAB2000 at multiple slab locations. One such set of pavement responses is the stress distribution at the top of the slab, an example of which is shown in Figure 4-1. The figure shows stresses in the X-direction (direction of traffic) and Y-direction (perpendicular to traffic direction) at the top of the test slab due to wheel load at the corner of the test slab. The dark blue portion of the contour plots is directly beneath the wheel, where the top of the slab is under compression. The red portion of the test slab corresponds to the region of peak tensile stresses in the slab.

Since concrete is substantially stronger in compression than in tension, peak tensile stresses are the critical pavement responses used in fatigue modeling. For slabs with smaller magnitude of negative *EBITD* (> –5ºC), zero *EBITD*, or positive *EBITD* (small upward curl, no curl or downward curl) peak critical stresses occur when the load is at the mid-slab edge (lane-

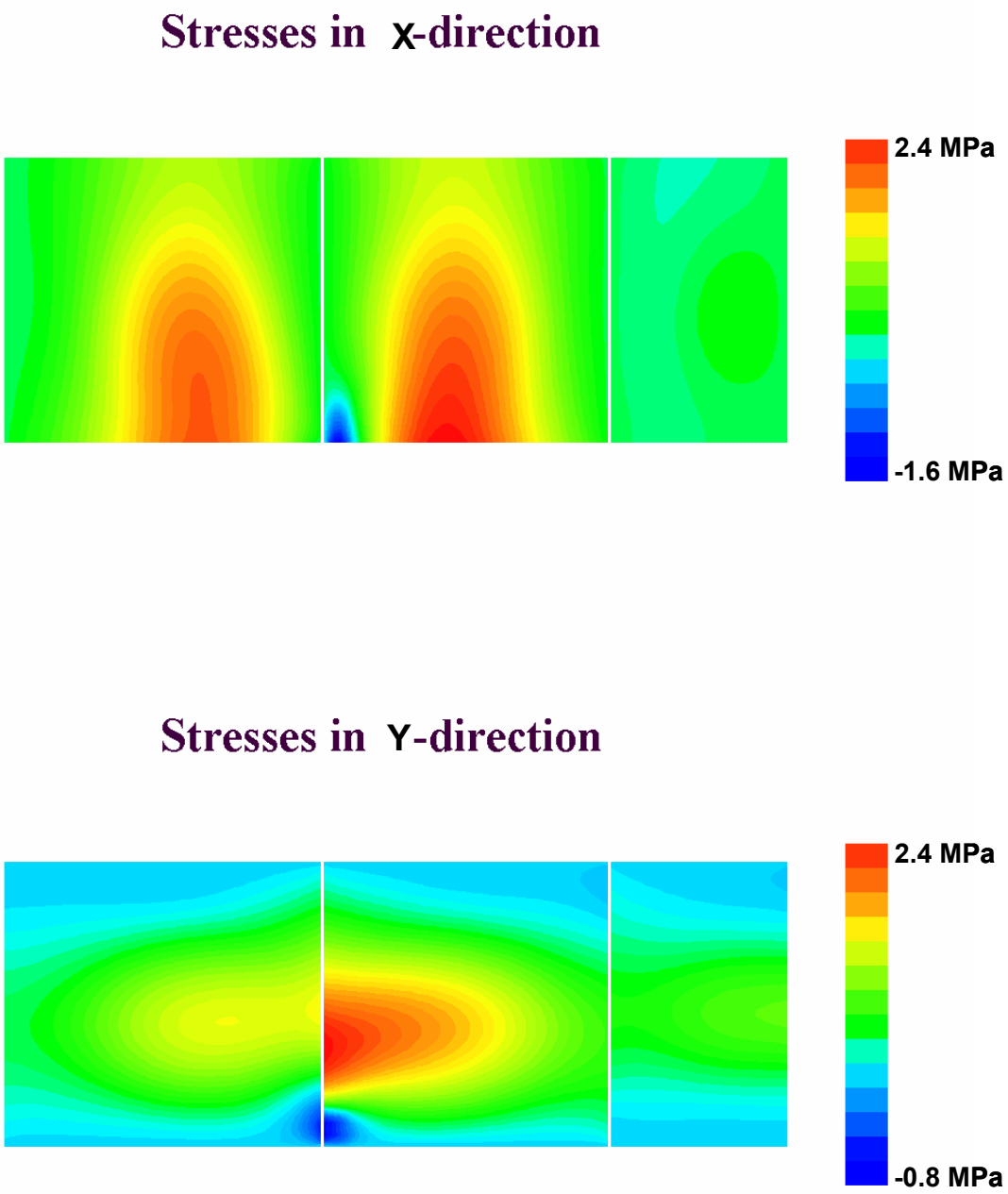

Figure 4-1. Stress distribution at the top of a test slab (Section 535FD) with corner loading and effective linear temperature difference of -25°C across the slab.

shoulder). In this case, the location of the peak critical stress is at the bottom of the slab at the mid-slab edge (beneath the load). The Palmdale test slabs had higher magnitude of negative *EBITD* (large upward curl), and therefore the peak tensile stresses occurred at the top of the slab, along the lane-shoulder edge, and the transverse joint edge, as shown in Figure 4-1, with the load at the corner of the slab. This occurrence of peak tensile stresses at the top of the slab is also supported by visual observations of cores taken at Palmdale. The cores drilled through cracks were wider at the surface, with some surface cracks not yet having propagated to the bottom, suggesting that the cracks initiated at the surface. Figure 4-2 from Heath and Roesler (1999)

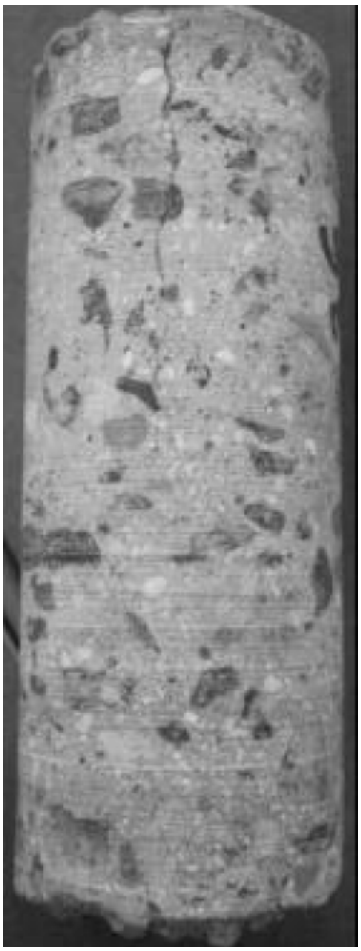

Figure 4-2. Core showing crack initiation at the surface of the slab at a Palmdale test section (photograph from Heath and Roesler, 1999).

shows one such core taken from a Palmdale test section. Because of this, edge loading was not considered in the fatigue analysis and peak stresses at critical locations at the top of the slab were used in the analysis.

Depending on the amount of upward curl (*TELTD*), the load level, and other input design and material parameters, the peak tensile stresses occurred at a distance of 1 to 2 m from the slab corner, at the slab edge along the lane-shoulder joint or along the transverse joint as shown in Figure 4-1.

For any particular test section, over the fatigue loading period, the location of peak tensile stress due to corner loading varied by a maximum of approximately ±0.7 m on the lane-shoulder edge and a maximum of approximately ±0.4 m on the transverse joint edge, relative to the peak stress locations corresponding to the zero measured temperature difference through the depth of the slab. This variation in peak stress locations was due to the influence of daily temperature cycling and depended on the maximum and minimum temperature differences through the depth of the slab during the fatigue loading period. A sensitivity analysis was performed using three different test sections (520FD, 535FD, and 539FD) to observe the effect of this variation on cumulative damage using the 2002 Design Guide fatigue model. Damage was computed (as described below) at several locations within the range of peak stress locations, along the transverse edge and the lane-shoulder edge. Because the stresses near the peak stress location were also high, and typically varied by less than 0.1 MPa within the range, particularly when temperature control was being used, the calculated cumulative damage was not very sensitive to computation location within the range of variation of the peak stress. Therefore, the cumulative damage analysis is not very sensitive to the exact locations of the peak stresses, and a small error in selection the location for cumulative damage analysis does not significantly affect the results

of the cumulative damage analysis. The critical damage location was generally the greatest at the stress location corresponding to the most negative measured temperature difference (or within 0.1 m). Based on this sensitivity analysis, the critical locations along the lane-shoulder and transverse edge were selected as the peak stress locations that corresponded to when the measured temperature difference through the depth of the slab was most negative (greatest amount of upward curl).

Peak tensile stresses at these two critical locations were calculated using ISLAB2000 for each two-hour time increment in order to account for the varying temperature differences in the slab throughout the fatigue damage loading period. The inputs used for ISLAB2000 were the same as those listed in Section 3.3.3. The ratio of the calculated stress to the concrete strength is the stress ratio corresponding to the time increment. This stress ratio is used to calculate the allowable number of load applications to failure for that time increment using the aforementioned fatigue models, represented by N_i in Equation 4-1. The number of load applications during the analysis time increment corresponds to n_i in Equation 4-1. The ratio of the actual number of HVS applications within the time increment to the calculated allowable number of load applications is the damage for that time increment. For each test slab, the computed damage for all time increments to observed failure is accumulated at each stress location. A flowchart depicting the steps for calculating cumulative fatigue damage is shown in Figure 4-3.

Cumulative damage was computed at both the right and left transverse edge critical location and the right and left lane-shoulder edge critical location, with the load placed at the (right or left) corner of the slab. The higher of the two values for the right and left transverse

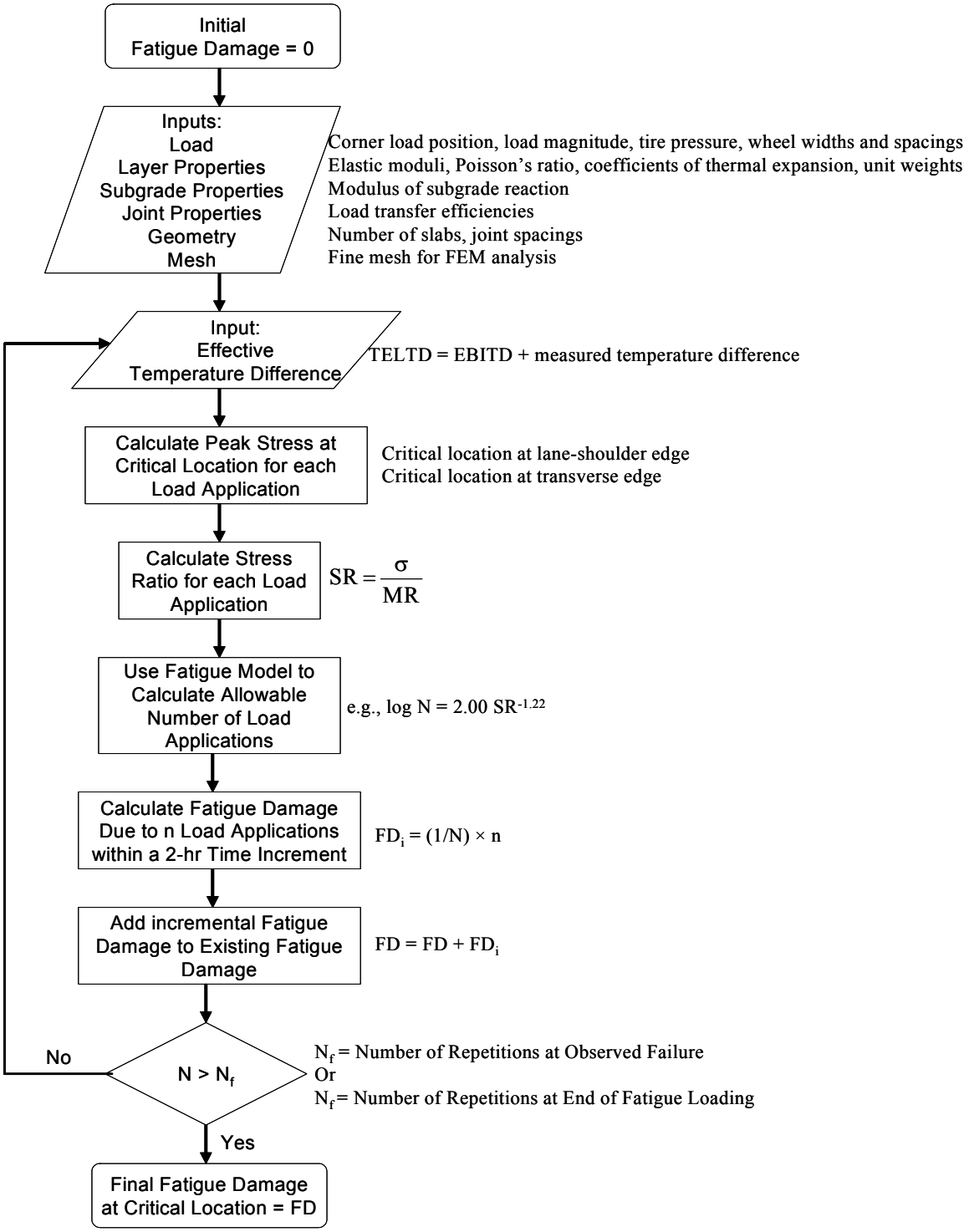

Figure 4-3. Flowchart depicting the steps for calculating cumulative fatigue damage.

edge (and likewise for the right and left lane-shoulder edge) is considered in this analysis as the cumulative damage for that edge.

4.4.2 Fatigue Analysis Results

The computed cumulative damage at the two peak stress locations is shown in Figure 4-4 for the Palmdale test sections based on the fatigue models listed in Section 4.3. The damage is computed until the appearance of the first crack. If a test slab exhibited longitudinal cracking, the cumulative damage computed at the transverse peak stress location is shown as "cracked" (represented by solid diamond markers) and the lane-shoulder peak stress location is shown as being "uncracked," (represented by hollow triangle markers). Likewise, if a test slab exhibited transverse cracking extending from the lane-shoulder joint, the cumulative damage is shown as

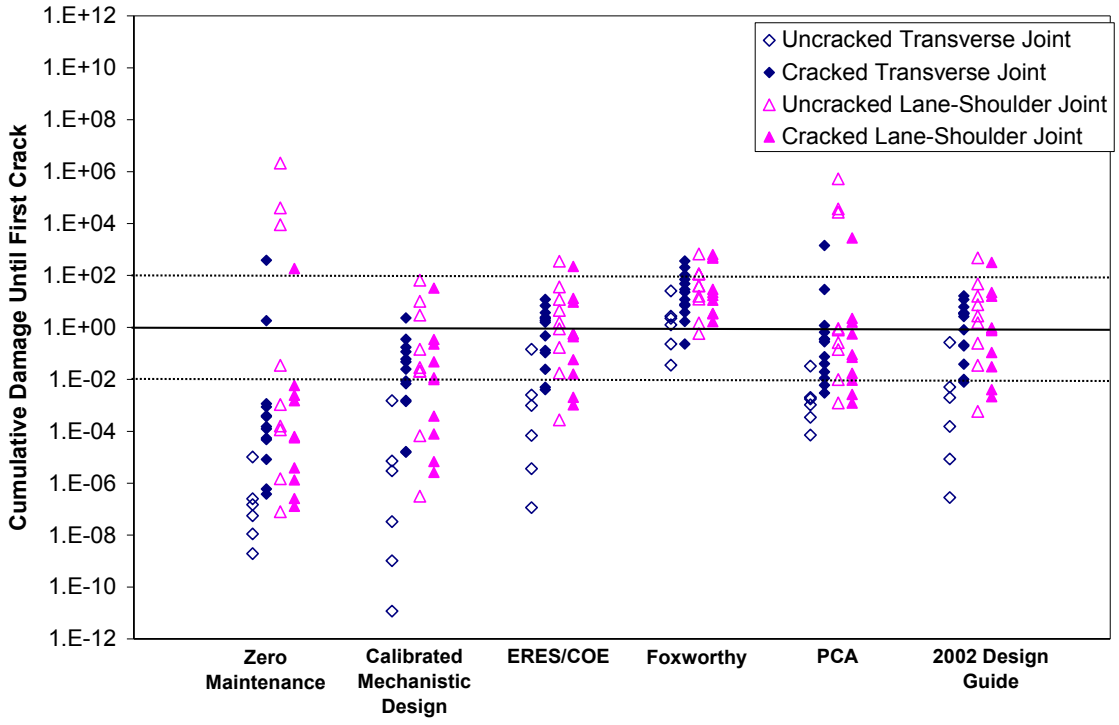

Figure 4-4. Calculated cumulative damage to first field-observed crack using various fatigue models for Palmdale test sections.

"cracked" (represented by solid triangle markers) and the transverse peak stress location is shown as being "uncracked," (represented by hollow diamond markers). The figure also shows cumulative damage at the peak stress locations for slabs that did not crack until the end of the fatigue loading for that particular test section (such as Sections 533FD, 538FD, and 541FD) which are also represented by hollow triangle and diamond markers in the figure. Corner breaks are shown as having cracked at both peak stress locations and are represented by solid triangle and diamond markers corresponding to both peak stress locations. For visual reference only, horizontal lines corresponding to cumulative damage of 0.01 and 100 are also shown. Figure 4-4 shows the tremendous amount of variability ranging several orders of magnitude, which is inherent to these models and suggests that they need to be refined in order to better predict fatigue cracking in field slabs.

In theory, the cumulative damage at the cracked peak stress locations for each test section should equal 1.0, and at the uncracked peak stress locations for all test sections should be less than 1.0. However, this may not be the case due to several reasons described in the following sections. The differences in the allowable number of load repetitions between the evaluated fatigue models resulted in significant differences in the calculated cumulative damage. Fatigue models have been developed and calibrated based on different data sources, failure definitions, stress computations, and stress components. Application of a fatigue model without proper calibration can lead to an erroneous conclusion. The lack of fit of the Zero-Maintenance model and the PCA model for the Palmdale data is not surprising because these two models were developed for laboratory beams using complete beam fracture as the failure criteria with stresses calculated at bottom of beam using bending beam equation, and were not calibrated for field pavement data. The lack of fit of the Foxworthy model is likely due to the fact that temperature

curling stresses were not included in the development of the model. The two models that show better fit with mean cumulative damage of cracked slabs of approximately 1.0 are the ERES/COE model and the 2002 Design Guide model, which are identical in functional form and have similar coefficients.

The transfer function used to convert fatigue damage into percent slabs cracked for the 2002 Design Guide model is shown in Figure 4-5 and given as:

$$Slabs\,Cracked, \% = \frac{100}{1 + FD^{-1.68}} \quad \textbf{(4-12)}$$

The transfer function suggests that roughly 2 percent of the slabs crack when cumulative fatigue damage reaches 0.1, and almost 98 percent of the slabs crack when the cumulative fatigue damage reaches 10 (with 50 percent slabs cracked at fatigue damage of 1.0). Ninety-six percent of slabs crack between cumulative fatigue damage ranging from 0.1 to 10.

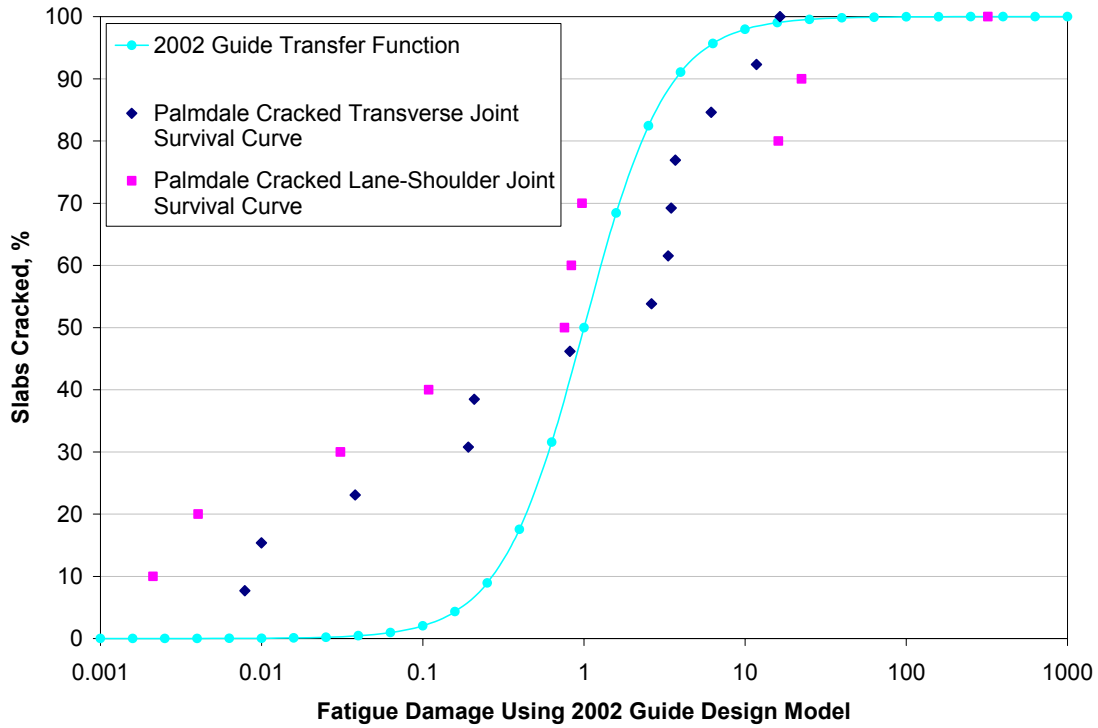

Figure 4-5. Calibrated curve relating fatigue damage to percent slabs cracked using the 2002 Design Guide model.

Figure 4-5 also shows the survival curve for the peak stress cracked locations at the transverse joint and the lane-shoulder joint for the Palmdale test sections. The survival curves were plotted using 2002 Design Guide fatigue model results shown in Figure 4-4 for the cracked locations (solid diamond markers and solid triangle markers). At each fatigue damage level, the cumulative percentages of cracked locations on the lane-shoulder joint and on the transverse joint were calculated. For example, 4 of 10 lane-shoulder joint locations were cracked when fatigue damage of 0.1 was reached based on fatigue damage calculated using the 2002 Design Guide model. Likewise, 2 of 13 transverse joint locations were cracked when fatigue damage of 0.01 was reached.

The survival curves along with Figure 4-4 indicate that the cracked peak stress locations using the 2002 Design Guide fatigue model for the Palmdale field test slabs had a wider cumulative damage range (from approximately 0.001 to 1000) as compared to the transfer function (Equation 4-12) developed for the 2002 Design Guide. While the 2002 Design Guide transfer function suggests that 96 percent of slabs crack between fatigue damage of 0.1 and 10, by comparison, only 62 percent of transverse joint locations and 40 percent of lane-shoulder joint locations cracked within this range. This indicates a higher amount of variability in the Palmdale fatigue results or that the fatigue model is overly sensitive to changes in stress.

The cumulative damage shown in Figure 4-4 was calculated assuming a linear measured temperature difference through the depth of the slab. This assumption does not significantly affect the results of the fatigue analysis because the measured temperature differences between the top and the bottom of the slab were small (of the order of a few ºC) relative to the back-calculated *EBITD*, resulting in only a small amount of nonlinearity, particularly when the temperature control box was used.

Another assumption in calculating the cumulative damage shown in Figure 4-4 was that the EBITD varied linearly through the depth of the slab. The analysis was also performed assuming that the *EBITD* varied bilinearly through the depth of the slab, as described in detail in Section 4.4.2.4. The results of that analysis also showed a large amount of variability and significant deviation for all models from the expected cumulative damage of 1.0. The deviation from the cumulative damage of 1.0 was not unexpected because none of the models were calibrated with the high stresses obtained with bilinear (or nonlinear) temperature distributions.

The inaccuracy of Miner's hypothesis as it applies to accelerated pavement testing results can be attributed to several reasons, including material variability, Miner's hypothesis limiting assumptions, early-age surface microcracking, and nonlinearity of curling, as described in the following subsections.

4.4.2.1 Material Variability

The fatigue models were developed for 50 percent of slab cracking (given a large section with number of slabs) corresponding to cumulative damage of 1.0. In the above analysis, fatigue damage was calculated for a single slab for each test section. The high variability in FSHCC properties resulted in variability in both strength and peak stresses due to applied load. As seen in Table 2-4, the coefficient of variation of strength alone can be as high as 19 percent. Variability in modulus of subgrade reaction, layer elastic moduli, concrete coefficient of thermal expansion, and other factors influencing stresses that are assumed the same for all test sections contribute to the variability in stress ratio and consequently allowable number of repetitions to failure and cumulative damage. Figure 4-6 and 4-7 show the calculated cumulative damage (with error bars) to the first field-observed crack for the various fatigue models conservatively assuming 15 percent coefficient of variation in stress ratio. The error bars represent the 95th

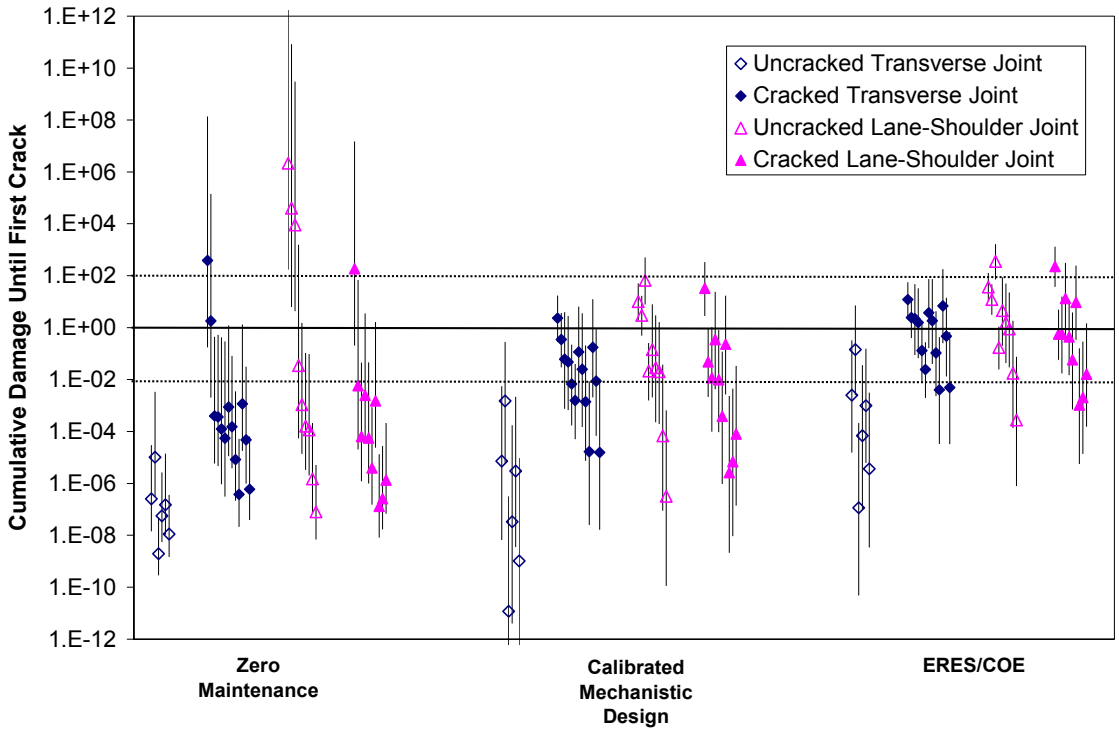

Figure 4-6. Calculated cumulative damage with error bars to first field-observed crack using Zero Maintenance, Calibrated Mechanistic Design, and ERES/COE fatigue models for Palmdale test sections.

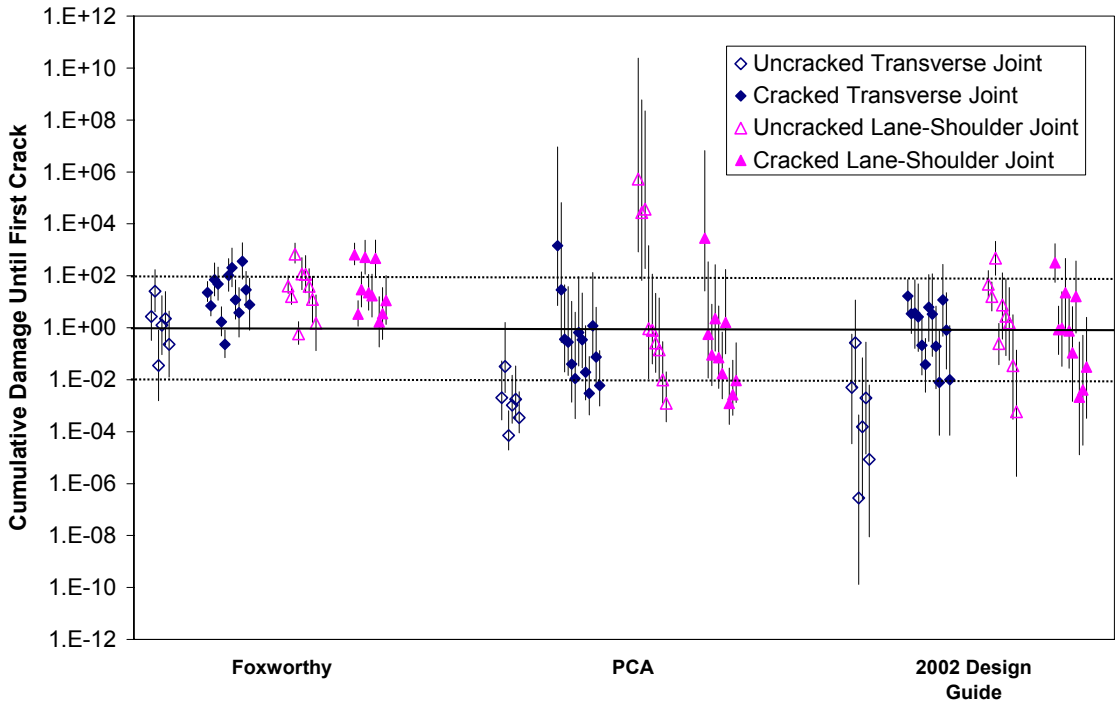

Figure 4-7. Calculated cumulative damage with error bars to first field-observed crack using Foxworthy, PCA, and 2002 Design Guide fatigue models for Palmdale test sections.

percentile range for the cumulative damage for any given test section, i.e., given the 15 percent coefficient of variation in stress ratio, there is a 95 percent probability that the true calculated cumulative damage is within the displayed range.

4.4.2.2 Miner's Hypothesis Limiting Assumptions

Miner's hypothesis has been used extensively in concrete and asphalt fatigue analysis to account for variable stress states over time. However, its mechanistic validity has been questioned over time by several researchers (Ioannides, 1995; Hilsdorf and Kesler, 1966; Holmen, 1979; Oh, 1991). Figure 4-4, 4-6, and 4-7 indicate that for any given fatigue model, Miner's sum does not predict fatigue failure with any accuracy for both fixed load and variable temperature loading, and variable load and temperature. Its ease of application in pavement design is the key factor that has prolonged its life. The main limitation of S-N curves relating stress to allowable number of load applications coupled with Miner's hypothesis lies in a phenomenological explanation of fatigue failure of concrete through the stress ratio.

The stress ratio approach assumes the stress state in the concrete is constant over the entire concrete fatigue life, thus disregarding incremental damage or more accurately, crack propagation. This is not a valid assumption, since the previous load cycles damage the concrete, which in turn increases the proceeding stress states in the concrete material. This is why Miner's hypothesis is not sustainable, and should not be expected to provide an intrinsic explanation for concrete fatigue failure. Furthermore, the following factors are known to affect the fatigue life of concrete and yet cannot be accurately accounted for in a stress ratio / Miner's hypothesis approach:

- Rest periods—Hilsdorf and Kesler (1966).
- Endurance limit, variable amplitude, stress history—Hildsdorf and Kesler (1966), Holmen (1979), Oh (1991).
- Loading rate—Raithby and Galloway (1974).
- Stress reversals—Tepfers (1982).
- Stress ranges—Aas-Jacobsen (1970), Tepfers (1979), Hsu (1981).

Further complicating matters are the concrete material size and geometry, which are not considered directly in any of the existing fatigue models but have shown to be a factor in the fatigue resistance of concrete (Littleton, 2003).

4.4.2.3 Early-Age Surface Microcracking

Another shortcoming of using Miner's hypothesis with fatigue damage models is that for new construction, an initial damage of zero is assumed, i.e., no initial cracks in the slab, which could effectively reduce the strength of the concrete slab. Weak zones in the concrete resulting from factors such as drying shrinkage, segregation, poor consolidation, etc. are not considered. Load transfer between a slab and adjacent slab or shoulder, slab-base friction, slab weight, etc., restrain shrinkage and result in early-age stresses and microcracking on the surface of the slab. Ytterberg (1987) even suggests that "…designers should consider eliminating (load transfer devices) from contraction joints…" While this may be an extreme sentiment since dowel bars provide useful functions in terms of reduced edge stresses (due to higher load transfer as compared to aggregate interlock joints) and decreased faulting, it does point to the effect of stresses on long-term slab strength, caused by dowel bars restraining curling of the slab during early-age strength gain.

Altoubat and Lange (2001) studied early-age uniaxial restrained shrinkage for a variety of concrete mixes. They observed that failure in restrained concrete occurs at a stress level less than the static tensile strength, and a strength reduction factor of 0.8 was typically obtained for the concrete mixtures in the study. They concluded that the key to prevention of early age microcracking is to limit stress buildup to 50 percent of the tensile strength at every point in time. Although the test slabs at Palmdale did not have visual cracks prior to fatigue testing, several of the longer slabs on the test strip cracked prior to any load application. The factors that caused the long slabs to crack prior to any loading are likely responsible for surface microcracking as a result of excessive early-age tensile stresses at the top of the intact slabs.

4.4.2.4 Nonlinearity of Curling

The stresses calculated in the cumulative damage procedure were calculated with ISLAB2000 using the sum of the temperature difference and the *EBITD*. The *EBITD*, estimated by using ISLAB2000, was the temperature difference across the slab at which the calculated loaded deflections at the slab corner matched those measured in the field. Two temperature distributions across the depth a slab, one linear and one quadratic, will produce identical deflections for the same temperature difference between the top and bottom of the slab. However, the two distributions can have significantly different stress profiles. The cumulative damage analysis performed does not account for the nonlinearity of the temperature gradient and particularly the drying shrinkage gradients. Several studies (Janssen, 1986; Jeong et al. 2001; Grasley, 2003; Lim et al., 2004) have shown that the moisture and shrinkage gradients through the depth of the slab are highly nonlinear, with drying taking place near the slab surface, resulting in low relative humidity in the concrete pores, and the moisture content of the concrete

is practically constant below this point, with almost 100 percent relative humidity in the concrete pores, as shown in Figure 4-8.

In this study, a bilinear model is used to simulate the nonlinearity of shrinkage gradient in the concrete slab. The bilinear model based on one proposed by Rasmussen and McCullough (1998) assumes that the full shrinkage occurs at the surface of a concrete pavement and no shrinkage occurs below the mid-depth of the slab. The shrinkage is assumed to decrease linearly between the top and center of the slab, as shown in Figure 4-9.

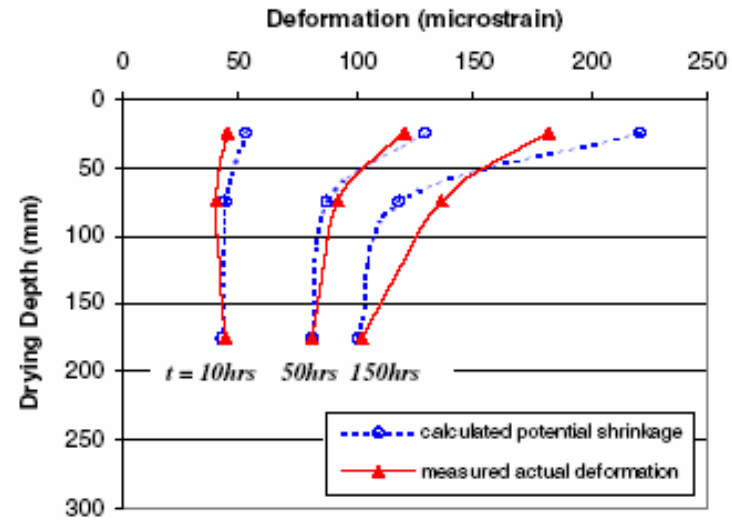

Figure 4-8. Change in shrinkage strains with depth over time (from Lim et al., 2004).

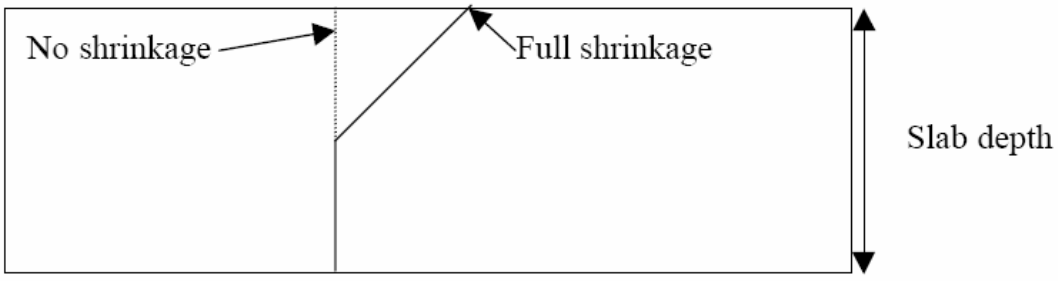

Figure 4-9. Slab shrinkage gradient bilinear model (from Rasmussen and McCullough, 1998).

In evaluating the applicability of existing fatigue models to the Palmdale data, peak stresses along the lane-shoulder joint and the transverse joint that corresponded to the load located at the slab corner were used. To get a better understanding of the variation in stresses at critical locations, a rolling wheel analysis of stresses at critical locations was conducted.

4.5 Rolling Wheel Load Analysis and Location of Peak Stresses

4.5.1 Influence Charts

ISLAB2000 was used to compute slab responses due to the combined effects of moving traffic load and environmental loading. The HVS load was modeled every 150 mm along the length of the slab. This is illustrated in Figure 4-10 and Figure 4-11, which show the influence chart for a moving HVS load applied at the edge of the slab for an undoweled section (Section 535FD), and a doweled widened lane section (Section 540FD), respectively. An influence chart is a graphic representation of a response (stress) at a fixed point due to placement of a static load at several different points, thus simulating the effect of a (non-dynamic) moving load. Both figures show stress reversals from tension to compression and back to tension for critical locations at the lane-shoulder joint. The critical location at the transverse joint is always in tension with the peak stress occurring when the load is at the slab corner. For each test section, influence charts were developed for several slab locations along the transverse joint edge and the longitudinal lane-shoulder joint edge, for a range of total effective linear temperature differences. Other examples of influence charts for the 100-mm nominal thickness Section 520FD, the 150-mm nominal thickness Section 524FD, and the 200-mm nominal thickness Section 530FD, at different temperature differences through the slab depth and several load levels are shown in the

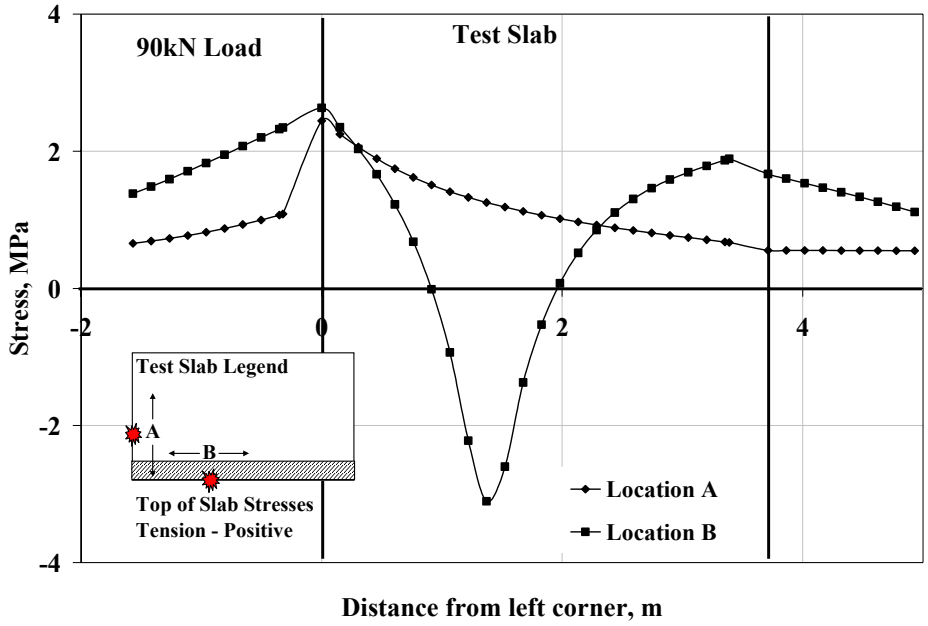

Figure 4-10. Influence diagram showing effect of 90-kN half-axle moving load on stresses at two critical locations on the slab (Section 535FD, *EBITD* = –33.3ºC, ΔT = 0ºC).

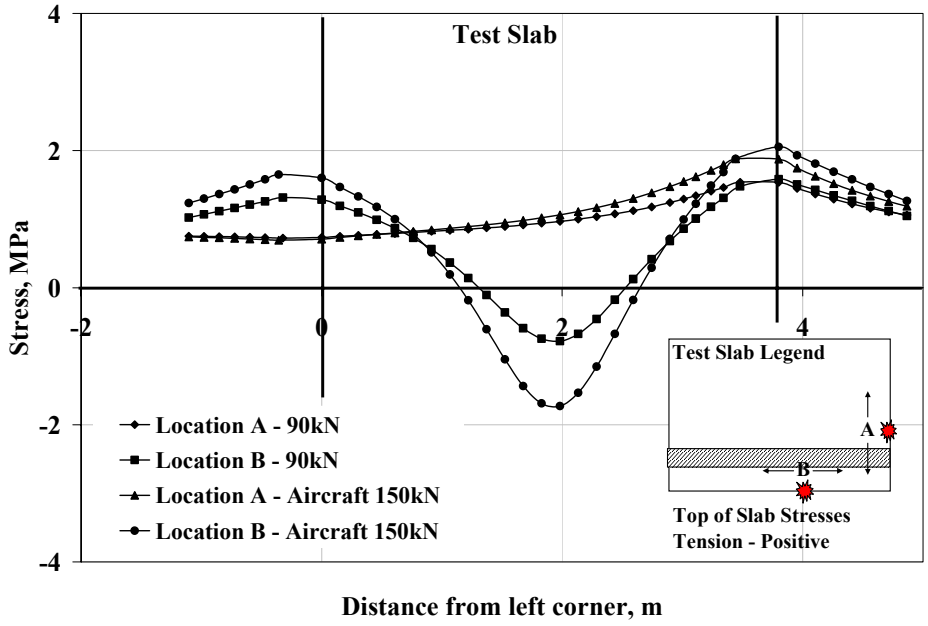

Figure 4-11. Influence diagram showing effect of 90-kN half-axle and 150-kN aircraft moving load on stresses at two critical locations on the slab (Section 540FD, *EBITD* = –17.1ºC, ΔT = 0ºC).

appendix in Figures A-37 through A-54. The following conclusions can be drawn from these influence lines:

- The total effective temperature difference in the slab has a significant effect on the peak stress for both the critical transverse joint location and the critical lane-shoulder edge location. However, the exact location of the peak stress depends on the magnitude of the temperature difference. The more negative the temperature difference, the greater the uplift at the slab corners, and further away from the corner and closer to the middle of the slab along the lane-shoulder edge and the transverse edge is the location of the peak stress.
- Depending on the magnitude of the temperature difference, the location of the peak stress can vary up to 2 m relative to the peak stress location during flat slab (zero *TELTD*) condition. This variation is smaller along the transverse joint edge and larger along the lane-shoulder joint edge.
- The critical location on the slab lane-shoulder joint edge typically experiences a stress reversal, i.e., the stress changes from tension to compression and back to tension under the influence of a moving load.
- The magnitude of the stress reversal depends on the slab thickness and the magnitude of the applied load. For cases in which the load is small or the slab thickness is large, there is no stress reversal.
- Both the magnitude of the applied load and the thickness of the slab significantly affect stresses in the slab, but do not affect the typical shape of the influence line.

4.5.2 Location of Maximum Slab Stresses

Many of the test sections at Palmdale, particularly on the South Tangent, had high magnitudes of *EBITD* (and *TELTD*) and were loaded at lower load levels. The influence chart for one such test section (Section 520FD) is shown in Figure 4-12. The influence chart shows stresses due to moving wheel load at the critical transverse edge location (A) and the critical lane-shoulder edge location (B). The influence chart also shows stresses in the longitudinal and transverse direction at the middle of the slab. For these test sections, the highest stresses occurred at the middle of the slab in the longitudinal direction. This can also be seen in Figure 4-13, for the critical corner loading case where the stresses are greatest at the middle of the slab. Using Miner's cumulative damage principles with any of the existing fatigue models, would suggest that for these test sections, the crack should initiate from the middle of the slab. However, this as not the case, as all cracks were observed to initiate from either the lane-shoulder edge or the

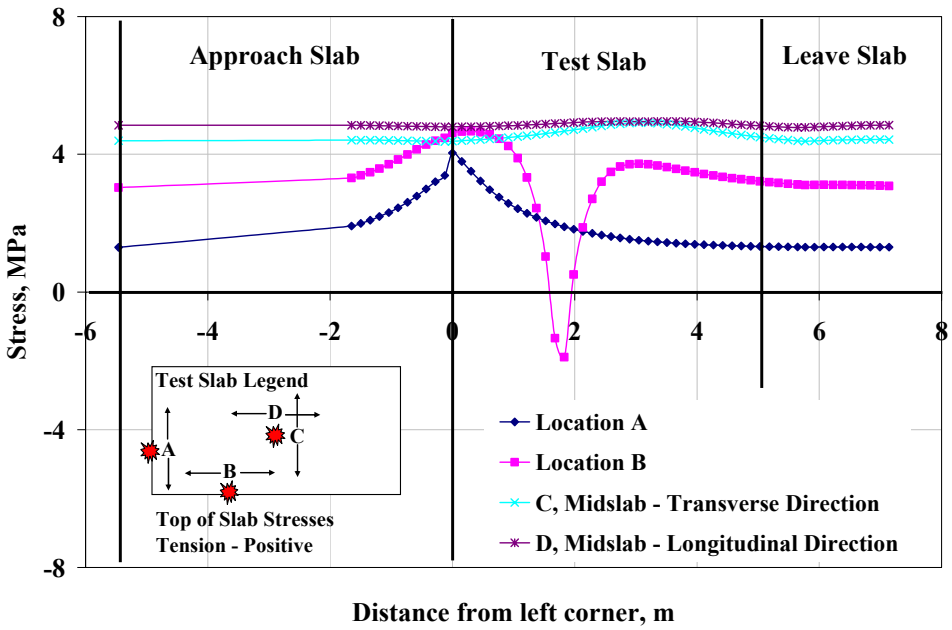

Figure 4-12. Influence diagram showing effect of 35-kN half-axle moving load on stresses at edge and midslab locations (Section 520FD, *EBITD* = –25.5ºC, ΔT = +2.5ºC).

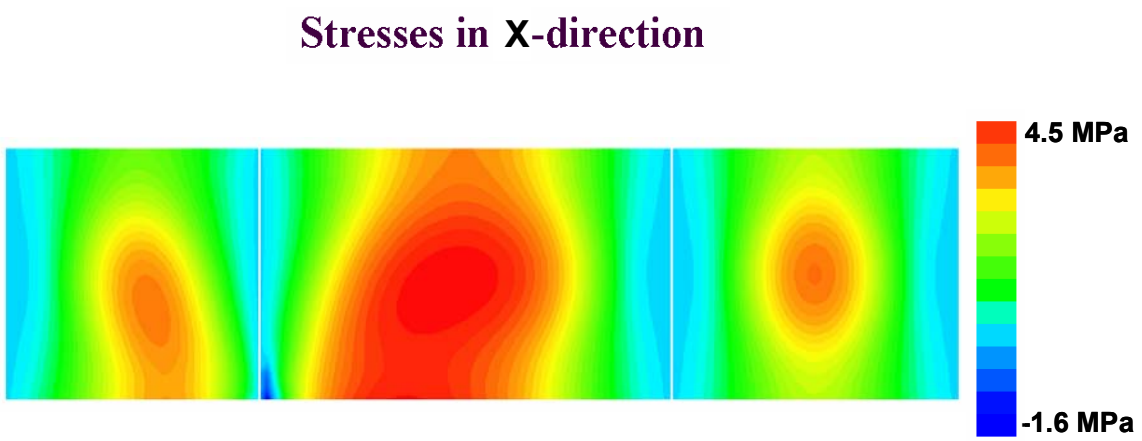

Figure 4-13. Stress distribution at the top of a test slab (Section 520FD) with corner loading and effective linear temperature difference of –23ºC across the slab showing peak stress at middle of the slab rather than the edge of the slab.

transverse joint edge. Many cracks turned into corner breaks without even passing through this location of maximum stress.

4.5.3 Peak Stresses at Transverse Joint Edges versus Peak Stresses at Lane-Shoulder Edges

The results of the influence chart analysis for all North Tangent and South Tangent test sections indicated that more than 85 percent of the corner loading cases resulted in peak stresses at the lane-shoulder joints being greater than the peak stresses at the transverse joints. This would suggest that a majority of the slabs tested at Palmdale should fail by means of transverse cracking. However, this was not the case as a significant number of slabs failed through longitudinal cracking or corner breaks, many of which seemed to start as longitudinal cracks and turn to form corner breaks.

The high amount of longitudinal cracking (and corner breaks originating from the transverse joint) observed at Palmdale were consistent with the considerable amount of longitudinal cracking and corner breaks typically seen in rigid pavements throughout California

and addressed by Hiller and Roesler (2002) through development of a procedure for transverse joint analysis.

In order to address these discrepancies regarding locations of peak stresses and locations of observed cracking using existing fatigue models, a model incorporating stress ranges along with peak stresses is developed in this research. Although accounting for all of the shortcomings of using Miner's hypothesis and cumulative damage approach is beyond the scope of this research, the fatigue model developed in this research takes a step forward by addressing some of the issues disregarded in existing fatigue models.

4.6 Fatigue Model Using Stress Ranges and Peak Stresses

Aas-Jacobsen (1970) studied the effect on minimum stress on fatigue failure of concrete and developed the following relationship between stress ratio, stress range, and number of load applications to failure.

$$SR = 1 - \beta(1 - R)\log N \quad \textbf{(4-13)}$$

where:
R = ratio of minimum stress to maximum stress during one load repetition
β = experimental constant

Aas-Jacobsen developed this model for compressive fatigue failure and determined β as 0.064. Tepfers and Kutti (1979) tested several 0.3 m × 0.15 m diameter concrete cylinders for fatigue failure in compression. Using results from their tests and those reported in literature, they found the value of β to 0.0685. Tepfers (1979) performed splitting tests for tensile failure of concrete cubes and concluded that the Equation 4-13 can be also used for tensile stresses. More recently, Hiller and Roesler (2002) have successfully used Aas-Jacobsen's model to develop a mechanistic-empirical design framework for the California Department of Transportation.

Hsu (1981) expanded Aas-Jacobsen's equation to incorporate the loading period for repetitive loads. Hsu's equation relating stress ratio to number of load applications for high-cycle fatigue (number of loading cycles between 1,000 and 10,000,000) is given as:

$$SR = 1 - \beta(1 - \eta R)\log N - \lambda \log T \quad \textbf{(4-14)}$$

where:
T = period of repetitive loads, seconds/cycle
β, η, λ = constants

Hsu calculated the values of β, η, λ as 0.0662, 0.556, and 0.0294, respectively, for high-cycle fatigue failure for laboratory specimens. For tensile fatigue failure of field slabs, these coefficients can be expected to be different. The Palmdale field data was used to develop coefficients for a model of the functional form shown in Equation 4-14.

4.6.1 Fatigue Model

Results from the influence charts were used to calculate peak tensile stresses, minimum stresses, and unloaded slab stresses for each two-hour time increment of fatigue loading. A fatigue model based on Equation 4-14 was developed using the peak tensile stresses and the stress ranges that corresponds to peak damage locations on both the lane-shoulder joint and the transverse joint. The fatigue model can be rewritten as:

$$\log N = \frac{1 - SR - \lambda \log T}{\beta(1 - \eta R)} \quad \textbf{(4-15)}$$

In the development of the fatigue model for this research, to make Equation 4-15 more general, the stress ratio, SR, was multiplied by a coefficient κ, which was obtained through calibration:

$$\log N = \frac{1 - (\kappa SR + \lambda \log T)}{\beta(1 - \eta R)} \quad \textbf{(4-16)}$$

Fatigue models were developed to obtain the coefficients κ, λ, η, and β for both linear and bilinear distribution of *EBITD* through the depth of the slab. In the development of fatigue models for this research, the ratio of unloaded stress to peak stress was used to represent the stress range experienced by the slab at the critical location, due to the moving load. For the transverse joint edge location, the unloaded slab stress was always the minimum tensile stress, as seen in Figure 4-10 through Figure 4-12 and Figure A-37 through Figure A-54. This was not the case at the lane-shoulder edge, which in many cases went through stress reversals due to the load being right on top of the critical location. However, since this minimum (or stress reversal) occurred very rapidly and lasted only a short duration of time (5 to 10 percent of total time), the longer duration unloaded slab stress was used as the basis for calculating the ratio *R*. The minimum or unloaded slab stress was typically the residual tensile stress on the approach or leave slab.

The fatigue models were developed using all North Tangent and South Tangent sections with back-calculated *EBITD*, shown in Table 3-7. For Sections 535FD through 541FD, the *EBITD* values obtained from 24-hour loaded deflection analysis were used. For the remaining sections the *EBITD* values corresponding to early fatigue load repetitions were used. In the development of the linear model, the *EBITD* was assumed to vary linearly through the full depth of the slab. For the bilinear model, the *EBITD* was assumed to vary linearly to the mid-depth of the slab as shown in Figure 4-9. The procedure used to develop the fatigue models are described in the following steps:

1. For each test section, the back-calculated *EBITD* was added to the minimum and maximum temperature differences measured during fatigue testing to obtain the range

of *TELTD* for that particular test section. When multiple thermocouple data were available, the averages of the box and shade thermocouple readings were used.

2. ISLAB2000, along with the slab geometry and material inputs listed in Section 3.3.4, was used to model the slab responses for combinations of various load levels, *TELTDs*, and LTEs, experienced by each slab until the first field-observed cracking.
3. As a first order of approximation, it was assumed that on any given edge (transverse edge or lane-shoulder edge) maximum damage occurred at the location of peak stresses at that edge, and therefore, responses computed at these two locations (for each slab corner) were used to develop the fatigue models. As discussed in Section 4.4.1, the critical locations on the lane-shoulder edge and on the transverse edge were selected as the peak stress locations on the two edges that corresponded to when the measured temperature difference through the depth of the slab was most negative (greatest amount of upward curl).
4. A matrix of unloaded and corner-loaded slab stresses was developed using the output results from ISLAB2000. The matrix included these stresses at various slab locations (left lane-shoulder edge, right lane-shoulder edge, left transverse edge, right transverse edge) for the range of load levels, *TELTDs*, and LTEs, experienced by each slab until the first field-observed cracking.
5. For each test section, this table was used to interpolate peak stress and unloaded stress experienced by the slab at the critical locations, for each time increment that thermocouple data was collected.

6. For each time increment, the peak stress was divided by the concrete flexural strength to obtain the stress ratio. The variable R representing the stress range experienced by the slab was calculated as the ratio of unloaded stress to peak stress.
7. Seed values were used for the coefficients κ, λ, η, and β, as a starting point for cumulative fatigue damage determination.
8. Using the model shown in Equation 4-16 for each test section, the cumulative damage to number of repetitions at observed failure (first crack) or end of fatigue loading (uncracked slab) was computed at critical locations on left lane-shoulder edge, right lane-shoulder edge, left transverse edge, right transverse edge, as depicted in the flowchart in Figure 4-3
9. For each edge (transverse and lane-shoulder), the greater of the two damages computed (left corner loading and right corner loading) was used as the peak damage for that edge.
10. If a crack was observed to begin or terminate at the transverse edge of a slab (longitudinal crack or corner break), the difference between the location of the crack and the peak stress was assumed to be due to variability, and the transverse edge was assumed cracked at the location of the peak stress.
11. If a crack was observed to begin or terminate at the lane-shoulder edge of a slab (transverse crack or corner break), the difference between the location of the crack and the peak stress was assumed to be due to variability, and the lane-shoulder edge was assumed cracked at the location of the peak stress.

12. Since cumulative damage is expected to be 1.0 at failure, for all cracked slab locations on both edges, the root mean square (RMS) error was calculated as the square root of the mean of the square of the difference in log FD and log 1.

$$RMS\ Error = \sqrt{\sum_k (\log FD - \log 1.0)^2} = \sqrt{\sum_k (\log FD)^2} \quad \textbf{(4-17)}$$

where:

k = All transverse and lane-shoulder joint locations with failure cracks.

13. An Excel macro was used in an iterative procedure that repeated Steps 7 through 12 by varying coefficients κ, λ, η, and β, to minimize the mean square error calculated in Step 12. The coefficients corresponding to the least mean square error are the ones used in the model (Equations 4-18 and 4-19).

The fatigue models are as follows:

$$\log N = \frac{1 - (0.465\,SR_B + 0.088 \log T)}{0.153(1 - 0.297\,R)}, \text{ using linear } EBITD \quad \textbf{(4-18)}$$

$$\log N = \frac{1 - (0.236\,SR'_B + 0.085 \log T)}{0.162(1 - 0.297\,R)}, \text{ using bilinear } EBITD \quad \textbf{(4-19)}$$

where:

N = allowable number of loads to first crack.
T = period of repetitive loads, seconds/cycle.
SR_B,
SR_B' = Stress ratio; ratio of peak stress to beam flexural strength using linear and bilinear *EBITD*, respectively.
R = Ratio of unloaded stress to peak stress.

The computed cumulative damage, until the appearance of the first crack, at the two peak stress locations for the Palmdale test sections is shown in Figure 4-14. If a test slab exhibited longitudinal cracking, the cumulative damage computed at the transverse peak stress location is

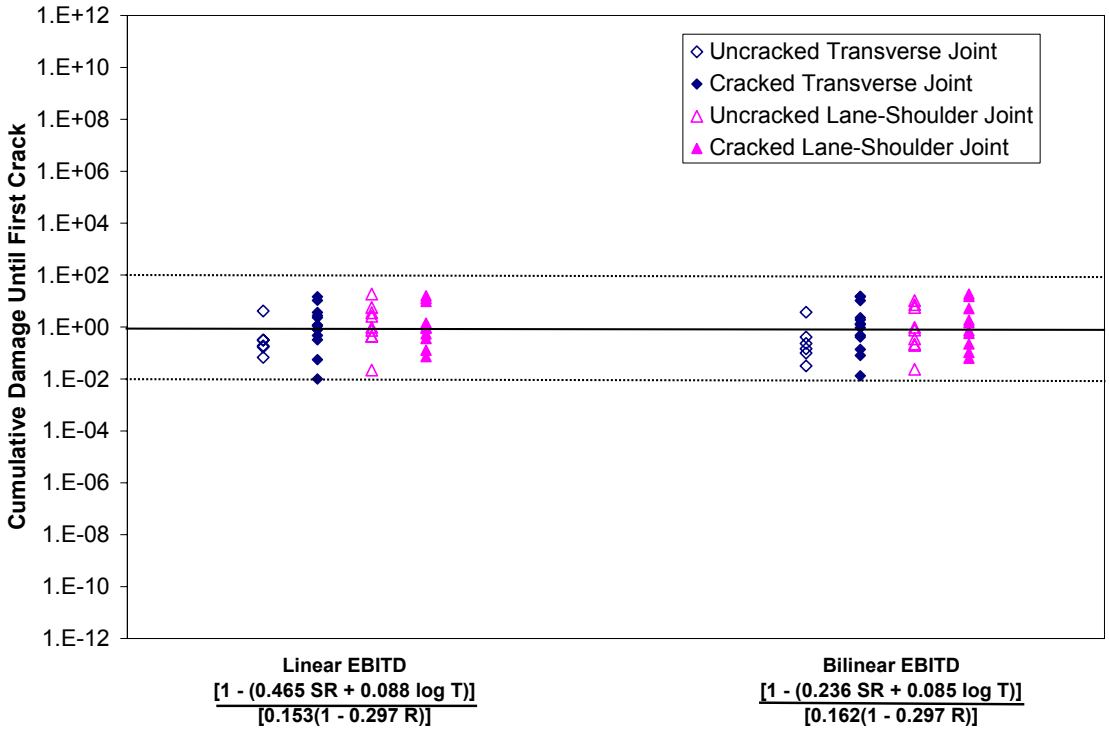

Figure 4-14. Calculated cumulative damage to first field-observed crack for Palmdale test sections.

shown as "cracked" (represented by solid diamond markers) and the lane-shoulder peak stress location is shown as being "uncracked," (represented by hollow triangle markers). Likewise, if a test slab exhibited transverse cracking extending from the lane-shoulder joint, the cumulative damage is shown as "cracked" (represented by solid triangle markers) and the transverse peak stress location is shown as being "uncracked," (represented by hollow diamond markers). The figure also shows cumulative damage at the peak stress locations for slabs that did not crack until the end of the fatigue loading for that particular test section (such as Sections 533FD, 538FD, and 541FD) which are also represented by hollow triangle and diamond markers in the figure. Corner breaks are shown as having cracked at both peak stress locations and are represented by solid triangle and diamond markers corresponding to both peak stress locations. For visual

reference only, horizontal lines corresponding to cumulative damage of 0.01 and 100 are also shown.

The root mean square (RMS) error (log scale) for the various fatigue models along with the deviation of log of mean fatigue damage from log (1.0) are shown in Table 4-2. The table shows that for the Palmdale test sections, the developed linear and bilinear models have lower error than existing fatigue models and are more evenly distributed about the expected mean fatigue damage of 1.0. While comparable results in terms of reduced error and reduced deviation of log of mean fatigue damage from log (1.0) can also be obtained through re-calibration of the existing fatigue models, the fatigue models developed, and in particular the bilinear model, are the only ones that address the discrepancies with regard to the location of peak stresses and observed cracking discussed in Sections 4.5.2 and 4.5.3. Including the ratio of peak stress to unloaded slab stress, results in reduced damage at the lane-shoulder edge relative to the transverse edge and improves the cracking parity between the two edges, as can be seen by the lower number of uncracked lane-shoulder joint locations (hollow triangles) with calculated damage greater than 1.0 as compared to the fatigue damage from existing models shown in Figure 4-4.

A graphical representation of the Palmdale model using linear *EBITD* showing the allowable number of load repetitions to fatigue damage of 1.0 is shown in Figure 4-15. Although not directly comparable because of differences in failure definitions, stress computations, and stress components used to calibrate those models, for sake of comparison, the other six fatigue models evaluated are also shown in the figure. The model indicates that at a stress ratio of 1.0, the pavement can carry roughly 10,000 load applications before appearance of first fatigue crack. This is likely due to slab support provided by the underlying layers and the subgrade, and due to

Table 4-2 Summary of Effectiveness of Various Fatigue Models as Applicable to the Cracked Peak Stress Locations for Palmdale Test Sections

Fatigue Model	Model Form - Allowable Number of Load Repetitions, N	Root Mean Square Error, log units	Average Model Deviation from Expected Fatigue Damage of 1.0, log units
Zero-Maintenance (1977)	$17.61 - 17.61\ SR$	4.35	-3.59
Calibrated Mechanistic Design (1993)	$2.81\ SR^{-1.221}$	2.77	-2.11
ERES/COE (1988)	$2.13\ SR^{-1.20}$	1.43	-0.43
Foxworthy (1985)	$(1.323/SR) + 0.588$	1.60	1.34
PCA (1983)	$11.737 - 12.077\ SR$	1.76	-0.68
2002 Design Guide (2002)	$2.0\ SR^{-1.22}$	1.34	-0.20
Palmdale Linear	$\frac{1-(0.465SR+0.088\log T)}{0.153(1-0.297R)}$	0.84	0.00
Palmdale Bilinear	$\frac{1-(0.236SR+0.085\log T)}{0.162(1-0.297R)}$	0.85	0.00

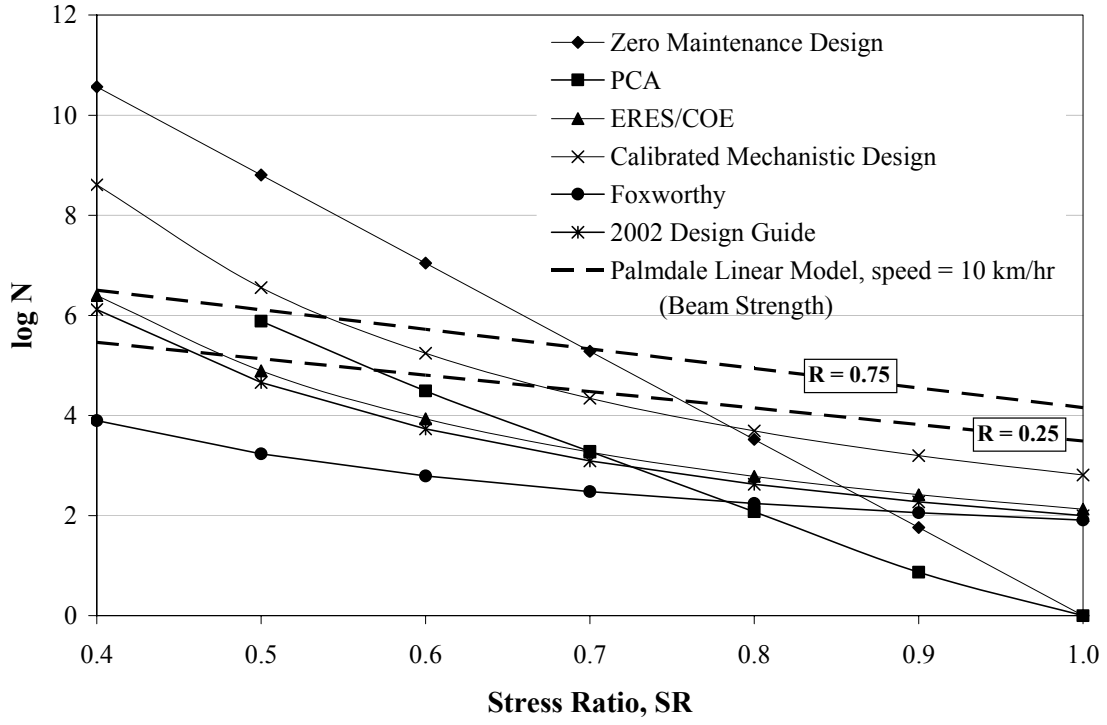

Figure 4-15. Comparison of number of allowable load applications to failure between existing fatigue models and Palmdale linear model using beam strength.

higher slab flexural strength compared to beam flexural strength as observed in laboratory testing by Roesler (1998) and Littleton (2003). For a given peak stress (or stress ratio), a smaller stress range (higher *R*) results in an increase in allowable number of repetitions. A change in ratio of unloaded slab stress to peak stress from 0.25 to 0.75, results in a 5- to 10-fold increase in allowable load applications before appearance of first crack. The Palmdale fatigue model (Log *N*) is also less sensitive to changes in stress ratios similar to the field derived fatigue equations from the AASHO Road Test (Vesic and Saxena, 1969; Treybig et al., 1977). The allowable repetitions to failure from laboratory derived concrete fatigue equations have also been extremely sensitive to stress ratio. This has resulted in heavy loads almost always consuming the majority of the pavement's fatigue life.

The Palmdale models were developed using beam flexural strength instead of slab flexural strength because data on slab flexural strength for the test sections were not collected. However, Roesler et al. (2003) and Littleton (2003) have found that the slab flexural strength can be more than two times higher than the beam flexural strength. Assuming the ratio as 2.0, Equation 4-17 and Equation 4-18 can be rewritten to incorporate slab strength as follows:

$$\log N = \frac{1-(0.930\,SR_S + 0.088\log T)}{0.153(1-0.297\,R)}\textbf{, using linear } \boldsymbol{EBITD} \qquad \textbf{(4-20)}$$

$$\log N = \frac{1-(0.472\,SR'_S + 0.085\log T)}{0.162(1-0.297\,R)}\textbf{, using bilinear } \boldsymbol{EBITD} \qquad \textbf{(4-21)}$$

where:

SR_S,
SR_S' = Stress ratio; ratio of peak stress to slab flexural strength using linear and bilinear *EBITD*, respectively

The Palmdale model using linear *EBITD* and slab flexural strength, showing the allowable number of load repetitions is shown in Figure 4-16. The other six fatigue models evaluated in this study are also shown. At a slab stress ratio of 1.0, the pavement can carry only

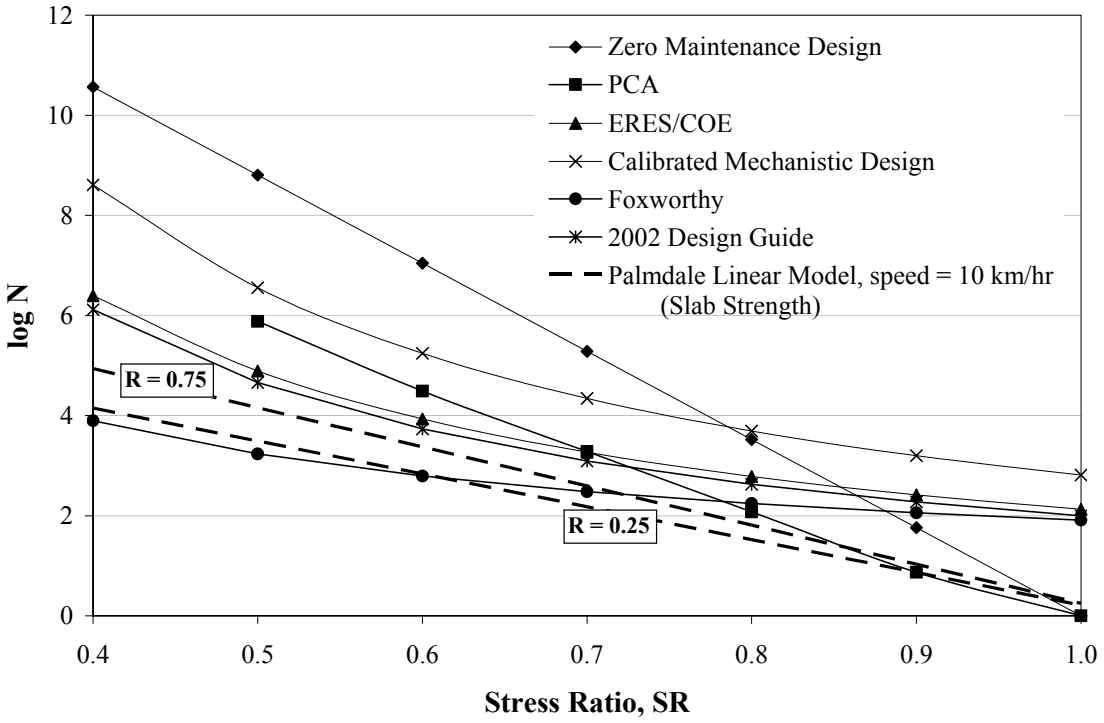

Figure 4-16. Comparison of number of allowable load applications to failure between existing fatigue models and Palmdale linear model using slab strength.

one load application before crack appearance. At high stress ratios, the effect of the ratio of unloaded slab stress to peak stress, R, is diminished.

The Palmdale model with bilinear *EBITD* and slab flexural strength is shown in Figure 4-17. Because of the significantly higher stresses calculated using the bilinear distribution, it cannot be directly compared to any of the existing models. The figure also shows that at high stress ratios, the effect of the ratio of unloaded slab stress to peak stress, R, is diminished, while at lower stress ratios (< 0.4), slab experiencing smaller variation in peak stress (R = 0.75) can carry more than 10 times as many load repetitions compared to a slab that experiences a larger variation in peak stress (R = 0.25).

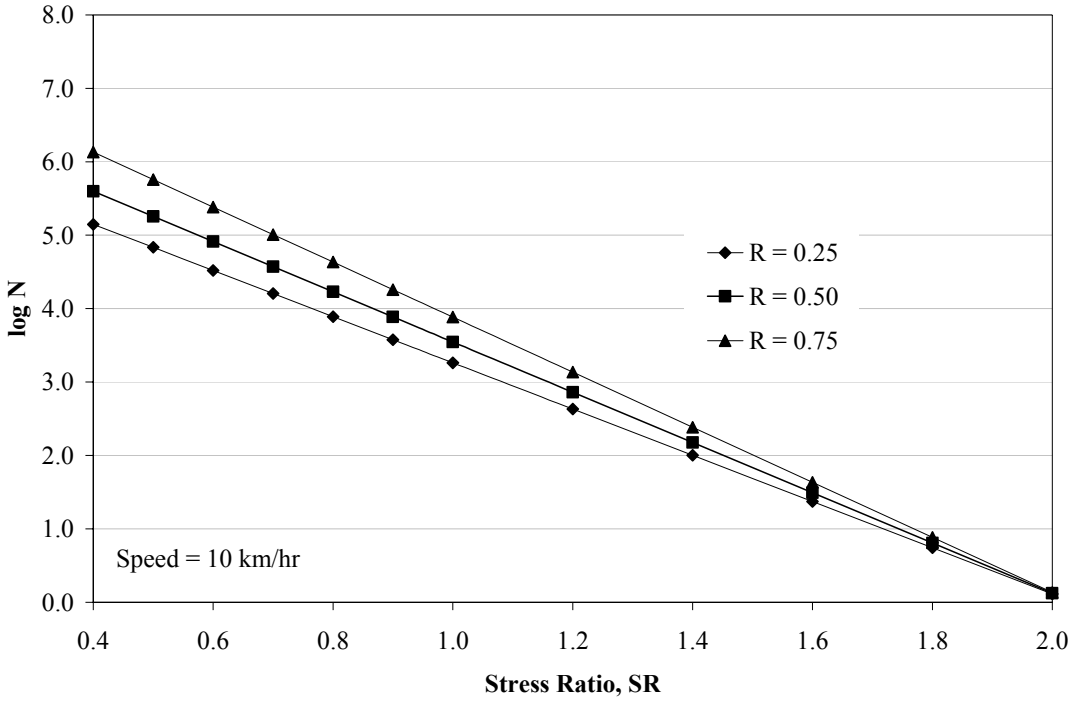

Figure 4-17. Number of allowable load applications to damage of 1.0 for Palmdale bilinear fatigue model using slab strength.

4.6.2 Crack Locations

Using the developed fatigue models shown in Equations 4-17 and 4-18, damage computations were performed for several locations along the transverse edge and the lane-shoulder edge. The locations of the maximum damage on these edges are expected to be the crack initiation locations. In the majority of cases, this location coincided with the location of peak stress along that edge. Ideally, an iterative procedure should be used to obtain this location of peak damage, and redevelop the model coefficients using the steps outlined in Section 4.6.1. However, since the difference in peak damage and the calculated damage were small, this iterative procedure was not performed. The difference in location of the peak damage and that used in developing the model were typically less than 0.1 m and a maximum of less than 0.2 m. Table 4-3 shows the observed crack locations and the predicted crack locations as distances from

Table 4-3 Observed Crack Locations and Predicted Critical Damage Locations for Palmdale Test Sections

Section ID	Crack Type	Observed Crack Location				Predicted Crack Location			
		Transverse Distance from Corner Measured on Transverse Joint, m		Longitudinal Distance from Corner Measured on Lane-Shoulder Joint From Slab Corner, m		Transverse Distance from Corner Measured on Transverse Joint From Slab Corner, m		Longitudinal Distance from Measured on Lane-Shoulder Joint From Slab Corner, m	
		From Left Corner	From Right Corner	From Left Corner	From Right Corner	From Left Corner	From Right Corner	From Left Corner	From Right Corner
519FD	LC	1.1	1.3	-	-	1.4	1.3	-	-
520FD	LC	1.1	1.2	-	-	1.2	1.2	-	-
523FD	CB	-	1.8	-	2.4	-	1.3	-	2.3
524FD	LC*	-	1.8	-	-	-	1.3	-	-
525FD	CB	-	1.7	-	1.8	-	1.4	-	1.8
526FD	CB	-	1.4	-	1.8	-	1.2	-	1.7
527FD	LC	1.5	-	-	-	1.5	-	-	-
528FD	TC	-	-	2.1	-	-	-	1.7	-
530FD	CB	-	1.4	-	1.4	-	1.4	-	1.7
531FD	CB	1.3	-	1.4	-	1.3	-	1.5	-
532FD	CB	-	1.4	-	1.6	-	1.4	-	1.6
533FD	Did not fail	-	-	-	-	-	-	-	-
534FD	CB	1.8	-	1.9	-	1.4	-	1.5	-
535FD	CB	1.6	-	3.2	-	1.3	-	1.6	-
537FD	TC	-	-	-	1.3	-	-	-	1.3
538FD	Did not fail	-	-	-	-	-	-	-	-
539FD	TC	-	-	-	1.6	-	-	-	1.7
540FD	CB	-	1.7	-	2.0	-	2.0	-	1.8
541FD	Did not fail	-	-	-	-	-	-	-	-

*Progressed after additional loading to CB.
LC = Longitudinal crack, CB = Corner break, TC = Transverse crack

the left and right slab corners for the test sections included in the analysis. Reasonable agreement was obtained between predicted crack locations and observed crack locations.

4.7 Summary of Cumulative Fatigue Damage Modeling

Miner's hypothesis for accumulation of damage and applicability of several concrete fatigue transfer functions was tested against the full-scale results from HVS fatigue testing of the Palmdale slabs. Peak tensile stresses at critical locations on the surface of the slab were calculated using ISLAB2000 for each two-hour interval of HVS loading. These stresses were used to compute stress ratio, which were then used in the fatigue models to compute cumulative damage until slab failure (first observed crack). The models showed high amount of variability and deviation from the expected fatigue damage of 1.0.

A model based on Hsu's adaptation of Aas-Jacobsen's model was used in order to incorporate stress range and loading frequency. For each test section, responses due to the moving wheel load were modeled with ISLAB2000 for a range of temperature differences using influence line plots. These plots were generated for several critical locations along the transverse and longitudinal joints. The influence line plots were used to estimate peak tensile stresses, unloaded slab stresses, and minimum stresses at the critical locations. These stresses were used to develop a linear and a bilinear fatigue model for the Palmdale test sections. These models have lower error than existing fatigue models and are more evenly distributed about the expected mean fatigue damage of 1.0. Reasonable correspondence was observed between predicted crack locations and observed crack locations at most test sections. The advantages of using the Palmdale models are summarized below:

1. The model coefficients were obtained using field data from full-scale test sections with more accurate and detailed information on mechanical load levels and position

on the slab, environmental loading parameters, pavement layer geometric and material properties, and the repetition level where concrete fatigue failure occurred.

2. The models incorporate stress ranges and time period of applied repeated loading.
3. For slabs with high magnitude of upward curl, using peak stresses only (and existing fatigue models) suggests that cracks would initiate from the middle of the slab. Incorporating stress ranges results in crack initiation from the transverse or longitudinal edges, as was observed in the test sections.
4. Using existing fatigue models, slabs are expected to crack first at the lane-shoulder joint in a majority of cases, contrary to field observations. By incorporating stress ranges, the Palmdale models address this disparity and reduce the probability of slab cracking at the lane-shoulder edge relative to the transverse edge.

The limitations of using the Palmdale models are summarized below:

1. The models do not address some of the other limitations of using Miner's hypothesis and cumulative damage such as rest periods, endurance limit, variable amplitude, stress history, etc.
2. The effect of slab size on slab strength is not included in these models.
3. The effects of reduced slab strength due to early-age microcracking from restrained shrinkage are not considered.
4. The models were developed using a small data set from field-tested sections at one location (Palmdale, CA).
5. The models are more computationally intensive than other fatigue models because they require determination of both peak stresses and stress ranges at critical locations on both lane-shoulder edges and transverse edges.

The assumptions based upon which the models were developed are as follows:

1. All plate theory assumptions and assumptions pertaining to the use of finite element analysis for concrete pavements listed in Section 1.5.
2. For a given pavement structure, geometry, and layer properties, and thermo-mechanical loading, slab stresses can be reasonably predicted using the finite element analysis program, ISLAB2000.
3. All layer thicknesses and material properties, particularly flexural strengths, for a given slab, are uniform and do not deviate significantly from the average values used.
4. The *EBITD* values calculated in Chapter 3 for all test sections are reasonably accurate. For test sections with *EBITD* calculated at only one corner of the slab, it is assumed that the calculated value represents the greater of the two corner *EBITD* values.
5. Superposition of *EBITD* and measured temperature difference is valid.
6. All test slabs are intact and without any significant microcracking damage that can result in a reduction in strength.
7. Support beneath the slab is uniform.
8. Cracking in the slabs at the test sections were instantaneous and were observed as soon as they occurred.
9. Miner's hypothesis and the cumulative damage approach are valid for modeling concrete fatigue damage.

5.0 MODELING SIZE EFFECT AND INITIAL SLAB CRACKING

The Palmdale cracking analysis performed in Chapter 4 is based on classic strength theory failure — an elastic analysis based on stresses at critical locations and a strength limit. In the analysis, the flexural strength of the slab was assumed to be independent of the size (thickness) of the slab and slab geometry and boundary conditions. However, several research studies (Blanks and McNamara, 1935; Neville, 1956; Kani, 1967; Taylor, 1972; Walsh, 1976; Sabnis and Mirza, 1979; Bazant, 1984; Hillerborg, 1989) have shown that the strength of a quasi-brittle specimen such as concrete, or more precisely, the nominal stress at failure depends on its size. An example of such an effect of size on uniaxial tensile strength of concrete specimen is shown in Figure 5-1 (Carpinteri and Ferro, 1994).

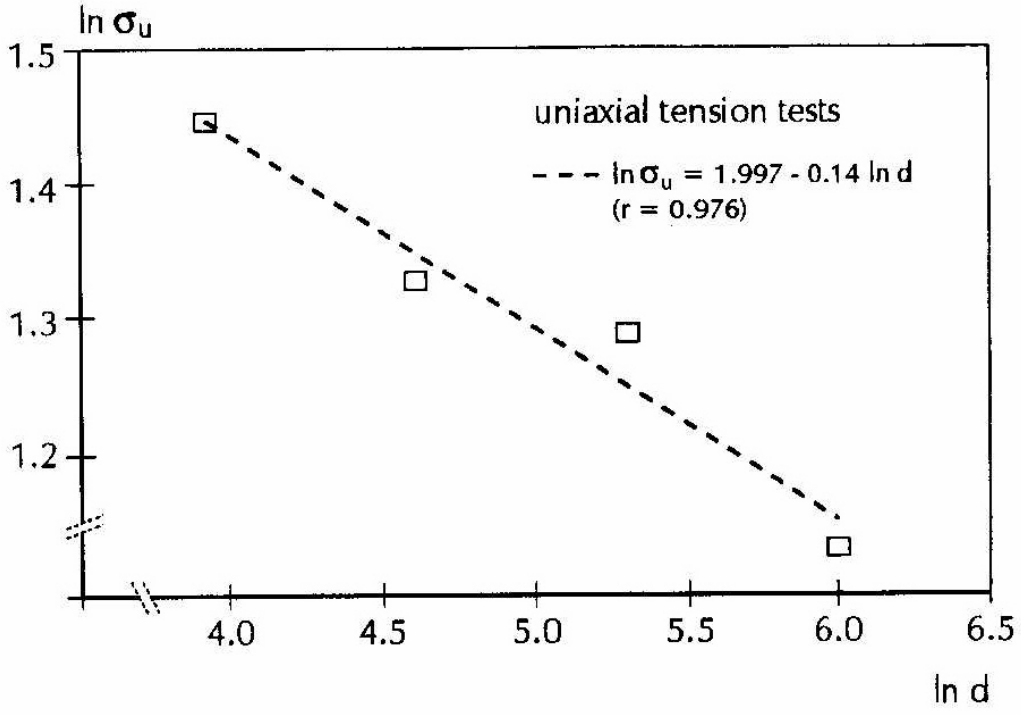

Figure 5-1. Effect of size on tensile strength (from Carpinteri and Ferro, 1994).

Another assumption in the cumulative damage analysis presented in Chapter 4 is that the initial slab damage at the critical stress locations was zero. However, tensile stresses on the surface of the slab, as a result of shrinkage restraint at early ages of the concrete strengthening, can create permanent damage at the micro-level. Altoubat and Lange (2001) state that "…stress development in the very early ages influences the performance of the material in the long run, even if the material sustains the stress without fracture." Early-age transverse cracking due to restrained shrinkage is an important consideration in bridge deck design because the cracks permit the ingress of harmful substances into the deck (Folliard et al., 2003). Several researchers (Babaei and Purvis, 1996; Krauss and Rogalla, 1996; French et al., 1999) have studied the phenomenon of restrained shrinkage cracking in bridge decks. However, it has generally not been a consideration in the design of concrete pavements.

Slabs with high amounts of drying shrinkage gradients, such as those at Palmdale, can be restrained from curling by load transfer with adjacent slabs and shoulder, weight of the slab, friction at the slab-base interface and friction with existing adjacent slabs. If the restraining stresses are small, it can be beneficial in terms of creep, which can reduce the magnitude of *EBITD* of the slab as described in Chapter 3. However, if excessive, the restraints can cause microcracking, resulting in reduced slab strength and earlier fatigue failure as compared to slabs with fewer restraints and lower tensile stresses at early age. A procedure to account for size effect, slab geometry and boundary conditions, and reduced strength due to surface microcracking is presented in this chapter.

5.1 Size Effect

The size of the structure, such as the thickness of a concrete pavement slab, for a quasi-brittle material affects the nominal strength of the structure. Two main size effects cause the

nominal strength to depend on structure size: statistical size effect and fracture mechanics size effect.

5.1.1 Statistical Size Effect

The statistical size effect is caused by the randomness of material strength and is based upon Weibull's (1939) model of a chain. The larger the size of a structure, the greater the likelihood of the existence of a defect or a critical microcrack that triggers failure. In the chain analogy, the load at failure of a chain is determined by the strength of the weakest link in the chain. The longer the chain, the smaller the strength value likely to be encountered in the chain, which results in a weaker chain.

5.1.2 Fracture Mechanics Size Effect

Fracture in materials occurs in one of three modes: Mode I (tensile opening), Mode II (plane shear), and Mode III (out-of-plane shear). These cracking modes are shown in Figure 5-2 (Van Mier, 1997). The opening Mode I is the most common form of failure of concrete materials. For each mode, Linear Elastic Fracture Mechanics (LEFM) defines a driving force called the stress intensity factor. The general form of the stress intensity factor for Mode I cracking can be written as:

$$K_I = \sigma\sqrt{\pi a}F\left(\frac{a}{h}\right) \qquad \textbf{(5-1)}$$

where:

σ = Farfield stress applied to the cracked specimen

$F\left(\frac{a}{h}\right)$ = nondimensional geometrical factor dependent specimen type and the ratio of crack depth to slab thickness.

a = crack depth

h = slab thickness.

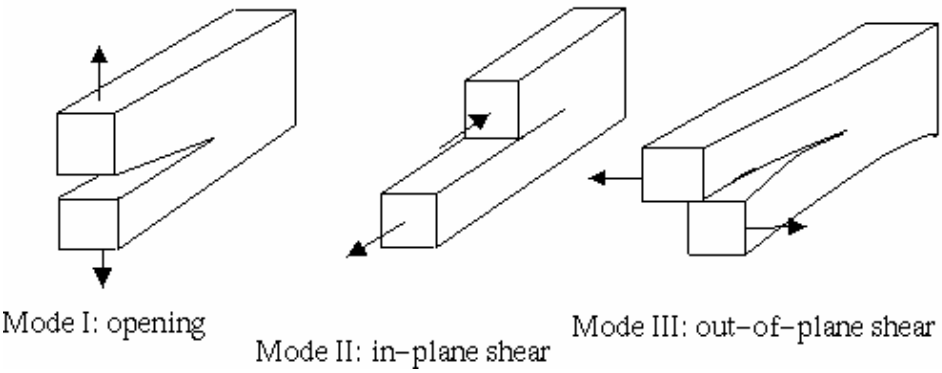

Figure 5-2. The three principal modes of cracking (from Van Mier, 1997).

Assuming LEFM is valid, the crack propagates when the stress intensity factor exceeds a critical value, the fracture toughness, K_{Ic}. This Mode I fracture toughness depends on the material and size of a structure and must be obtained experimentally. It represents the ability of a material to resist unstable crack growth in the presence of an initial crack. The nominal strength of the structure or the stress at the point of unstable crack propagation is given by:

$$\sigma_N = \frac{K_{Ic}}{\sqrt{\pi a}F\left(\frac{a}{h}\right)} \qquad \textbf{(5-2)}$$

where:
K_{Ic} = Fracture toughness of the material, kPa√m

For geometrically similar structures of different sizes, K_{Ic}, $F\left(\frac{a}{h}\right)$ and $\left(\frac{a}{h}\right)$ are constants.

Taking the logarithm of both sides of Equation 5-2, log σ_N is a linear function of log h with slope –0.5. Therefore, by applying dimensional analysis to the parameters, the effect of size on nominal strength can be predicted for materials governed by LEFM. As the crack progresses,

crack length (a) increases and $F\left(\frac{a}{h}\right)$ also changes, the combined effect of which results in a decrease in σ_N.

For quasi-brittle materials such as concrete, the size effect does not follow the LEFM straight line (on a bilogarithmic plot) unless the structure is considered large. Deviating from the constraints of LEFM, Bazant (1984) proposed the size effect law (SEL) based on an effective elastic crack approach for which LEFM, nonlinear fracture mechanics, and strength theory concepts were combined together as shown in Figure 5-3.

$$\sigma_N = \frac{Bf_t'}{\sqrt{1+\frac{h}{h_0}}} \qquad \textbf{(5-3)}$$

where:

f_t'	=	tensile strength of the material, introduced for dimensional purposes
B	=	dimensionless constant
h_0	=	constant with dimensions of length

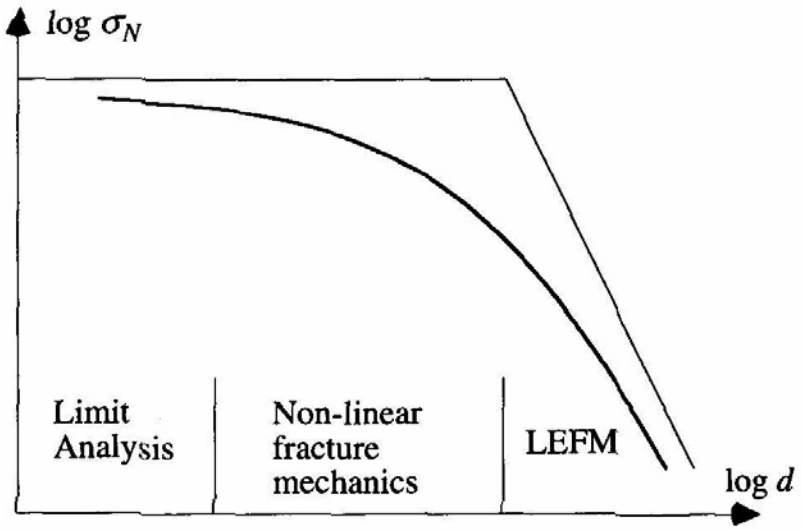

Figure 5-3. Effect of size on strength of quasibrittle materials (from Bazant, 1984).

The fracture mechanics size effect is due to the release of stored energy of the structure into the fracture front (Bazant and Planas, 1997). Before a critical macroscopic crack can form or propagate, the zone of distributed microcracks (also called softening or fracture process zone), must grow and dissipate energy. Formation and growth of these microcracks consumes a large amount of energy in the cracking process, serving as a mechanism of concrete toughening. Unstable crack growth does not occur until the fracture process zone reaches a critical length. As shown in Figure 5-4, when the crack band extends by Δa, the additional strain energy dissipated comes from cross-hatched strip of horizontal dimension Δa. Larger structures have greater area of the cross-hatched strip and more energy is released from the strip for the same extension of the crack band. Because of the greater amount of energy available, cracks in large structures propagate quicker than those in smaller structures.

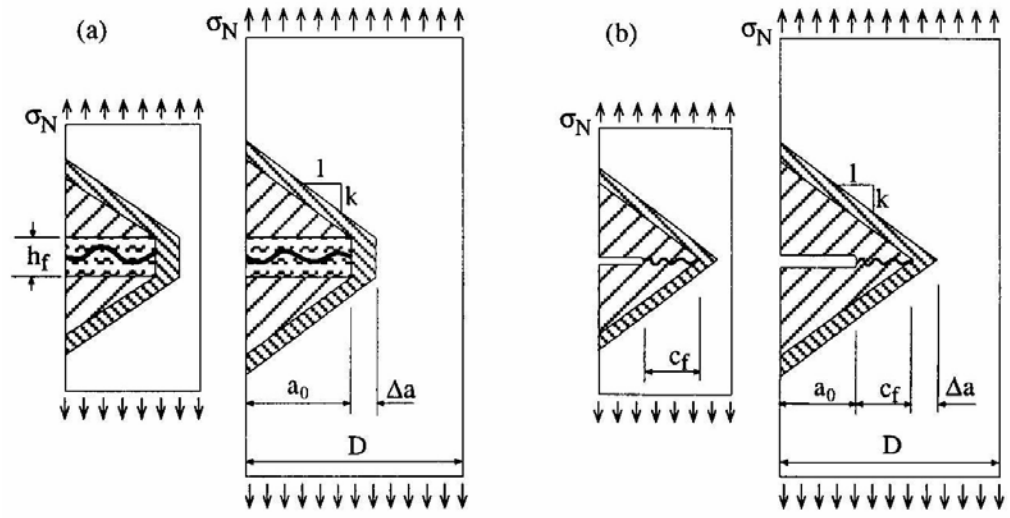

Figure 5-4. Fracture mechanics size effect for (a) blunt crack band and (b) slit-like process zone (from Bazant and Planas, 1997).

5.2 Early-Age Surface Microcracking

The FSHCC used for the Palmdale test sections was a high early strength concrete with a superplasticizer. A characteristic of the cement used in the FSHCC is its high amount of drying shrinkage. During the early ages of concrete strength gain, the slabs undergo significant shrinkage at the surface of the slab with less shrinkage at the bottom of the slab. This differential shrinkage causes the slab to lift at the corners and edges of the slab, which is mostly responsible for the effective built-in curling of the slab.

The shrinkage strain alone does not cause stresses at the surface of the slab. The forces and pressures provided by restraint cause stress (Folliard et al., 2003). Restrained shrinkage cracking occurs when concrete is prevented from making volumetric changes by a source of restraint. In the case of concrete pavements, this restraint can be from the slab self-weight that resists the curling of the slab, the friction between the base layer and the slab, and from load transfer between the slab and adjacent slabs or the shoulder. Due to the high shrinkage characteristics and high early-age elastic modulus of the FSHCC, which is typical of a high performance concrete that is fast-setting, it is more susceptible to shrinkage cracking if adequate curing during early age is not provided. Burrows (1998) goes as far as to state that the high early strength and other guidelines for high performance concrete "guarantee severe cracking from self-stress of thermal contraction, autogenous shrinkage, and drying shrinkage."

Altoubat and Lange (1995) suggested that the rate of early age shrinkage is of primary concern for restrained shrinkage cracking. Folliard et al. (1993) conducted restrained shrinkage test (AASHTO PP34) on several types of concrete mixtures. The test involves casting a concrete ring around the perimeter of a steel ring. After a curing period, the concrete is allowed to dry from its circumferential face. Four strain gages, spread equally around the circumference, are placed at mid-height of the steel ring. Shrinkage of the concrete ring results in compressive

strains in the steel ring that are measured by the strain gages. The restrained shrinkage history, shown as the average of the strains measured by these strain gages, for the first three days of drying is shown in Figure 5-5.

The slope of a given curve can be interpreted as the rate of early age restrained shrinkage. Their study showed that the HPC mixture has the highest slope, which indicates a large potential for cracking. In the ring test experiment, the HPC was the second mixture to crack. The concrete mixture with the Type K shrinkage-compensating cement and the one with the shrinkage-reducing admixture (SRA) had the smallest slope, suggesting low restrained shrinkage cracking potential. These ring specimens of these two concrete mixtures did not crack through the duration of the test.

The high susceptibility of HPC to restrained shrinkage cracking observed by Folliard et al. was also a factor for the Palmdale test sections. Although the test slabs at Palmdale did not have visual cracks prior to fatigue testing, several of the longer (5.8 m) untested slabs on the test

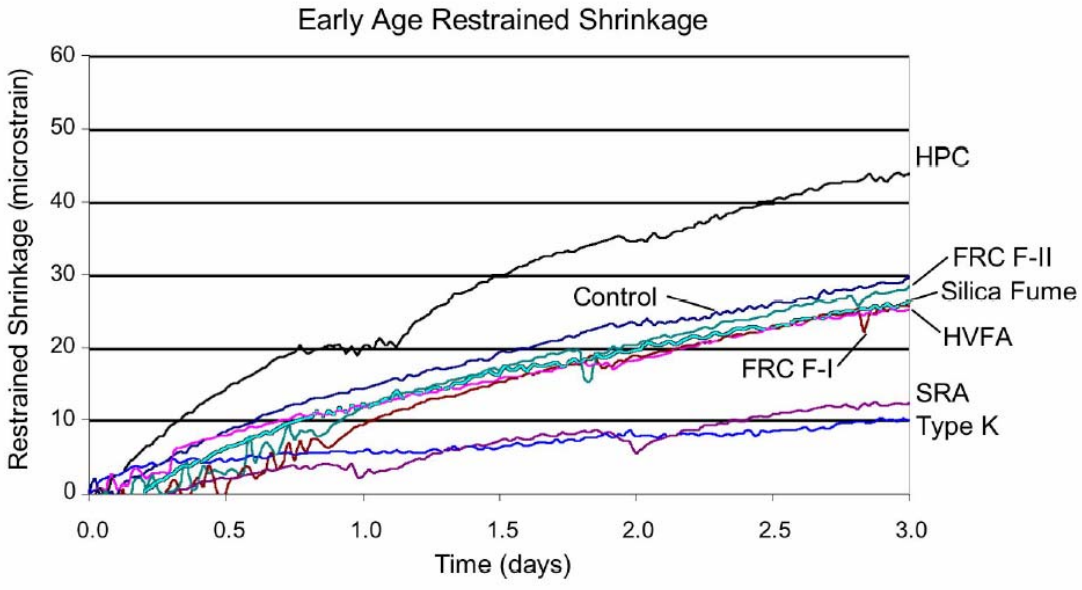

Figure 5-5. Restrained shrinkage at early age (from Folliard et al., 1993).

strip cracked prior to any load application. Trenching and coring data also showed that all of the test slabs cracked from the top down (Heath and Roesler 2000). Several of the tested slabs cracked with very few load repetitions, which suggests permanent damage and strength loss at slab surface of these slabs due to early age restrained shrinkage. The factors that cause the long slabs to crack prior to any loading could be responsible for tensile stresses at the top of the intact tested slabs, resulting in microcracking at the surface, and weakening of the slab.

Altoubat and Lange (2001) observed that in restrained specimen, the high stress at early ages can cause permanent damage at the microstructural level, leading to cracking sooner than predicted by simple strength criteria. They suggested that for concrete subjected to sustained load at early ages such as from drying shrinkage under restrained conditions, a strength reduction factor, such as 0.8 for uniaxial tension must be applied.

For this analysis, a slab of thickness h with surface microcracking is assumed to behave as a slab with surface crack depth, a_e. This depth a_e (*effective initial crack depth)* is not the depth of a real observable crack at the surface of the slab. Rather, it is the effective crack depth due to microcracking at the critical stress locations of the surface of a slab and is responsible for the reduction in nominal strength and a decrease in fatigue life of the slab.

5.3 Modeling Size Effect and Early-Age Surface Microcracking

When a surface crack is introduced in a concrete slab, the stiffness of the slab perpendicular to the crack is less than the plate stiffness in the direction of the crack. Based on LEFM principles, Rice and Levy (1972) developed a procedure for analyzing a surface crack in a plate. Roesler and Khazanovich (1997) revised Rice's derivations for partial-depth crack analysis following the steps taken in a similar paper by Linkov and Tutinas (1988). The analysis was used to modify ILLI-SLAB into ILSL97, a finite element program for analysis of partial-depth

cracked slabs. Figure 5-6 shows a schematic of a surface cracked plate in combined bending and tension.

The stress intensity factor for a surface cracked plate of unit width with thickness *h* and crack depth *a*, such as the one shown in Figure 5-6 is given by (Anderson, 1991):

$$K_I = \frac{1}{\sqrt{h}}\left[P f_t(\xi) + \frac{M}{h} f_b(\xi) \right] \quad \textbf{(5-4)}$$

where:

ξ = $\left(\frac{a}{h}\right)$
P = normal force
M = bending moment
f_t, f_b = geometric factors for normal and bending forces, respectively.

$$f_t(\xi) = \frac{\sqrt{2\tan\left(\frac{\pi}{2}\xi\right)}}{\cos\left(\frac{\pi}{2}\xi\right)}\left[0.752 + 2.02(\xi) + 0.37\left\{1 - \sin\left(\frac{\pi}{2}\xi\right)\right\}^3 \right] \quad \textbf{(5-5)}$$

$$f_b(\xi) = \frac{6\sqrt{2\tan\left(\frac{\pi}{2}\xi\right)}}{\cos\left(\frac{\pi}{2}\xi\right)}\left[0.923 + 0.199\left\{1 - \sin\left(\frac{\pi}{2}\xi\right)\right\}^4 \right] \quad \textbf{(5-6)}$$

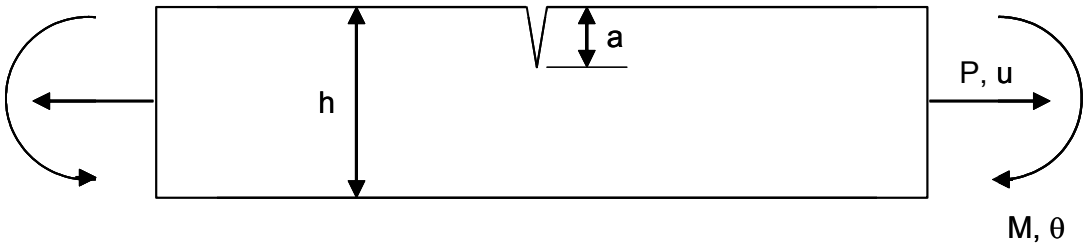

Figure 5-6. Edge cracked plate in combined bending and tension.

In the development of the finite element model, Roesler and Khazanovich assumed that the slab was unrestrained from horizontal movements and therefore, the normal force P = 0. Equation 5-4 then reduces to:

$$K_I = \frac{1}{\sqrt{h}}\left[\frac{M}{h} f_b(\xi)\right] \quad \textbf{(5-7)}$$

The resulting moment at the crack tip, M, in the plane of the crack is calculated by multiplying the crack rotation by its stiffness component, LS.

$$M = [LS](\theta) \quad \textbf{(5-8)}$$

where:

$$LS = \frac{Eh^2}{2(1-\upsilon^2)}[C_{22}]^{-1} \quad \textbf{(5-9)}$$

$$\begin{aligned} C_{22} = {} & \frac{-424.43}{\pi} + \frac{3766.09 \ln\left[\cos\left(\frac{\pi}{4}\xi\right) + \sin\left(\frac{\pi}{4}\xi\right)\right]}{\pi} + \left\{108.1 \sec\left(\frac{\pi}{2}\xi\right)^2 [5.39462 \right. \\ & - \cos(\pi\xi) - 0.480905\cos(2\pi\xi) + 0.0126386\cos(3\pi\xi) - 6.86882\times10^{-5}\cos(4\pi\xi) \\ & - 8.5199\sin\left(\frac{\pi}{2}\xi\right) - 3.10192\sin\left(\frac{3\pi}{2}\xi\right) + 0.0830853\sin\left(\frac{5\pi}{2}\xi\right) \\ & \left. - 0.00131881\sin\left(\frac{7\pi}{2}\xi\right)]\right\}/\pi \end{aligned} \quad \textbf{(5-10)}$$

E = elastic modulus of slab
υ = Poisson's ratio of slab
θ = crack rotation.

Details of the development of the above equations are included in Roesler and Khazanovich (1997).

The properties of the Palmdale slabs (elastic modulus, Poisson's ratio, modulus of subgrade reaction) were used in ILSL97 to estimate the crack rotation θ, due to a 57-kN dual wheel load (tire pressure, 690 kPa) placed at the mid-slab edge of a single slab. The crack

rotations were estimated for 4 slab thicknesses, 101 mm, 152 mm, 203 mm, and 254 mm, and for crack depths ranging from 0.05 to 0.5 h.

The goal of this analysis was to determine the reduction in strength due to the existence of a full-length crack of depth (a), as detailed in this section. The analysis assumes that this strength reduction due to the existence of a crack is independent of the load location, existence of adjacent slabs, and curling in the slab. Therefore, ILSL97 was used in the analysis, where the load is symmetrically placed on the slab over the crack, causing a moment (M) in the slab. Because of this assumption, a corner loading scenario was not explicitly modeled.

The crack rotations calculated using ILSL97 was used in Equation 5-8 to calculate the bending moment, M, which was used in Equation 5-7 to obtain the stress intensity factor as a function of ξ. A plot of stress intensity factor versus crack depth to thickness ratio is shown in Figures 5-7 through 5-9 for four slab thicknesses and three slab lengths (3.35, 4.57, and 5.79 m). The figures show that stress intensity factor is a function of both slab thickness and crack depth to thickness ratio.

Bazant and Becq-Giraudon (2002) list the results of 94 studies that measured fracture parameters. In these studies, the fracture toughness, K_{Ic}, for concrete ranged from 100 $\text{kPa}\sqrt{\text{m}}$ to 2,200 $\text{kPa}\sqrt{\text{m}}$. For example, if the concrete toughness for the test slab was 1,000 $\text{kPa}\sqrt{\text{m}}$, the figures show that at this load level, a crack of length 0.1h would propagate on a 101-mm slab and a 152-mm slab, but would not propagate on a 203-mm slab or a 254-mm slab. At this load level, a crack of length greater than 0.3h would propagate on a 203 mm slab (crack length = 61 mm), and a crack of length greater than 0.5h would propagate on a 254-mm slab (crack length = 127 mm).

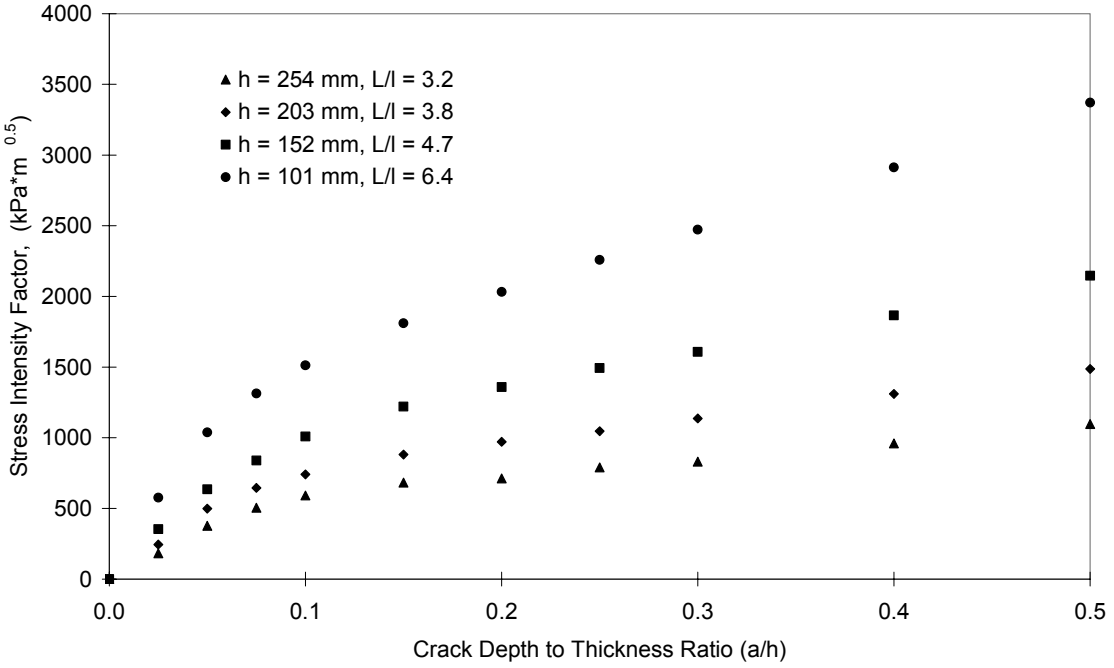

Figure 5-7. Effect of slab thickness and crack depth on stress intensity factor (L = 3.35 m).

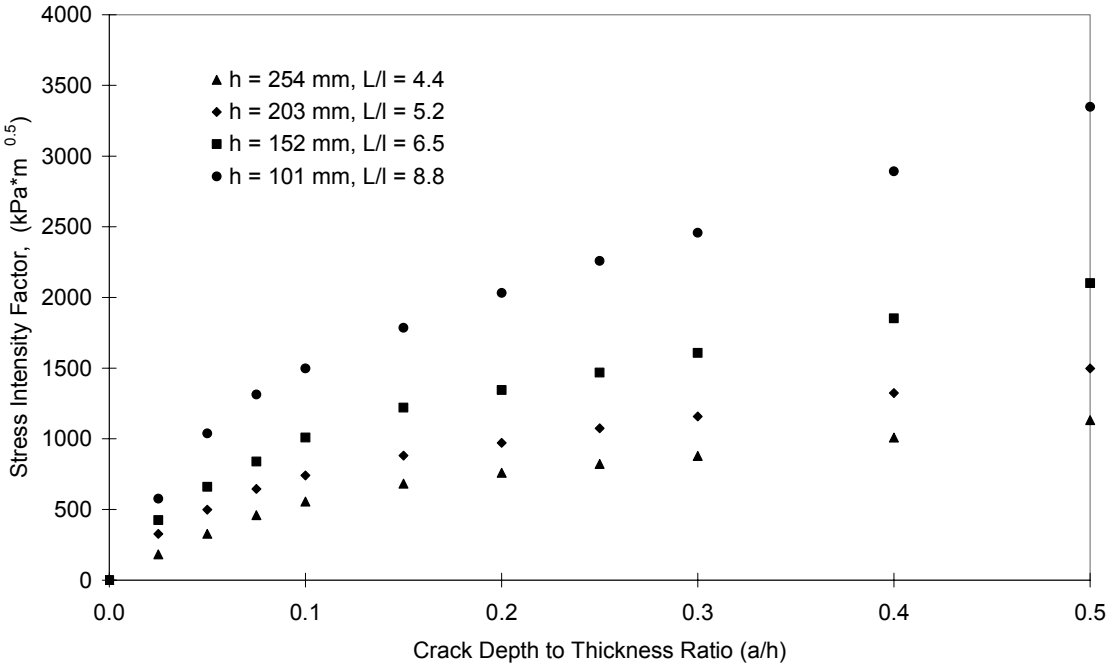

Figure 5-8. Effect of slab thickness and crack depth on stress intensity factor (L = 4.57 m).

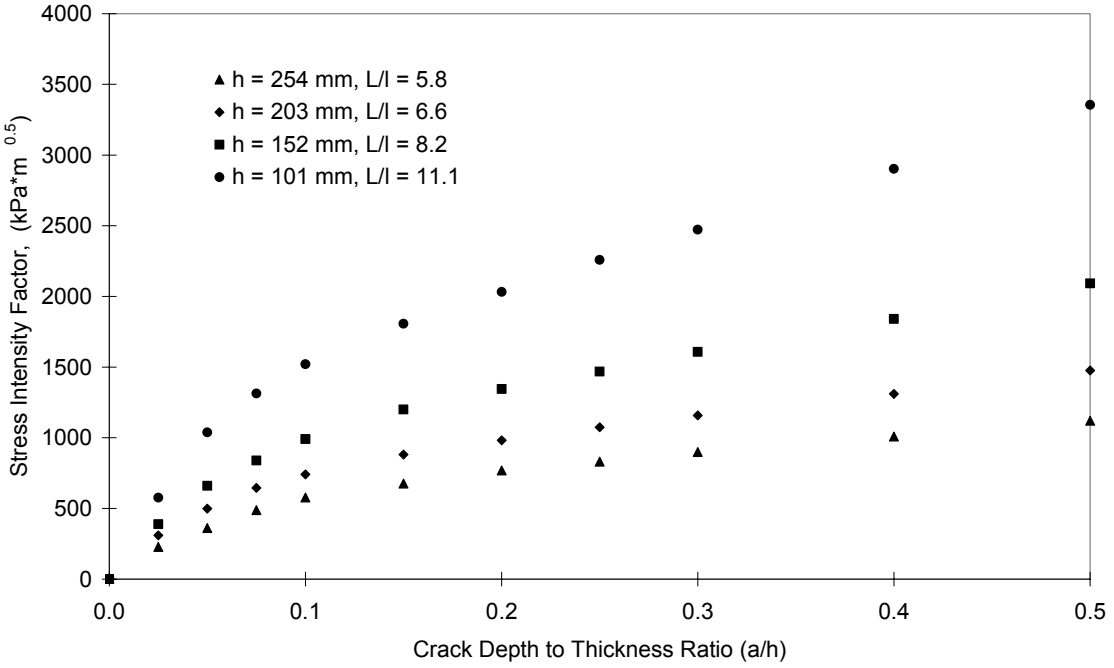

Figure 5-9. Effect of slab thickness and crack depth on stress intensity factor (L = 5.79 m).

Figure 5-10 shows a plot of stress intensity factor versus crack depth to thickness ratio for one thickness (203 mm) and three slab lengths (3.35, 4.57, and 5.79 m). The figure shows that the slab length does not significantly affect the stress intensity factor. This is likely due to the assumption in ILSL97 that the slab was unrestrained from horizontal movements and therefore the normal forces are zero. Another factor is the significantly larger dimension of slab length to the thickness of the slab (L/h > 16).

Because no significant difference was observed between slabs of various lengths, an average of the three lengths was used in the remaining analyses. The average slab length for the Palmdale test slabs was modeled as 4.5 m. The stress intensity factors for the average slab length were determined by sixth order polynomials. The models are shown in Figure 5-11 for various slab thicknesses and are given in Equations 5-11 through 5-14.

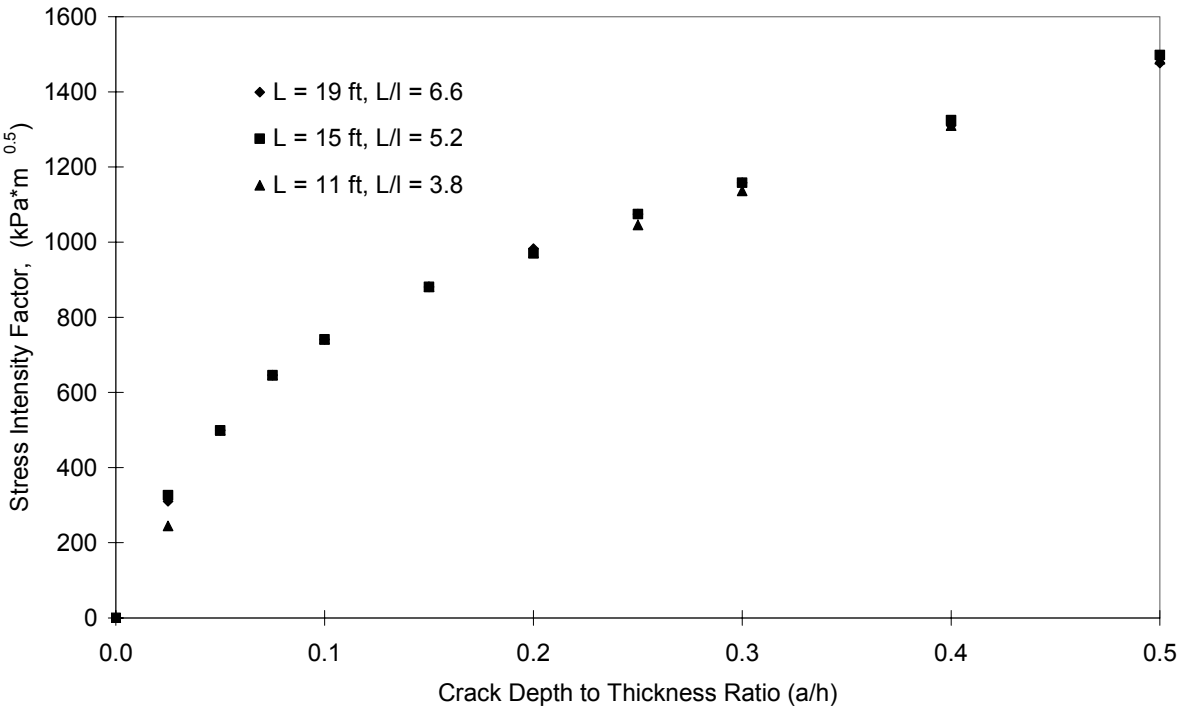

Figure 5-10. Effect of joint spacing and crack depth on stress intensity factor (h = 203 mm).

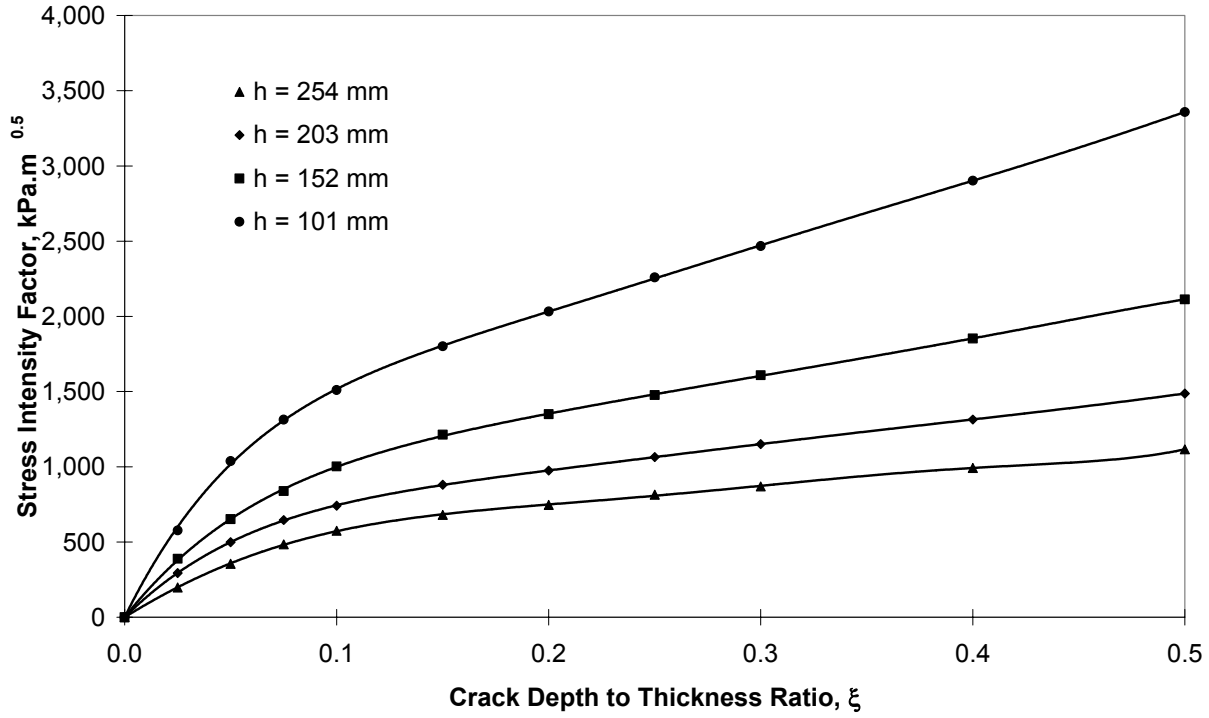

Figure 5-11. Modeling of stress intensity factors for various slab thicknesses using sixth-order polynomials.

$$K_I = -1.304\times10^6\xi^6 + 2.655\times10^6\xi^5 - 2.167\times10^6\xi^4 + 9.084\times10^5\xi^3 - 2.067\times10^5\xi^2 + 2.867\times10^4\xi,\ h = 101\,mm \quad \textbf{(5-11)}$$

$$K_I = -7.566\times10^5\xi^6 + 1.431\times10^6\xi^5 - 1.124\times10^6\xi^4 + 4.754\times10^5\xi^3 - 1.153\times10^5\xi^2 + 1.776\times10^4\xi,\ h = 152\,mm \quad \textbf{(5-12)}$$

$$K_I = -5.349\times10^5\xi^6 + 1.125\times10^6\xi^5 - 9.487\times10^5\xi^4 + 4.123\times10^5\xi^3 - 9.816\times10^4\xi^2 + 1.398\times10^4\xi,\ h = 203\,mm \quad \textbf{(5-13)}$$

$$K_I = 1.103\times10^6\xi^6 - 1.442\times10^6\xi^5 + 6.040\times10^5\xi^4 - 4.433\times10^4\xi^3 - 3.048\times10^4\xi^2 + 8.740\times10^3\xi,\ h = 254\,mm \quad \textbf{(5-14)}$$

The general form of the stress intensity factor can be written as:

$$K_I = \sigma\sqrt{\pi a}f(\xi) \quad \textbf{(5-15)}$$

For a slab of unit width under the action of the bending moment M calculated from Equation 5-8, the stress σ is calculated as:

$$\sigma = \frac{6M}{h^2} \quad \textbf{(5-16)}$$

The calculated stress intensity factors (Equations 5-11 through 5-14) and the stresses calculated from Equation 5-16 are used in Equation 5-15 to develop the geometrical factor, $f(\xi)$. The geometrical factors for all 4 thicknesses turn out to be identical because of the bending only assumption in ILSL97. This would not be the case if normal forces (due to friction, shrinkage, etc.) are assumed non-zero. The geometrical factor is given in Equation 5-17 and shown in Figure 5-12 as a function of crack depth to thickness ratio for all slab thicknesses. This geo-

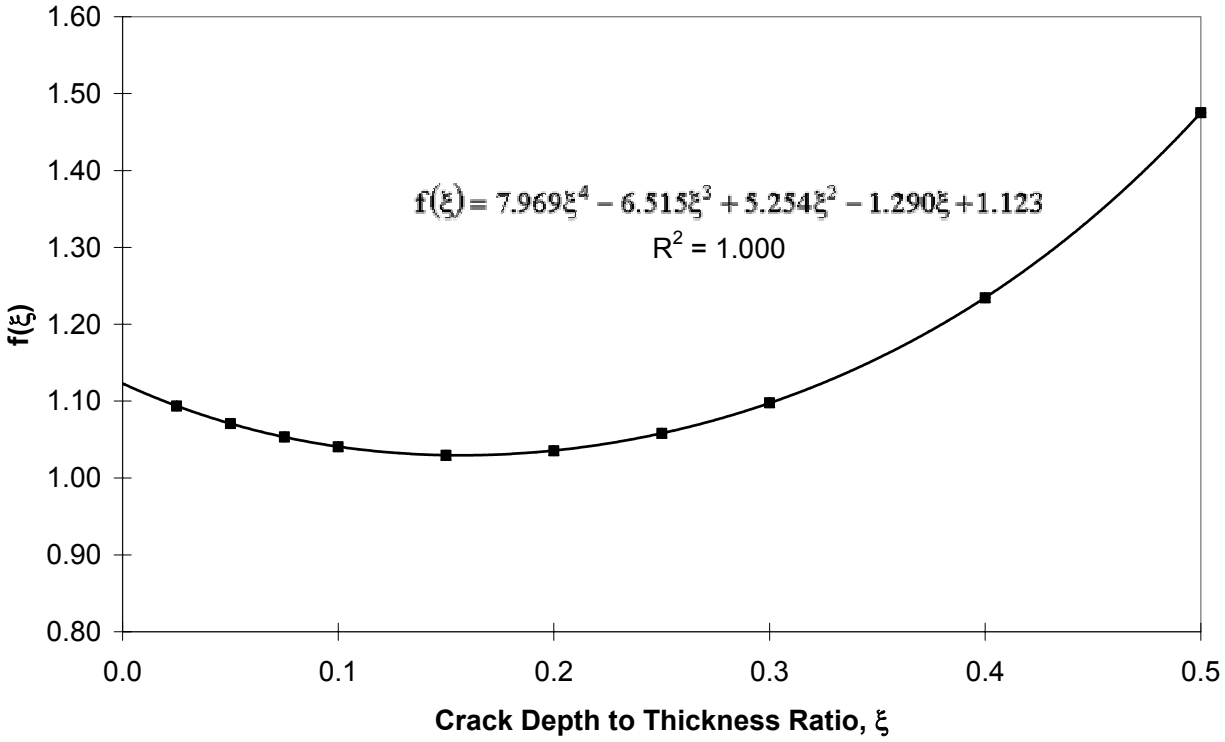

Figure 5-12. Geometric factor as a function of crack depth to thickness ratio.

metrical factor is used in the following steps to determine the reduction in nominal strength of a slab due to the size effect and the existence of an effective crack depth, a_e.

$$f(\xi) = 7.969\xi^4 - 6.515\xi^3 + 5.254\xi^2 - 1.290\xi + 1.123 \qquad \textbf{(5-17)}$$

Bazant and Kazemi (1990) modified the size effect law to incorporate the shape of the structure. The modified size effect law, which could more appropriately be called the size-shape effect law (Bazant and Planas, 1997) is given as:

$$\sigma_N = \frac{K_{If}}{\sqrt{g'(\xi)c_f + g(\xi)h}} \qquad \textbf{(5-18)}$$

where:
K_{If} = critical stress intensity factor for an infinite structure
c_f = length of the fracture process in an infinite structure.

$$g(\xi) = \pi \xi f^2(\xi) \quad \textbf{(5-19)}$$

where:
$g'(\xi)$ = first derivative of $g(\xi)$ with respect to ξ.

$$g'(\xi) = \pi f(\xi)[f(\xi) + 2\xi f'(\xi)] \quad \textbf{(5-20)}$$

The size effect law given in Equation 5-18 is valid only for notched (or cracked) specimen. Bazant (1997) developed the *universal size effect law* to incorporate both notched/cracked and notchless specimen as given in Equation 5-21.

$$\sigma_N = \frac{K_{If}}{\sqrt{g'(\xi)c_f + g(\xi)h}} \left\{ 1 + \left[\left(\bar{\eta} + \frac{4g'(\xi)h}{\langle -g''(\xi) \rangle \kappa c_f} \right) \left(1 + \frac{g(\xi)h}{g'(\xi)c_f} \right) \right]^{-1} \right\} \quad \textbf{(5-21)}$$

where:
κ = 1.4 for notchless specimen and 1.0 for notched or cracked specimen.
$\bar{\eta}$ = 0.5

$\langle -g''(\xi) \rangle$ = $(-g''(\xi))$ for notchless specimen and 0 for notched or cracked specimen

$g''(\xi)$ = second derivative of $g(\xi)$ with respect to ξ.

When $\langle -g''(\xi) \rangle = 0$, the term in the solid square brackets in Equation 5-21 becomes zero, and the equation is reduced to Equation 5-18. The two fracture parameters K_{If} and c_f are independent of specimen size and geometry and are dependent on concrete material used in the slab. Ideally, these parameters should be experimentally determined for the concrete used at Palmdale. However, since this data is not available for the materials used at Palmdale, these

values were estimated using material properties such as compressive strength, water-cement ratio, aggregate type, and maximum aggregate size, as described below.

Several researchers have conducted experiments on laboratory concrete specimens to calculate the above-mentioned fracture parameters. Bazant and Becq-Giraudon (2002) constructed a database of fracture parameters and other material properties from 238 test data from the available literature. They used the database to develop approximate mean prediction formulae for the fracture parameters using 28-day compressive strength, maximum aggregate size, water-cement ratio, and aggregate type (river or crushed) shown in Equation 5-22 and Equation 5-24.

$$G_f = \alpha_0 \left(\frac{f'_c}{0.051} \right)^{0.46} \left(1 + \frac{d_a}{11.27} \right)^{0.22} \left(\frac{w}{c} \right)^{-0.30} \quad \textbf{(5-22)}$$

where:

α_0 = 1.0 for rounded aggregates, 1.44 for crushed or angular aggregates
f_c' = compressive strength of concrete, MPa
d_a = maximum aggregate size, mm
$\left(\frac{w}{c} \right)$ = water/cement ratio.

G_f is the initial fracture energy (N/m) or the energy required to create a unit crack surface as determined by the size effect method (SEM) and is by definition, independent of the structure size as well as geometry (Bazant and Planas, 1997). G_f corresponds to the area under the initial tangent of the stress-separation curve shown in Figure 5-13. G_f can be used to calculate the critical stress intensity factor for an infinite structure using the relation:

$$K_{If} = \sqrt{E' G_f} \quad \textbf{(5-23)}$$

where:

E' = elastic modulus E for plane stress.

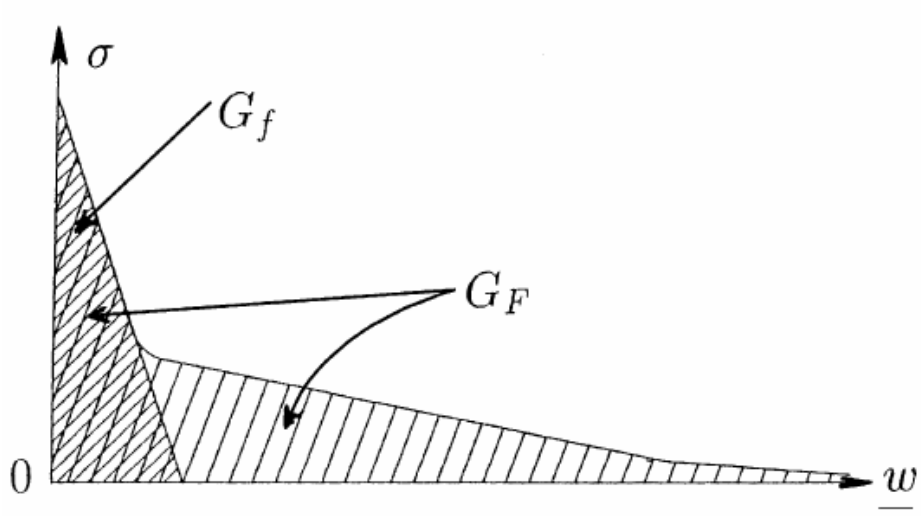

Figure 5-13. Softening stress-separation curve of cohesive crack model and area representing G_f (from Bazant and Becq-Giraudon, 2002).

$$\log_{10} c_f = \gamma_0 \left(\frac{f'_c}{0.022} \right)^{-0.019} \left(1 + \frac{d_a}{15.05} \right)^{0.72} \left(\frac{w}{c} \right)^{0.20} \quad \textbf{(5-24)}$$

where:

γ_0 = 1.0 for rounded aggregates, 1.12 for crushed or angular aggregates.

Using the average values for the Palmdale North and South Tangent test sections as 37.34 MPa for the compressive strength, 25 mm for maximum aggregate size, and 0.44 for the water-cement ratio, the critical stress intensity factor for an infinite structure was calculated as 1,500 $\text{kPa}\sqrt{\text{m}}$ and the length of the fracture process in an infinite structure was calculated as 47 mm. These concrete fracture properties were used in the universal size effect law (Equation 5-21) along with $g(\xi)$ and $g'(\xi)$ from Equations 5-19 and 5-20 to model the effect of size on the nominal strength of uncracked and partially-cracked concrete slabs, as shown in Figure 5-14.

The nominal strength of slabs relative to an uncracked 152-mm slab as a function of thickness for uncracked slabs is shown in Figure 5-15. This figure was used to estimate the size effect on nominal strength of slabs to be used in the fatigue analysis. The nominal strength of

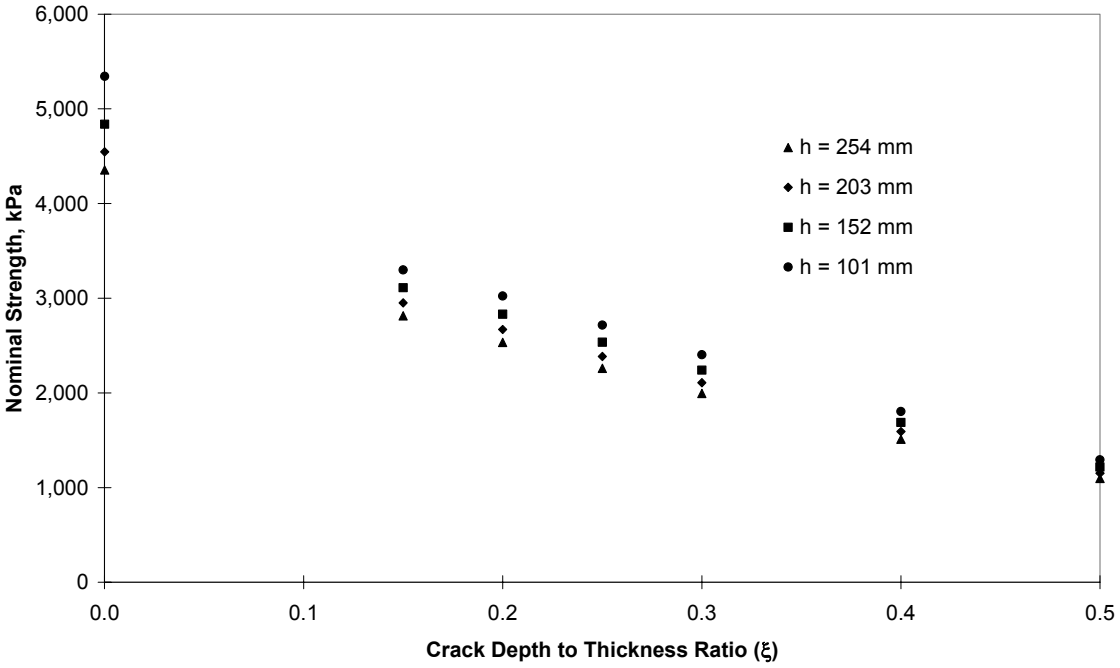

Figure 5-14. Effect of thickness and crack depth on nominal strength for Palmdale concrete using the Universal Size Effect Law.

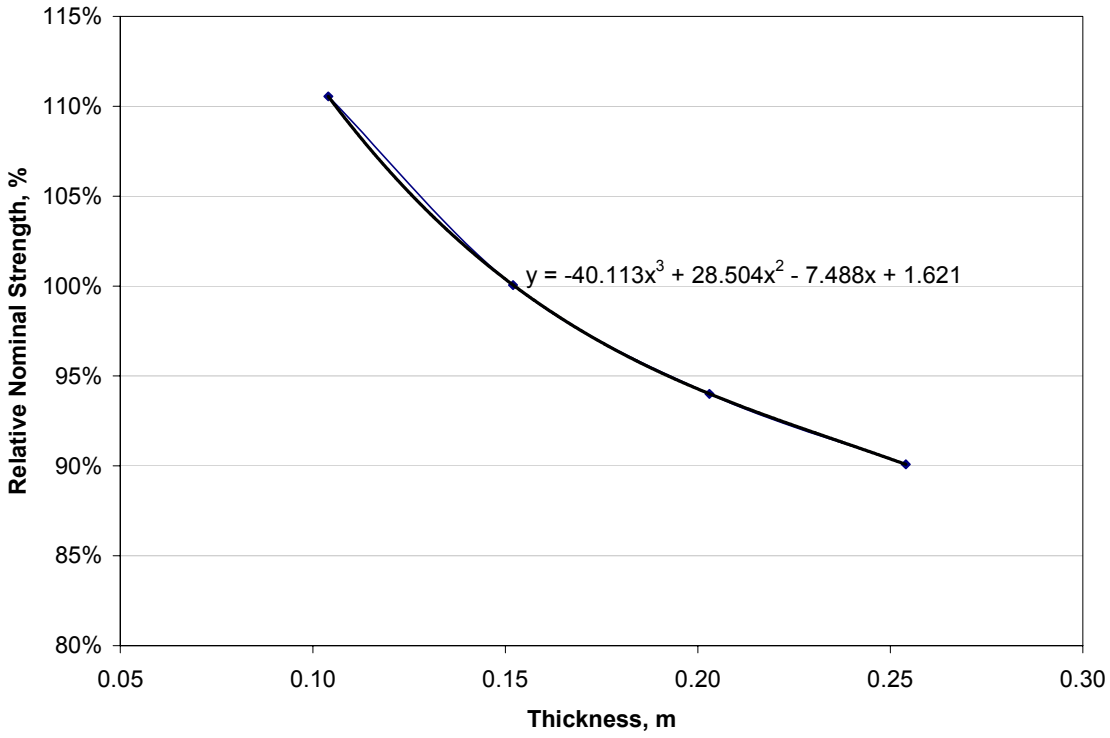

Figure 5-15. Nominal strength of uncracked (notchless) slabs of various thicknesses relative to 152-mm slab strength.

slabs relative to an uncracked 152 mm slab for various slab thicknesses and crack depth to thickness ratios is shown in Figure 5-16. This figure was used to estimate the reduction in slab strength due to early age surface microcracking resulting from restraint stresses for several slab thicknesses. As described earlier, it was assumed that a slab of thickness h with surface microcracking behaves as a slab with an initial surface crack depth, a_e.

5.4 Size Effect Analysis for Palmdale Slabs

The thickness of a pavement slab affects its nominal strength as shown in Figure 5-15. This figure was used to scale the strength of the Palmdale slabs to account for the difference in thickness between slabs from one test section to another. Table 5-1 shows the nominal strength of the Palmdale test slabs as a percent of 152-mm slab strength. The nominal strength of the 152-mm slab was assumed as 100 percent since the 4-point bending tests for estimating the flexural

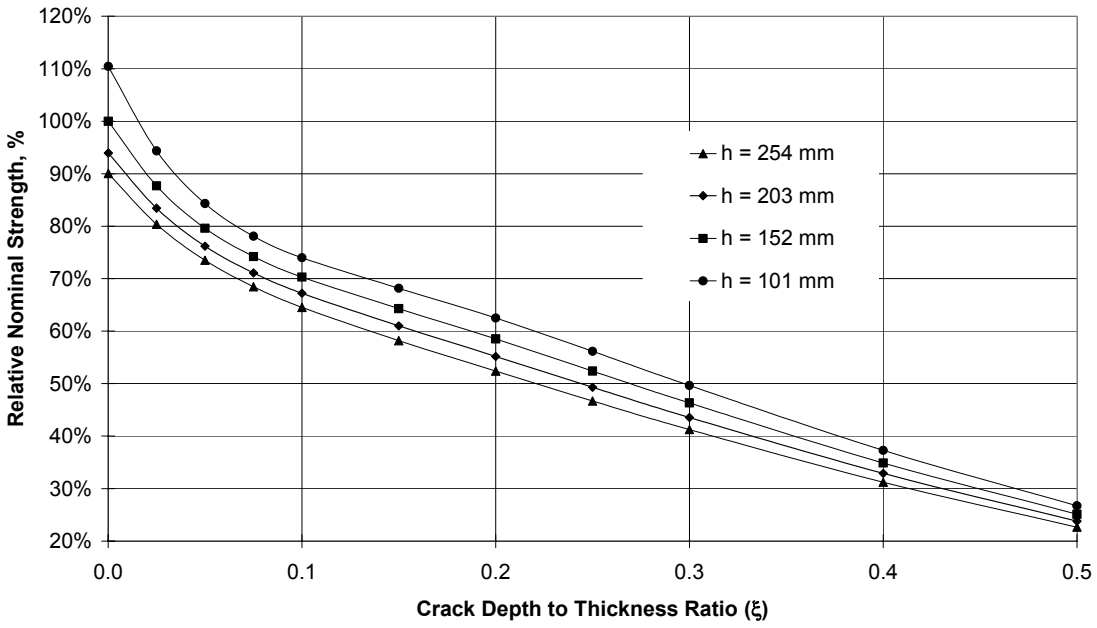

Figure 5-16. Nominal strength of slabs of various thicknesses and crack depths relative to 152-mm slab strength.

Table 5-1 Effect of Thickness on Nominal Strength of Uncracked (Notchless Slabs for the Palmdale Test Sections

Section Location and Base Type	Section ID	Actual Slab Thickness, mm	Relative Nominal Strength, percent
South Tangent	519FD	94	113.6
	520FD	109	109.2
	523FD	171	97.3
	524FD	165	98.1
	525FD	175	96.9
	526FD	185	95.7
	527FD	170	97.5
	528FD	195	94.7
	530FD	220	92.6
	531FD	204	93.9
North Tangent	532FD	225	92.2
	533FD	220	92.6
	534FD	228	92.0
	535FD	220	92.6
	537FD	213	93.2
	538FD	221	92.5
	539FD	203	94.0
	540FD	223	92.4
	541FD	244	90.9

strength of the slabs were performed on 152-mm specimens. This flexural strength had been used to develop the fatigue damage models in Chapter 4. Assuming that the concrete fracture properties for an infinite specimen correctly describes failure for both the beam and slab geometric conditions, the same reduction factors can be applied to the beam strength as well as the slab strength.

The coefficients of the model developed in Section 4.6.1 were re-calibrated to account for the difference in strength between sections due to the size effect. The same steps (1 through 13)

described in Section 4.6.1 were followed with the exception that for each test section, the strengths used to develop the models in Section 4.6.1 were multiplied by the relative nominal strength percentage shown in Table 5-1. For the development of these models, the *effective initial crack depth* was assumed zero. A model combining both size effect and *effective initial crack depth* is developed in Section 5.5. The resulting models accounting for the slab size effect are given as:

$$\log N = \frac{1 - (0.414\,\overline{SR_B} + 0.091 \log T)}{0.155(1 - 0.304\,R)}, \text{ using linear } EBITD \qquad \textbf{(5-25)}$$

$$\log N = \frac{1 - (0.225\,\overline{SR'_B} + 0.083 \log T)}{0.165(1 - 0.335\,R)}, \text{ using bilinear } EBITD \qquad \textbf{(5-26)}$$

where:

$\overline{SR_B}$, $\overline{SR'_B}$ = Stress ratio: ratio of peak stress to size-dependent beam flexural strength using linear and bilinear *EBITD*, respectively.

The computed cumulative damage until the appearance of the first crack at the two peak stress locations for the Palmdale test sections is shown in Figure 5-17.

The root mean square error for the two models shown in Equations 5-25 and 5-26 are 0.85 and 0.87 (log scale), respectively. The two models have almost very similar coefficients as the models developed earlier in Section 4.5.2 and have roughly the same root mean square error. The size effect for the Palmdale sections was not a significant contributing factor because of the slab thicknesses used. All of the slabs at Palmdale were relatively thin slabs. As shown in Figure 5-3, the effect of specimen size on the nominal strength of the structure is a logarithmic function of slab thickness. The size effect on slab strength would be a more significant factor if the slab thicknesses tested had a larger range.

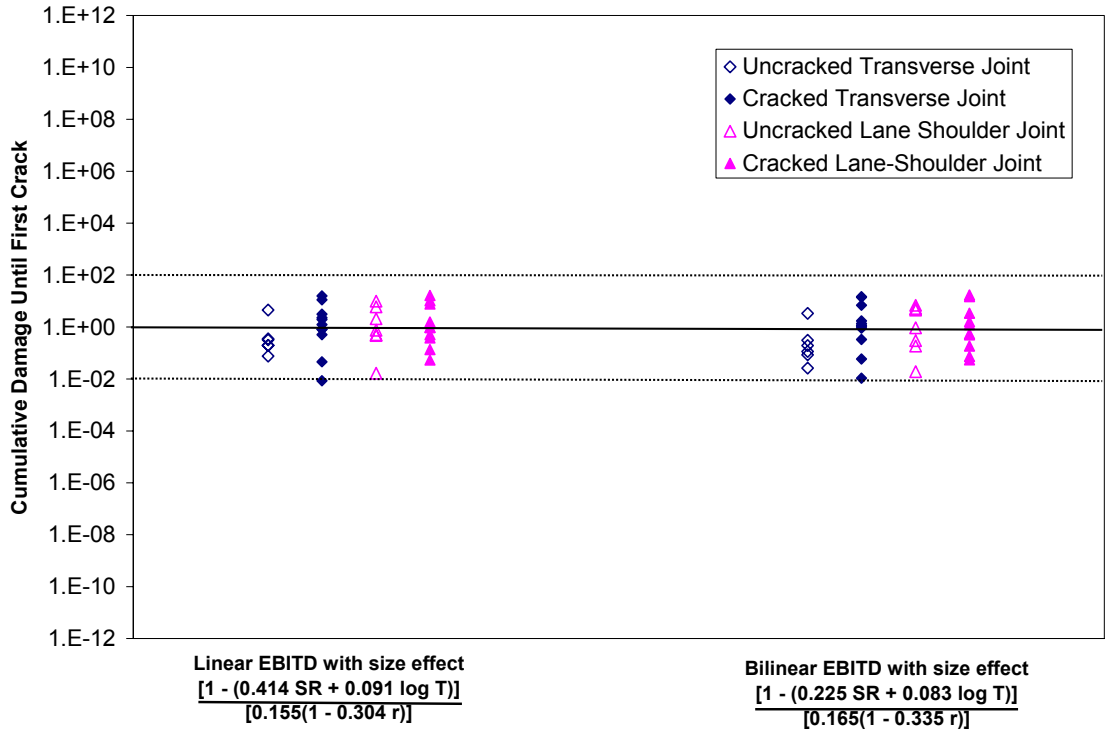

Figure 5-17. Calculated cumulative damage to first field-observed crack for Palmdale test sections incorporating effect of thickness on concrete strength.

Assuming the ratio of slab strength to beam strength as 2.0, Equations 5-25 and 5-26 can be rewritten to incorporate slab strength as follows:

$$\log N = \frac{1-(0.828\,\overline{SR_S}+0.091\log T)}{0.155(1-0.304\,R)}, \text{ using linear } \textit{EBITD} \qquad \textbf{(5-27)}$$

$$\log N = \frac{1-(0.450\,\overline{SR'_S}+0.083\log T)}{0.165(1-0.335\,R)}, \text{ using bilinear } \textit{EBITD} \qquad \textbf{(5-28)}$$

where:

$\overline{SR_S}$, $\overline{SR'_S}$ = Stress ratio: ratio of peak stress to size-dependent slab flexural strength using linear and bilinear *EBITD*, respectively.

5.5 Early Age Surface Microcracking Analysis for Palmdale Slabs

The reduction in strength of concrete slabs due to surface microcracking is modeled as a crack of depth a_e, that is, the *effective initial crack depth*. The result of this initial crack is a reduction in nominal strength of the slab. A consequence of the reduction in nominal strength of the slab is a decrease in load carrying capacity of the slab. For the Palmdale slabs, this reduction was a factor contributing to the higher variability in performance. While some slabs gained adequate strength before significant restraint stresses developed, resulting in only a small amount of surface microcracking and thus a lower *effective initial crack depth*, other slabs developed significant restraint stresses at early age from load transfer with adjacent slab/shoulder and weight of the slab, which caused a greater amount of surface microcracking and thus a greater *effective initial crack depth*. The higher shrinkage concrete used at Palmdale likely compounded the variability. The development of shrinkage strains are significantly affected by ambient conditions such as air temperature, relative humidity, wind speed, etc., as described in Chapter 3. Because of these factors, different slabs would have been at different points in their strength development when shrinkage stresses reached critical levels, resulting in variability in the extents and locations of surface microcracking.

Note that this *effective initial crack depth* represents only the critical stress location and represents the reduction in strength of the slab due to restraint stresses at these locations. Other locations on the test slab can be expected to have different *effective initial crack depth* due to different restraint stresses at early age.

Sections 530FD, 533FD and 534FD performed considerably better than other sections and lasted significantly longer than the cumulative damage model developed in Equations 5-25 and 5-26 suggest. These sections were assumed to have a small *effective initial crack depth* of 10 to 15 mm. This assumption was made on the following basis: the average-performing sections

(section with cumulative damage of 1.0) could not be assumed to have zero *effective initial crack depth* because then the sections performing better than the average section would essentially have a negative *effective initial crack depth.* Since this is not possible, the best performing sections were assumed to have the smallest *effective initial crack depth*. This assumption is consistent with work completed by Grasley (2003) who found that surface microcracking occurs on concrete to relieve the high calculated shrinkage stresses due to the nonlinear moisture gradient. The depth of the surface microcracking was found to be on the order of 10 mm, which means that even good performing sections had some level of initial cracking.

This step shifts the fatigue damage function such that an intact slab, with no initial cracking, fails at a damage of 1.0 using the unreduced strength. All slabs with non-zero initial cracking are assumed to fail earlier than cumulative damage of 1.0 if unreduced strength is used, and fail at a cumulative damage of 1.0 if reduced strength is used to account for the *effective initial crack depth.* The values of 10 to 15 mm were chosen based on the fact that even the best performing sections would have some amount of initial damage. For slabs with low shrinkage characteristics that do not curl significantly and remain supported on the base during early-age strength development, this value can approach zero.

The first step in the development of a new model to account for restraints and initial cracking was to estimate the *effective initial crack depth* for the Palmdale slabs. The strengths for Sections 530FD, 533FD and 534FD were reduced using Figure 5-16 and assuming an *effective initial crack depth* of 10 to 15 mm. The coefficient A, for the bilinear model (Equation 5-26), was re-calculated using this reduced strength, following the steps outlined in Section 4.6.1. As described earlier, this process shifts the damage equation such that a slab with unreduced strength fails when cumulative damage equals 1.0. Using this shifted model, the reduced strength

for each section was back-calculated, such that using it in the stress ratio computation, would result in cumulative damage of 1.0 at failure for that particular critical location, if cracking was observed at that location. If no cracking was observed at the critical location, the calculation was still performed, but the calculated value was assumed to be a lower limit for the reduced strength, suggesting the actual nominal strength is greater than the calculated value, which is why the location did not crack.

The reduced strength values estimated for transverse edge and lane-shoulder edge critical locations were used in Figure 5-16 to back-calculate the *effective initial crack depth* for that critical location. The results are shown in Table 5-2 and 5-3 for the transverse joint critical stress locations and in for the lane-shoulder edge critical stress location, respectively. The

Table 5-2 Back-calculated *Effective Initial Crack Depth* at Transverse Joint Locations for Palmdale Test Sections

Section Location and Base Type	Section	Load Transfer Devices	Shoulder Type	Nominal Design Thickness, mm	Cracked?	*Effective initial crack depth, a_e,* mm	*Nominal effective initial crack depth, a_e,* mm
South Tangent: 150mm aggregate base	519FD	None	AC	100	Yes	33	35
	520FD				Yes	43	
	523FD	None	AC	150	Yes	41	40
	524FD				Yes	43	
	525FD				Yes	67*	
	526FD				Yes	78*	
	527FD				Yes	27	
	528FD	None	AC	200	No	<72	60
	530FD				Yes	11*	
	531FD				Yes	57	
North Tangent: 100mm cement-treated base over 150mm aggregate subbase	532FD	None	AC	200	Yes	63	60
	533FD				No	<44*	
	534FD				Yes	16*	
	535FD				Yes	61	
	537FD	Dowel bars	Tied concrete	200	No	<126	85
	538FD				No	<93	
	539FD	Dowel bars	600 mm widened lane with AC	200	No	<95	85
	540FD				Yes	89	
	541FD				No	<131	

*Exceptions to the nominal effective initial crack depth due to higher or lower stresses during early age.

Table 5-3 Back-calculated *Effective Initial Crack Depth* at Lane-Shoulder Joint Locations for Palmdale Test Sections

Section Location and Base Type	Section	Load Transfer Devices	Shoulder Type	Nominal Design Thickness, mm	Cracked?	*Effective initial crack depth, a_e,* mm	*Nominal effective initial crack depth, a_e,* mm
South Tangent: 150mm aggregate base	519FD	None	AC	100	N	<31	25
	520FD				N	<39	
	523FD	None	AC	150	Y	34	30
	524FD				N	<31	
	525FD				Y	65*	
	526FD				N	<74*	
	527FD				N	<27*	
	528FD	None	AC	200	Y	64	60
	530FD				Y	11*	
	531FD				Y	55	
North Tangent: 100mm cement-treated base over 150mm aggregate subbase	532FD	None	AC	200	Y	59	60
	533FD				N	<35*	
	534FD				Y	16*	
	535FD				N	<61	
	537FD	Dowel bars	Tied concrete	200	Y	111*	85
	538FD				N	<86	
	539FD	Dowel bars	600 mm widened lane with AC	200	Y	89	85
	540FD				Y	83	
	541FD				N	<114	

*Exceptions to the nominal *effective initial crack depth* due to higher or lower stresses during early age.

estimated *effective initial crack depth*s for critical locations with cracks are shown in the tables. Also shown are the upper limits of *effective initial crack depths* for critical locations that did not exhibit cracking.

For each of the six pavement types tested at Palmdale (100 mm, 150 mm, and 200 mm with aggregate base; 200 mm with cement-treated base; 200 mm with cement-treated base. dowel bars, and tied PCC shoulders; and 200 mm with cement-treated base, dowel bars, and widened lanes) a *nominal effective initial crack depth* was calculated by taking an average (resolution of 5 mm) of *effective initial crack depths* for that design feature and ignoring the extreme values. This was done solely for the purposes of incorporating restraints due to these design features into a new fatigue model, and to ignore the extreme variability that can occur due

to compounding factors such as ambient condition variability, material variability, thickness variability, shrinkage variability, restraint variability, etc.

As expected, the slabs with the highest restraint, thicker slabs, and sections with dowel bars had higher *nominal effective initial crack depth*. Some sections had exceptionally high or low *effective initial crack depth* as compared to the *nominal effective initial crack depth*. This was likely due to differences in time of restraint stress development during early age relative to the strength gain of the concrete and to compounding effects of the many sources of variability listed above.

The coefficients for the bilinear fatigue model was redeveloped following Steps 1 through 13 in Section 4.6.1, but using reduced strength from Figure 5-16 and based on *nominal effective initial crack depth* for that test section. Since the model was developed using the strength reduction chart shown in Figure 5-16 which incorporates size effect, the fatigue model shown in Equation 5-29 encompasses both size effect and initial cracking.

$$\log N = \frac{1 - (0.125\,SR''_B + 0.083\log T)}{0.165(1 - 0.335\,R)}\text{, using bilinear } \textit{EBITD} \qquad \textbf{(5-29)}$$

where:

SR_B'' = Stress ratio: ratio of peak stress to size-dependent beam flexural strength reduced to account for initial cracking due to shrinkage restraints.

The computed cumulative damage at the two peak stress locations until the appearance of the first crack for the Palmdale test sections after incorporating the strength reduction due to early age surface microcracking is shown in Figure 5-18.

Figure 5-18 is shown using a range of 10^{-12} to 10^{12}, in order to compare it with other such figures throughout this research. Dashed horizontal lines are shown at damages of 0.01 and 100 for visual reference. All data points on the transverse joint edge and the lane shoulder edge for which *EBITD* values were back-calculated (Talbe 3-7) are included in the analysis. Figure 5-18

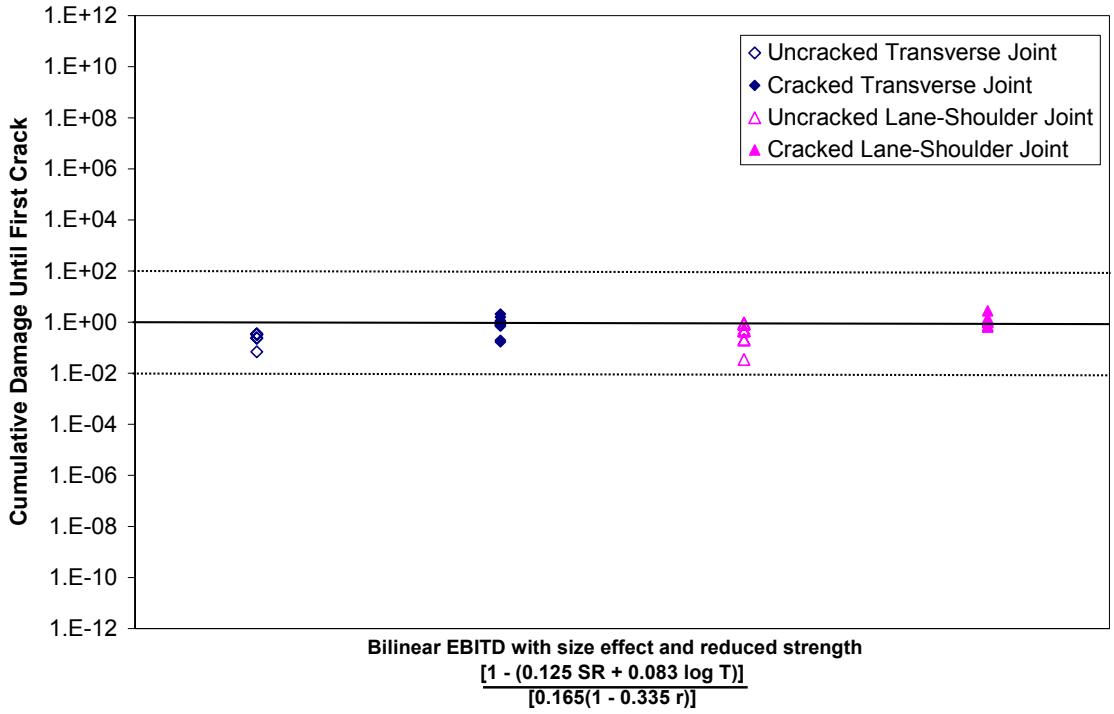

Figure 5-18. Calculated cumulative damage to first field-observed crack for Palmdale test sections incorporating effect of thickness and early-age surface microcracking on concrete strength.

is repeated in Figure 5-19 for a range of 0.01 to 100. As expected, the uncracked locations have cumulative damage less than 1.0 and the cracked locations have cumulative damage of 1.0. The root mean square error using the cracked slabs is reduced to 0.41 (on log scale), suggesting an improvement of the fatigue model by incorporating initial cracking resulting from early-age restraints.

5.6 Summary of Size Effect and Initial Slab Surface Microcracking

The pavement sections at Palmdale were constructed of concrete that was susceptible to high early age shrinkage. The ambient conditions during paving contributed to high differential shrinkage at early ages when the concrete was gaining strength. Restraints from adjacent slabs

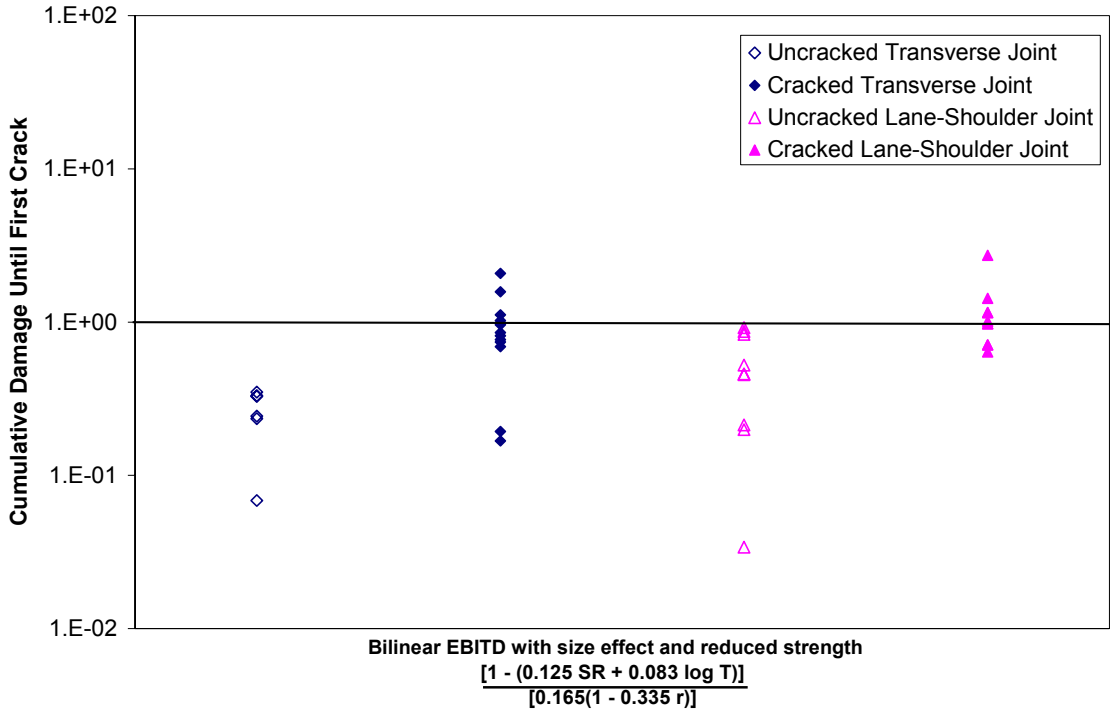

Figure 5-19. Calculated cumulative damage to first field-observed crack for Palmdale test sections incorporating effect of thickness and early-age surface microcracking on concrete strength.

and the test slab's self-weight resulted in excessive stresses at the surface of the slab before adequate concrete strength gain was achieved. These shrinkage stresses resulted in microcracking at the surface, which caused a reduction in the flexural capacity of the slab.

A procedure to model the early-age surface microcracking due to restraint stresses based on fracture mechanics principles was developed in this Chapter. A parameter, the *effective initial crack depth,* was introduced to model the strength loss due to early age surface microcracking. This parameter can vary from one slab to another depending on how the restraint stresses in the slab developed during concrete strength gain. However, an overall trend of slabs with higher restraint (thicker slabs and sections with load transfer devices) showed higher *effective initial crack depth*. Because of the extreme conditions at Palmdale and the excessive shrinkage

characteristics of the concrete, the *effective initial crack depth* was an important parameter affecting the performance of the slabs. This may not be the case for all concrete pavement sections but the resultant fatigue algorithm from this analysis can be utilized in initially cracked or uncracked slabs.

If concrete with lower shrinkage is used, and if adequate curing is provided then the *effective initial crack depth* would be negligible and would not be a crucial factor in pavement performance. Since the model was developed using mechanistic-empirical principles of stresses and damage, it could still be used in these cases (zero initial crack depth) as long as the all the stresses (load and nonlinear temperature) and strength variations are taken into consideration. The model shown in Equation 5-29 is the first and only procedure to incorporate the following in pavement fatigue modeling:

1. Stress ranges and time period of applied repeated loading.
2. Effect of size (thickness) on concrete slab strength.
3. Slab surface microcracking due to early-age restrained shrinkage.

The limitations of using the fatigue algorithm are:

1. The models do not address some of the other limitations of using Miner's hypothesis and cumulative damage such as rest periods, endurance limit, variable amplitude, stress history, etc.
2. The models were developed using a small data set from field-tested sections at one location (Palmdale, CA).
3. The models are more computationally intensive than other fatigue models because they require determination of both peak stresses and stress ranges at critical locations

on both lane-shoulder edges and transverse edges. They also require the development of strength reduction curves and estimation of *effective initial crack depth.*

4. The procedure developed is only a first step in incorporating the principles of fracture mechanics to cracking in field pavement slabs. With a constant furthering of the state-of-the-art in the field of fracture mechanics, particularly as it relates to slabs on grade, this procedure will need to be updated.

The assumptions based upon which the models were developed are listed below:

1. All plate theory assumptions and assumptions pertaining to the use of finite element analysis for concrete pavements listed in Section 1.5.
2. For a given pavement structure, geometry, and layer properties, and thermo-mechanical loading, slab stresses can be reasonably predicted using the finite element analysis program, ISLAB2000.
3. All layer thicknesses and material properties, particularly flexural strengths, for a given slab, are uniform and do not deviate significantly from the average values used.
4. The *EBITD* values calculated in Chapter 3 for all test sections are reasonably accurate. For test sections with *EBITD* calculated at only one corner of the slab, it is assumed that the calculated value represents the greater of the two corner *EBITDs*.
5. Superposition of *EBITD* and measured temperature difference is valid.
6. Support beneath the slab is uniform.
7. Cracking in the slabs at the test sections were instantaneous and were observed as soon as they occurred.

8. Miner's hypothesis and the cumulative damage approach are valid for modeling concrete fatigue damage.
9. The transverse edge and the lane-shoulder edge are assumed to crack and fail independently and the cracking/failure of one edge is assumed not to affect stresses or damage at the other edge.
10. Location of maximum surface damage due to early-age restraint coincides with (or is close to) the location of peak critical stresses.
11. The reduction in strength due to early-age microcracking can be represented as an effective initial crack on the surface of the slab.
12. The Universal Size Effect Law is valid and accurately predicts nominal strength as a function of fracture parameters and the slab's geometry factor.

6.0 CONCLUSIONS

Curling is an important phenomenon that significantly affects the load carrying capacity and fatigue life of a concrete pavement. Several components contribute to the total amount of curling. While curling caused by temperature gradients through the depth of the slab fluctuates intraday, the remaining components are relatively stable through the life of the pavement. The cumulative effect of these nonlinear components — built-in temperature gradient, drying shrinkage gradient, moisture gradient, and creep — can be defined as an effective built-in temperature difference, *EBITD*. The *EBITD* is a linear temperature difference between the top and bottom of a concrete slab that produces the same deflection response as the cumulative effects of nonlinear built-in temperature gradient, nonlinear moisture gradient (reversible), and nonlinear shrinkage gradient, reduced over time by creep.

Traditional methods of back-calculating *EBITD* of in-service pavements using unloaded slab deflections have been cumbersome and involve instrumentation and measurement of movement of individual slabs over a 24-hour period. Another drawback is that the traditional methods of back-calculating built-in curl cannot be used for slabs with high negative built-in curl, because the slab corners never come into full contact with the base. To overcome these drawbacks, a procedure to back-calculate built-in curl based on loaded slab deflections was developed. The load can be either traffic loading, such as using an HVS, or simulated loading, such as using an HWD or an FWD. The advantage of using an HWD or an FWD is that a large number of slabs can be tested over a relatively short period of time without any embedded instrumentation, making it an efficient and cost-effective procedure to back-calculate *EBITD* of in-service pavements.

The results of back-calculating *EBITD* using loaded slab deflection analysis indicated that:

- The slabs tested at Palmdale had high *EBITD* values (–20ºC to –35ºC) for sections with low restraint (undoweled Sections 519FD through 535FD) and low to moderate *EBITD* values (0ºC to –20ºC) for sections with higher restraint (doweled Sections 537FD through 541FD). The restraints due to load transfer devices such as dowel bars appear to restrict the upward curl of the slabs during early age, likely through tensile creep mechanisms, resulting in lower *EBITD* for doweled slabs. The high amount of *EBITD* measured for the Palmdale test slabs was due to the fact that they were constructed of fast-setting high-early-strength concrete with superplasticizer and approximately 400 kg per cubic meter of high shrinkage cement. The fact that the slabs were paved during daytime and in desert conditions with low ambient humidity and high wind speed also contributed to the high *EBITD*.
- The slab's self-weight also acts as a restraint to the curling of the slab. Thinner slabs typically had higher magnitude *EBITD* as compared to thicker slabs. However, a reduction in magnitude of *EBITD* was seen for very thin slabs (less than 100 mm). This can be explained by the fact that the most significant component of *EBITD* is the differential drying shrinkage between the top 50 mm of the slab and the bottom of the slab. As slabs get closer to 50 mm in thickness, the differential drying shrinkage is reduced, resulting in lower *EBITD* contribution from differential drying shrinkage.
- The presence or absence of the cement-treated base course did not seem to be a factor affecting the curling of the slabs. However, if the concrete layer was bonded to the base layer, the type of base might have affected *EBITD*.

- On all sections, the corners of the slab had a higher magnitude *EBITD* compared with the mid-slab edge.
- The doweled sections had more uniform restraint at the joints resulting in similar *EBITD* for both sides of the slabs. The slabs with undoweled joints may or may not have an asymmetric curvature because the *EBITD* depends on the aggregate interlock restraint between adjacent slabs, which could vary from one joint to another.
- The dependence of *EBITD* on aggregate interlock restraint can result in *EBITD* values that vary from slab to slab.

The most significant effect of slab curling is its affect on slab stresses and load-carrying capacity. Several procedures have been developed to model the fatigue damage due to repeated load application. Miner's hypothesis for accumulation of damage and applicability of several concrete fatigue transfer functions was tested against the full-scale results from HVS testing. Peak tensile stresses at critical locations were used to calculate cumulative damage with various fatigue models. The results of the damage accumulation analysis showed that Miner's approach cannot be used to predict the timing or number of load repetitions corresponding to slab cracking with any level of accuracy. This was found for full-scale fatigue testing with a fixed load and varying temperature, and for varying load and temperature. The existing fatigue models tested were based on a given set of data, stress calculations, and failure definitions, and could not be extrapolated accurately to another loading condition without a "calibration" phase.

Another drawback is that using peak stresses to calculate cumulative damage may result in discrepancies between predicted locations of maximum damage and observed locations of cracking, particularly for slabs with high magnitude of *EBITD*. Also, only two existing fatigue

models incorporate both load and curling stresses. None of the existing fatigue algorithms or design procedures has been calibrated for longitudinal cracking and corner breaks, or for slabs with high negative built-in curl.

In order to overcome some of the shortcomings of existing procedures, a linear model and a bilinear model that incorporates stress range and loading rate along with peak stresses was developed. The linear model assumes *EBITD* decreases linearly from the top of the slab to the bottom of the slab. The bilinear model assumes *EBITD* decrease linearly from the top of the slab to the middle of the slab, and is zero from the middle of the slab to the bottom of the slab. The models were calibrated for transverse cracking, longitudinal cracking, and corner breaks, and because of the inclusion of stress range, can also be used for slabs that exhibit high negative built-in curl. These models have better fit to the Palmdale data than existing fatigue models and are more evenly distributed about the expected mean fatigue damage of 1.0. Reasonable correspondence was observed between predicted crack locations and observed crack locations on most of the test sections.

In existing fatigue damage accumulation procedures, the initial damage in the slab is assumed zero for new construction. However, tensile stresses due to restraints from slab weight, slab-base friction, and load transfer devices, can result in microcracking and reduction in strength of a slab, particularly for slabs made of concrete with high early-age shrinkage. Also, in existing fatigue models, slabs of all thicknesses are assumed to have equivalent flexural strength. However, fracture mechanics principles suggest that the nominal strength of concrete decreases with increase in size.

A procedure to model size effect and the early-age surface microcracking due to restraint stresses based on nonlinear fracture mechanics was developed in this research. A parameter, the

effective initial crack depth was introduced to model the strength loss due to early age surface microcracking. This parameter can vary from one slab to another depending on how the restraint stresses in the slab developed during concrete strength gain. However, an overall trend of slabs with higher restraint (thicker slabs and sections with load transfer devices) showed higher *effective initial crack depth*. Because of the extreme conditions at Palmdale and the excessive shrinkage characteristics of the concrete, the *effective initial crack depth* was an important parameter affecting the performance of the slabs.

7.0 SUGGESTIONS FOR FUTURE RESEARCH

Several new concepts were introduced in this research including:

1. Measurement of *EBITD* using falling weight deflectometer and in general, loaded slab deflections.
2. Fatigue model incorporating linear and bilinear *EBITD*, stress range, and loading rate, along with peak stresses.
3. *Effective Initial Crack Depth* as a measure of early-age surface microcracking due to restraint stresses and effect of slab thickness on strength.

All of these hypotheses and their applicability to a wide range of pavements and conditions need to be tested and evaluated. The principles used in this research can be used to improve upon them and develop useful analytical tools to better model fatigue cracking failure in rigid pavements. Research also needs to be done in measuring and predicting *EBITD* for a wide range of factors (material properties, climate conditions, geographical location, restraints, etc.) for use in mechanistic-empirical based design procedures. Finally, fracture mechanics principles offer a more powerful substitute to Miner's hypothesis for cumulative damage analysis and must be further researched to eliminate many of the limitations of this fatigue damage design tool.

REFERENCES

Aas-Jacobsen, K. *Fatigue of Concrete Beams and Columns.* Bulletin No. 70-1, NTH Institutt for Betonkonstruksjoner, Trondheim, 1970.

Abrams, M. S. and Orals, D. L. Concrete Drying Methods and Their Effect of Fire Resistance. *Moisture in Materilas in Relation to Fire Tests*, American Society for Testing and Materials, STP 385, ASTM, West Conshocken, PA, 1965, pp. 52–73.

Al-Nasra, M. and Wang, L. R. Parametric Study of Slab-on-Grade Problems Due to Initial Warping and Point Loads. *ACI Structural Journal*, Vol. 91, No. 2. 1994, pp. 198–210.

Altoubat, S. and Lange, D. *Early thermal changes*. Report of RILEM Technical Committee 181-EAS, edited by A. Bentur, (RILEM Publications, France), Vol. 1, 1995.

Altoubat, S. A. and Lange, D. A. Creep, Shrinkage, and Cracking of Restrained Concrete at Early Age. *ACI Materials Journal*, Vol. 98, No. 4, 2001, pp. 323–331.

Anderson, T. L. *Fracture Mechanics: Fundamentals and Applications*. CRC Press, Boca Raton, FL, 1991.

Armaghani, J. M., Larsen, T. J., and Smith, L. L. Temperature Response of Concrete Pavements. In *Transportation Research Record No. 1121,* TRB, National Research Council, Washington, D.C., 1986, pp. 23–33.

Babaei, K. and Purvis, R. L. Premature Cracking of Concrete Bridge Decks: Cause and Methods of Prevention. *Proceedings, 4th International Bridge Engineering Conference*, 1996.

Barenberg, E. J. and Thompson, M. R. *Calibrated Mechanistic Design Procedure for Pavements, Phase 2 NCHRP 1-26.* National Cooperative Highway Research Program/Transportation Research Board, National Research Council, Washington, D.C., 1992.

Baroughel-Bouny, V. Texture and Moisture Properties of Ordinary and High-Performance Cementitious Materials. *Proceedings of Seminaire RILEM 'Benton: du Materiau a la Structure.'* Arles, France, 1996.

Bazant, Z. P. Size Effect in Blunt Fracture: Concrete, Rock, Metal. *Journal of Engineering Mechanics*, ASCE, Vol. 104, 1984, pp. 518–535.

Bazant, Z. P. Scaling of Quasibrittle Fracture: Asymptotic Analysis. *International Journal of Fracture*, Vol. 83, 1997, pp. 19–40.

Bazant, Z. P. and Becq-Giraudon, E. Statistical Prediction of Fracture Parameters of Concrete and Implications for Choice of Testing Standard. *Cement and Concrete Research*, Vol. 32, 2002, pp. 529–556.

Bazant, Z. P. and Kazemi, M. T. Determination of fracture energy, process zone length and brittleness number from size effect, with application to rock and concrete. *International Journal of Fracture*, Vol. 44, pp. 111–131.

Bazant, Z. P. and Planas, J. *Fracture and Size Effect in Concrete and Other Quasibrittle Materials*, CRC Press, Boca Raton, FL, 1997.

Beckemeyer, C. A., Khazanovich, L., and Yu, H. T. Determining Amount of Built-in Curling in Jointed Plain Concrete Pavement: Case Study of Pennsylvania I-80. In *Journal of Transportation Research Board, Vol. 1809*, TRB, National Research Council, Washington, D.C., 2002, pp. 85–92.

Bissonnette, B. and Pigeon, M. Tensile Creep at Early Ages of Ordinary, Silica Fume, and Fiber Reinforced Concretes. *Cement and Concrete Research*, Vol. 25, No. 5, 1995, pp. 1075–1085.

Bissonnette, B., Pierre, P., and Pigeon, M. Influence of Key Parameters on Drying Shrinkage of Cementitious Materials. *Cement and Concrete Research*, Vol. 29, 1999, pp. 1655–1662.

Blanks, R. F. and McNamara, C. C. Mass Concrete Tests in Large Cylinders. *Journal of the American Concrete Institute*, Vol. 31, No. 3, 1935, pp. 280–303.

Bloom, R. and Bentur, A. Free and Restrained Shrinkage of Normal and High-Strength Concretes. *ACI Materials Journal*, Vol. 92, No. 2, 1995.

Burrows, R.D. *The Visible and Invisible Cracking of Concrete*, American Concrete Monograph No. 11, 1998.

Byrum, C. R. Analysis by High-Speed Profile of Jointed Concrete Pavement Slab Curvatures. In *Transportation Research Record 1730*, TRB, National Research Council, Washington, D.C., 2000, pp. 1–9.

CAL/APT Contract Team—University of California at Berkeley, Dynatest Consulting Inc., and CSIR, Division of Roads and Transport Technology. *Test Plan for CAL/APT Goal LLPRS-Rigid Phase III*, Test Plan prepared for California Department of Transportation, 1998.

Carlson, R. W. Drying Shrinkage of Concrete as Affected by Many Factors. *Proceedings of the American Society for Testing and Materials*, ASTM, West Conshohocken, PA, Vol. 38, Pt. II, 1938, pp. 419–440.

Carpinteri, A. and Ferro, G. Size Effects on Tensile Fracture Properties: A Unified Explanation Based on Disorder and Fractality of Concrete Microstructure. *Materials and Structures*, Vol. 27, No. 174, 1994, pp. 563–571.

Childs, L. D. and Kapernick, J. W. Tests of Concrete Pavements on Gravel Subbases. *Proceedings of the American Society of Civil Engineers, ASCE*, Vol. 84, HW3, 1958.

Collins, T. M. Proportioning High-Strength Concrete to Control Creep and Shrinkage. *ACI Materials Journal*, Vol. 86, No. 6, 1989, pp. 576–580.

Crovetti, J. A., and Darter, M. I. Void Detection for Jointed Concrete Pavements. *Transportation Research Record*, Vol. 1041, TRB, National Research Council, Washington, D.C., 1985.

Darter, M. I. *Design of Zero-Maintenance Plain Jointed Concrete Pavement, Volume I—Development of Design Procedure*. FHWA-RD-77-111, Federal Highway Administration, Washington, D.C., 1977.

Darter, M. I. *A Comparison Between Corps of Engineers and ERES Consultants, Inc. Rigid Pavement Design Procedures*. Technical Report Prepared for the United States Air Force SAC Command. Savoy, IL, 1988.

Darter, M. I. and E. J. Barenberg. *Zero-Maintenance Pavements: Results of Field Studies on the Performance Requirements and Capabilities of Conventional Pavement Systems,* FHWA-RD-76-105, Federal Highway Administration, Washington, D.C., 1976.

Darter, M. I. and Barenberg, E. J. *Design of Zero-Maintenance Plain Jointed Concrete Pavement, Volume 1—Development of Design Procedures*. Report FHWA-RD-77-111, FHWA, U.S. Department of Transportation, 1977.

Darter, M., Khazanovich, L., Snyder, M., Rao, S., and Hallin, J. Development and Calibration of a Mechanistic Design Procedure for Jointed Plain Concrete Pavements. *Proceedings, 7th International Conference on Concrete Pavements,* Orlando, FL, 2001.

du Plessis, L. *HVS Test Results on Fast-Setting Hydraulic Cement Concrete, Palmdale, California Test Sections, North Tangent*. Draft report prepared for California Department of Transportation. Pavement Research Center, CAL/APT Program, Institute of Transportation Studies, University of California, Berkeley, 2002.

du Plessis, L. *Environmental Influences on the Curling of Concrete Slabs at the Palmdale HVS Test Site*. Draft report prepared for California Department of Transportation. Pavement Research Center, CAL/APT Program, Institute of Transportation Studies, University of California, Berkeley, 2002.

du Plessis, L., Bush, D., Jooste, F., Hung, D., Scheffy, C., Roesler, J. R., Popescu, L., and Harvey, J. *HVS Test Results on Fast-Setting Hydraulic Cement Concrete, Palmdale, California Test Sections, South Tangent*. Report prepared for California Department of Transportation. Pavement Research Center, CAL/APT Program, Institute of Transportation Studies, University of California, Berkeley, 2002.

Eisenmann, J. and Leykauf, G. Effect of Paving Temperatures on Pavement Performance. *Proceedings, 2nd International Workshop on Theoretical Design of Concrete Pavements*, Spain, 1990.

Fang, Y. Environmental Influences on Warping and Curling of PCC Pavements. *Proceedings, 7th International Conference on Concrete Pavements*, Orlando, FL, 2001.

FHWA. *Techniques for Pavement Rehabilitation*. Publication No. FHWA HI-98-033, Federal Highway Administration, McLean, VA, 1998.

Folliard, K.J., Ohta, M., Rathje, E., and Collins, P. Influence of Mineral Admixtures on Expansive Cement Mortars. *Cement and Concrete Research*, Vol. 27, No. 3, pp. 424–432, 1994.

Folliard, K. J. and Berke, N. S. Properties of High-Performance Concrete Containing Shrinkage-Reducing Admixture." *Cement and Concrete Research*, Vol. 27, No. 9, pp. 1357–1364, 1997.

Folliard, K., Smith, C., Sellers, G., Brown, M., Breen, J. E. *Evaluation of Alternative Materials to Control Drying Shrinkage Cracking in Concrete Bridge Decks*, Technical Report FHWA/TX-04/0-4098-4, Center for Transportation Research, University of Texas, Austin, 2003.

Foxworthy, P. T. *Concepts for the Development of a Nondestructive Testing and Evaluation System for Rigid Airfield Pavements*. Ph. D. Dissertation, University of Illinois, Urbana, IL, 1985.

French, C., Eppers, L., Le, Q., and Hajjar, J. F. Transverse cracking in concrete bridge decks. In *Transportation Research Record* 1688, TRB, National Research Council, Washington, D.C., 1999, p 21-29.

Gebler, S. H. *The Effects of High Range Water Reducers on the Properties of Freshly Mixed and Hardened Flowing Concrete*. Research and Development Bulletin No. RD081.01T, Portland Cement Association, Skokie, IL, 1982.

Grasley, Z. C. *Internal Relative Humidity, Drying Stress Gradients, and Hygrothermal Dilation of Concrete*. Master's Thesis, University of Illinois, Urbana, IL, 2003.

Hall, K.T., Darter, M. I., Hoerner, T. E., and Khazanovich, L. *LTPP Data Analysis—Phase I: Validation of Guidelines for k-Value Selection and Concrete Pavement Performance Prediction,* Technical Report FHWA-RD-96-198, 1997, ERES Consultants, Inc., Champaign, IL.

Hansen, W., Smiley, D. L., Peng, Y., and Jensen, E. A. Validating Top-Down Premature Transverse Slab Cracking in Jointed Plain Concrete Pavement. In *Transportation Research Record 1809*, TRB, National Research Council, Washington, D.C., 2002, 52–59.

Hatt, W. K. The Effect of Moisture on Concrete. *Transactions, ASCE*, 1925, Paper No. 157, pp. 270–315.

Heath, A. and Roesler, J. R. *Shrinkage and Thermal Cracking of Fast Setting Hydraulic Cement Concrete Pavements in Palmdale, California.* Draft report prepared for California Department of Transportation. Pavement Research Center, CAL/APT Program, Institute of Transportation Studies, University of California, Berkeley, 1999.

Heath, A. C. and Roesler, J. R. Top-Down Cracking of Rigid Pavements Constructed with Fast Setting Hydraulic Cement Concrete. In *Transportation Research Record 1712*, TRB, National Research Council, Washington, D.C., 2000, 3–12.

Hiller, J. E. and Roesler, J. R. Transverse Joint Analysis for use in Mechanistic-Empirical Design of Rigid Pavements. In *Journal of Transportation Research Board 1809*, TRB, National Research Council, Washington, D.C., 2002, pp. 42–51.

Hillerborg, A. Fracture Mechanics and the Concrete Codes. *Fracture Mechanics: Applications to Concrete*, ACI-SP118, Ed. V. Li and Z. P. Bazant, 1989, pp. 157–170.

Hilsdorf, H. and Kesler, C. E. Fatigue Strength of Concrete under Varying Flexural Stresses. *Proceedings, American Concrete Institute*, Vol. 63, 1966, pp. 1059–1075.

Holmen, J. O. Fatigue of Concrete by Constant and Variable Amplitude Loading. *Bulletin No. 79-1*, *Division of Concrete Structures*, NTH, Trondheim, 1979.

Holt, E. and Leivo, M. Cracking Risks Associated with Early Age Shrinkage. *Cement and Concrete Composites*, Vol. 26, 2004, pp. 521–530.

Hsu, T. Fatigue of Plain Concrete. *Journal of the American Concrete Institute*, Vol. 78, No. 4, 1981, pp. 292–305.

Hveem, F. N. *A Report of an Investigation to Determine Causes for Displacement and Faulting at the Joints in Portland Cement Concrete Pavements on California Highways*, Research Report, Materials and Research Department, Division of Highways, State of California, Sacramento, CA, 1949.

Hveem, F. N. Slab Warping Affects Pavement Joint Performance. *Proceedings American Concrete Institute*, Vol. 47, 1951, pp. 797–808.

Ioannides, A. M., Thompson, M. R., and Barenberg, E. J. Westergaard Solutions Reconsidered. *Transportation Research Record 1043*, TRB, National Research Council, Washington, D.C., 1985, pp. 13–23.

Ioannides, A. M. *Fracture Mechanics Applications in Pavement Engineering: A Literature Review*. Contract No. DACA39-94-C-0121, U.S. Army Engineer Waterways Experiment Station, Vicksburg, MS, 1995.

Janssen, D. J. Moisture in Portland Cement Concrete. In *Transportation Research Record 1121*, TRB, National Research Council, Washington, D.C., 1986, pp. 40–44.

Jeong, J. H., Wang, L., and Zollinger, D. G. A Temperature and Moisture Module for Hydrating Portland Cement Concrete Pavements. *Proceedings*, *7th International Conference on Concrete Pavements*, Vol. 1, Orlando, FL, Sept., 2001, pp. 9-22.

Kani, G. N. J. How Safe Are Our Large Reinforced Concrete Beams? *Journal of American Concrete Institute*, Vol. 63, No. 3, 1967; pp. 128–141.

Keene, P. W. The Effect of Air-Entrainment on the Shrinkage of Concrete Stored in Laboratory Air. *Concrete Research*, Vol. 13, No. 38, 1961, pp. 55–60.

Keeton, J. R. *Shrinkage Compensating Cement for Airport Pavement*. Report No. FAA-RD-79-11, Phase 2, Federal Aviation Administration, Washington, D.C., 1979.

Khazanovich, L. *Structural Analysis of Multi-Layered Concrete Pavement Systems.* Ph. D. Thesis, University of Illinois, Urbana-Champaign, Urbana, IL, 1994.

Khazanovich, L., Yu, H. T., Rao, S., Galasova, K., Shats, E., and Jones, R. *ISLAB2000 —Finite Element Program for Rigid and Composite Pavements, User's Guide*. ERES Consultants, Champaign, IL, 2000.

Kovler, K. A New Look at the Problem of Drying Creep of Concrete under Tension. *Journal of Materials in Civil Engineering*, American Society of Civil Engineers, Vol. 11, No. 1, 1999, pp. 84–87.

Krauss, P.D., and Rogalla, E.A., *Transverse Cracking in Newly Constructed Bridge Decks*. National Cooperative Highway Research Program (NCHRP) Report 380, Transportation Research Board, 1996.

Larson, G. and Dempsey, B. J. *Enhanced Integrated Climatic Model – Version 2.0*, DTFA, MNDOT 72114, 1997.

Leonards, G. A. and Harr, M. E. Analysis of Concrete Slabs on Ground. *Journal of the Soil Mechanics and Foundations Division*. Proceedings of the American Society of Civil Engineers, ASCE, June 1959, pp. 35–58.

Lim, S., Jeong, J-H, and Zollinger, D. G. Moisture Profiles and Shrinkage in Early-Age Concrete. Paper presented at 2004 TRB Annual Meeting, TRB, National Research Council, Washington, D.C., 2004.

Linkov, A. M. and Tutinas, V. V. Analysis of Beams with Transverse Cracks. *Issledovaniya po Mekhanike Stroil' nykh KOnstrucktsii I Materialov*, LISI, Leningrad, 1988, pp. 119–124 (in Russian).

Littleton, P. C. *Effect of Stress State on Concrete Slab Fatigue Resistance*. Master's Thesis, University of Illinois, Urbana, IL, 2003.

Mather, B. Reports of the Committee on Durability of Concrete—Physical Aspects—Drying Shrinkage. *Highway Research News*, Mar. 1963, pp. 26–29, and Nov. 1964, pp. 34–38.

Meininger, R. C. *Drying Shrinkage of Concrete*. Engineering Report No. RD3 (A Summary of Joint Research Laboratory Series J-135, J-145, 173, and D-143), National Ready Mix Concrete Association, Silver Springs, 1966.

Miner, M. A. Cumulative Damage in Fatigue. *Transactions, American Society of Mechanical Engineers,* Vol. 67, pp. A159–A164.

Nagataki, S. Shrinkage Restraints in Concrete Pavements. *Journal of the Structural Division, Proceedings of the American Society of Civil Engineers*, ASCE, 1970, pp. 1333–1358.

Neville, A. M. Influence of Size of Concrete Test Cubes on Mean Strength and Structural Deviation. *Magazine of Concrete Research,* Vol. 8, No. 23, 1956, pp. 101–110.

Neville, A. M. and Meyers, B. L. Creep of Concrete: Influencing Factors and Prediction. *Proceedings of the Symposium on Creep of Concrete, Detroit, MI,* American Concrete Institute, 1964, pp. 1–33.

Oh, B. H. Cumulative Damage Theory of Concrete under Variable-Amplitude Fatigue Loadings. *ACI Materials Journal*, Vol. 88, No. 1, 1991, pp. 41–48.

Ostergaard, L., Lange, D. A., Altoubat, S. A., and Stang, H. Tensile Basic Creep of Early Age Concrete Under Constant Load. *Cement and Concrete Research*, Vol. 31, 2001, pp. 1895–1899.

Packard, R. G. 1973. *Design of Concrete Airport Pavement*. Engineering Bulletin EB050.03P. Portland Cement Association, Skokie, IL.

Packard, R. G. and Tayabji, S. D. Mechanistic Design of Concrete Pavements to Control Joint Faulting and Subbase Erosion. *International Seminar on Drainage and Erodability at the Concrete Slab-Subbase-Shoulder Interfaces*, Paris, France, 1983.

Paillere, M., Buil, M., and Serrano, J.J. Effect of Fiber Addition on the Autogenous Shrinkage of Silica Fume Concrete. *ACI Materials Journal*, Vol. 86, No. 2, 1989.

PCA. *Design and Control of Concrete Mixtures*. Portland Cement Association, Skokie, IL, 13th Ed., 1994.

Perenchio, W. F. The Drying Shrinkage Dilemma. *Concrete Construction*, 1997, pp. 379–383.

Pickett, C. The Effect of Change in Moisture-Content on the Creep of Concrete under a Sustained Load. *ACI Materials Journal*, Vol. 38, pp. 333–356.

Pittman, D.W., Ramey, G., Webster, G., and Carden, A. Laboratory Evaluation of Concrete Mixture Designs Employing Type I and Type K Cement. *Journal of Materials in Civil Engineering*, Vol. 11, No. 2, pp. 144–150, 1999.

Poblete, M., Salsilli, R., Valenzuela, A., and Spratz, P. Field Evaluation of Thermal Deformations in Undoweled PCC Pavement Slabs. In *Transportation Research Record 1207*, TRB, National Research Council, Washington, D.C., 1987, pp. 217–228.

Powers, T. C. Causes and Control of Volume Change. *Journal, PCA Research and Development Laboratories*, Vol. 1, No. 1, 1959, pp. 29–39.

Raithby, K. D. and Galloway, J. W. Effects of Moisture Condition, Age, and Rate of Loading on Fatigue of Plain Concrete. *Abeles Symposium, Fatigue of Concrete, ACI Publication SP-41*, 1974, pp. 15–34.

Rao, C., Barenberg, E. J., Snyder, M. B., and Schmidt, S. Effects of Temperature and Moisture on the Response of Jointed Concrete Pavements. *Proceedings, 7th International Conference on Concrete Pavements*, Orlando, FL, 2001.

Rao, S. and Roesler, J. R. Characterizing Effective Built-In Curling from Concrete Pavement Field Measurements. *Journal of Transportation Engineering*, American Society of Civil Engineers, Reston, VA, Vol. 131, No. 4, 2005.

Rao, S. and Roesler, J. R. Non-Destructive Testing of Concrete Pavements for Characterization of Effective Built-In Curling. *ASTM Journal of Testing and Evaluation*, American Society for Testing and Materials, publication pending, manuscript ID No. 12338, 2005.

Rasmussen, R. O. and McCullough, B. F. *A Foundation for High Performance Jointed Concrete Pavement Design and Construction Guidelines.* Transtec consultants, Austin, Texas, 1998.

Rice, J. R. and Levy, N. The Part-Through Surface Crack in an Elastic Plate. *Journal of Applied Mechanics*, Vol. 39, 1972, pp. 185–194.

Rixom, M. R. and Waddicor, J. Role of Lignosulfonates as Superplasticizers. *Developments in the Use of Superplasticizers*. SP-68, American Concrete Institute, Detroit, MI, 1981, pp. 359–379.

Roesler, J. R. and Khazanovich, L. Finite Element Analysis of Portland Cement Concrete Pavements with Cracks. In *Journal of Transportation Research Board No. 1568*, TRB, National Research Council, Washington, D.C., 1997, pp. 1–9.

Roesler, J. R. *Fatigue of Concrete Beams and Slabs*. Ph. D. Dissertation, University of Illinois, Urbana, IL, 1998.

Roesler, J. R., Harvey, J., Hung, D., du Plessis. L., and Bush, D. Evaluation of Longer-Life Concrete Pavements for California using Accelerated Pavement Testing. *Proceedings - Accelerated Pavement Testing International Conference*, Reno, NV, 1999.

Roesler, J. R., Scheffy, C., Ali, A., and Bush, D. *Construction, Instrumentation, and Testing of Fast-Setting Hydraulic Cement Concrete in Palmdale, California*. Report prepared for California Department of Transportation, Pavement Research Center, CAL/APT Program, Institute of Transportation Studies, University of California, Berkeley, 2000.

Roesler, J. R., Lange, D., and Ulreich, G. *Fracture Behavior of Full-Scale, Fiber-Reinforced Concrete Slabs*. Final Report for W.R. Grace, Inc., University of Illinois, Urbana, IL, 2003.

Rufino, D., Roesler, J. R., Barenberg, E. J., and Tutumluer, E. Analysis of Pavement Responses to Aircraft and Environmental Loading at Denver International Airport. *Proceedings, 7th International Conference on Concrete Pavements,* Orlando, FL, 2001.

Rufino, D. Ph. D. Thesis, University of Illinois, Urbana-Champaign, IL, 2004.

Sabnis, G. M. and Mirza, S. M. Size Effect in Model Concretes. *Proceedings ASCE Structural Division*, ST6, Vol. 105, No. 6, pp. 1007–1020.

Salsilli, R. A., Barenberg, E. J., and Darter, M. I. Calibrated Mechanistic Design Procedure to Prevent Transverse Cracking of Jointed Plain Concrete Pavements. *Proceedings, 5th International Conference on Concrete Pavements,* West LaFayette, IN, 1993.

Schmidt, S. *Built-In Curling and Warping in PCC Pavements*. M. S. Thesis, University of Minnesota, 2000.

Schmitt, T. R., and Darwin, D. Effect of material properties on cracking in bridge decks. *Journal of Bridge Engineering,* Vol. 4, No. 1, 1999, pp. 8–13.

Smith, K. and Roesler, J. R. Review of Fatigue Models for Concrete Airfield Pavement Design. *ASCE Airfield Pavement Specialty Conference*, Las Vegas, NV, September 21-24, 2003.

Stockett, A. L., Schneider, A. M., and Mardulier, F. J. An Analysis of Drying Shrinkage Data for Portland Cement Mortar and Concrete. *Journal of Materials*, Vol. 2, No. 4, 1967, pp. 829–842.

Subramanian R., Tia, M., Bergin, M. J., and Ishee, C. Evaluation of the Effects of a Shrinkage Reducing Admixture on the Potential Shrinkage Induced Stresses in Concrete. Paper presented at 2004 TRB Annual Meeting, TRB, National Research Council, Washington, D.C., 2004.

Suprenant, B. A. Why Slabs Curl—Part I. *Concrete International*, March 2002, pp. 56–61.

Suprenant, B. A. Why Slabs Curl—Part II. *Concrete International*, April 2002, pp. 59–64.

Tabatabaie, A. M. *Structural Analysis of Concrete Pavement Joints*. Ph. D. Thesis, University of Illinois, Urbana-Champaign, IL, 1977.

Tabatabaie, A. M., Barenberg, E. J., and Smith, R. E. *Longitudinal Joint Systems in Slip-Formed Rigid Pavements, Volume II—Analysis of Load Transfer Systems for Concrete Pavements*. U. S. Department of Transportation, Report No. FAA-RD-79-4.

Tabatabaie, A. M. and Barenberg, E. J. Structural Analysis of Concrete Pavement Systems. *Transportation Engineering Journal*, ASCE, Vol. 106, No. 5, pp. 493–506.

Taylor, F. P. J. The Shear Strength of Large Beams. *Journal of Structural Engineering*, ASCE, Vol. 98, 1972, pp. 2473–2490.

Tazawa, E. and Miyazawa, S. Experimental Study on Mechanism of Autogenous Shrinkage of Concrete *Cement and Concrete Research*, Vol.25, No.8, 1995, pp. 1633–1638.

Tepfers, R. and Kutti, T. Fatigue Strength of Plain, Ordinary, and Lightweight Concrete. *ACI Journal, Proceedings*, Vol. 76, No. 5, 1979, pp. 635–652.

Tepfers, R. Tensile Fatigue Strength of Plain Concrete. *ACI Journal, Proceedings*, Vol. 76, No. 8, 1979, pp. 919–933.

Tepfers, R. Fatigue of Plain Concrete Subjected to Stress Reversals. *ACI Publication SP-75*, 1982, pp. 195–217.

Timoshenko, S. and Woinowsky-Krieger, S. *Theory of Plates and Shells*. McGraw-Hill, Inc., 1959.

Tremper, B. and Spellman, D. L. Shrinkage of Concrete—Comparison of Laboratory and Field Performance. In *Highway Research Record No. 3*, TRB, National Research Council, Washington, D.C., 1963, pp. 30–61.

Treybig, H., McCullough, G., Smith, P., and Quintus, H.V. Overlay Design and Reflection Cracking Analysis for Rigid Pavements: Vol. 1, Development of New Design Criteria. Report No. FHWA-RD-77-6, Vol. 1, FHWA, Washington, D.C., 1977.

Troxell, G. E., Davis, H. E., and Kelly, J. W. *Composition and Properties of Concrete*. 2nd edition, McGraw-Hill Book Co., New York, NY, 1968.

Ullidtz, P. *ELCON: Evaluation of Layer Moduli and Overlay Design (ELMOD) for Concrete,* Dynatest Engineering A/S, Denmark, 1987.

Van Mier, J. G. M. *Fracture Processes of Concrete.* CRC Press, Boca Raton, FL, 1997.

Vandenbossche, J. M. *Interpreting Falling Weight Deflectometer Results for Curled and Warped Portland Cement Concrete Pavements*. Ph. D. Thesis, University of Minnesota, Minneapolis, MN, 2003.

Vesic, A.S. and Saxena, S.K. "Analysis of Structural Behavior of Road Test Rigid Pavements," *Highway Research Board*, No. 291, Washington, D.C., 1969.

Walker, W. W. and Holland, J. A. The First Commandment for Floor Slabs—Thou Shalt Not Curl Nor Crack…(hopefully). *Concrete International*, Vol. 21, No. 1, January 1999, pp. 47–53.

Walsh, P. F. Crack Initiation in Plain Concrete. *Magazine of Concrete Research*, Vol. 28, 1976, pp. 37–41.

Washa, G. W. Volume Changes and Creep. *Significance of Tests and Properties of Concrete and Concrete Aggregates*. American Society for Testing and Materials, STP-169, ASTM, Philadelphia, PA, 1955, pp. 115–128.

Weibull, W. *A Statistical Theory for the Strength of Materials*. Swedish Royal Institute for Engineering Research, Stockholm, 1939.

Whiting, D. *Effects of High Range Water Reducers of Some Properties of Fresh and Hardened Concretes*. Research and Development Bulletin No. RD061.01T, Portland Cement Association, Skokie, IL, 1979.

Wu, C. L., Mack, J. W., Okamoto, P. A., and Packard, R. G. Prediction of Faulting of Joints in Concrete Pavements. *Proceedings, 5th International Conference on Concrete Pavements,* West LaFayette, IN, 1993.

Ytterberg, R. F. Shrinkage and Curling of Slabs on Grade, Part I—Drying Shrinkage. *Concrete International*, Vol. 9, No. 4, April 1987, pp. 22–31.

Ytterberg, R. F. Shrinkage and Curling of Slabs on Grade, Part II—Warping and Curling. *Concrete International*, Vol. 9, No. 5, May 1987, pp. 54–61.

Ytterberg, R. F. Shrinkage and Curling of Slabs on Grade, Part III—Additional Suggestions. *Concrete International*, Vol. 9, No. 6, June 1987, pp. 72–81.

Yu, H. T. and Khazanovich, L. Effects of Construction Curling on Concrete Pavement Behavior. *Proceedings, 7th International Conference on Concrete Pavements*, Orlando, FL, 2001.

Yu, H. T., Khazanovich, L., Darter, M. I., and Ardani, A. Analysis of Concrete Pavement Responses to Temperature and Wheel Loads Measured from Instrumented Slabs. In *Journal of Transportation Research Board No. 1639*, TRB, National Research Council, Washington, D.C., 1998, pp. 94–101.

Yu, H. T., Khazanovich, L., and Darter, M. I. Consideration of JPCP Curling and Warping in the 2002 Design Guide. Paper presented at 2004 TRB Annual Meeting, TRB, National Research Council, Washington, D.C., 2004.

Zollinger, D. G. and Barenberg, E. J. *Proposed Mechanistic Based Design Procedure for Jointed Concrete Pavements*. IHR-518, Illinois Cooperative Research Program, University of Illinois, Urbana, IL, 1989.

APPENDIX A: DEFLECTION, RESIDUALS, AND INFLUENCE CHART DATA FROM ALL TESTS

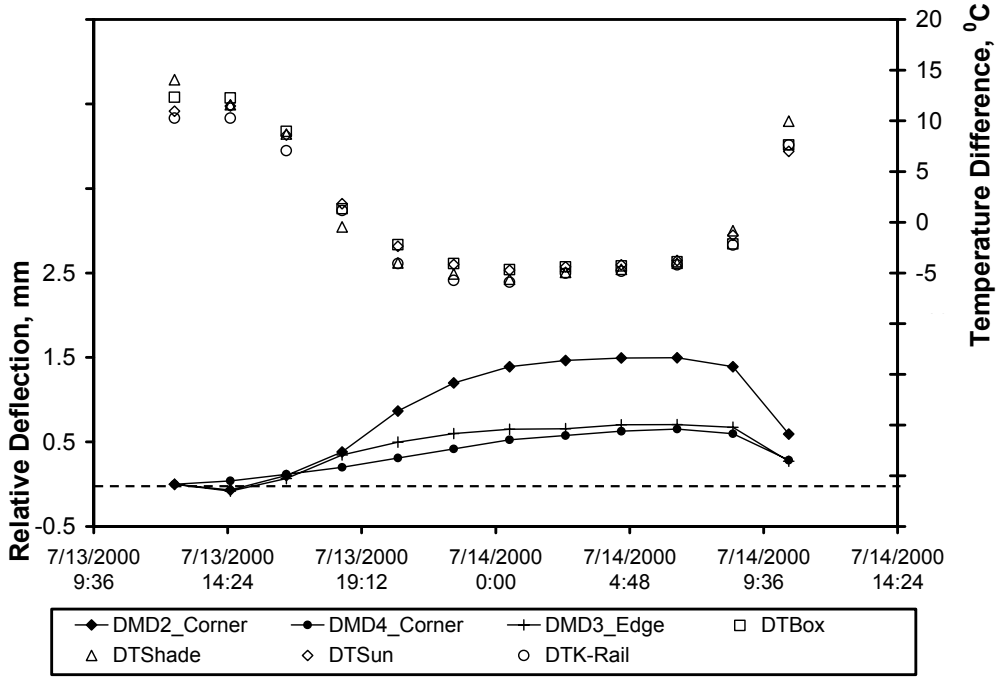

Figure A-1. 24-hour unloaded slab (537FD) relative deflections with no HVS and no temperature control box.

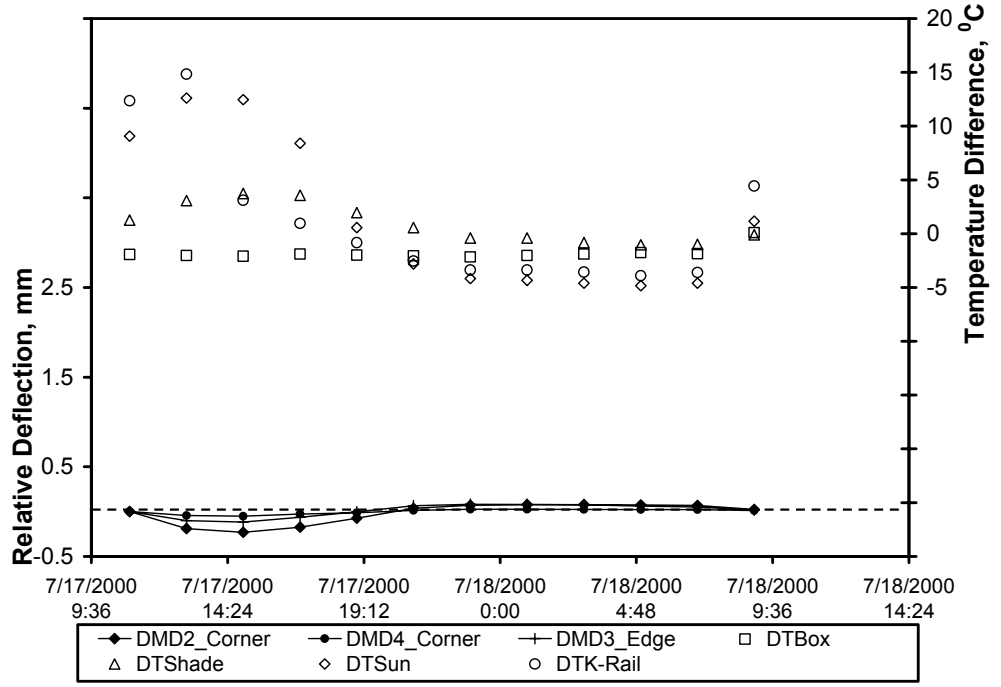

Figure A-2. 24-hour unloaded slab (537FD) relative deflections with HVS and temperature control box.

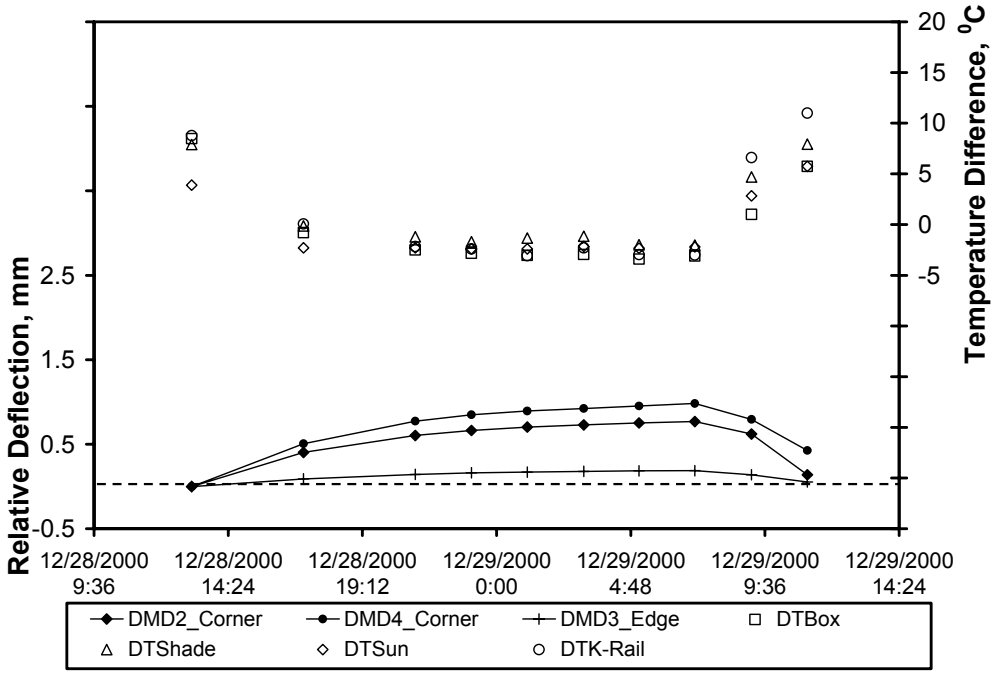

Figure A-3. 24-hour unloaded slab (538FD) relative deflections with no HVS and no temperature control box.

24-hour unloaded slab (538FD) relative deflections with HVS and temperature control box (no data).

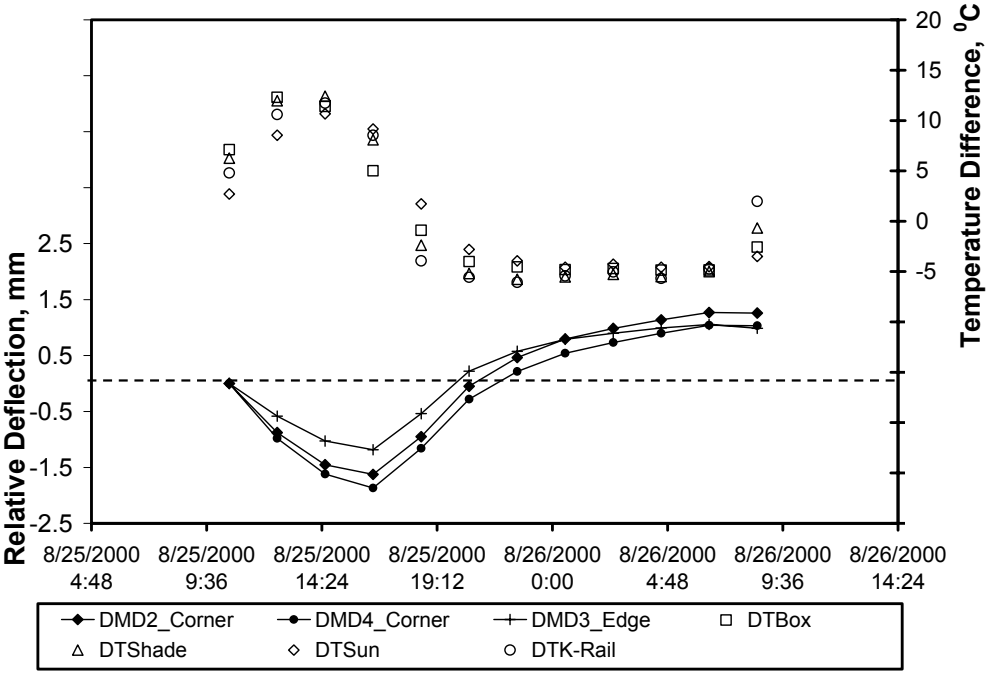

Figure A-4. 24-hour unloaded slab (539FD) relative deflections with no HVS and no temperature control box.

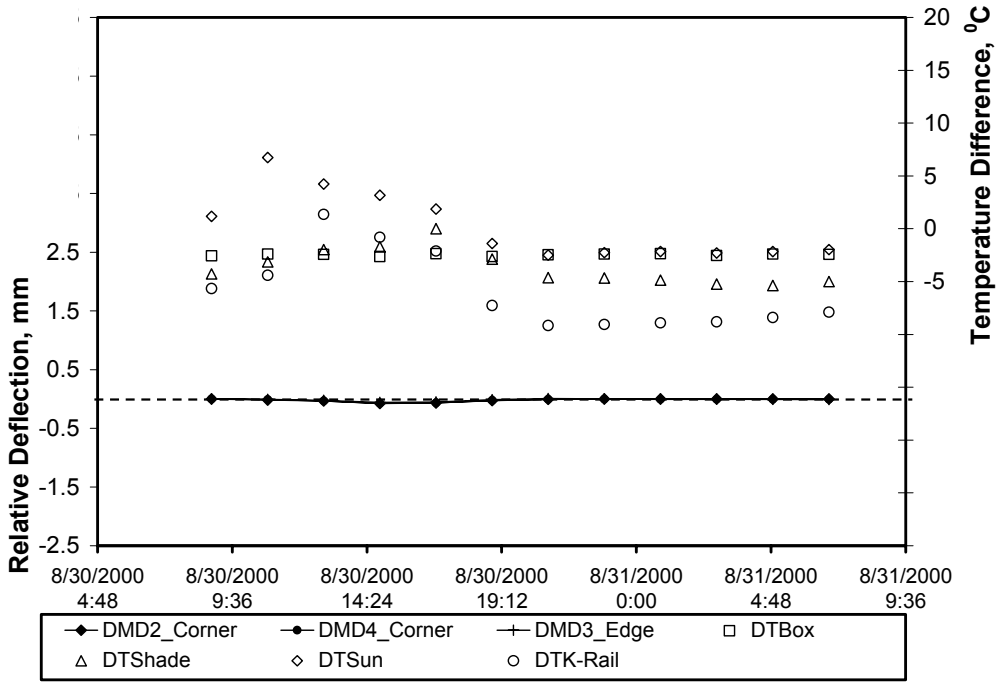

Figure A-5. 24-hour unloaded slab (539FD) relative deflections with HVS and temperature control box.

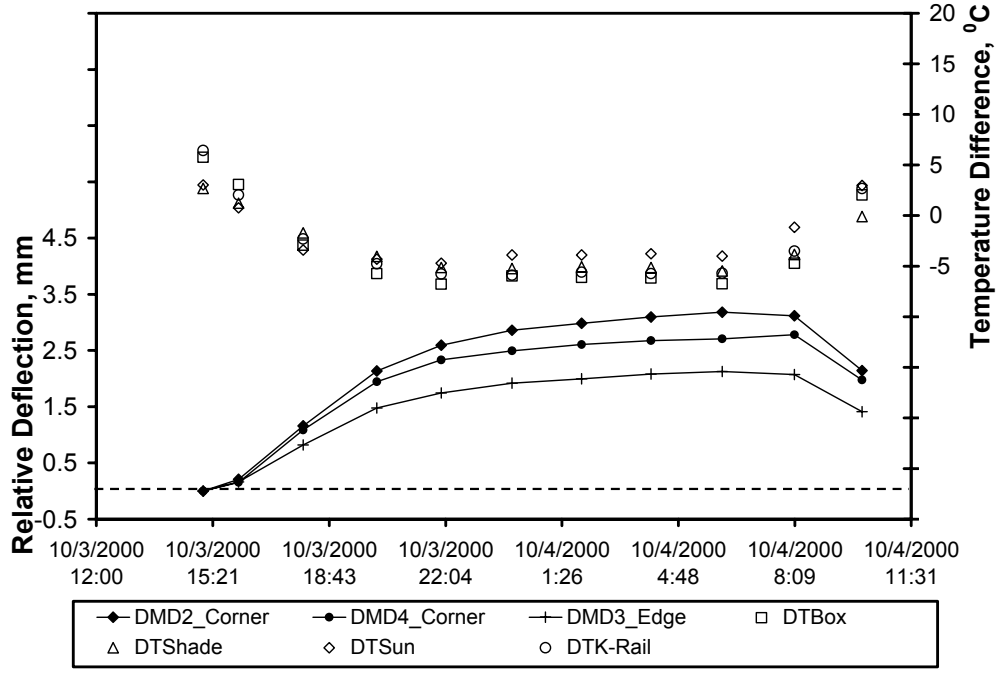

Figure A-6. 24-hour unloaded slab (540FD) relative deflections with no HVS and no temperature control box.

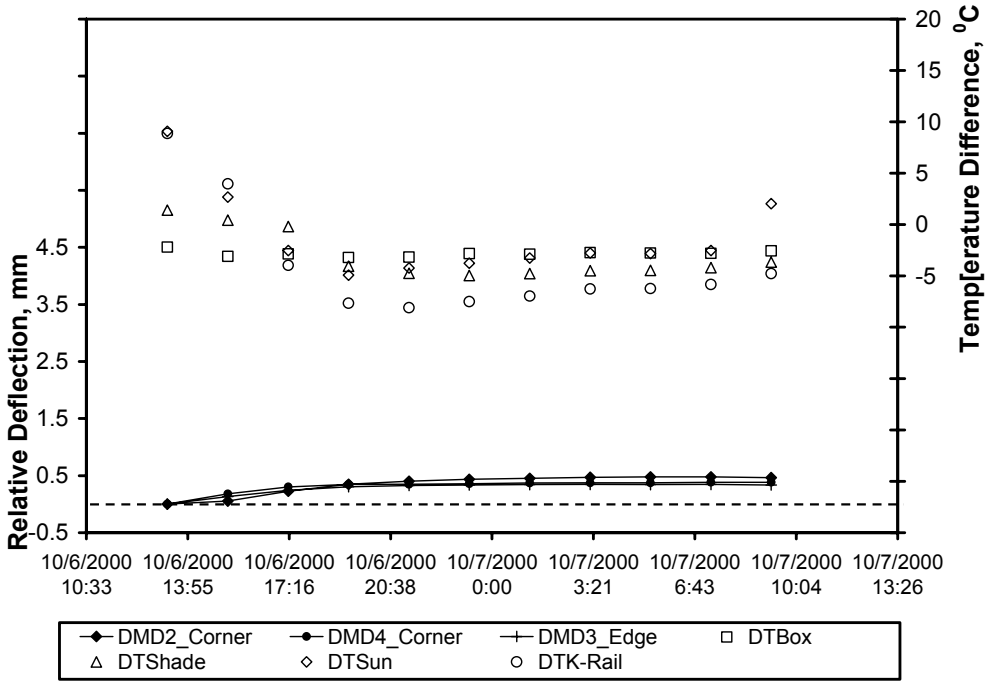

Figure A-7. 24-hour unloaded slab (540FD) relative deflections with HVS and temperature control box.

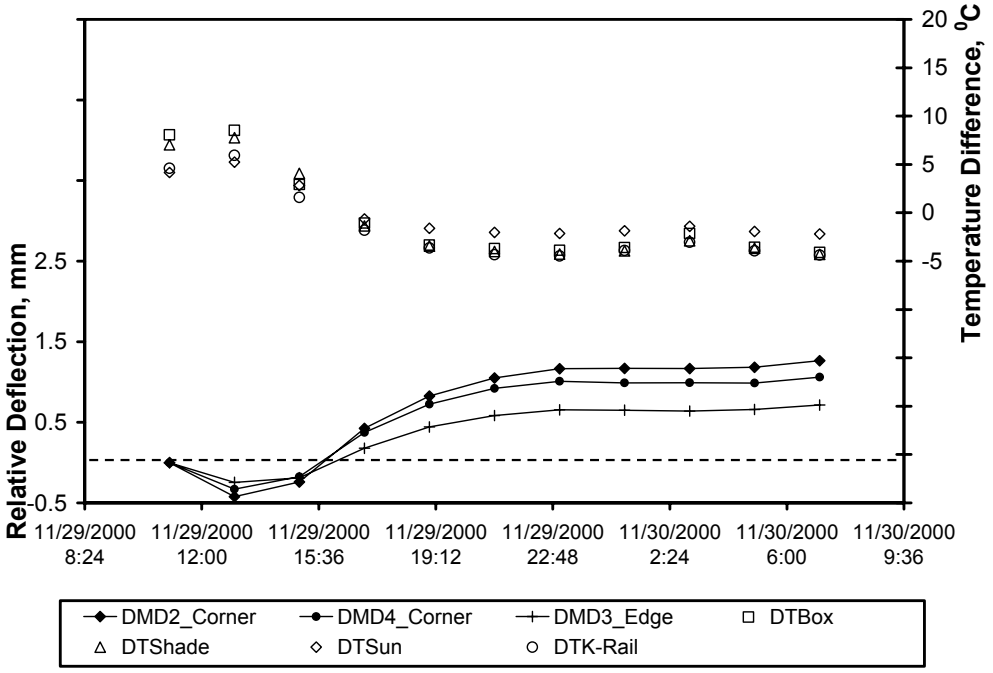

Figure A-8. 24-hour unloaded slab (541FD) relative deflections with no HVS and no temperature control box.

24-hour unloaded slab (541FD) relative deflections with HVS and temperature control box (no data).

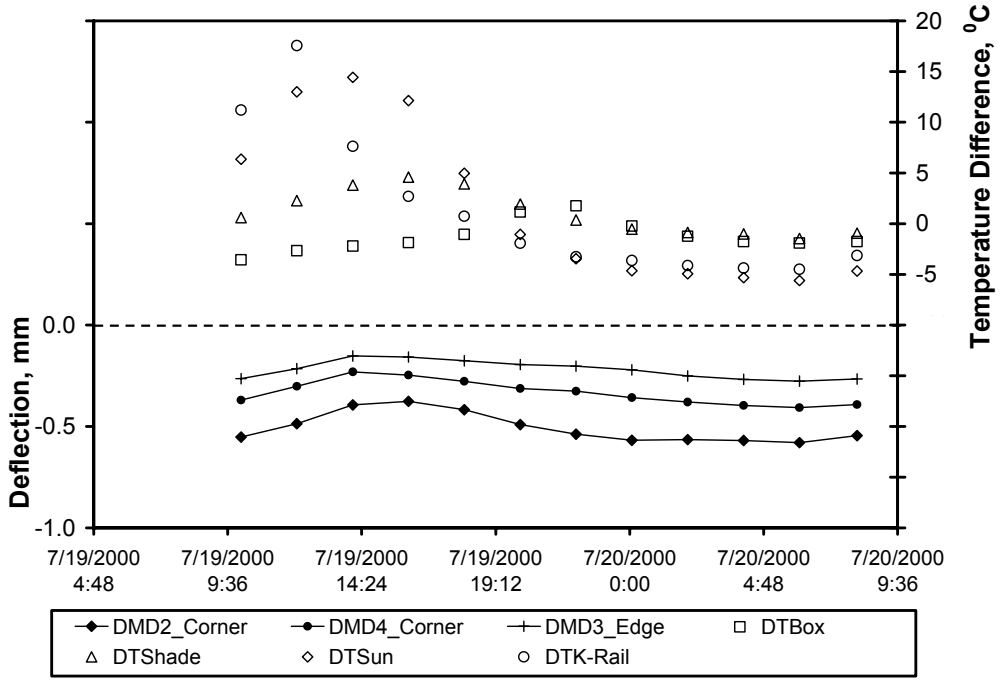

Figure A-9. 24-hour 40-kN dual-wheel half-axle loaded slab (537FD) deflections without using the temperature control box.

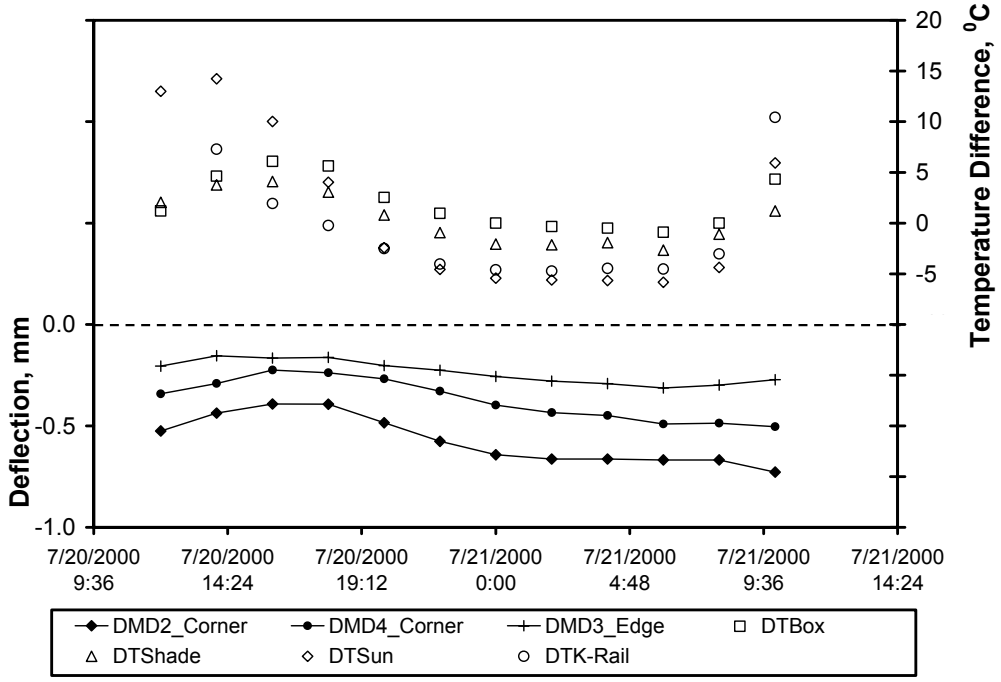

Figure A-10. 24-hour 40-kN dual wheel half-axle loaded slab (537FD) deflections with use of the temperature control box.

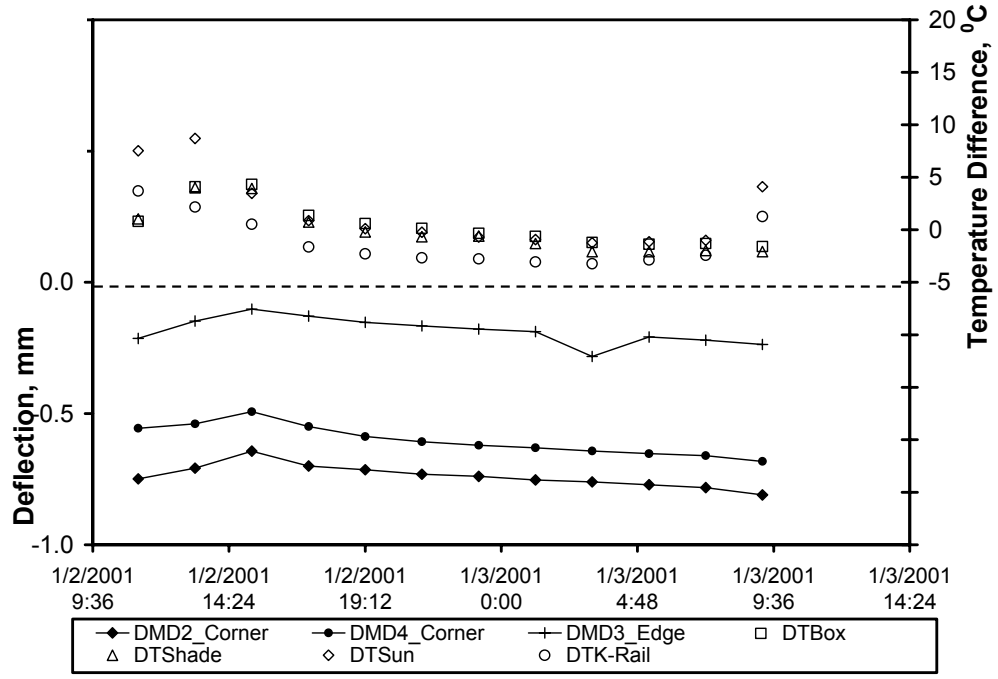

Figure A-11. 24-hour 40-kN dual-wheel half-axle loaded slab (538FD) deflections without using the temperature control box.

24-hour 40-kN dual wheel half-axle loaded slab (538FD) deflections with use of the temperature control box (no data).

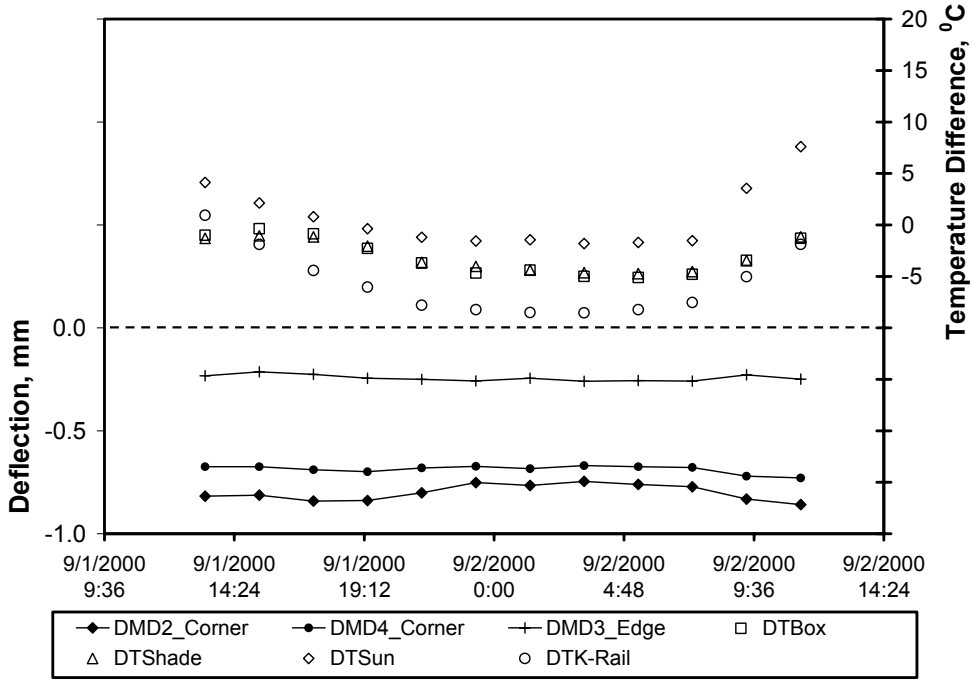

Figure A-12. 24-hour 40-kN dual-wheel half-axle loaded slab (539FD) deflections without using the temperature control box.

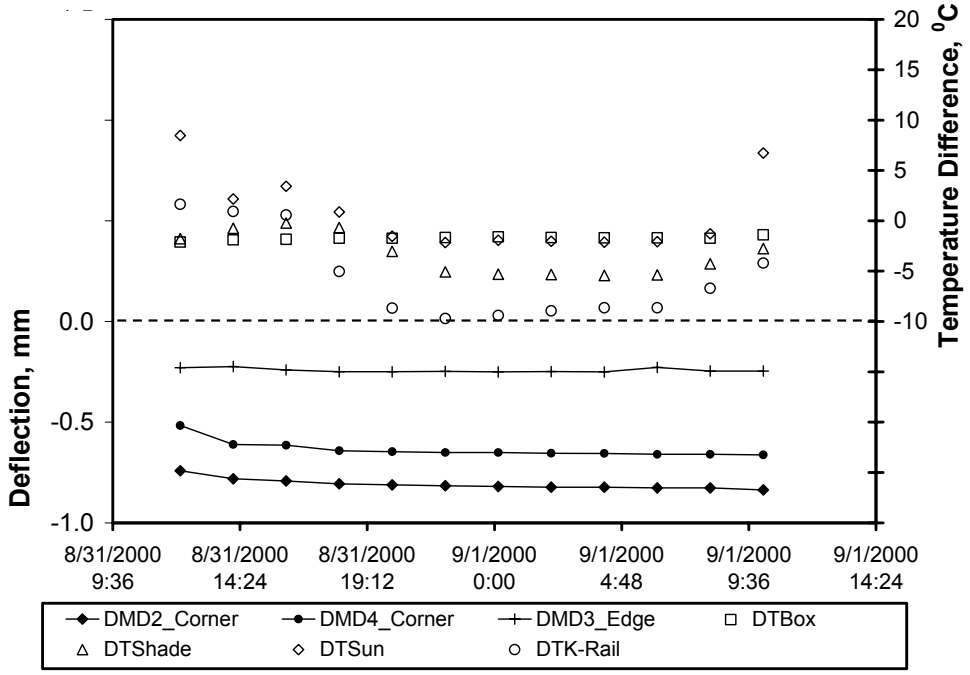

Figure A-13. 24-hour 40-kN dual wheel half-axle loaded slab (539FD) deflections with use of the temperature control box.

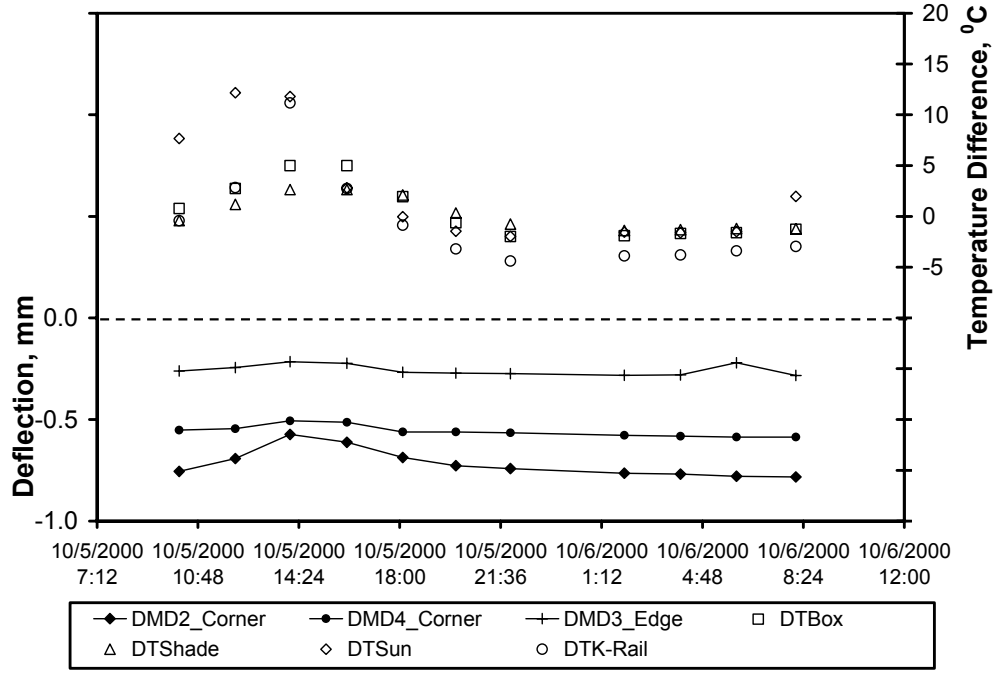

Figure A-14. 24-hour 40-kN dual-wheel half-axle loaded slab (540FD) deflections without using the temperature control box.

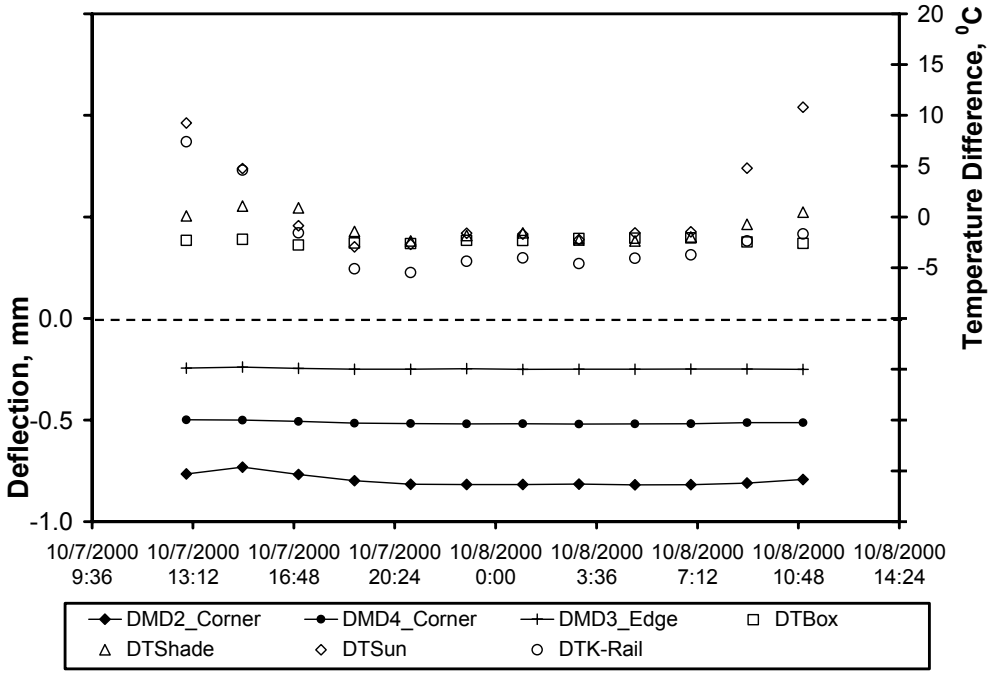

Figure A-15. 24-hour 40-kN dual wheel half-axle loaded slab (540FD) deflections with use of the temperature control box.

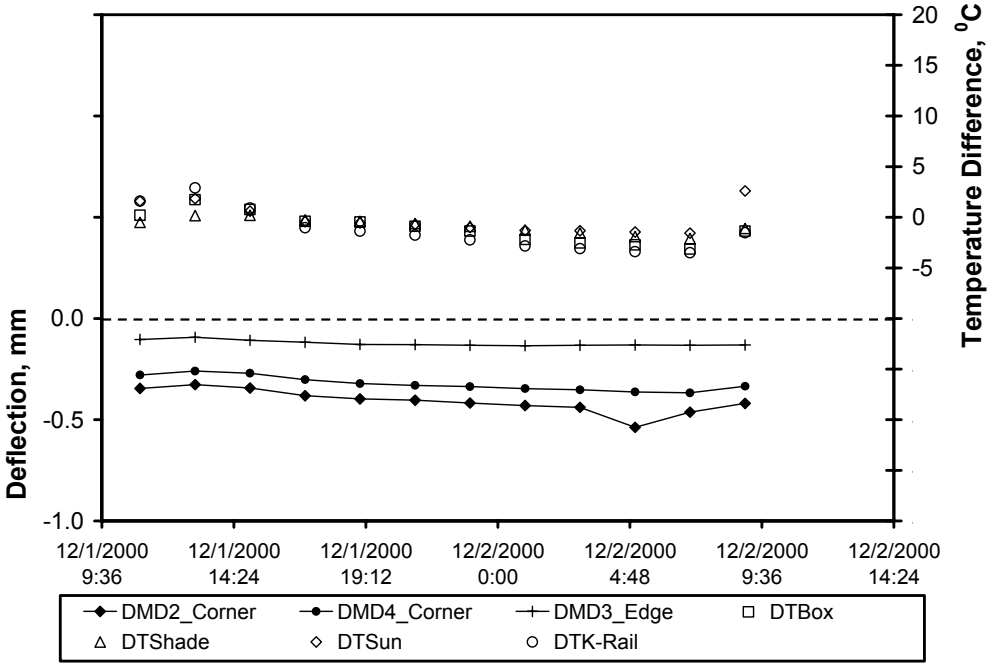

Figure A-16. 24-hour 40-kN dual-wheel half-axle loaded slab (541FD) deflections without using the temperature control box.

24-hour 40-kN dual wheel half-axle loaded slab (541FD) deflections with use of the temperature control box (no data).

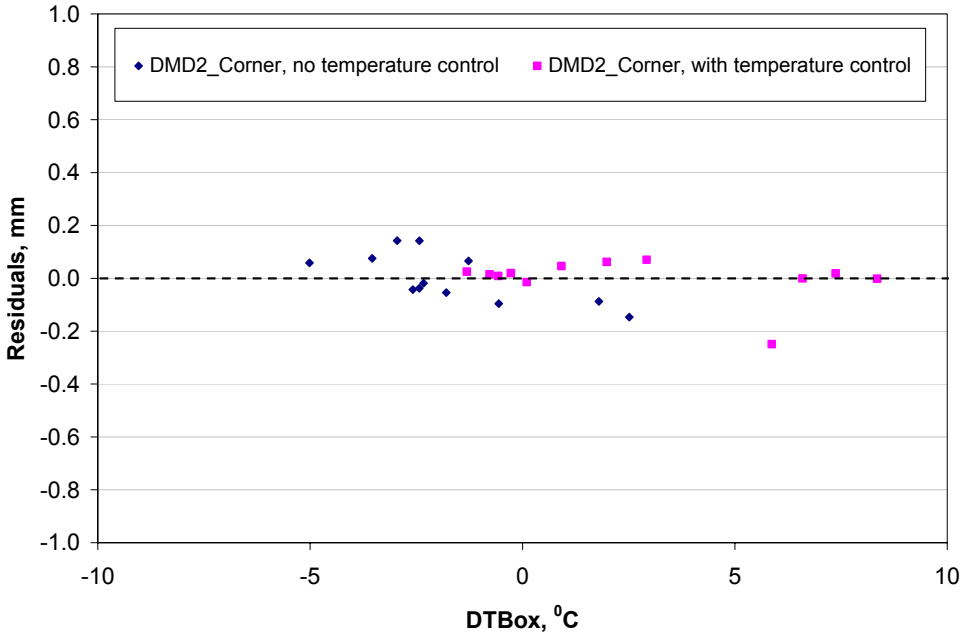

Figure A-17. Residuals (difference in measured deflections and predicted deflections) as a function of temperature difference (box) for DMD2 measured with and without temperature control for Section 537FD.

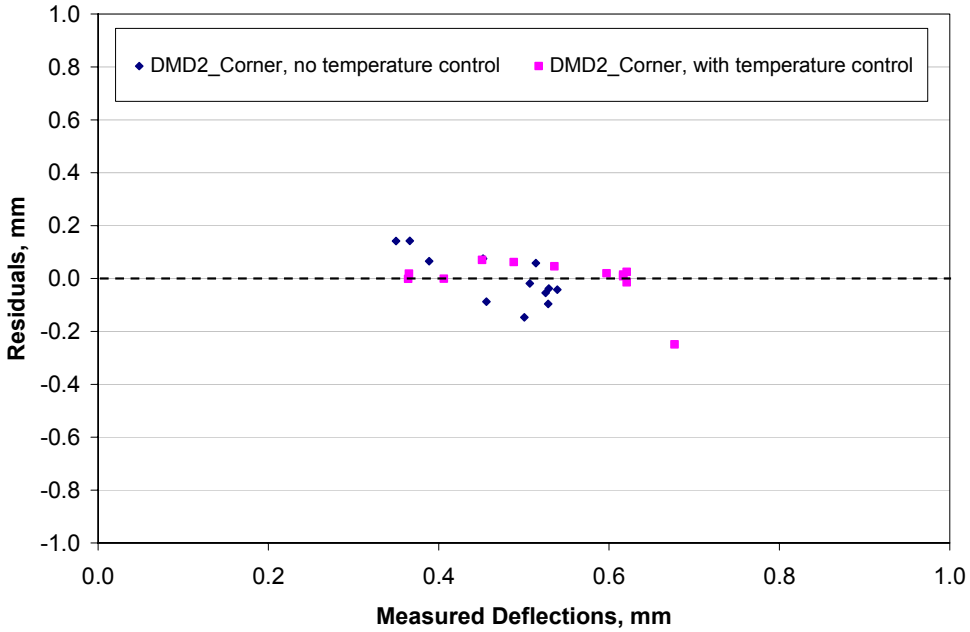

Figure A-18. Residuals (difference in measured deflections and predicted deflections) as a function of measured deflections for DMD2 measured with and without temperature control for Section 537FD.

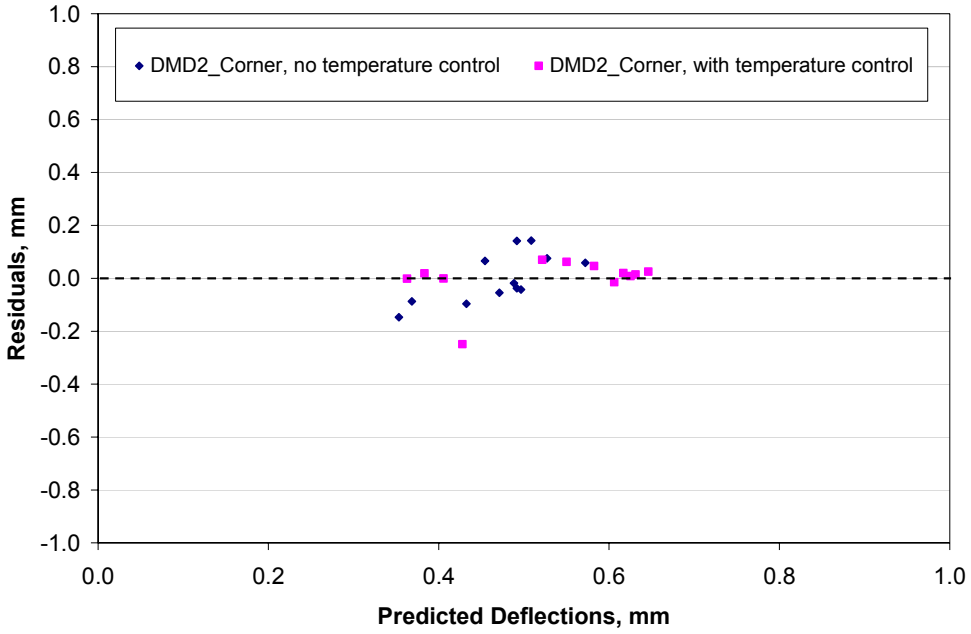

Figure A-19. Residuals (difference in measured deflections and predicted deflections) as a function of predicted deflections for DMD2 measured with and without temperature control for Section 537FD.

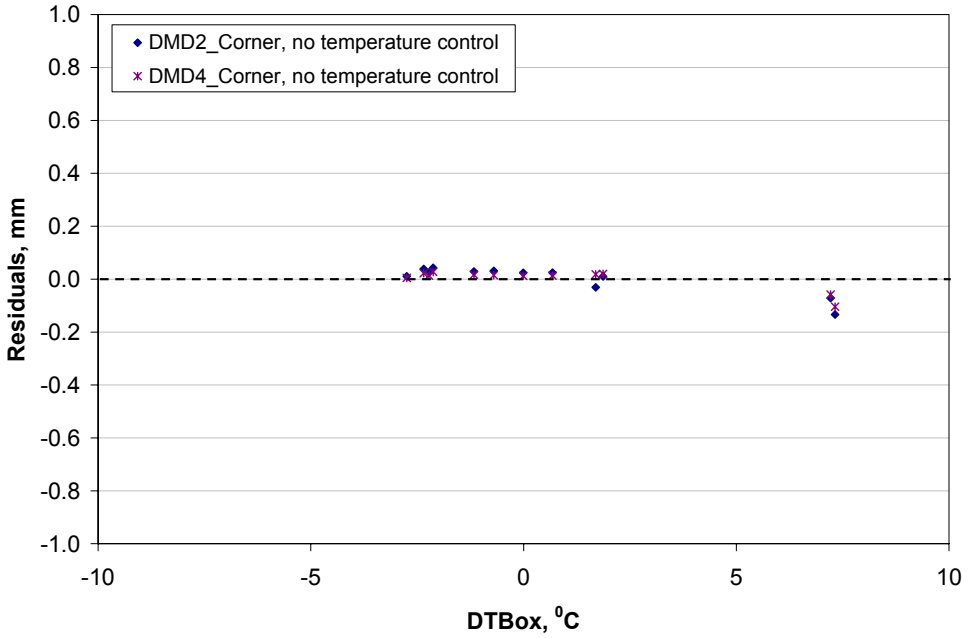

Figure A-20. Residuals (difference in measured deflections and predicted deflections) as a function of temperature difference (box) for DMD2 and DMD4 measured without temperature control for Section 538FD.

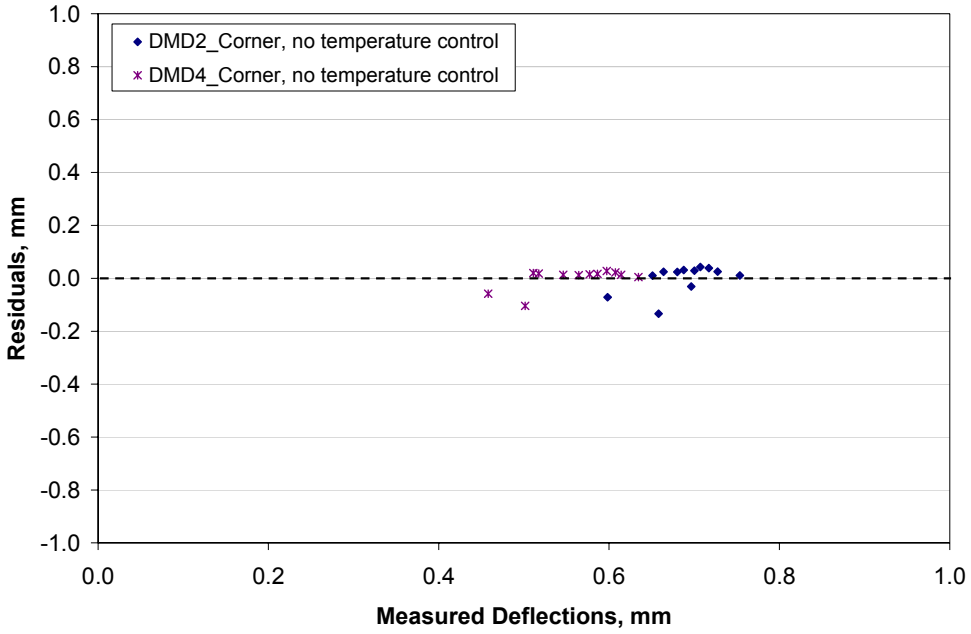

Figure A-21. Residuals (difference in measured deflections and predicted deflections) as a function of measured deflections for DMD2 and DMD4 measured without temperature control for Section 538FD.

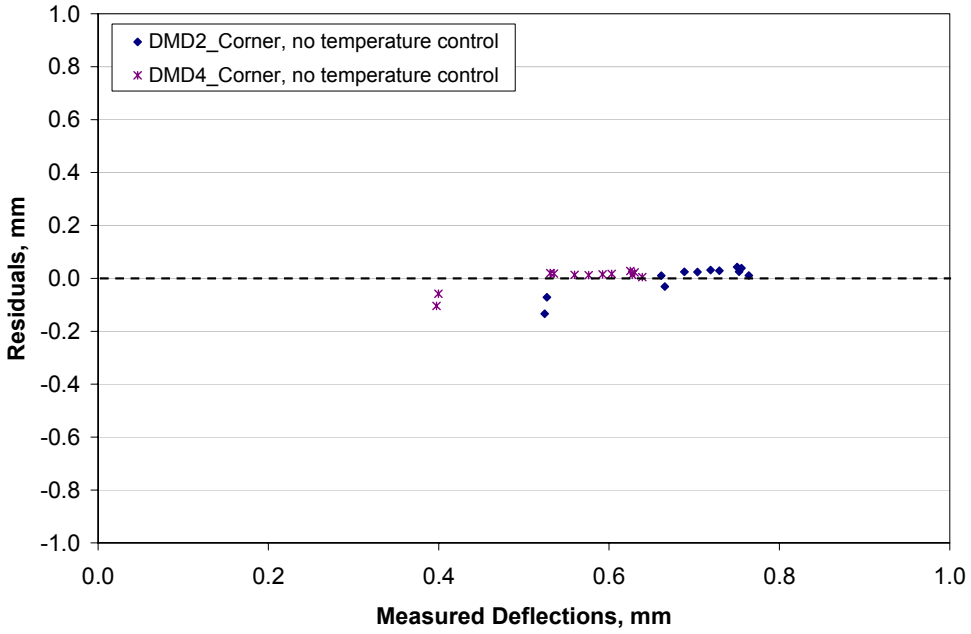

Figure A-22. Residuals (difference in measured deflections and predicted deflections) as a function of predicted deflections for DMD2 and DMD4 measured without temperature control for Section 538FD.

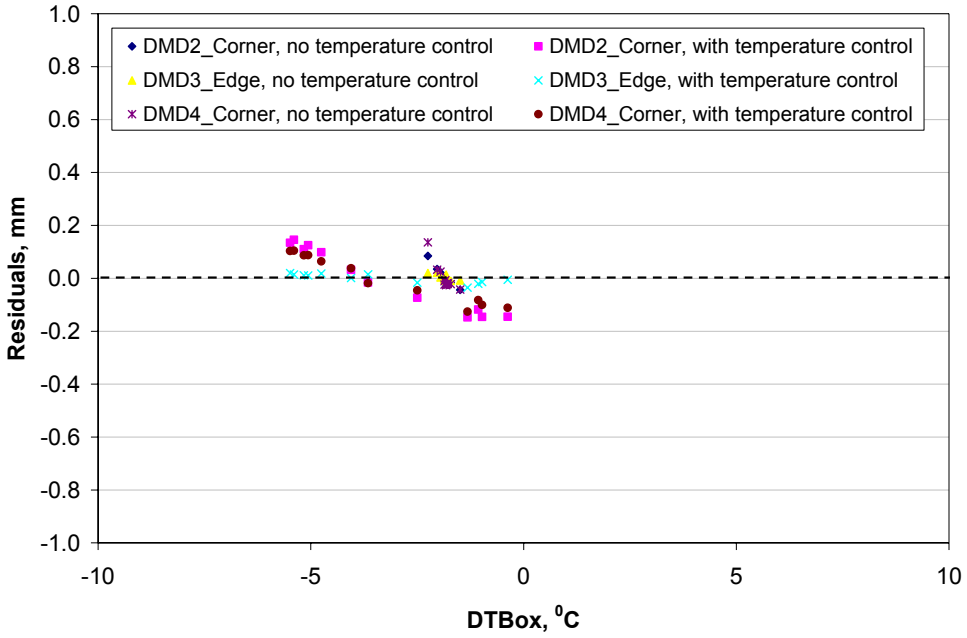

Figure A-23. Residuals (difference in measured deflections and predicted deflections) as a function of temperature difference (box) for DMD2, DMD3, and DMD4 measured with and without temperature control for Section 539FD.

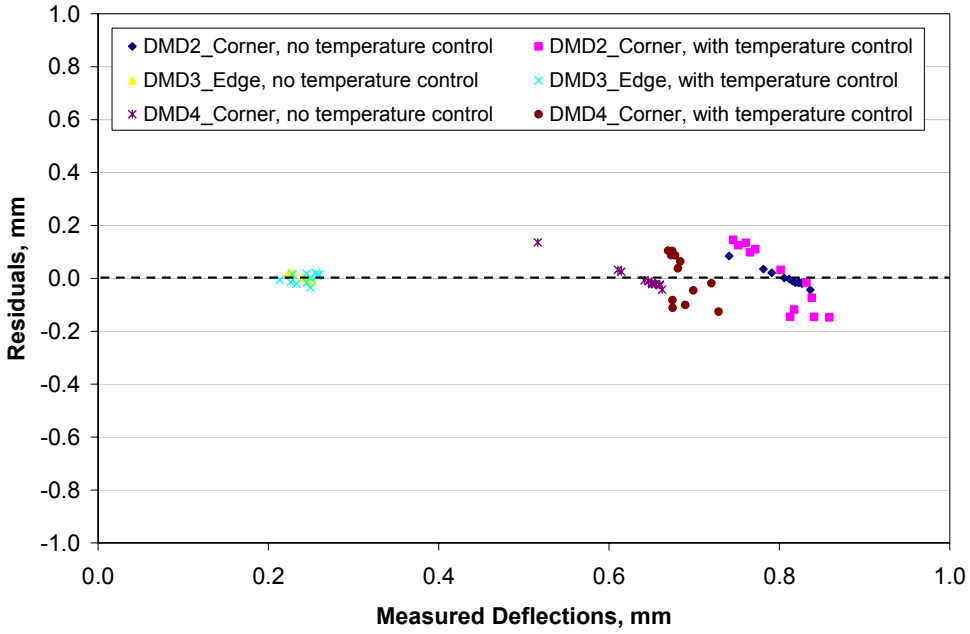

Figure A-24. Residuals (difference in measured deflections and predicted deflections) as a function of measured deflections for DMD2, DMD3, and DMD4 measured with and without temperature control for Section 539FD.

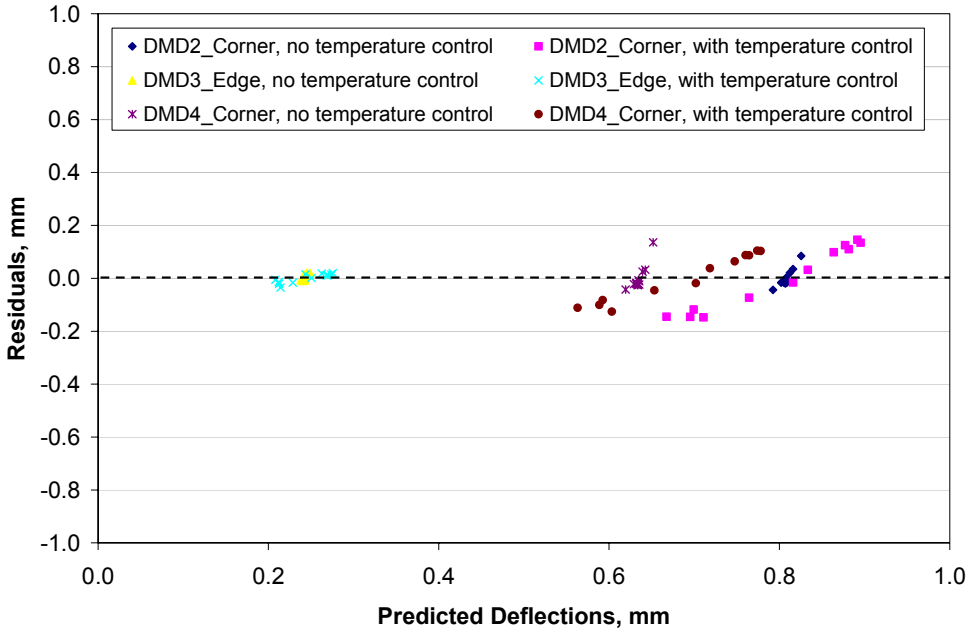

Figure A-25. Residuals (difference in measured deflections and predicted deflections) as a function of predicted deflections for DMD2, DMD3, and DMD4 measured with and without temperature control for Section 539FD.

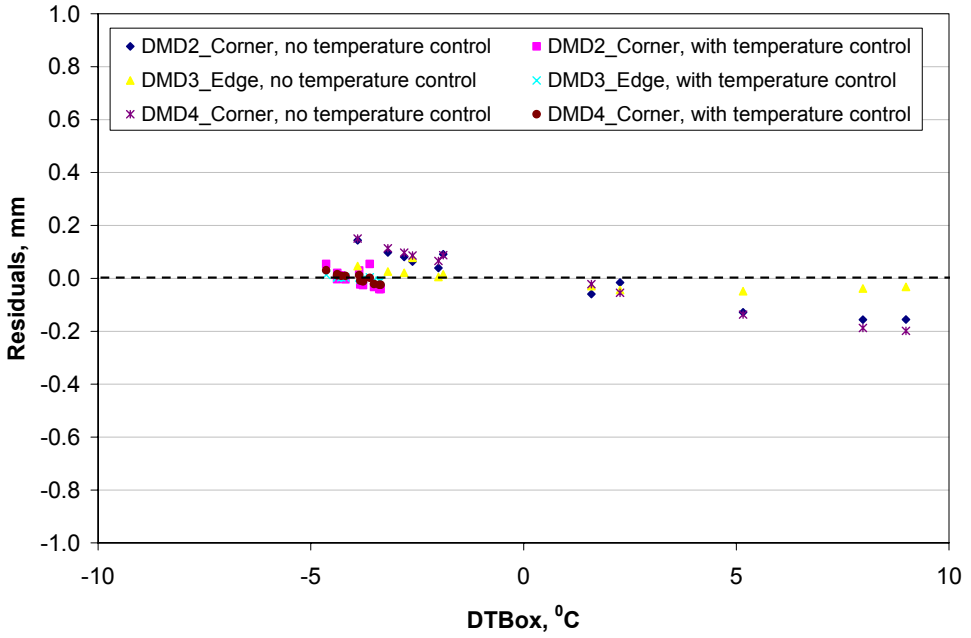

Figure A-26. Residuals (difference in measured deflections and predicted deflections) as a function of temperature difference (box) for DMD2, DMD3, and DMD4 measured with and without temperature control for Section 540FD.

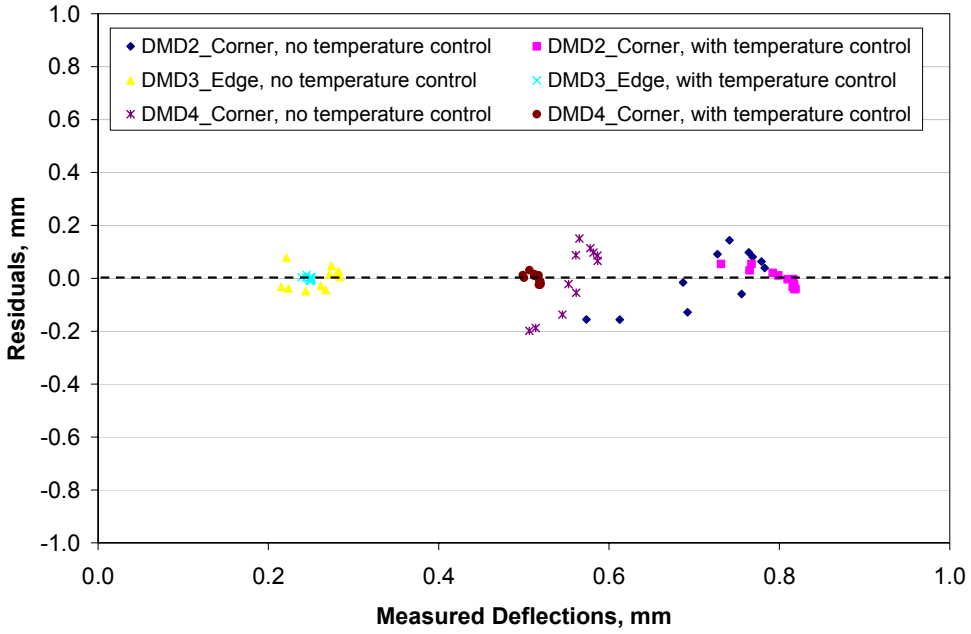

Figure A-27. Residuals (difference in measured deflections and predicted deflections) as a function of measured deflections for DMD2, DMD3, and DMD4 measured with and without temperature control for Section 540FD.

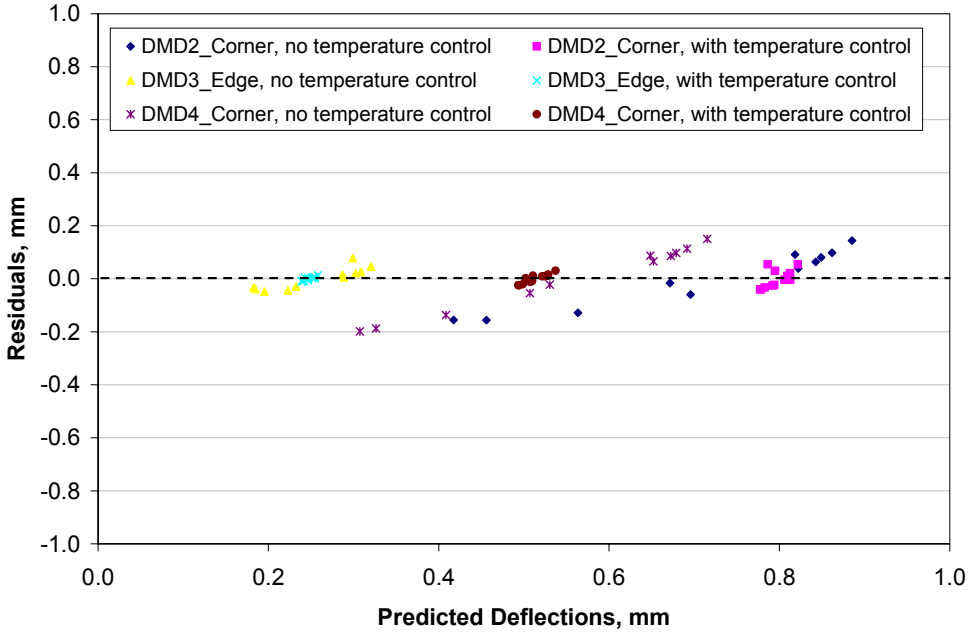

Figure A-28. Residuals (difference in measured deflections and predicted deflections) as a function of predicted deflections for DMD2, DMD3, and DMD4 measured with and without temperature control for Section 540FD.

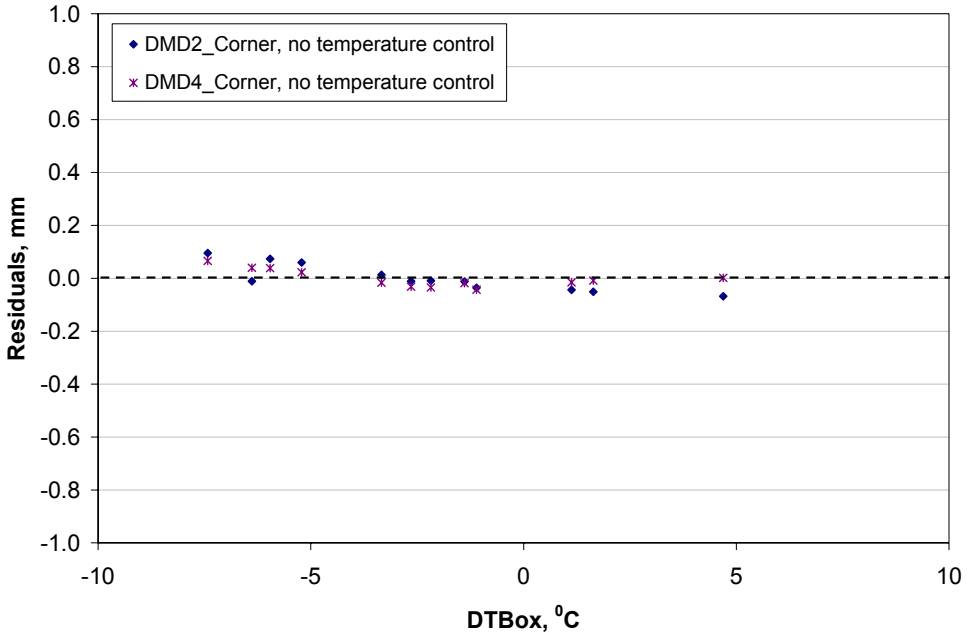

Figure A-29. Residuals (difference in measured deflections and predicted deflections) as a function of temperature difference (box) for DMD2 and DMD4 measured without temperature control for Section 541FD.

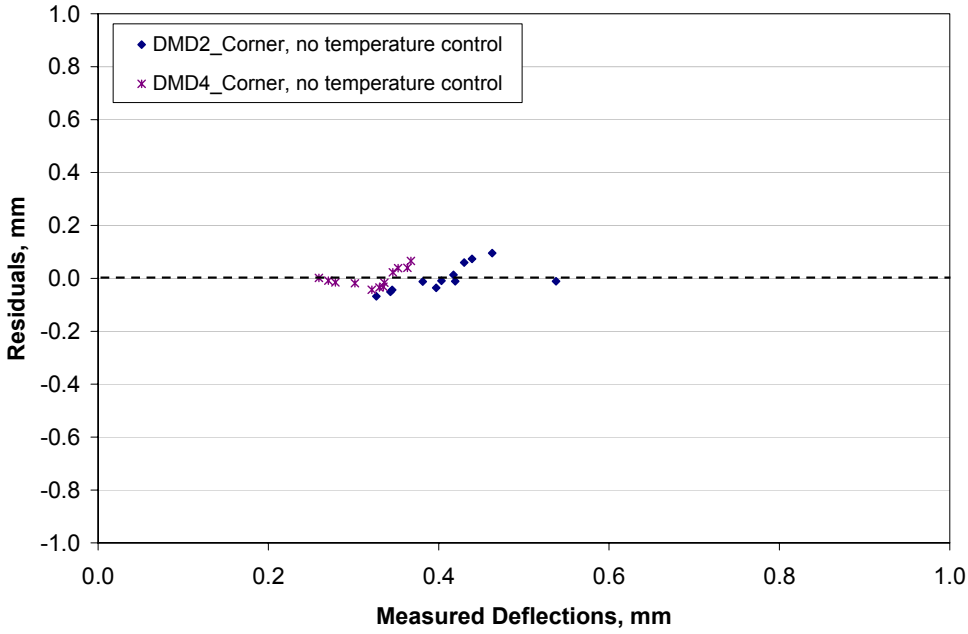

Figure A-30. Residuals (difference in measured deflections and predicted deflections) as a function of measured deflections for DMD2 and DMD4 measured without temperature control for Section 541FD.

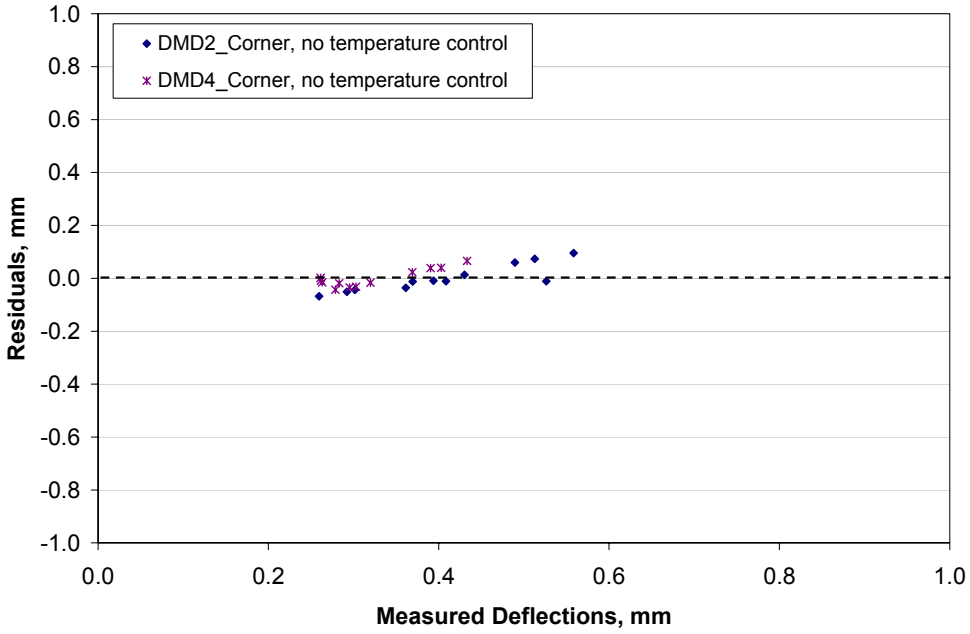

Figure A-31. Residuals (difference in measured deflections and predicted deflections) as a function of predicted deflections for DMD2 and DMD4 measured without temperature control for Section 541FD.

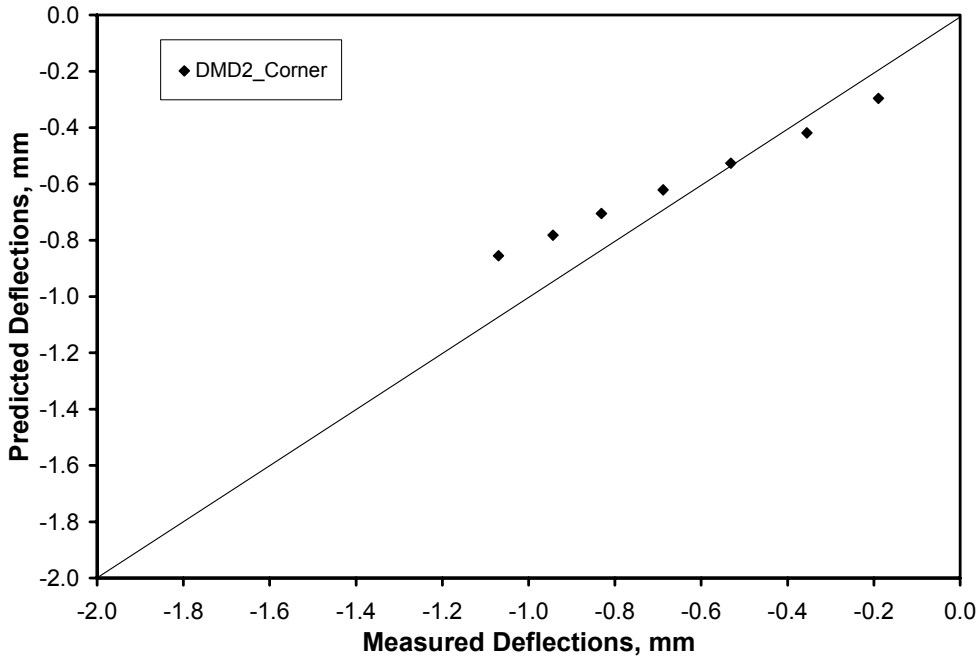

Figure A-32. Measured and predicted corner (DMD2) deflections for Section 537FD under the influence of 20- to 80-kN incremental loads with no significant differences in slab temperature gradients.

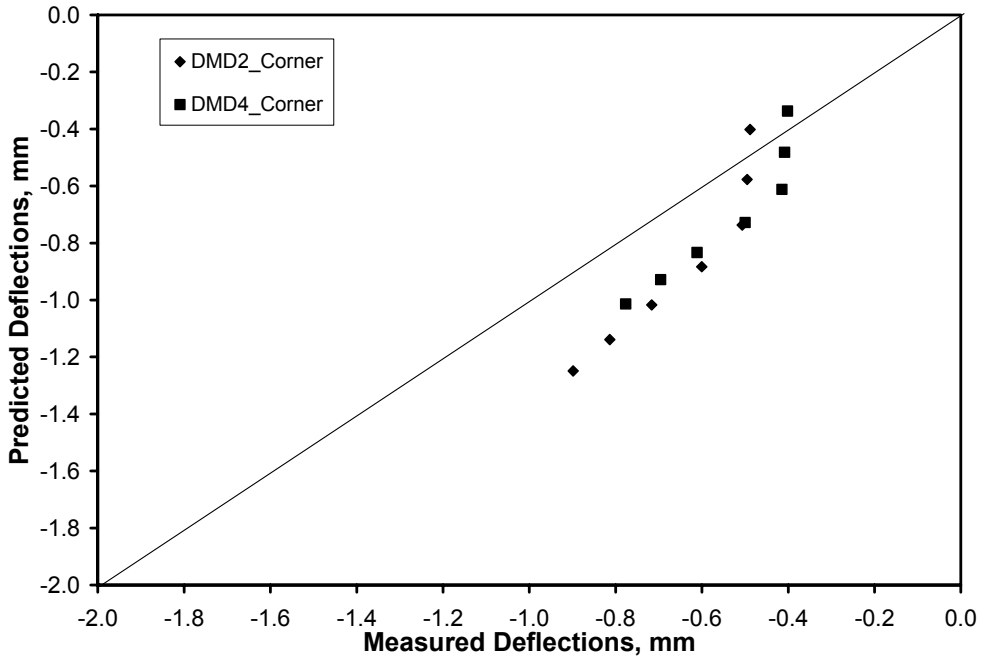

Figure A-33. Measured and predicted corner (DMD2 and DMD4) deflections for Section 538FD under the influence of 20- to 80-kN incremental loads with no significant differences in slab temperature gradients.

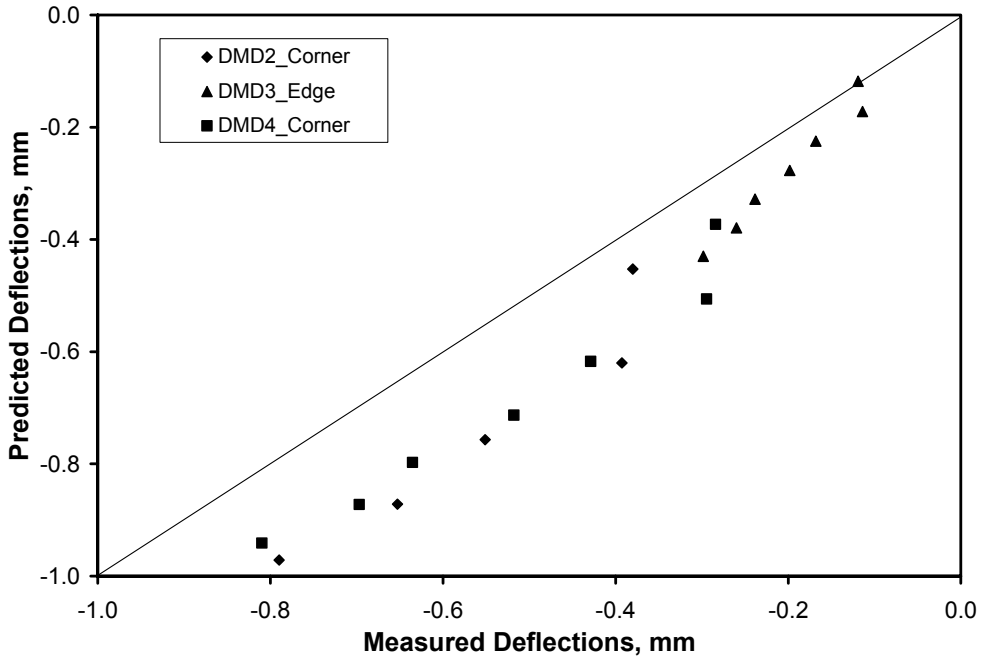

Figure A-34. Measured and predicted corner (DMD2 and DMD4) and edge (DMD3) deflections for Section 539FD under the influence of 20- to 80-kN incremental loads with no significant differences in slab temperature gradients.

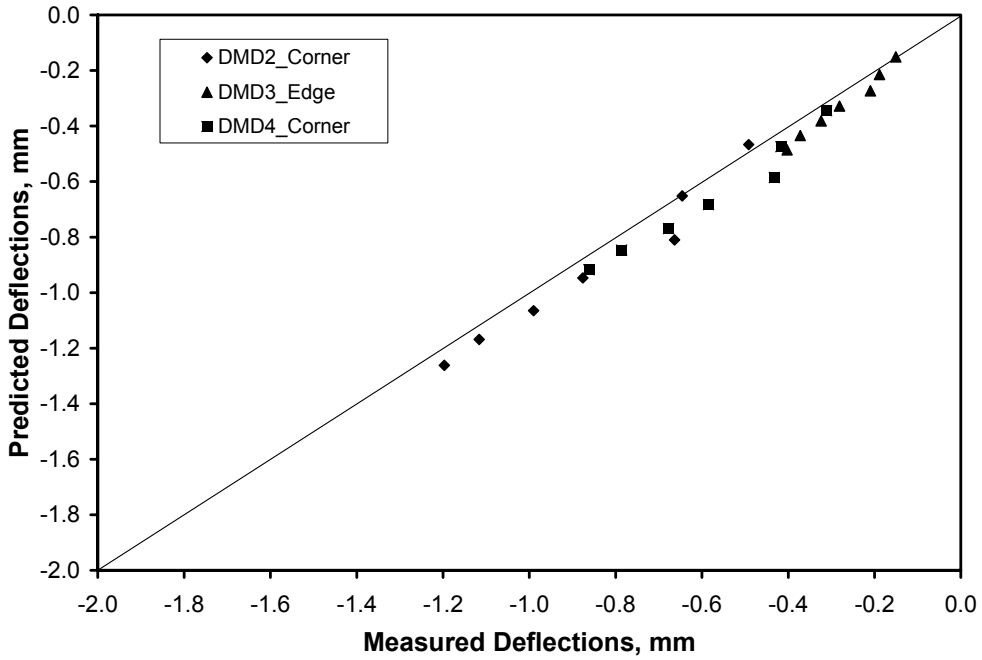

Figure A-35. Measured and predicted corner (DMD2 and DMD4) and edge (DMD3) deflections for Section 540FD under the influence of 20- to 80-kN incremental loads with no significant differences in slab temperature gradients.

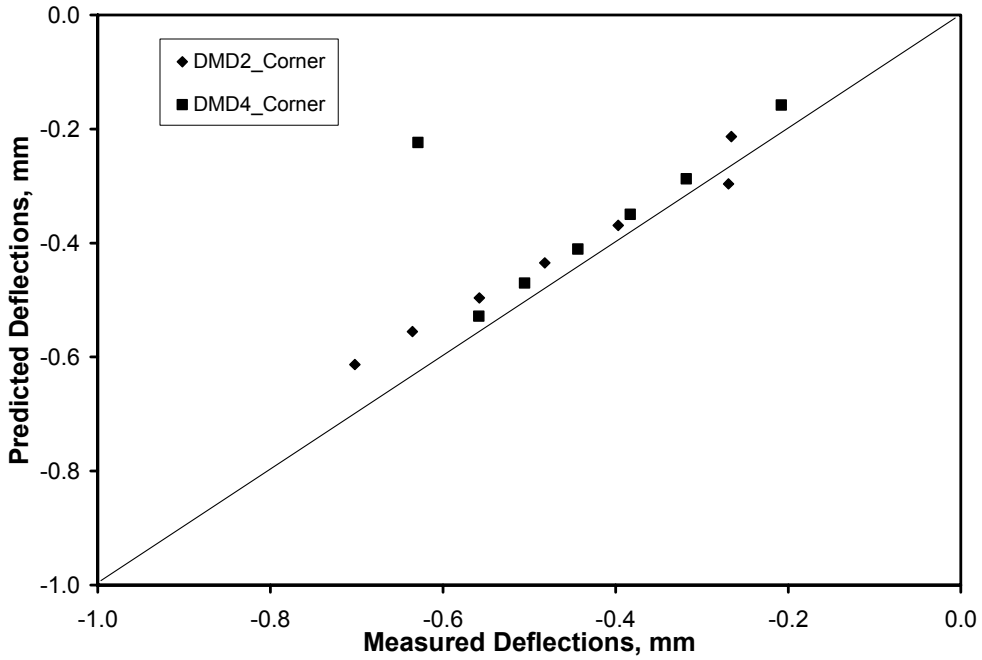

Figure A-36. Measured and predicted corner (DMD2 and DMD4) deflections for Section 541FD under the influence of 20- to 80-kN incremental loads with no significant differences in slab temperature gradients.

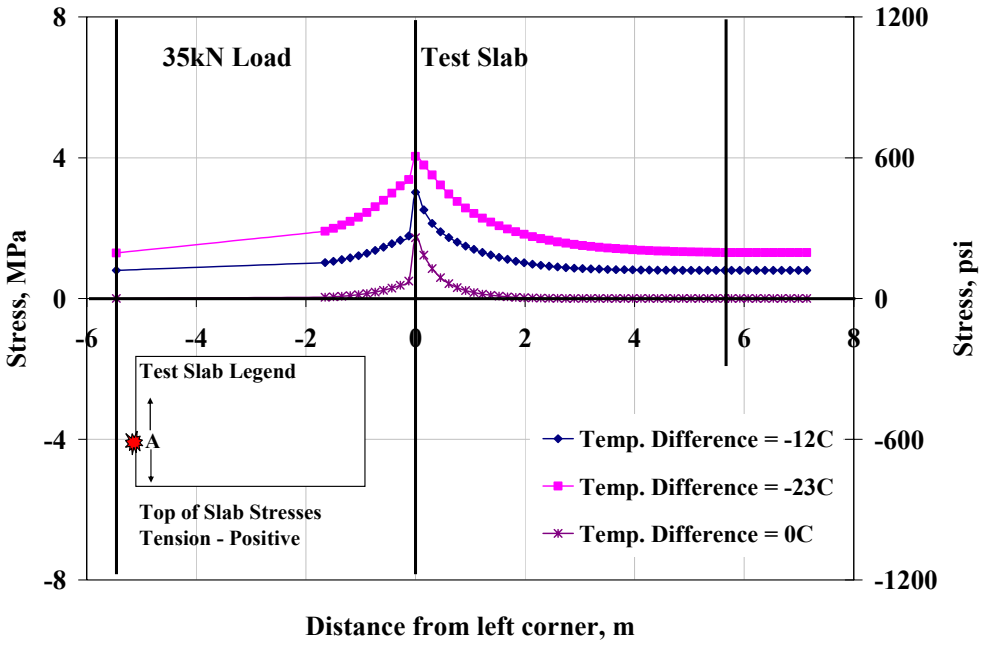

Figure A-37. Influence diagram showing effect of 35-kN moving load on transverse stresses at the transverse joint (Section 520FD, 100-mm slab).

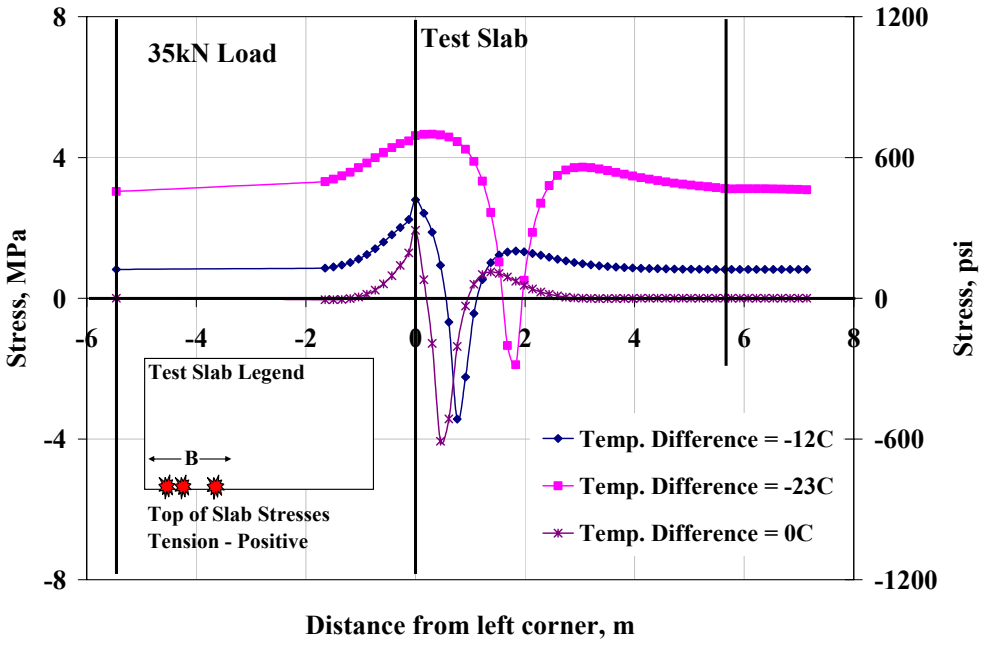

Figure A-38. Influence diagram showing effect of 35-kN moving load on longitudinal stresses at the lane-shoulder joint (Section 520FD, 100-mm slab).

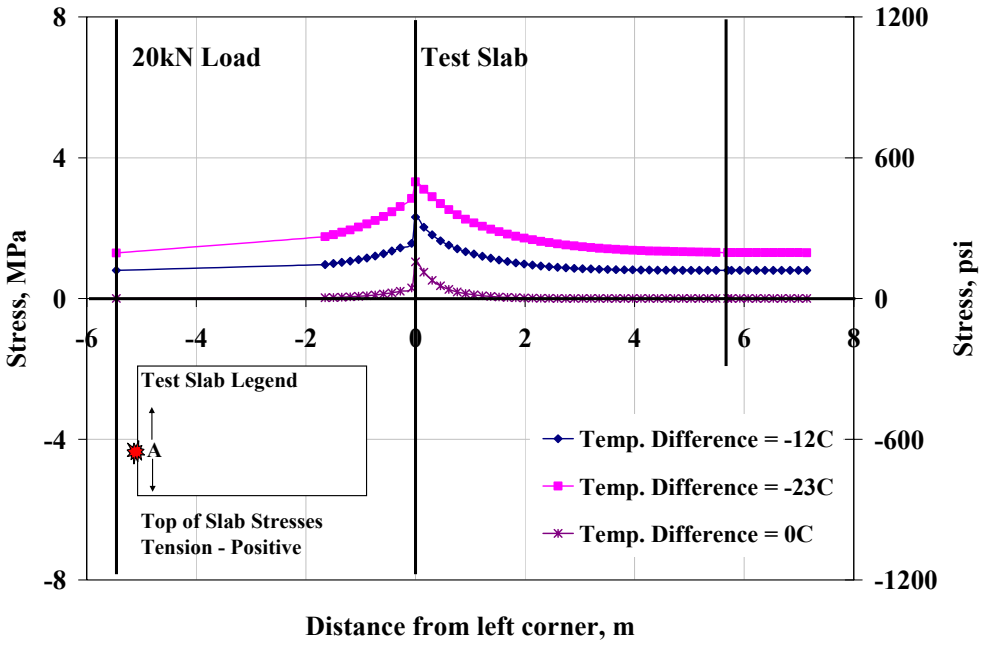

Figure A-39. Influence diagram showing effect of 20-kN moving load on transverse stresses at the transverse joint (Section 520FD, 100-mm slab).

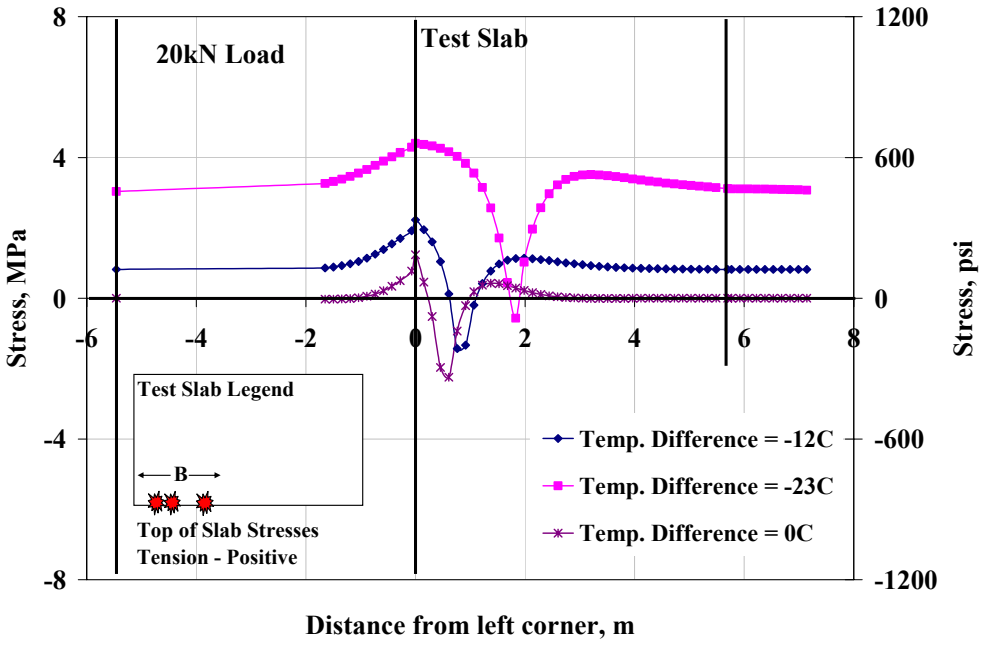

Figure A-40. Influence diagram showing effect of 20-kN moving load on longitudinal stresses at the lane-shoulder joint (Section 520FD, 100-mm slab).

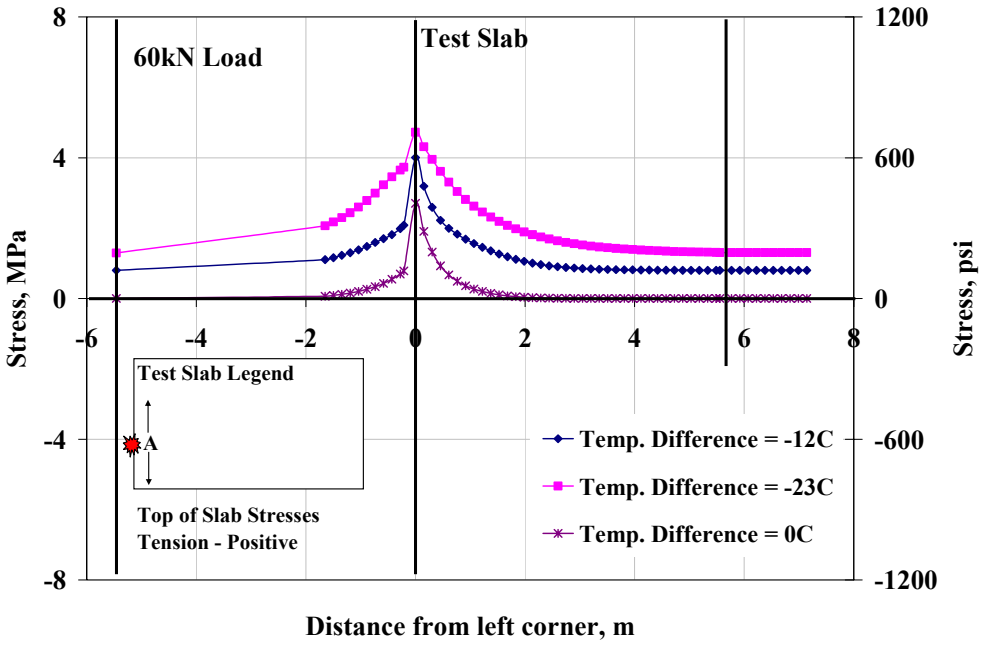

Figure A-41. Influence diagram showing effect of 60-kN moving load on transverse stresses at the transverse joint (Section 520FD, 100-mm slab).

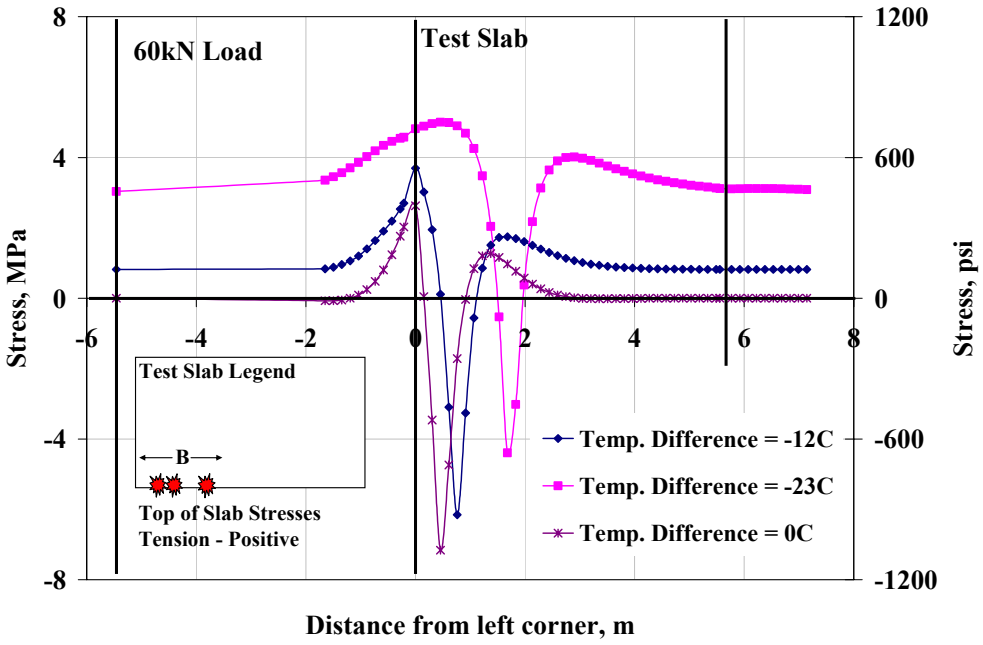

Figure A-42. Influence diagram showing effect of 60-kN moving load on longitudinal stresses at the lane-shoulder joint (Section 520FD, 100-mm slab).

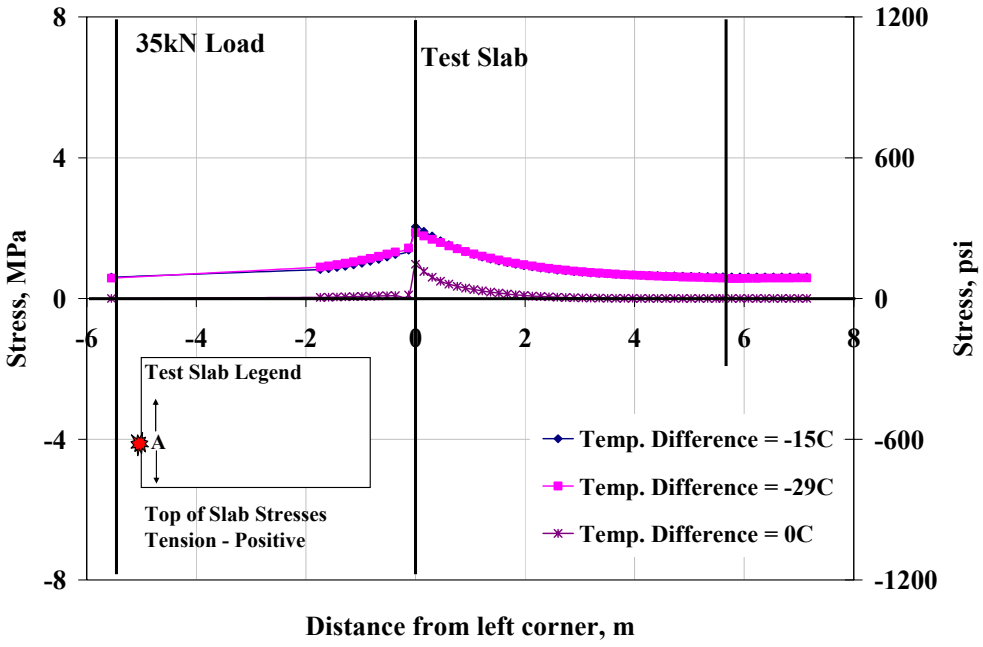

Figure A-43. Influence diagram showing effect of 35-kN moving load on transverse stresses at the transverse joint (Section 524FD, 150-mm slab).

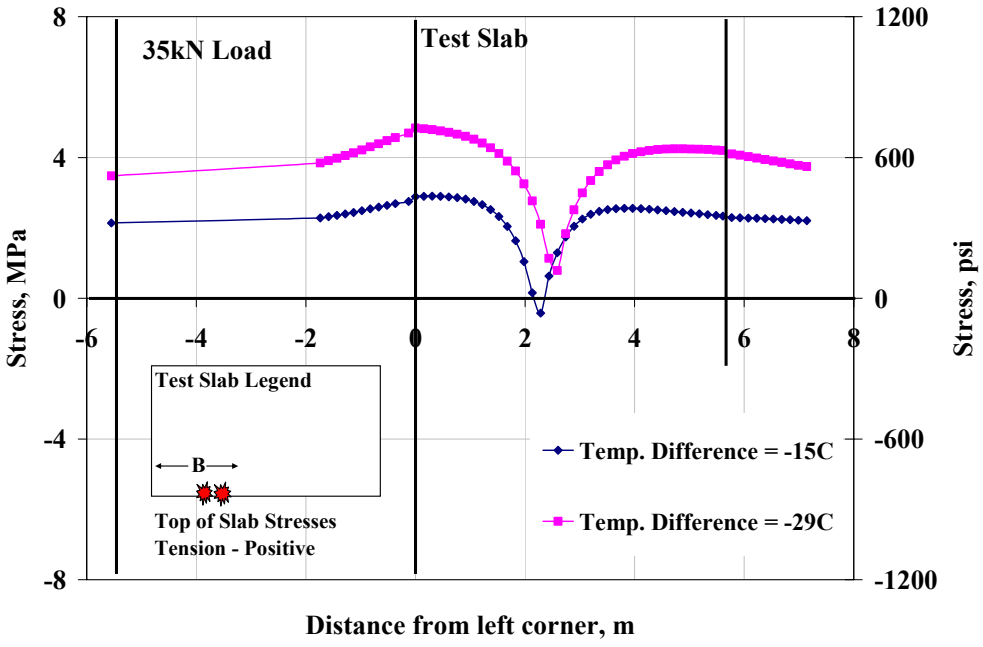

Figure A-44. Influence diagram showing effect of 35-kN moving load on longitudinal stresses at the lane-shoulder joint (Section 524FD, 150-mm slab).

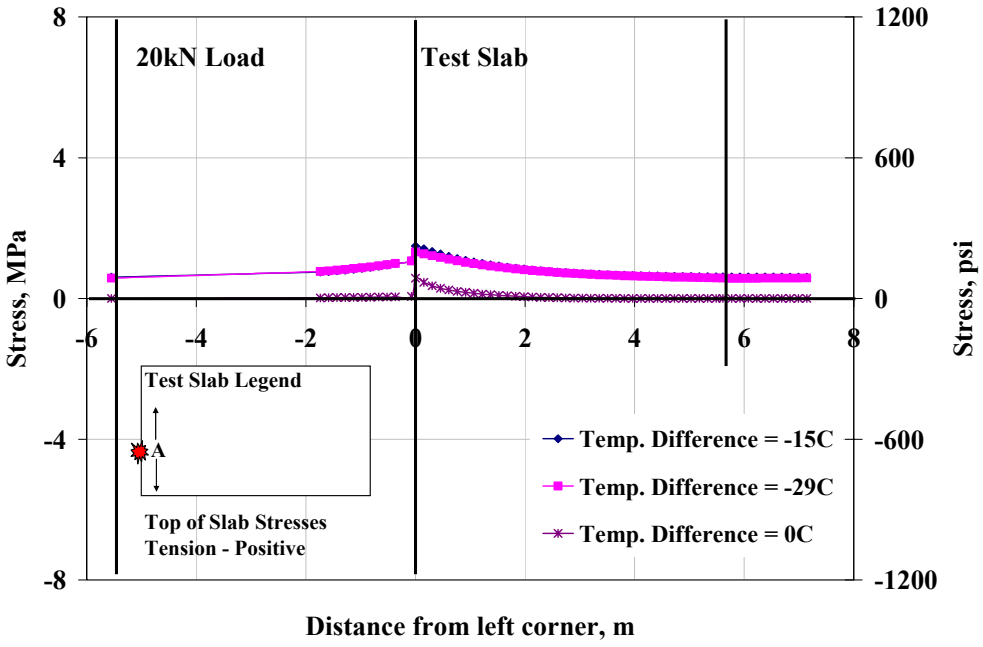

Figure A-45. Influence diagram showing effect of 20-kN moving load on transverse stresses at the transverse joint (Section 524FD, 150-mm slab).

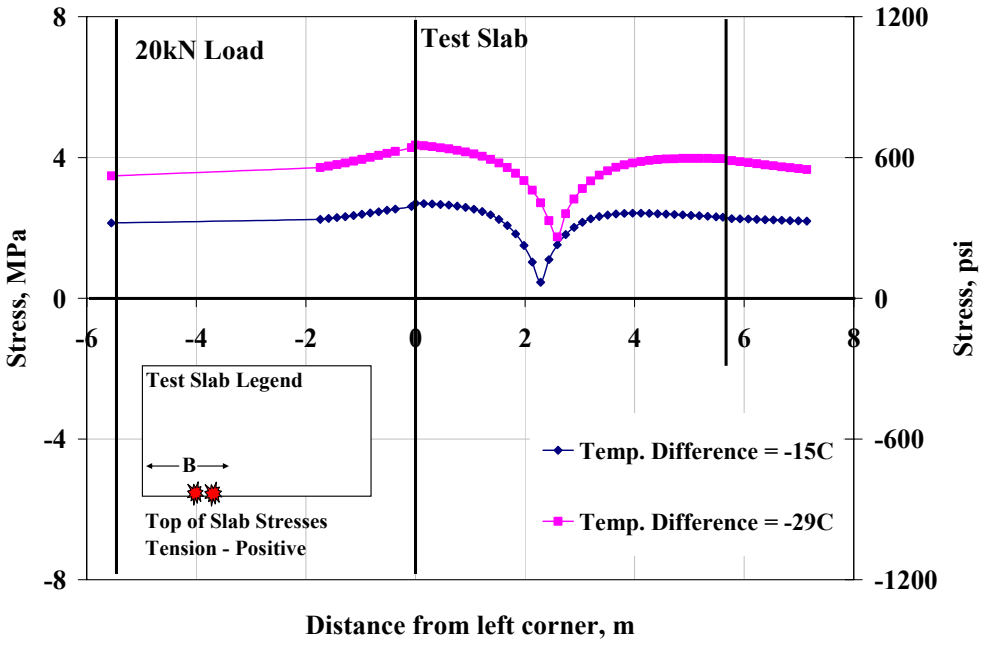

Figure A-46. Influence diagram showing effect of 20-kN moving load on longitudinal stresses at the lane-shoulder joint (Section 524FD, 150-mm slab).

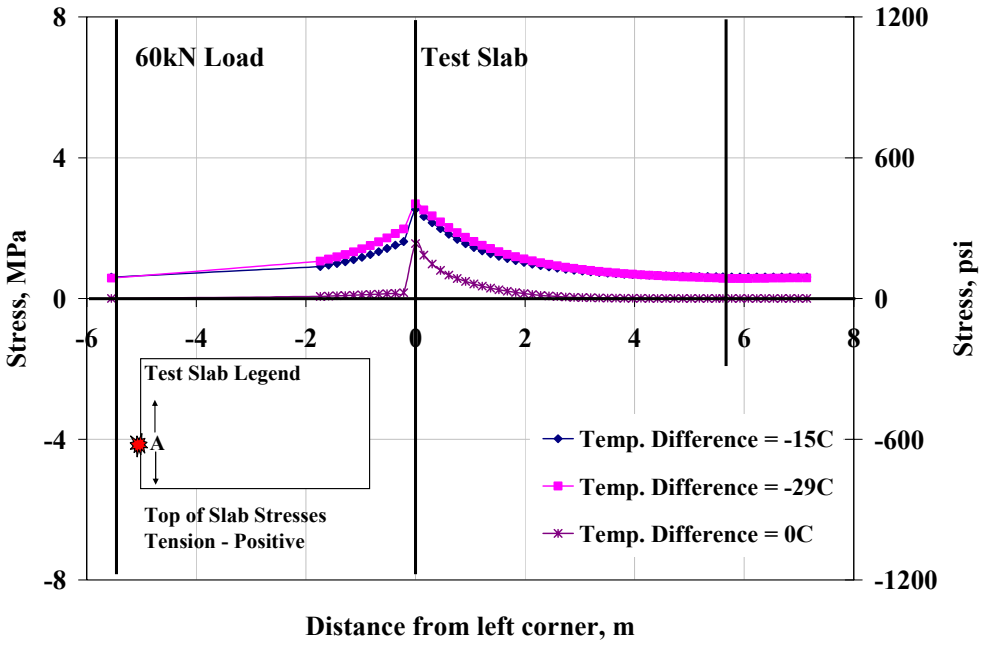

Figure A-47. Influence diagram showing effect of 60-kN moving load on transverse stresses at the transverse joint (Section 524FD, 150-mm slab).

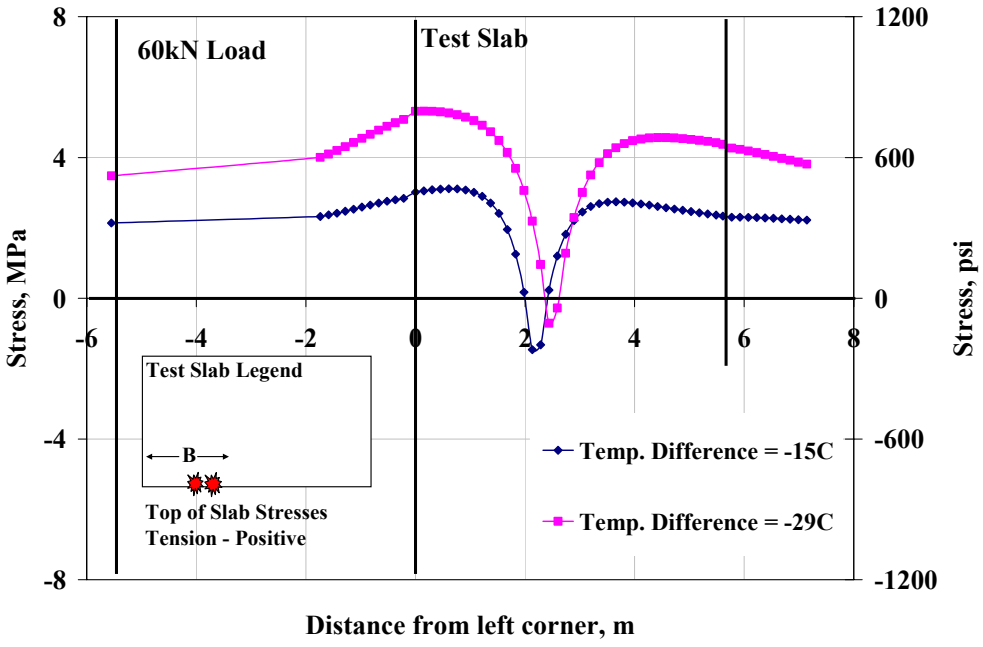

Figure A-48. Influence diagram showing effect of 60-kN moving load on longitudinal stresses at the lane-shoulder joint (Section 524FD, 150-mm slab).

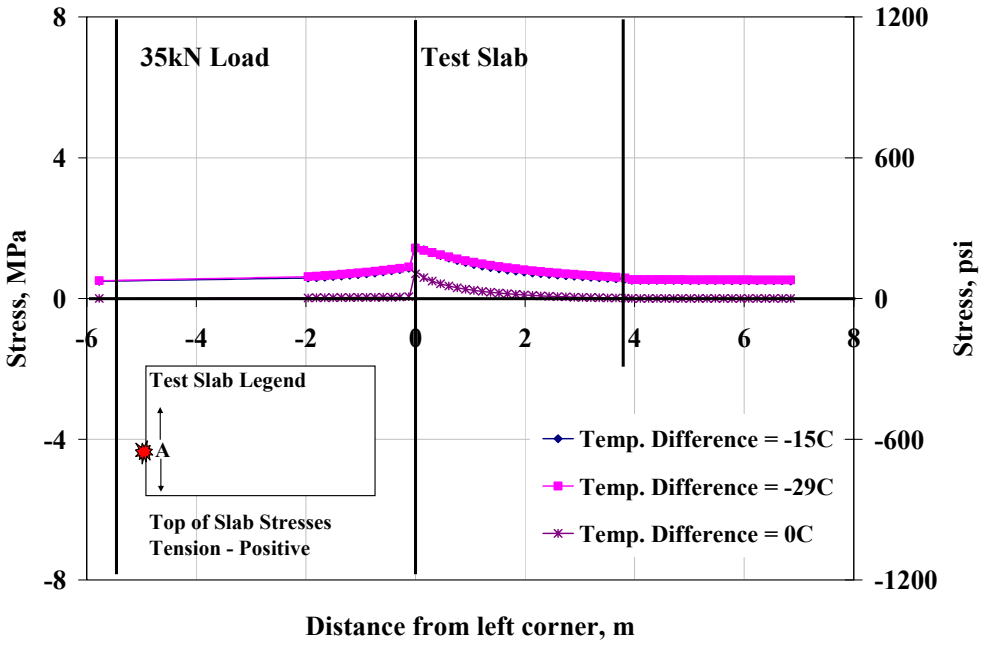

Figure A-49. Influence diagram showing effect of 35-kN moving load on transverse stresses at the transverse joint (Section 530FD, 200-mm slab).

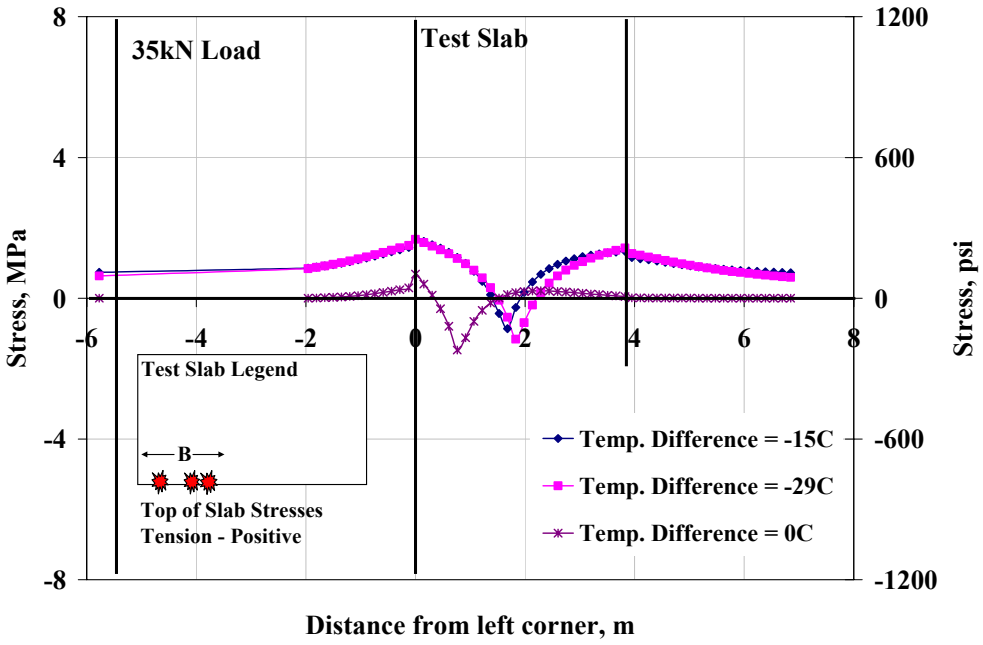

Figure A-50. Influence diagram showing effect of 35-kN moving load on longitudinal stresses at the lane-shoulder joint (Section 530FD, 200-mm slab).

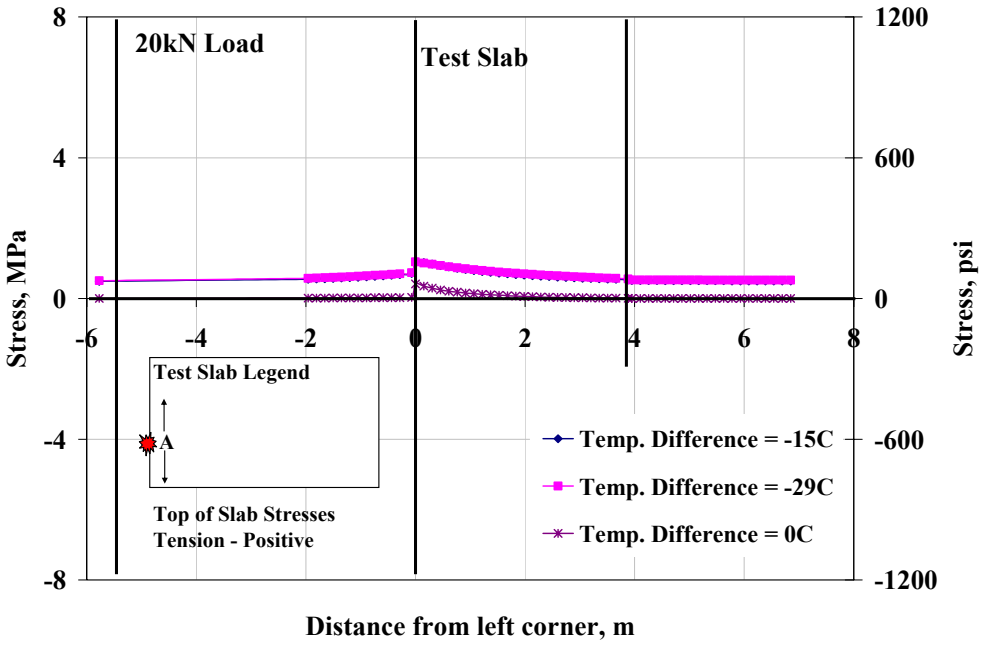

Figure A-51. Influence diagram showing effect of 20-kN moving load on transverse stresses at the transverse joint (Section 530FD, 200-mm slab).

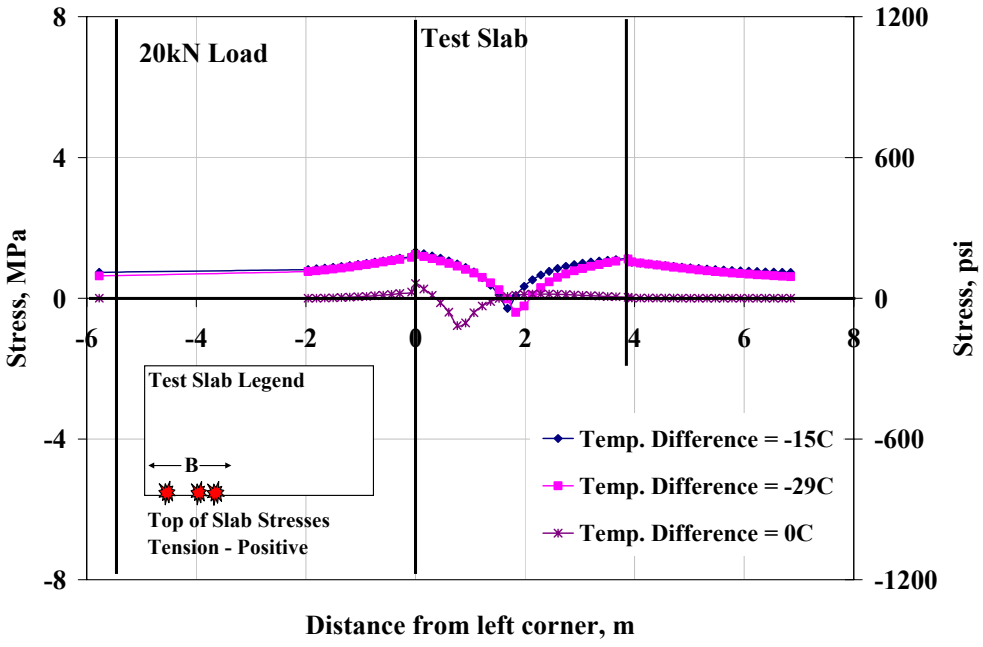

Figure A-52. Influence diagram showing effect of 20-kN moving load on longitudinal stresses at the lane-shoulder joint (Section 530FD, 200-mm slab).

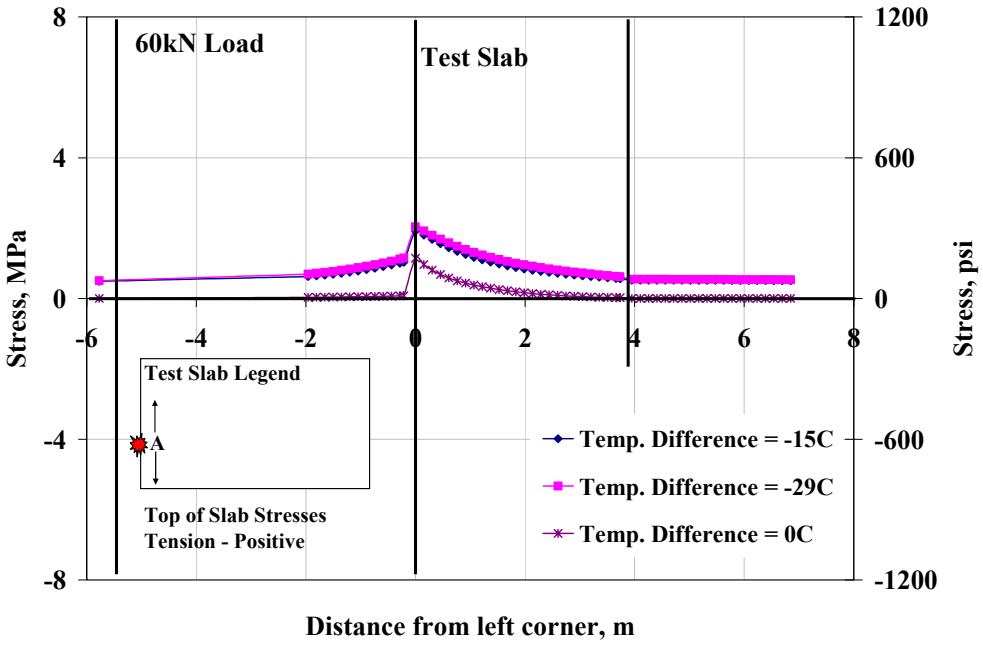

Figure A-53. Influence diagram showing effect of 60-kN moving load on transverse stresses at the transverse joint (Section 530FD, 200-mm slab).

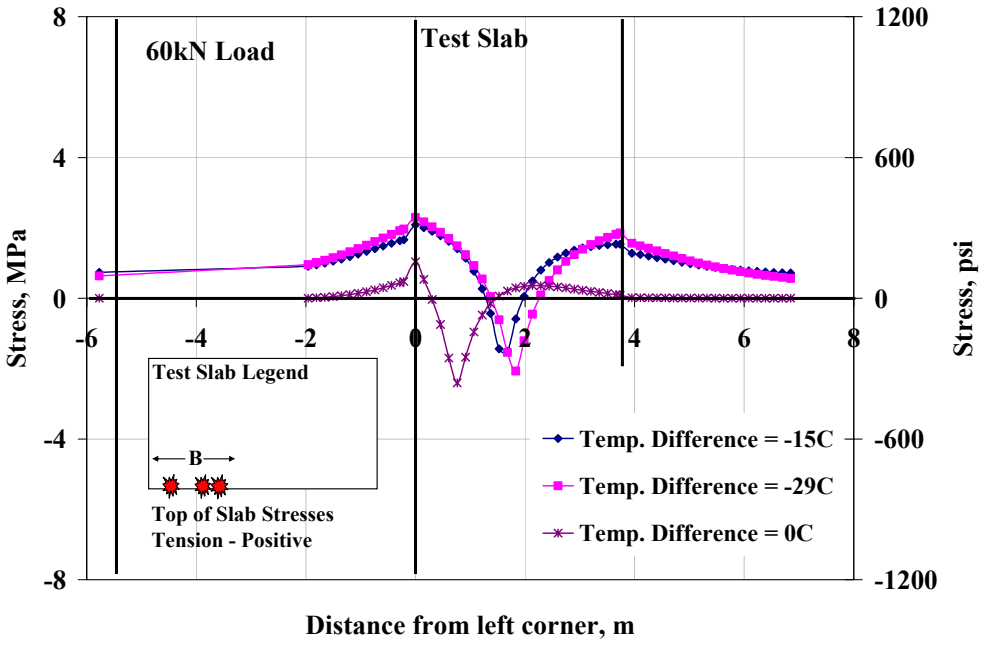

Figure A-54. Influence diagram showing effect of 60-kN moving load on longitudinal stresses at the lane-shoulder joint (Section 530FD, 200-mm slab).

APPENDIX B: FACTORS AFFECTING DIFFERENTIAL SHRINKAGE THROUGH THE DEPTH OF THE SLAB

Several factors affect differential shrinkage through the depth of the slab, including, shrinkage characteristics of the concrete mix, atmospheric relative humidity, saturation level of underlying layers, curing conditions, and concrete modulus of elasticity, as discussed below.

Shrinkage Characteristics

The shrinkage characteristics of a concrete mix are most significantly affected by aggregate properties, cement type and quantity, and amount of mix water.

Aggregate Properties

Some of the earliest experiments on shrinkage gradients and moisture loss were performed by Carlson (1938). He tested 150-mm concrete cubes made with varying combinations of three different cements and two aggregate types. The cubes were cast in copper forms and the tops of the cubes were exposed to a drying environment of 27ºC and 50 percent RH. Measurements of moisture loss and shrinkage were taken at various distances from the exposed concrete surface after 600 days. Carlson's results (Figure B-1) show that the shrinkage gradient through the cube is significantly affected by the cement properties and aggregate type. The figure shows shrinkage through the slab depth as a percent of surface shrinkage.

Meininger (1966) tested shrinkage characteristics of 75 × 100 × 400 mm prisms of concrete with various coarse aggregates that were dried at about 21ºC and 50 percent RH. The results of his test are shown in Table B-1. He concluded that due to the source of coarse aggregate alone, concrete shrinkage can vary up to 100 percent. Fine aggregate can have up to a 20 percent effect on concrete shrinkage. A change in both coarse aggregate and fine aggregate

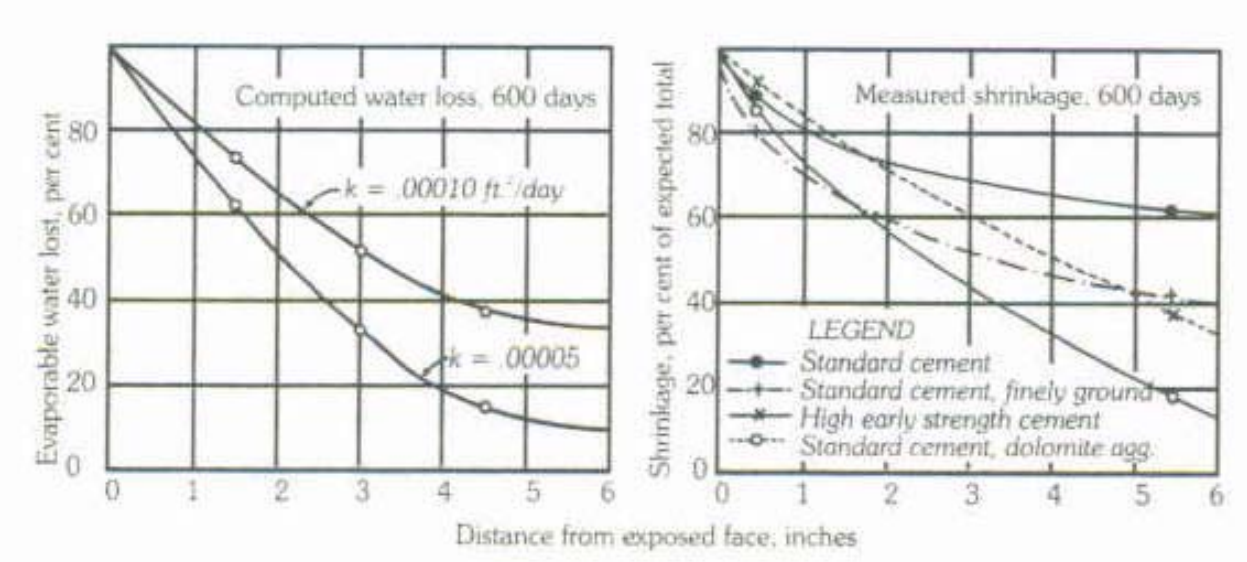

1 in = 25.4 mm, 1 ft = 0.305 m

Figure B-1. Comparison between computed distribution of drying and measured distribution of shrinkage in 150-mm cubes of concrete drying from one face only (from Carlson, 1938).

Table B-1 Effect of Coarse Aggregate on Drying Shrinkage of Concrete (Meininger, 1966)

	Shrinkage, microstrains	
Coarse aggregate rock types	**7 days drying**	**182 days drying**
Quartz	180	530
Igneous, andesite, sandstone	180	560
Greywacke, quartz, limestone, granite	200	620
Granite, quartzite	220	640
Schist, granite gneiss	210	660
Impure limestone, sandstone, igneous	230	640
Igneous	210	700
Sandstone, limestone	240	700
Granite, granite gneiss	240	750
Sandstone	230	740
Sandstone, greywacke	290	920
Sandstone, greywacke	300	900
Sandstone, greywacke	320	990

can result in an increase of up to 150 percent. Meininger also suggested that going from 64 mm maximum aggregate size to 10 mm maximum aggregate size would increase shrinkage by as much as 25 percent. Other reports also suggest using the largest possible size aggregate (Collins, 1989; Babaei and Purvis, 1994; Krauss and Rogalla, 1996).

Krauss and Rogalla (1996) observed that aggregate type was the most significant concrete material factor affecting when concrete cracked. Limestone aggregate concretes were the most resistant to cracking, while river gravel had the shortest time to cracking of the aggregates tested. Burrows (1998) also studied the effect of the type of aggregate used on the drying shrinkage of concrete. As shown in Table B-2, quartz and limestone exhibited the least drying shrinkage and sandstone the highest. Babaei and Purvis (1994) recommended that aggregates should have high specific gravity and that coarse aggregate absorption should be less than 0.5 percent and fine aggregate absorption less than 1.5 percent. The Portland Cement Association (PCA) bulletin on "Design and Control of Concrete Mixtures" recommends avoiding aggregates containing excessive amounts of clay in order to minimize drying shrinkage (PCA, 1994).

Table B-2 One-year Drying Shrinkage for Various Aggregate Types (Burrows, 1998)

Coarse Aggregate	**One-Year Shrinkage, %**
Sandstone	0.097
Basalt	0.068
Granite	0.063
Limestone	0.050
Quartz	0.040

Cement Type and Quantity

Cement type and quantity also affects shrinkage characteristics of a concrete mix since contraction of the cement paste is the cause of shrinkage in concrete (Ytterberg, 1987). The two cement factors that affect shrinkage are coarseness and C_3A content. Studies by Tremper and Spellman (1963), Whiting (1979), and Troxell et al. (1968) suggest that high C_2S and low C_3A are desirable in cements in order to produce concrete with lower shrinkage. In Tremper and Spellman's study, the concrete containing high C_3A and high alkali had 20 percent greater shrinkage than the concrete containing the Type II low alkali cement. Tremper and Spellman also suggest that concrete containing coarse ground cement has lower shrinkage and curling than concrete containing fine ground cement. In a similar study, Stockett et al. (1967) reported that Type II portland cement mortar had lower shrinkage than mortars made from Types I and III cements. These results are consistent with those in more recent reports such as those by Krauss and Rogalla (1996) and Burrows (1998).

Washa (1955) observed that increasing cement content from 280 to 450 kg of cement per cubic meter may increase shrinkage by about 25 percent. Similar results were observed by Troxell et al. (1968), who observed shrinkage of 560, 640, and 700 microstrains for mixes with 280, 325, and 400 kg/m^3, respectively. Meininger (1966) also reported a 15 percent change in shrinkage for change in cement source, and approximately a 10 percent change in shrinkage when cement quantity was changed from 307 to 418 kg/m^3.

Bloom and Bentur (1995) tested both free and restrained shrinkage of several normal and high-performance concretes and concluded that mixes containing higher cement content cracked much sooner due to greater shrinkage than those with lower cement contents. Similar results were observed by Krauss and Rogalla (1996), Schmitt and Darwin (1999), and French et al. (1999).

Shrinkage-Reducing Admixtures

One way of reducing shrinkage in concrete is through the use of shrinkage-reducing admixtures or shrinkage-compensating cement. Ytterberg (1987) states that "…edge curling is generally less (with shrinkage compensating concrete) than with conventional portland cement concrete." Recently, after evaluating several concrete mixtures with varying water-cement ratios with and without shrinkage reducing admixtures, Subramaniam et al. (2004) concluded that free shrinkage (and stresses) were significantly reduced (by as much as 50 percent) with the addition of shrinkage reducing admixtures for all concretes tested. In another study, Folliard and Berke (1997) observed that shrinkage-reducing admixtures were effective in reducing the shrinkage of high-performance concrete, resulting in a significant decrease in restrained shrinkage cracking, as shown in Table B-3. Similar results were observed by Holt and Leivo (2004) as shown in Figure B-2.

Table B-3 Summary of Free Shrinkage Measurements and Restrained Shrinkage Ring Cracking (Folliard and Berke, 1997)

Mixture Description	28-Day Drying Shrinkage (%)	120-Day Drying Shrinkage (%)	Average Time to Ring Cracking (days)	Average Crack Area per Ring (mm^2)
Control Concrete	0.049	0.070	44	5.9
Concrete with 1.5%SRA	0.032	0.050	No cracks after 120 days	0
Silica Fume Concrete	0.051	0.077	38	25.3
Silica Fume Concrete with 1.5%SRA	0.024	0.044	95	3.1

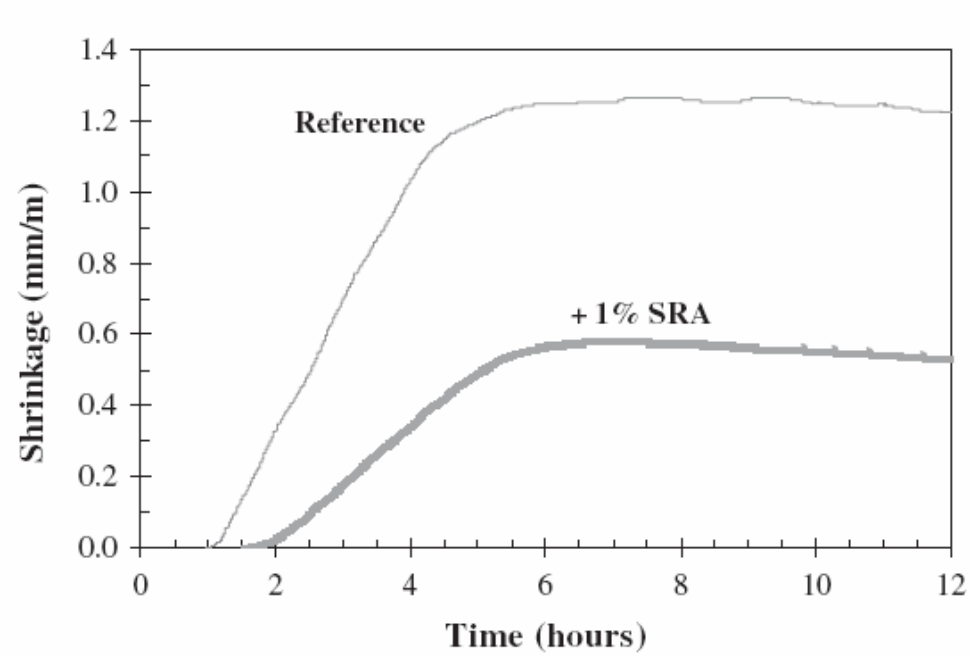

Figure B-2. Average effect of adding 1 percent shrinkage-reducing admixture to high-strength concrete on early age drying shrinkage after casting (from Holt and Leivo, 2004).

Shrinkage-Compensating Cement

Shrinkage-compensating cement is a material that causes expansion of concrete during curing. The restraint on the expansion results in the concrete being subject to compression the first few days after placement. The pre-compression resulting from the expansion restraint balances out the shrinkage stresses, which reduces drying shrinkage.

Folliard et al. (1994) observed that the shrinkage-compensating concrete expands under restraint by about 0.04–0.08 percent during the moist-curing period. Pittman et al. (1999) observed that mortar bars with Type K cement expanded up to 4 times as much as those made with Type I cement (Figure B-3). They tested a number of different shrinkage-compensating concrete mixtures and found that the expansion restraint substantially reduces net shrinkage. The shrinkage-compensating concrete bars exhibited significant early (first 7 days) expansion as long as the concrete mixtures were exposed to moist curing. The expansion was followed by

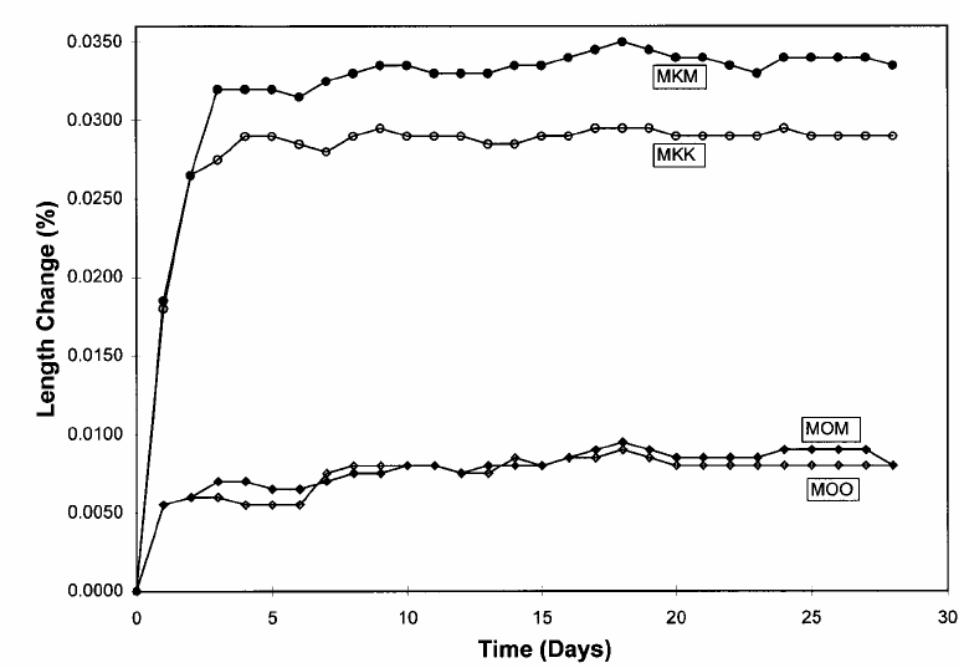

Figure B-3. Mortar mixture bar expansions of shrinkage-compensating Type K cement (MKM and MKK), and Type I cement (MOM and MOO) (from Pittmann et al., 1999).

shrinkage after the 7-day moist cure period. The net volume change with the shrinkage-compensating concrete mixtures was a small net expansion or shrinkage. They conclude that the shrinkage-compensating concrete mixtures would cause much less shrinkage under restraint as compared to concrete mixtures using Type I portland cement.

Mix Water

All of these studies on the effects of aggregate and cement type indicate that shrinkage is mostly related to the water demand of each constituent material in the mix, and suggest that drying shrinkage is mostly caused by two factors: 1) Materials with high water demand; 2) Coarse aggregates that are moisture sensitive and that actually shrink when dried (Ytterberg, 1987). Thus, drying shrinkage can be reduced by using less water in the concrete. Some ways to reduce water content are:

- Coarser sand
- Aggregates free of clay and other fine materials
- Coarser ground cement
- Cement with low C_3A content
- Largest possible maximum sized coarse aggregate
- Shortest travel time from central mix plant to job
- Fewest agitating revolutions after complete mixing is achieved
- Lower mixture temperatures.

Although using less water in the concrete reduces shrinkage, this is not the case if water is reduced beyond an optimum point (for a fixed amount of cement) particularly by using high-range water reducers (HRWRs) or superplasticizers, because a consequence of using less water in the mix is an increase in autogenous shrinkage. Whiting (1979) showed that concrete made with HRWRs that contained 10 to 20 percent less water had only slight reductions in shrinkage compared to a low slump control concrete. Similar results were observed by Rixom and Waddicor (1981), who observed little difference in shrinkage between a control with a 0.65 water-cement ratio and a concrete containing HRWRs. In fact, at double dosage rates of HRWRs, shrinkage of concrete made with HRWRs was greater than the shrinkage of the control concrete. Likewise, Gebler (1982) concluded that there was essentially no difference in shrinkage using HRWRs. Holt and Leivo (2004) observed much higher autogenous shrinkage at early age after casting for concretes with low water-cement ratio as shown in Figure B-4. Their results are consistent with those reported by Baroghel-Bouny (1996) who observed greater long-term autogenous shrinkage for cement pastes with lower water-cement ratio as shown in Figure B-5.

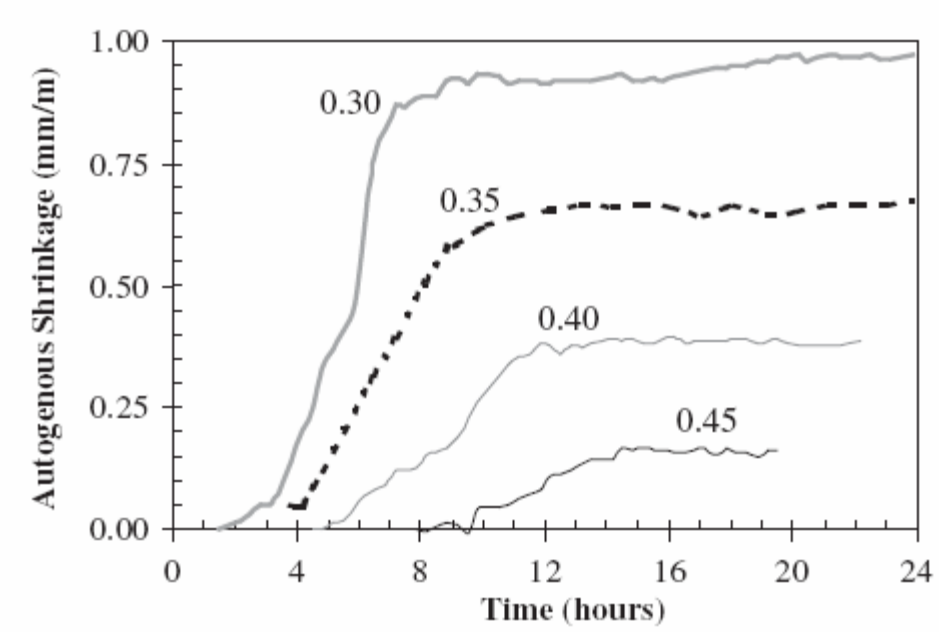

Figure B-4. Effect of water-cement ratio on early age autogenous shrinkage of mortar after casting (from Holt and Leivo, 2004).

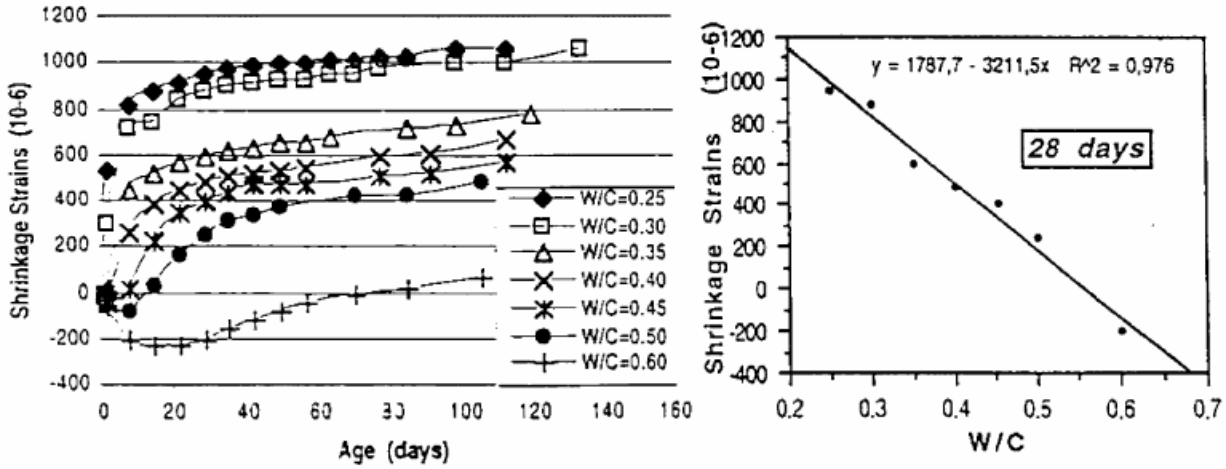

Figure B-5. Correlation between autogenous strain and water-cement ratio for cement pastes aged to 28 days (from Baroghel-Bouny, 1996).

Because both higher water content (to an extent before significant autogenous shrinkage) and higher cement content are both associated with increased shrinkage, several studies suggest maximizing aggregate volume (reducing paste content) to reduce shrinkage potential (Collins, 1989; Babaei and Purvis, 1994; Schmitt and Darwin, 1999; French et al., 1999). Schmitt and Darwin (1999) recommended that the combined volume fraction of water and cement should not exceed 27 percent. Babaei and Purvis (1994) recommended that the water content in the concrete mix should be less than 192 kg/m^3. Bissonnette et al. (1999) conducted drying shrinkage tests on several 4 × 8 × 32 mm and 50 × 50 × 400 mm specimens of paste and mortar. Figure B-6 shows that samples with higher paste volume had higher ultimate weight loss and consequently higher ultimate shrinkage.

It should be noted that while concrete with higher water content shrinks more, an increase in creep tends to offset the increased shrinkage. Many of the factors that influence shrinkage characteristics of a concrete mix also affect creep characteristics of the mix.

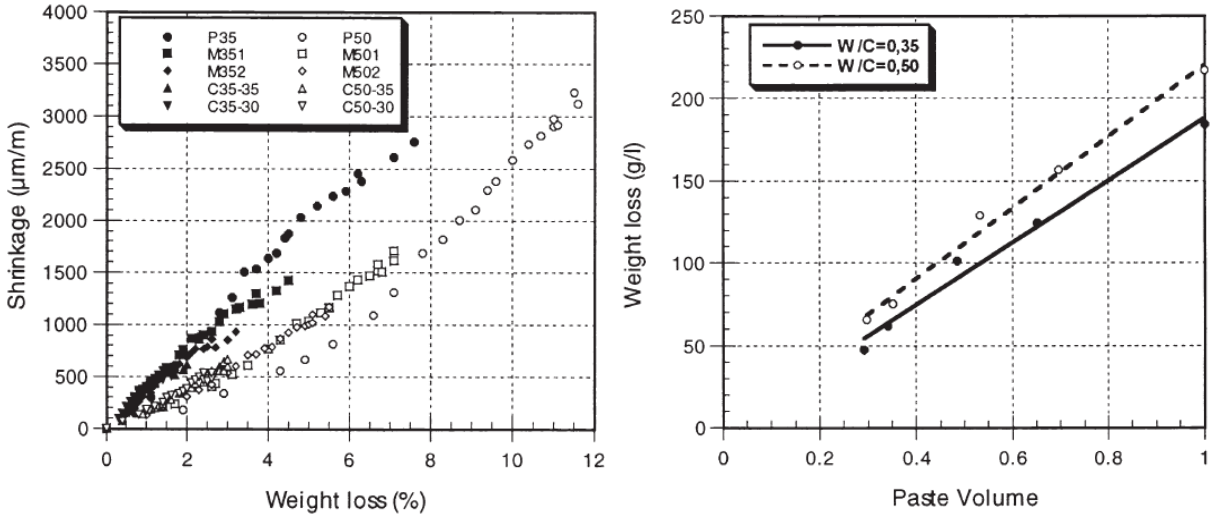

Figure B-6. Relation between shrinkage and weight loss and between weight loss per unit volume and paste volume (from Bissonnette et al., 1999).

Relative Humidity

Relative humidity is an important factor that affects the shrinkage gradient since concrete loses more water at lower ambient relative humidity, resulting in more shrinkage. Figure B-1 (Carlson, 1938) shows that greater moisture loss and shrinkage occurs near the exposed surface, and that the amount of moisture loss and shrinkage decreases with increasing distance from the exposed surface. Abrams and Orals (1965) measured relative humidity at various depths in 150 mm concrete slabs exposed to ambient humidity ranging from 10 percent RH to 75 percent RH. The bottoms of the slabs were maintained at 75% RH and 90% RH. The results shown in Figure B-7 indicate that concrete loses more moisture and at a faster rate at a lower relative humidity.

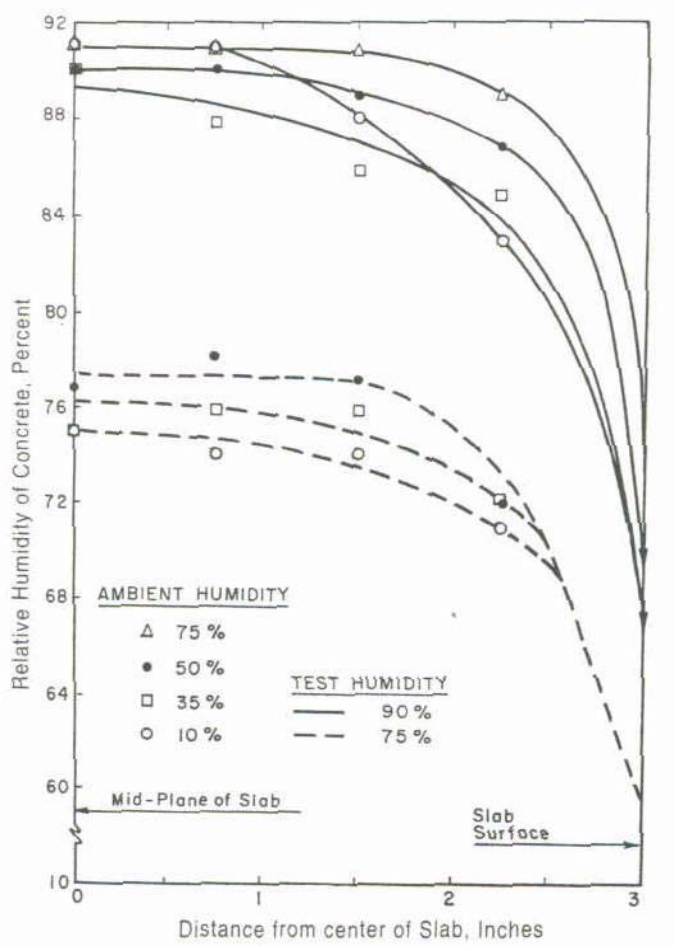

1 in = 25.4 mm

Figure B-7. Effect of ambient humidity gradient through slab sections (from Abrams and Orals, 1965).

Keeton (1979) developed shrinkage gradient models for 380 mm slabs exposed to relative humidity ranging from 20 percent RH to 100 percent RH as shown in Figure B-8. At 20 percent RH, shrinkage difference between the top and bottom surface of the slab was 200 microstrains, as compared to 50 microstrains at 90 percent RH. The higher shrinkage gradients at lower relative humidity values result in greater curling moment and greater upward slab curling. In a recent study on drying shrinkage of various 4 × 8 × 32 mm specimen, Bissonnette et al. (1999) also observed the considerable influence of ambient relative humidity (Figure B-9). Based on free shrinkage tests on normal and high-performance concrete, Altoubat and Lange (2001) observed that shrinkage characteristics at early ages immediately after casting are less influenced by ambient conditions because shrinkage is driven by a complex combination of internal drying,

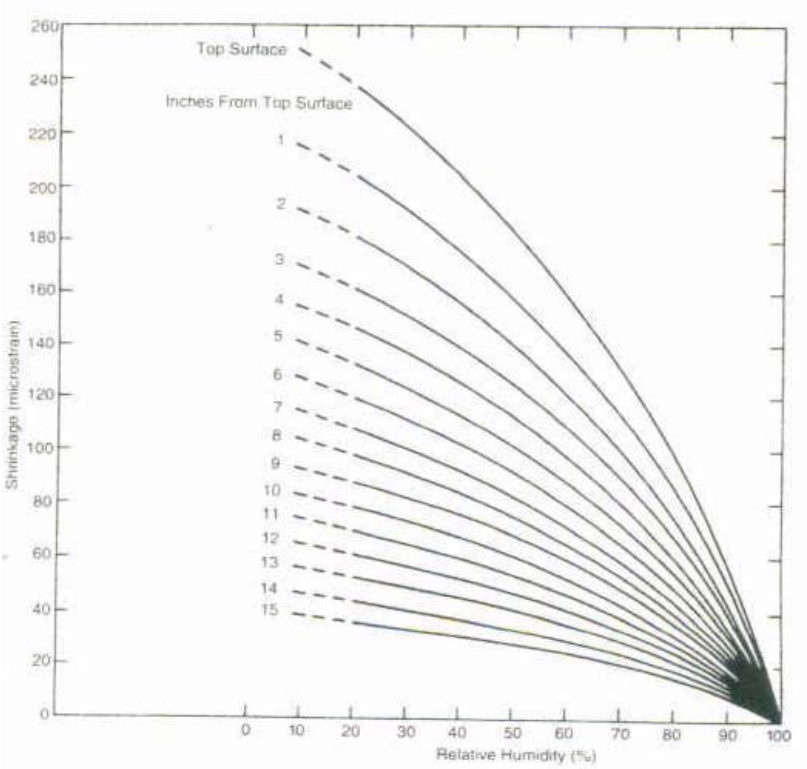

Figure B-8. One year of shrinkage data for a 380 mm slab as a function of relative humidity with only the top surface exposed to drying (from Keeton, 1979).

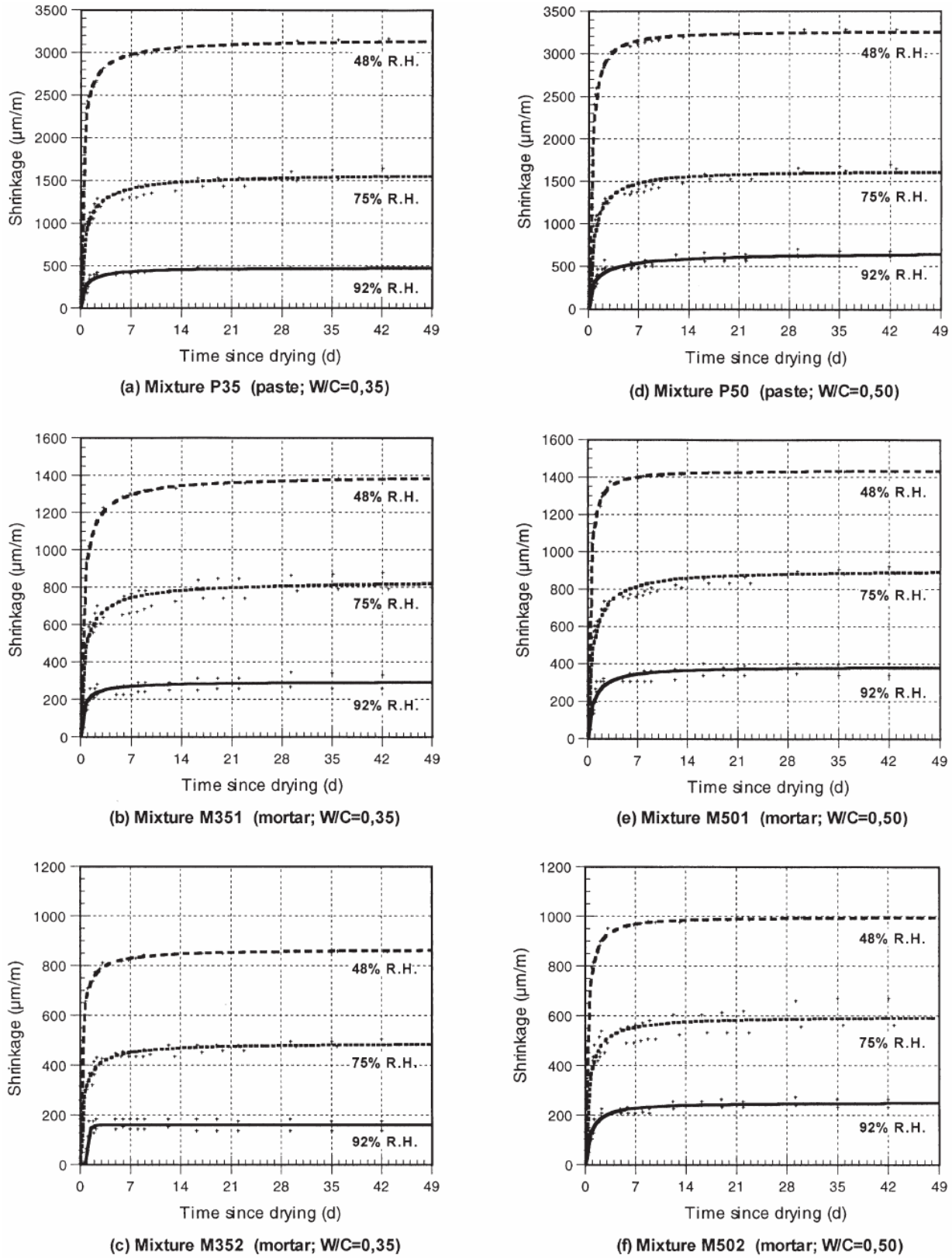

Figure B-9. Drying shrinkage results of various 4 × 8 × 32 mm specimen (from Bissonnette et al., 1999).

external drying, and thermal effects. The results of these studies suggest that ambient conditions are more influential during the later stages of concrete strength development, after the concrete has set.

Moisture from Underlying Layers

Because curling in concrete slabs is caused by shrinkage gradients between the top of the slab and the bottom of the slab, moisture content of the underlying layers that provide the internal relative humidity for the bottom of the slab is just as important as the ambient relative humidity of the air that affects the internal relative humidity at the top of the slab. Nagataki (1970) tested 100 × 100 × 500 mm concrete specimens cured for 7 days and then exposed them to a drying environment of 24ºC and 50 percent RH. One specimen was exposed to drying on all sides, one only to drying from the top, and one to drying on the top with the bottom on wet sand at 10 percent moisture content. The results shown in Figure B-10 illustrate that the shrinkage gradient was small for the specimen exposed to drying on all sides, and was greatest for the specimen with the bottom in contact with moist sand. In this case, the differential shrinkage between the top of the slab and the bottom of the slab was greater than 400 microstrains. Leonards and Harr (1959) observed that slabs drying on a saturated subbase curled upwards to a greater extent than an identical slab drying on a dry granular subbase as shown in Figure B-11.

Concrete Curing

Curing is not a significant factor that affects the concrete's drying shrinkage. Test data show that moist curing does not affect differential shrinkage between the top and bottom of the slab and therefore does not reduce curling. Although curing has no effect on whether a slab will curl or how much it will curl, the duration of curing does influence when a slab will curl (Suprenant, 2002). Several studies (Carlson, 1938; Keene, 1961; Childs and Kapernick, 1958;

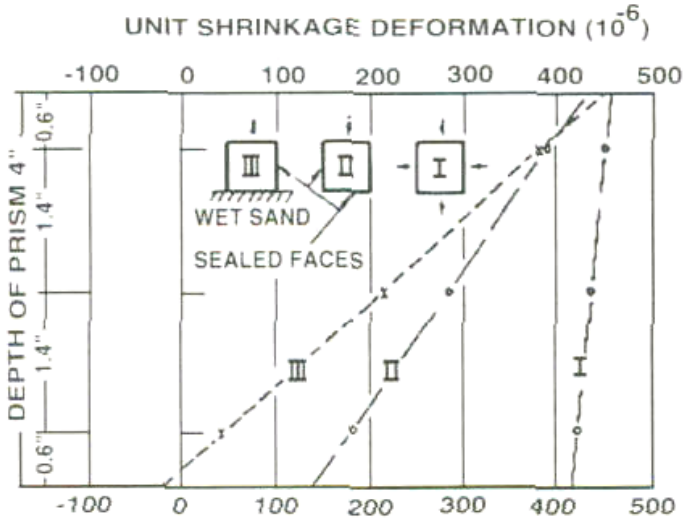

1 in = 25.4 mm

Figure B-10. Distribution of unit shrinkage deformation in prisms under different drying conditions (from Nagataki, 1970).

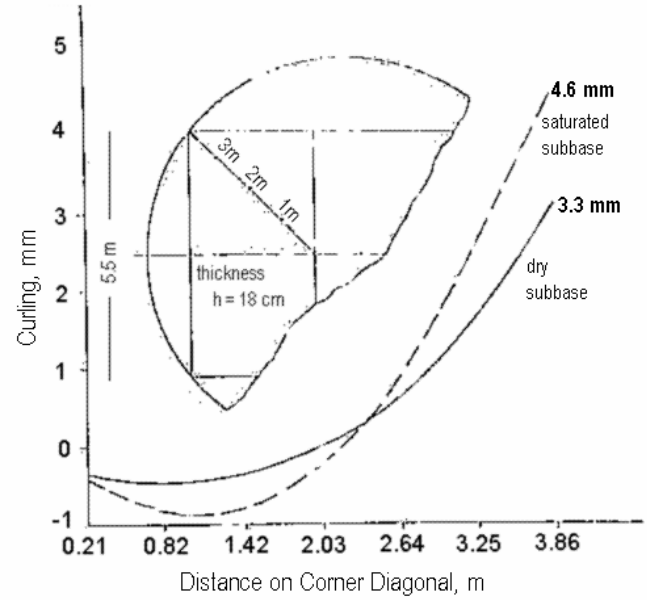

Figure B-11. Upward curvature of slab after initial drying cycle on dry granular subbase and on a saturated subbase (from Leonards and Harr, 1959).

Tremper and Spellman, 1963; and Perenchio, 1997) show no benefit of duration of curing on shrinkage. Meininger (1966) suggests a maximum of 5 percent reduction in shrinkage for concrete cured 7 days instead of 3 days.

All of these studies suggest that extended curing time only delays curling but does not reduce it. However, the delay in curling due to curing does result in reduced stresses and lower cracking potential during early age when the concrete has not gained adequate strength. Adequate and timely curing is a key factor in reducing early-age cracking. Figure B-12 shows the effect of one of the factors (wind speed) during curing and its effect on early-age shrinkage.

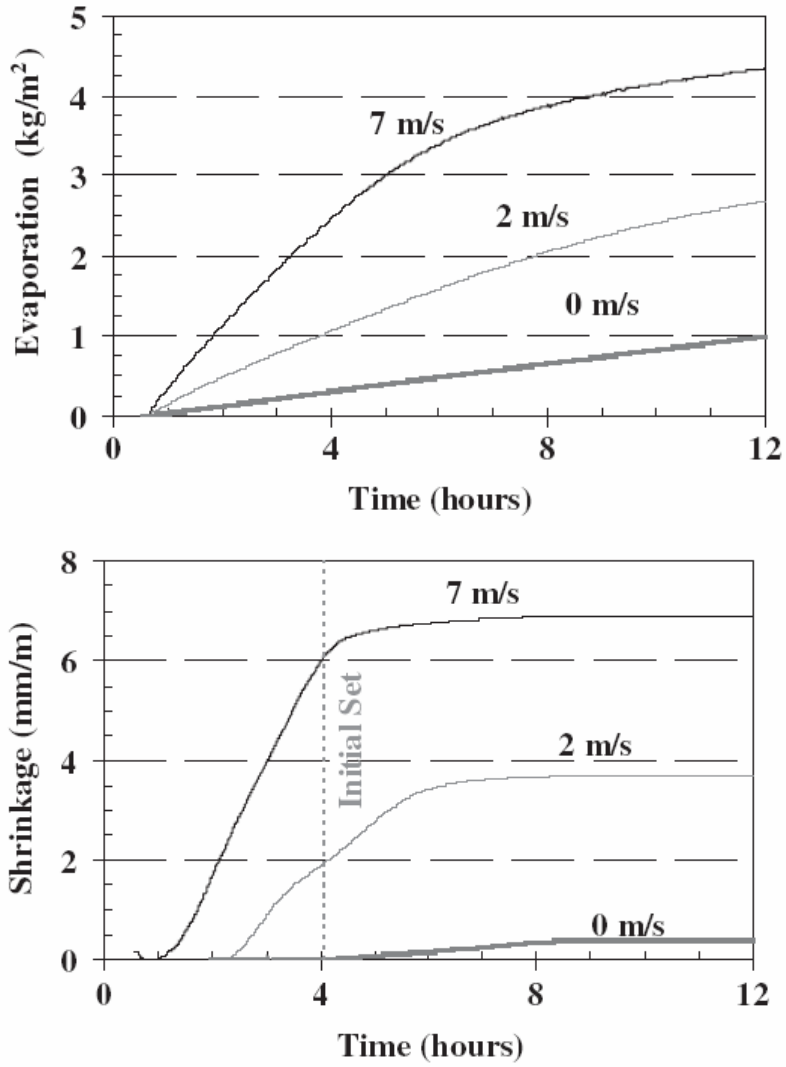

Figure B-12. Early-age evaporation and horizontal drying shrinkage from a slab at three different wind speeds (from Holt and Leivo, 2004).

FACTORS AFFECTING CREEP DUE TO SLAB RESTRAINT

The two phenomena, shrinkage and creep of concrete are influenced by common processes and the mix characteristics that affect shrinkage also affect creep. Altoubat and Lange (2001) observed that the tensile creep at early age was proportional to the free shrinkage as shown in Figure B-13. The ratio of creep to shrinkage ranged from 0.5 to 0.6 for all mixtures, including normal concrete and high-performance concrete, irrespective of their water/cement ratio, suggesting that factors affecting shrinkage also affect creep characteristics.

Bissonnette and Pigeon (1995) performed drying shrinkage and creep tests under tension of concrete mixtures with and without silica fume at two water/cement ratios (0.35 and 0.55). Their results, shown in Figure B-14 indicated that tensile creep increases with an increase in water to cement ratio and was not significantly influenced by the use of silica fume.

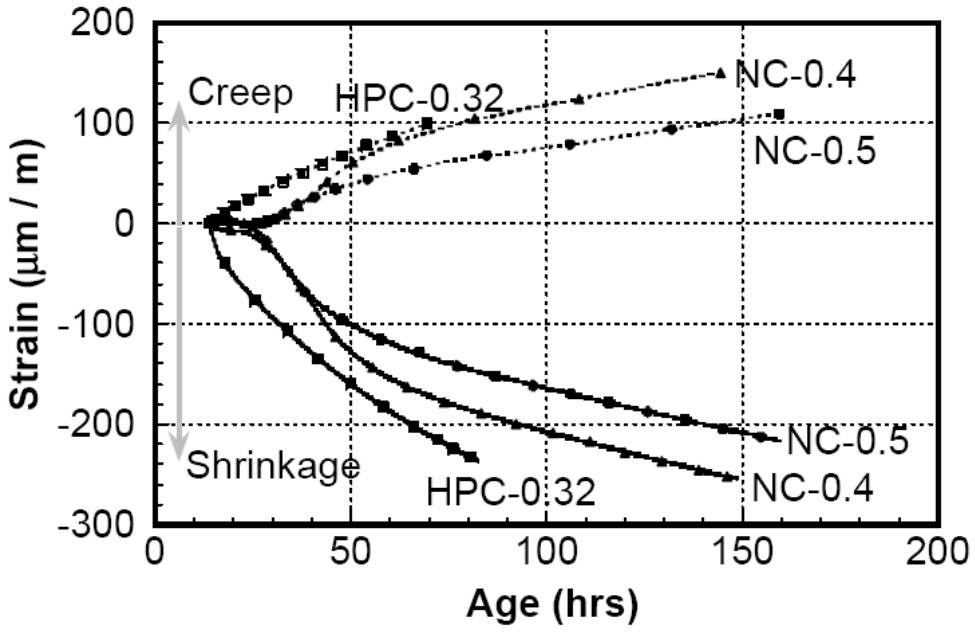

Figure B-13. Shrinkage and creep strains after casting for plain concrete mixtures (from Altoubat and Lange, 2001).

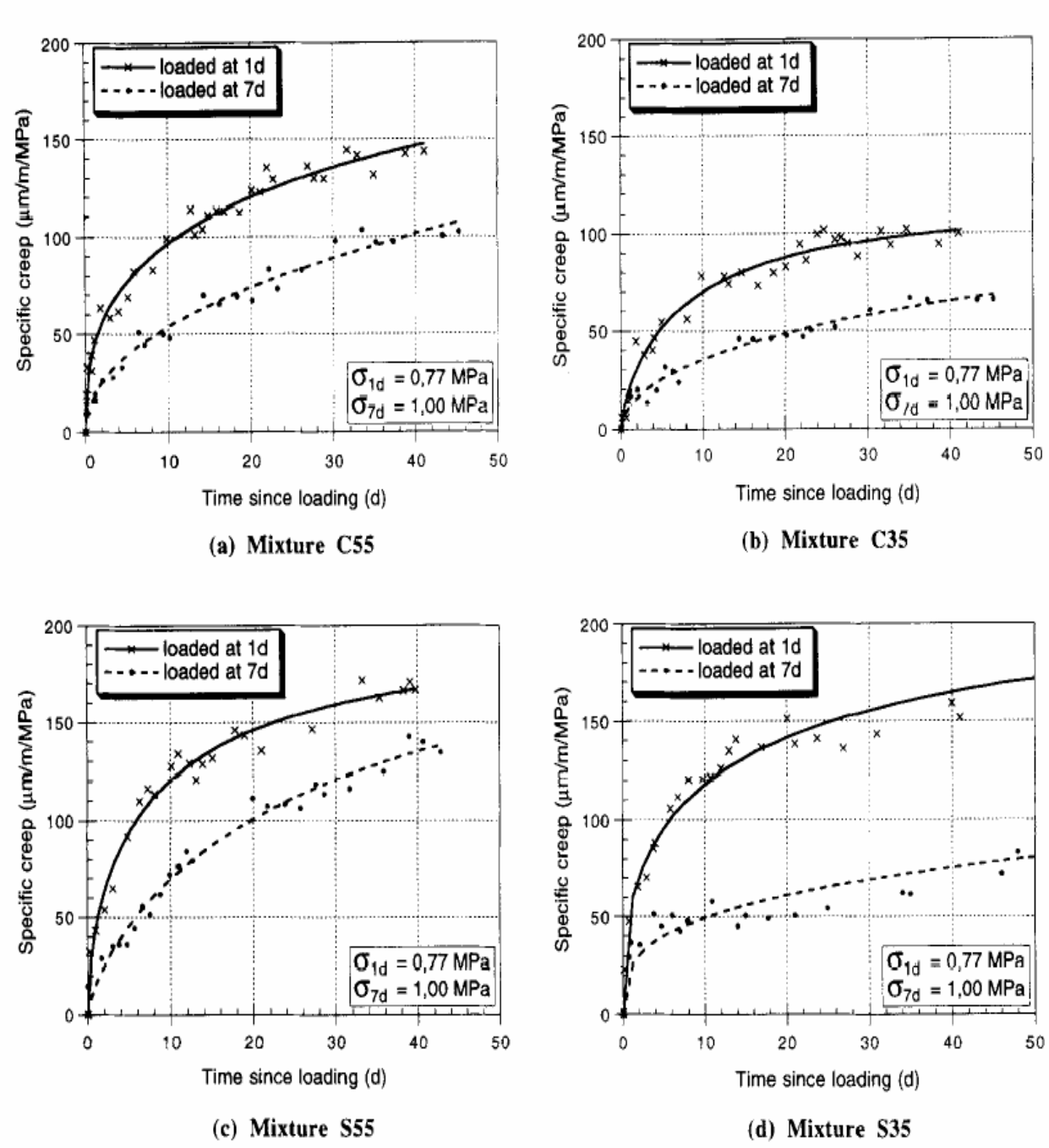

Figure B-14. Specific total tensile creep at 50 percent relative humidity of two concrete mixtures (ordinary and with silica fume) at two water-cement ratios (0.55 and 0.35) (from Bissonnette and Pigeon, 1995).

Other factors that influence creep are the magnitude of applied tensile stresses and the age at loading as shown in Figure B-15 by Ostergaard et al. (2001). The greater the applied tensile stress (load) and the earlier the load is applied, the higher the tensile creep strains that are developed. These results are similar to those observed by Bissonnette and Pigeon (1995) as shown in Figure B-14. For concrete pavement slabs, the tensile stresses at the top of the slab (for an upward curled slab) and at the bottom of the slab (for a downward curled slab) are provided by the restraints such as load transfer with adjacent slabs, slab self-weight, and friction between the slab and the base. These factors, therefore affect the amount of creep in a concrete slab.

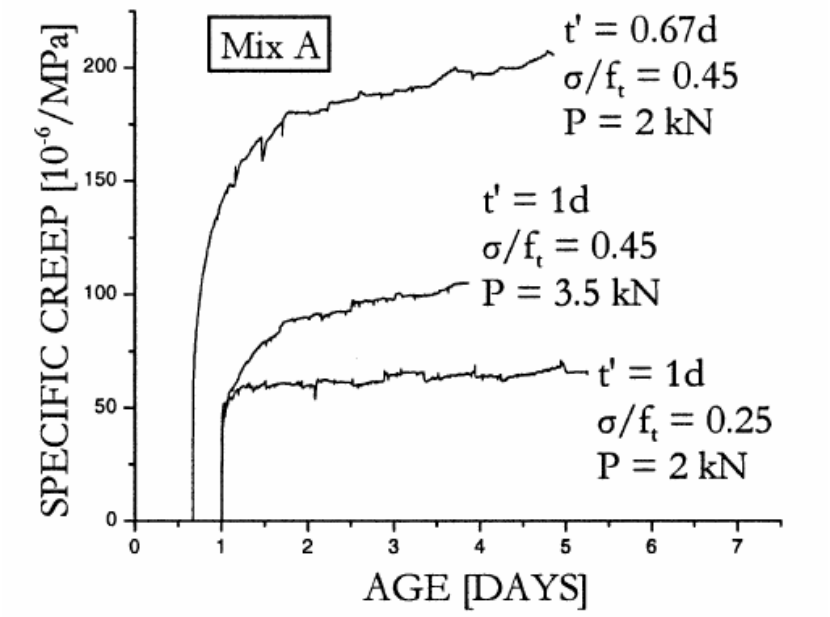

Figure B-15. Effect of applied load and age at loading on tensile creep (from Ostergaard et al., 2001).